Titre: Title:	Flow-Induced Vibrations of In-Line Cylinder Arrangements at Low Reynolds Numbers
Auteur: Author:	Kintak Raymond Yu
Date:	2014
Type:	Mémoire ou thèse / Dissertation or Thesis
Référence: Citation:	Yu, K. R. (2014). Flow-Induced Vibrations of In-Line Cylinder Arrangements at Low Reynolds Numbers [Thèse de doctorat, École Polytechnique de Montréal]. PolyPublie. https://publications.polymtl.ca/1571/

Document en libre accès dans PolyPublie
Open Access document in PolyPublie

URL de PolyPublie: PolyPublie URL:	https://publications.polymtl.ca/1571/
Directeurs de recherche: Advisors:	Dominique Pelletier, Stéphane Étienne, & Alexander Hay
Programme: Program:	Génie mécanique

UNIVERSITÉ DE MONTRÉAL

FLOW-INDUCED VIBRATIONS OF IN-LINE CYLINDER ARRANGEMENTS AT LOW
REYNOLDS NUMBERS

KINTAK RAYMOND YU
DÉPARTEMENT DE GÉNIE MÉCANIQUE
ÉCOLE POLYTECHNIQUE DE MONTRÉAL

THÈSE PRÉSENTÉE EN VUE DE L'OBTENTION
DU DIPLÔME DE PHILOSOPHIÆ DOCTOR
(GÉNIE MÉCANIQUE)
NOVEMBRE 2014

UNIVERSITÉ DE MONTRÉAL

ÉCOLE POLYTECHNIQUE DE MONTRÉAL

Cette thèse intitulée :

FLOW-INDUCED VIBRATIONS OF IN-LINE CYLINDER ARRANGEMENTS AT LOW
REYNOLDS NUMBERS

présentée par : YU Kintak Raymond
en vue de l'obtention du diplôme de : Philosophiæ Doctor
a été dûment acceptée par le jury d'examen constitué de :

M. TRÉPANIER Jean-Yves, Ph.D., président
M. PELLETIER Dominique, Ph.D., membre et directeur de recherche
M. ÉTIENNE Stéphane, Doctorat, membre et codirecteur de recherche
M. HAY Alexander, Ph.D., membre et codirecteur de recherche
M. GOSSELIN Frédérick, Doctorat, membre
M. OLIVIER Mathieu, Ph.D., membre externe

ACKNOWLEDGEMENT

RÉSUMÉ

Les vibrations induites par sillage (*Wake-Induced Vibration* ou WIV en anglais) est un type d'interactions fluide-structure qui peut se produire quand deux corps ou plus, montés élastiquement, sont disposés l'un derrière l'autre dans un écoulement transverse. Dans cette configuration, le corps situé en aval est soumis non seulement à son propre lâcher tourbillonnaire mais également à celui généré par le cylindre amont. Par conséquent, le corps aval peut osciller fortement avec des amplitudes maximales pouvant atteindre A/D=10 (Paidaussis *et al.* (2011)). Les WIV sont encore mal connues. Même un leader mondial en classification dans le domaine de l'ingénierie offshore ne sait pas comment traiter les phénomènes d'interférences entre plusieurs colonnes montantes avec WIV (Det Norske Veritas (2009)). La plus part des études effectuées considèrent simplement une configuration en tandem d'une paire de cylindres. Peu d'études ont été réalisées avec plus de deux corps montés élastiquement.

En 2009, Étienne *et al.* ont considéré 3 cylindres arrangés en ligne dans un écoulement uniforme. Pour un nombre de Reynolds de 200 et une vitesse réduite de 8, ils ont montré par simulation numérique que les cylindres pouvaient subir de fortes oscillations. En 2013, Oviedo-Tolentino *et al.* ont étudié expérimentalement les oscillations de 10 cylindres placés les uns derrière les autres pour un facteur de masse amortissement de $m^*\zeta = 0.13$. Ils ont confirmé que le troisième cylindre, c'est à dire celui placé derrière les deux premiers, peut subir des oscillations transverses plus importantes encore que celles subies par le deuxième cylindre. Ces grandes oscillations peuvent non seulement causer une fatigue excessive des matériaux mais également provoquer des collisions entre les cylindres. Ainsi, les WIV peuvent poser de sérieux problèmes lors de la conception de nombreux systèmes en ingénierie.

À la lumière de ces études récentes, il est donc nécessaire d'approfondir l'étude des comportements de plusieurs corps placés les uns derrière les autres dans un écoulement transverse et montés élastiquement. Mise à part les fortes oscillations observées, de nombreux aspects des WIV de plusieurs cylindres en ligne restent très mal connus : les réponses fréquentielles et les amplitudes maximales produites, l'influence du nombre de Reynolds de l'écoulement, les effets dus à des ratios de masse ou des facteurs de masse amortissement faibles, etc.

Cette thèse vise à explorer numériquement les réponses d'oscillations induites par sillage de 3 cylindres circulaires disposés en ligne et ayant un nombre de masse faible et un amortissement nul pour de faibles nombres de Reynolds. Pour atteindre cet objectif de recherche, on procède en trois étapes.

La première étape consiste à s'assurer que l'outil numérique utilisé pour effectuer les simulations est correctement implémenté. Les tests de vérification du code sont basés sur

la méthode de la solution manufacturée pour des problèmes d'interactions fluide-structure où la structure peut être modélisée comme un corps rigide. Aucune solution manufacturée pour de type de problèmes n'est disponible. Ainsi on a développé une procédure générique pour produire des solutions manufacturées afin de vérifier les codes de calcul d'interactions fluide-structure. Cette procédure est appliquée à des cas bi- et tridimensionnels.

Dans une deuxième étape, on étudie les réponses des Vibrations Induites par Vortex (VIV) à bas nombres de Reynolds d'un cylindre isolé ayant un ratio de masse nulle $m^* = 0$ et qui peut osciller librement dans les directions parallèle (X) et transverse à l'écoulement (Y). Cette étude est nécessaire car les WIV sont souvent comparées aux VIV mais les réponses d'un cylindre à ratio de masse faible et à bas nombres de Reynolds sont mal documentées dans la littérature puisque l'on trouve des résultats très variés. Ainsi, on a effectué une étude paramétrique sur le nombre de Reynolds et la vitesse réduite. Ces résultats sont comparés avec ceux des oscillations XY pour $m^* = 1$ d'une part ; et avec ceux des oscillations Y seules pour les deux ratios de masse. Ces études ont montré que pour un ratio de masse nul, l'amplitude maximale des oscillations XY est d'environ $A_Y = 0.9D$ alors que si seuls les mouvements suivant Y sont permis on trouve $A_Y = 0.6D$. Par ailleurs, contrairement à la littérature existante, on a observé que les amplitudes maximales d'oscillations sont influencées par le nombre de Reynolds. Par ailleurs, les amplitudes maximales ne sont pas observées pour la même valeur de la vitesse réduite pour tous les nombres de Reynolds. Enfin, le nombre de masse critique est de $m^*_{\text{critique}} = 0.117$ pour les oscillations Y seules et de $m^*_{\text{critique}} = 0.106$ pour les oscillations XY.

Une comparaison entre les résultats obtenus et des études expérimentales pour un nombre de masse faible et des nombres de Reynolds modérément élevés indique que les réponses ne sont pas identiques. Cependant, nos résultats à bas nombres de Reynolds reproduisent l'essentiel des caractéristiques des réponses pour des nombres de Reynolds plus élevés. Par conséquent, la simulation à bas nombres de Reynolds des VIV, et par extension des WIV, permet de représenter qualitativement les caractéristiques principales des réponses à nombres de Reynolds plus élevés.

Dans une troisième partie, on étudie les réponses des vibrations induites par sillage de 3 cylindres circulaires disposés en ligne. On considère des ratios de masse faibles et un amortissement nul à bas nombres de Reynolds. On compare ces résultats avec ceux de 2 cylindres en tandem et ceux d'un seul cylindre dans les mêmes conditions. La présence du troisième cylindre induit des différences significatives par rapport au cas de 2 cylindres en tandem. L'amplitude maximale des oscillations a été augmentée d'environ 30% dans la direction transversale. En outre, de très grandes oscillations sont observées dans la direction de l'écoulement pour des vitesses réduites supérieures à 9. Ces oscillations peuvent être aussi importantes que

celles observées dans la direction transversale. Clairement, ces grandes oscillations dans les deux directions peuvent entraîner une fatigue importante des matériaux. Et, les oscillations dans la direction selon laquelle les cylindres sont alignés augmentent considérablement les chances de collisions entre les cylindres. Une autre caractéristique intéressante est que le spectre en fréquence est beaucoup plus riche. En particulier, une composante basse fréquence est présente pour les deuxième et troisième cylindres. Par ailleurs, les diagrammes de phase et les cartes de Poincaré montrent que les effets non-linéaires ont été augmentés de façon spectaculaire avec l'introduction du troisième cylindre. Ce résultat est confirmé par les importantes variations observées dans les structures tourbillonnaires. Ainsi, même à ces faibles nombres de Reynolds, les réponses de vibrations de 3 cylindres en ligne semblent posséder un caractère chaotique. Ce système dynamique fluide-structure semble approcher le chaos par la voie quasi-périodique. Sur la base de nos résultats de VIV à 2 degrés de liberté, on peut raisonnablement penser que les réponses seront encore plus grandes et chaotiques à des nombres de Reynolds plus élevés. En conclusion, étant donné le caractère chaotique des réponses de 3 cylindres en ligne, il est très risqué de prédire leurs comportements en extrapolant les résultats de 2 cylindres en tandem. L'effet des WIV doit être pleinement considéré lorsque plusieurs corps sont disposés en ligne dans un écoulement transverse.

ABSTRACT

Wake-induced vibration (WIV) is a type of fluid-structure interaction (FSI) that may occur when there are two or more elastically mounted bodies, arranged one after the other, in a cross flow. Here, the downstream body is not only affected by the vortices generated behind the body itself, but also is subjected to the influence of the wake developed behind the upstream body. Under these two disturbances, the downstream body can develop severe oscillations with a maximum amplitude as large as $A/D = 10$ (Paidoussis et $al.$ (2011)). The knowledge of WIV is still so limited that even in the recommended practice for riser interference from a world class leader in offshore engineering classification does not know yet how to consistently incorporate the consideration of WIV (Det Norske Veritas (2009)). Most investigations consider the configuration with a tandem cylinder pair placed in a uniform flow. Very little is known when there are more than two elastically mounted structural bodies.

In a brief investigation, Etienne et $al.$ (2009) numerically showed that three freely oscillating cylinders arranged in-line, in a uniform flow at the Reynolds number of $Re = 200$ and at a fixed reduced velocity of $U_r = 8$, can develop significant vibrations. A recent original experiment by Oviedo-Tolentino et $al.$ (2013), who studied the oscillation response of ten collinear cylinders with a medium large mass-damping factor ($m^*\zeta = 0.13$) placed in a uniform flow, confirmed that the cylinders behind the second one can develop transverse oscillations that are actually larger than those of the second cylinder. These more severe oscillations, not only can cause fatigue of material, but also can potentially lead to collisions among the cylinders. These conditions pose great challenges for engineering design.

Based on these recent findings, it is therefore important to take a closer look at the behavior of multiple elastically mounted bodies arranged in-line placed in a cross flow. Apart from the more significant oscillations observed, many important aspects about WIV of multiple in-line cylinders, $e.g.$ the low mass ratio, the low mass-damping factor, the maximum oscillation amplitude, the frequency responses, and the effect of Reynolds number, $etc.$, remain essentially unknown.

This thesis aims to numerically explore the wake-induced vibration responses of three circular cylinders with low mass ratio and zero damping arranged in-line at low Reynolds number in order to advance the fundamental engineering knowledge regarding multiple elastically mounted in-line bodies placed in a cross flow. To reach this research goal, we have identified three specific objectives.

We first verify the correctness of the numerical code using the method of manufactured solution for fluid-structure interaction problems; for which the structure can be modeled as a

rigid body. The manufactured solution for such class of FSI problem has yet to be reported. We have developed a generic systematic synthesis procedure to construct a manufactured solution which can be well applied to any FSI problem. We demonstrate the feasibility of the synthesis procedure with two dimensional and three dimensional problems.

Then, we establish the benchmarking limiting vortex-induced vibration (VIV) responses of an isolated cylinder, having zero mass ratio $m^* = 0$, which can freely oscillate in both the streamwise and the transverse directions (XY oscillation) at low Reynolds numbers. This is needed since the responses of WIV are often compared with those of VIV, and the results for VIV of an isolated cylinder with low mass ratio at low Reynolds numbers are rather scattered. More specifically, we perform a parametric study with respect to the Reynolds number and the reduced velocity. For comparisons, we also determine the XY oscillation responses with $m^* = 1$, and the responses of transverse-only (Y-only) oscillation with both mass ratios. We observe that for a cylinder with $m^* = 0$, the peak transverse oscillation amplitude for XY oscillation is about $A_Y = 0.9D$ and for Y-only oscillation, it is about $A_Y = 0.6D$. In contrast to the results reported in the literature, we observe that at the laminar flow regime, the peak oscillation amplitude is also affected by an increase of Reynolds number. Also, the location of the peak oscillation amplitude will not always occur at the same reduced velocity for all Reynolds numbers. The critical mass ratio for Y-only oscillation is about $m^*_{critical} \approx 0.117$ and $m^*_{critical} \approx 0.106$ for the XY oscillation.

A comparison between our present results with the experimental results of an isolated cylinder, with small mass ratio at moderately high Reynolds numbers, demonstrates that although the two responses are not entirely the same, the low Reynolds number responses do carry the essential of the high Reynolds number response characteristics. Therefore, simulations at low Reynolds number for the problems of vortex-induced vibrations, and naturally for wake-induced vibration as well, shall be able to qualitatively represent the overall characteristics of the oscillation responses at higher Reynolds numbers.

Finally, we examine the wake-induced vibration responses of three circular cylinders with low mass ratio arranged in-line at low Reynolds number. We compare the results of the three freely oscillating cylinders arranged in-line with those of a tandem cylinder pair and those of an isolated cylinder under the same conditions. The presence of the third cylinder induces distinctive different responses as compared to the case of the tandem cylinder pair. The maximum oscillation amplitude has been increased for about 30% in the transverse direction. However, significant oscillations now appear in the streamwise direction at above the reduced velocity of $U_r \approx 9$ which can be as large as those in the transverse direction. There is no doubt that these excessive oscillations in both the streamwise and transverse directions can cause severe material fatigue. The significant streamwise oscillation amplitudes, in particular,

also largely increase the probabilities of collisions among the cylinders. Another interesting characteristics is that the frequency spectrum of the response is generally very rich and there is now a clear dominant low frequency component, in particular for the second and the third cylinders. Overall, the phase diagram and the Poincaré map show that the nonlinearity has been increased dramatically with the introduction of the third cylinder. This is confirmed with the substantial variations observed in the vortical structure pattern. Even at such low Reynolds numbers, the free oscillations of three in-line cylinders already seem to approach a chaotic response. In particular, there is evidence that fluid-structure system approaches to chaos via the quasi-periodic route. Based on our two degrees of freedom VIV results, we can expect even more complex and severe oscillation responses at higher Reynolds number. We conclude that due to such high level of nonlinearities, it is therefore highly risky to predict the free oscillation behaviors of multiple in-line cylinders by extrapolating those of the tandem cylinder pair. The effect of wake-induced vibrations must be properly addressed when multiple in-line bodies may be subjected to a cross flow.

TABLE OF CONTENTS

LIST OF TABLES

LIST OF FIGURES

CHAPTER 1

INTRODUCTION

1.1 Background

Fluid-structure interaction (FSI) refers to the complex mutual influence between structures and the fluids nearby. Under the influence of surrounding flow, structures may deform, be displaced or even develop oscillations. The movements of the structures can, in turn, change the characteristics of the flow field; which results in different effects onto the structure inducing other structural motions. Fluid-structure interaction gives rise to plenty of fascinating complex fluid and structural dynamic phenomena which are at the same time of practical significance. Consequently, this phenomenon has become a recent focal point of research.

Many structures are in the form of circular cylinders, in particular those in engineering applications. Naturally, there is a lot of interests in understanding fluid-structure interactions for cylindrical structures. The classification of these phenomena is generally based upon the configuration and the number of the cylinders involved as well as the characteristics of the surrounding flow. Typically, investigations are based on experiments. With the recent advancement of computer technologies, numerical simulations are also frequently employed, especially for flow conditions at low Reynolds numbers.

Wake-induced vibration (WIV) is a type of fluid-structure interaction, under the subgroup of flow-induced vibration (FIV), that may occur when there are two or more elastically mounted bodies, arranged one after the other, in a cross flow. For example, in offshore engineering applications, multiple risers may be subjected to such a condition depending on the incoming flow direction. Another example is the overhead power transmission line bundle under cross wind. Here, the downstream body is not only affected by the vortices generated behind the body itself, but also is subjected to the wake developed behind the upstream body. Under these two influences, the downstream body can develop severe oscillations with the maximum amplitude measured from peak to peak as large as $A/D = 10$ (Paidoussis *et al.* (2011)). Most wake-induced vibration investigations consider the configuration with a tandem cylinder pair placed in a uniform flow. Many aspects of wake-induced vibrations still remain largely unknown. In particular, the knowledge of wake-induced vibrations is so limited that even in the recommended practice for riser interference from a world class leader in offshore engineering classification does not know yet how to consistently incorporate the consideration of wake-induced vibrations (Det Norske Veritas (2009)).

The responses of the wake-induced vibration are often compared with those of the vortex-induced vibrations (VIV), which consider the structural vibrations caused only by the vortices shedded behind a single elastically mounted isolated structure in cross flow without the impinging wake coming from upstream. Logically, many aspects of this simpler problem have been better understood. Two recent research topics include the characterization of the vortex-induced vibration responses when the isolated body is allowed to move in both the streamwise and the transverse directions, as well as when the structure is of a low mass ratio. The latter aspect is particularly important for offshore engineering application.

Much less is known regarding the free oscillation characteristics when there are more than two elastically mounted structural bodies placed in a cross flow. In a brief investigation, Etienne *et al.* (2009) numerically showed that three freely oscillating cylinders arranged in-line, in a uniform flow at the Reynolds number of $Re = 200$ and at a fixed reduced velocity of $U_r = 8$, can develop significant vibrations. How would the response characteristics vary when the reduced velocity changes? A more recent original experiment of ten collinear cylinders, with a medium large mass-damping factor ($m^*\zeta = 0.13$), placed in a uniform flow, Oviedo-Tolentino *et al.* (2013) confirmed that the cylinders behind the second one can develop transverse oscillations that are actually larger than those of the second cylinder. What would be the oscillation characteristics when the mass-damping factor is small (an essential factor in offshore engineering application)? Unfortunately, apart from the more significant oscillations observed, many important aspects about wake-induced vibrations of multiple in-line cylinders, *e.g.* the low mass ratio, the low mass-damping factor, the maximum oscillation amplitude, the frequency responses, and the effect of Reynolds number, *etc.*, remain essentially unknown. Certainly, they deserve further investigations.

The more severe oscillations, not only can cause fatigue of material, but also can potentially lead to collisions among the cylinders. These conditions pose great challenges for engineering design safety. Based on these recent findings, it is therefore important to take a closer look at the behavior of multiple elastically mounted bodies arranged in-line placed in a cross flow. The results will contribute to advancements in fundamental engineering knowledge. The implication from the findings may ultimately demand a revision of the safety best practice for offshore engineering riser interference.

1.2 Research goal, objectives and methodology

This thesis aims to numerically explore the wake-induced vibration responses of three circular cylinders with low mass ratio and zero damping arranged in-line at low Reynolds numbers in order to advance the fundamental engineering knowledge regarding multiple elastically

mounted in-line bodies placed in a cross flow.

We first verify the correctness of the numerical code using the method of manufactured solution for the fluid-structure interaction problems; for which, the structure can be modeled as a rigid body. Manufactured solution for such case has yet to be reported.

Then, we establish the limiting vortex-induced vibration responses of an isolated cylinder, having zero mass ratio $m^* = 0$, which can freely oscillate in both the streamwise and the transverse directions at low Reynolds numbers. For comparisons, we also determine the responses for the case with $m^* = 1$, and the responses of transverse-only oscillation with both mass ratios. This is necessary because the response of wake-induced vibrations are often compared with those of vortex-induced vibrations, and the results for the vortex-induced vibration responses of an isolated cylinder with low mass ratio at low Reynolds numbers are rather scattered.

After establishing the baseline vortex-induced vibration response reference, we then apply the tool to examine the wake-induced vibration responses of three circular cylinders with low mass ratios arranged in-line at low Reynolds number. In particular, we compare the results for the three cylinders case with those of a tandem cylinder pair and those of an isolated cylinder under the same conditions.

1.3   Outline of the chapters

After the introductory chapter, we will review relevant literature results in chapter 2. Chapter 3 contains more detailed discussion about the research objectives and methodology. The papers focused on the development of the manufactured solution, the limiting vortex-induced vibration responses at low Reynolds number, and the response characteristics of wake-induced vibrations of three in-line cylinders will be presented in chapters 4 to 6 respectively. In chapter 7, we will summarize and discuss the principal findings before the concluding chapter 8.

CHAPTER 2

REVIEW OF LITERATURE

In this chapter, we will review several relevant results in the literature regarding wake-induced vibrations and numerical simulations of fluid-structure interactions. Wake-induced vibrations are typically investigated with a cylinder pair arranged in tandem and the results are often compared with those of an isolated cylinder. In both cases, the cylinder(s) can either be fixed or can oscillate freely. We emphasize in those results of low mass ratio and at low Reynolds numbers.

Next, we will review several essential elements of numerical simulations of fluid-structure interactions. Two important considerations of numerical simulations are the correctness of the computational results and the efficiency of the numerical methods. We will outline the standard procedures to ensure the correctness of the computational fluid dynamics (CFD) results, namely code verification, calculation verification and validation. Lastly, we will briefly survey the subject of parallel computing which is the de-facto approach to improve computational efficiency.

2.1 FSI responses of an isolated cylinder and a tandem cylinder pair in uniform cross flow

We begin our review with the fundamental results of an isolated cylinder, followed by those of the tandem cylinder pair. In both cases, the results of the fixed cylinder(s) will be discussed before those of the freely oscillating cylinder(s).

2.1.1 Flow characteristics of uniform flow passing a fixed cylinder

The problem of uniform flow passing a fixed cylinder provides an opportunity to investigate the rich phenomena of vortex wake dynamics without the interference of the structural motion. The knowledge of vortex wake dynamics is the key to understanding the onset of vortex-induced vibration. For which, the oscillation of the cylinder is caused by the vortices shedded behind the cylinder itself.

There is a vast amount of research about uniform flow passing a fixed cylinder. Overall, the flow characteristic in the wake region is complex and involves interactions among the boundary layer, the separating free shear layer and the wake. These different flow components are schematically shown in figure 2.1.
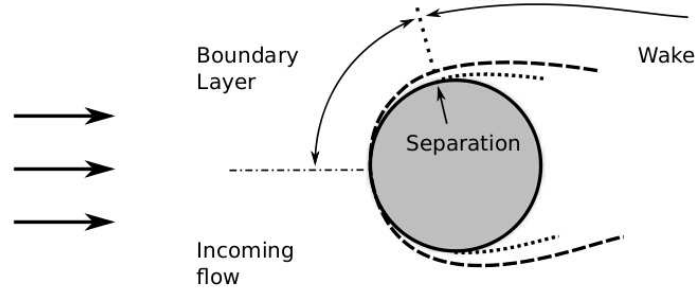
Figure 2.1 Flow region around a fixed cylinder. Based on Sumer (2006).

It has been found that uniform flow passing a fixed cylinder is strongly characterized by the Reynolds number of the cylinder:

$$Re = \frac{UD}{\nu} \tag{2.1}$$

where U is the free stream velocity, D is the diameter of the cylinder and ν is the kinematic viscosity of the fluid. When the Reynolds number increases from 0 to 10^7, the flow characteristics change in a sequence that can be classified into several "flow regimes".

In the following, we will take a brief look at several aspects of flow characteristics with respect to these flow regimes. In particular, we will discuss the basic mechanism of vortex shedding, the characteristics of the vortex shedding frequency and the forces by the flow on the fixed cylinder. We will also review recent findings about the three dimensional vortical structures. Lastly, we will briefly highlight some influencing factors for the flow characteristics.

Classification of flow regime
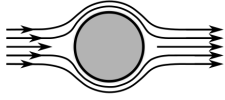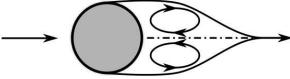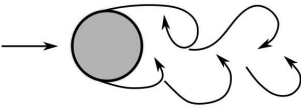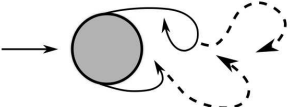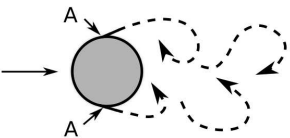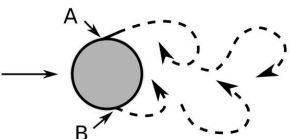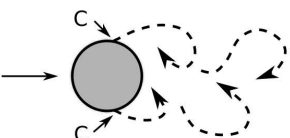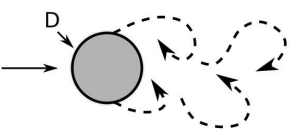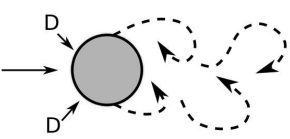
We begin with the classification of the flow regimes summarized in table 2.1. Note that for the terminology, the descriptions of the flow regimes and the associated ranges of Reynolds number, there are different preference among various researchers. Here, we follow the works of Roshko (1961), Schewe (1983), and Sumer (2006).

When $Re < 5$, no separation is observed.

For $5 < Re < 40$, a fixed pair of symmetric vortices are formed in the wake. An increase in the Reynolds number elongates the length of these symmetric vortices.

When $Re > 40$, the wake becomes unstable and vortices starts to be shedded alternatively one at time from each side of the cylinder. The collection of vortices shedded are often referred to as a vortex street. For $40 < Re < 200$, the vortex street remains laminar and it is nominally

Table 2.1 Flow regimes with respect to Re for a stationary circular cylinder in a uniform flow. (Sumer (2006)).

	No separation. Creeping flow.	$Re < 5$
	A fixed pair of symmetric vortices.	$5 < Re < 40$
	Laminar vortex street	$40 < Re < 200$
	Transition to turbulence in the wake.	$200 < Re < 300$
	Wake fully turbulent. A: Laminar boundary layer (BL) separation.	$300 < Re < 3 \times 10^5$ Subcritical
	A: Laminar BL separation. B: Turbulent BL separation; but BL laminar.	$3 \times 10^5 < Re < 3.5 \times 10^5$ Critical (Lower transition)
	C: Turbulent BL separation. BL partly laminar, partly turbulent.	$3.5 \times 10^5 < Re < 1.5 \times 10^6$ Supercritical
	D: BL fully turbulent (one side).	$1.5 \times 10^6 < Re < 4 \times 10^6$ Upper transition
	D: BL fully turbulent (both sides).	$4 \times 10^6 < Re$ Transcritical

two dimensional. Williamson (1996) observed that three dimensional flow features start to occur only at $Re \approx 190$.

As the Re is increased above 200, transition towards turbulence begins to occur in the following sequence. First, it appears in the wake region. Then, the interface between the laminar and turbulent regions gradually migrates upstream towards the cylinder to the separation points. Next, the separation point becomes turbulent. And eventually, the boundary layer itself also becomes turbulent.

More specifically, for $200 < Re < 300$, turbulence can be observed in the wake and the vortex shedding pattern becomes distinctly three-dimensional.

For $Re > 300$, the wake becomes fully turbulent. However, both the upper and lower boundary layer separation points remain laminar. The range of $300 < Re < 3 \times 10^5$ is called subcritical flow regime.

For $3.0 \times 10^5 < Re < 3.5 \times 10^5$, the boundary separation point is laminar on one side, but turbulent on the other. The asymmetric flow condition results in a non zero mean lift on the cylinder. This regime is called the critical flow regime (or the lower transition regime). Schewe (1983) mentioned that the side exhibiting turbulent boundary separation may occasionally change to the other side depending on flow condition.

The supercritical flow regime refers to the Re range of $3.5 \times 10^5 < Re < 1.5 \times 10^6$. Here, the boundary layer separation are turbulent on both sides. The interface between the laminar and turbulent regions are now somewhere between the stagnation point and the turbulent separation points.

At $Re \approx 1.5 \times 10^6$, the boundary layer on one side becomes completely turbulent. But the boundary layer remains partly laminar and partly turbulent on the other side. This flow characteristics remains in the upper-transition flow region ($1.5 \times 10^6 < Re < 4.5 \times 10^6$).

For $Re > 4.5 \times 10^6$, the boundary layer on the cylinder is essentially fully turbulent. The flow regime is called transcritical.

Vortex shedding mechanism

Here, we describe the basic mechanism of vortex shedding proposed by Gerrard (1966). From table 2.1, we see that vortex shedding is essentially present in all flow regimes (except for $Re < 5$). Common to all these different flow regimes, boundary layer separation occurs at around the widest section of the cylinder due to the great adverse pressure behind the cylinder. At the boundary layer separation locations, shear layers are formed. Since the flow velocity at the shear layer closer to the free stream is higher than that near the cylinder, the shear layers roll up inward and form vortices (Blevins (2000)). For $Re < 40$, the wake is steady and symmetric vortices pair are formed.

Vortex shedding begins at $Re = 40$. At this moment, the wake becomes unsteady and the symmetric vortices pair now become unstable such that one vortex may grow larger than the other (Sumer (2006)). Referring to figure 2.2(a), the larger vortex (I) eventually become strong enough to draw the smaller vortex (II) to travel across the wake towards itself. Note that the two vortices rotates in opposite directions: the top vortex rotates in the clockwise direction while the bottom vortex rotates in the anti-clockwise direction. The smaller vortex (II) gradually approaches the base of the large vortex (I), and eventually cuts off the supply of vorticity to the larger vortex from its boundary layer. At this moment, the large vortex (I) detaches (or sheds off) from the cylinder and is advected downstream by the flow. The originally smaller vortex (II) now becomes the larger one and as illustrated in figure 2.2(b), it in turn attracts a new smaller vortex (III). The vortices are shedded alternately from the two sides of the cylinder.

Hence, we see that vortex shedding can only happen when there are interactions between the two vortex group adjacent to the body. There are researches attempting to prohibit vortex shedding by interfering with interactions of the two adjacent vortex group (Sumer (2006)).
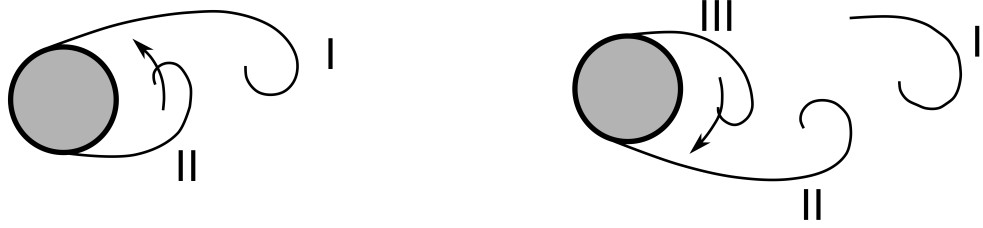
(a) Before shedding vortex I.   (b) Before shedding vortex II.

Figure 2.2 Basic mechanism of vortex shedding. Based on Sumer (2006).

Vortex shedding frequency

The vortex shedding frequency is often non-dimensionalized in the form of the Strouhal number St as follows:

$$St = \frac{f_f D}{U} \tag{2.2}$$

where f_f is the vortex shedding frequency, U is the free stream velocity and D is the diameter of the cylinder. The Strouhal number depends strongly on the Reynolds number as it is shown in figure 2.3.
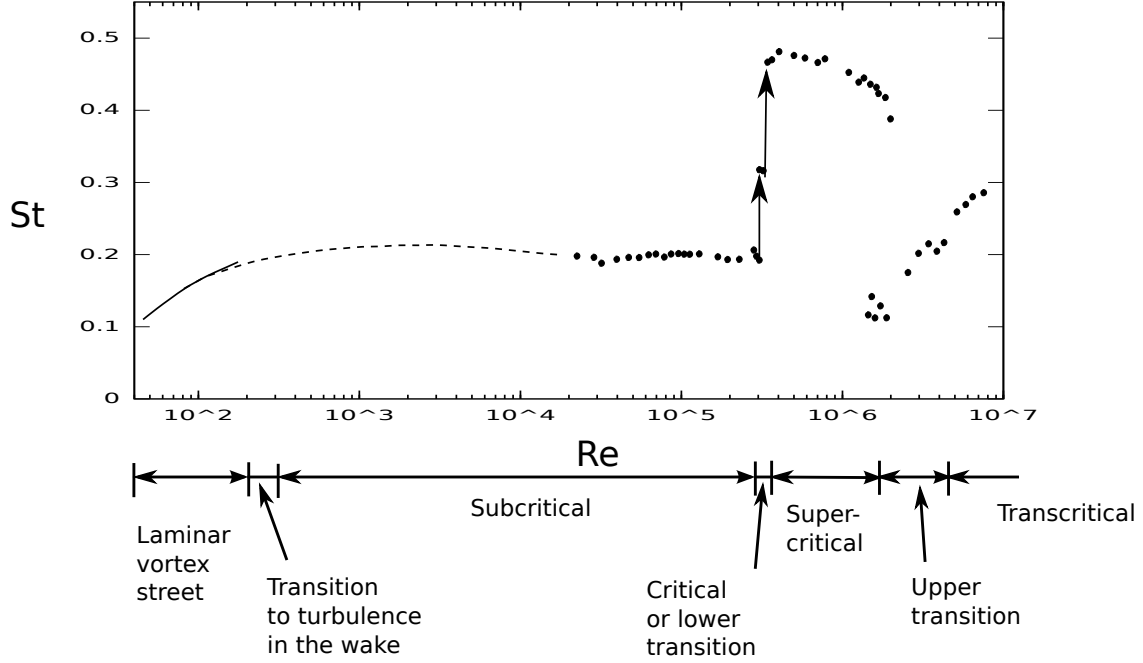
Figure 2.3 Experimental data of Strouhal number for a circular cylinder. Solid line: Williamson (1989), Dash line: Roshko (1961), Dots: Schewe (1983) (Sumer (2006)).

We see that the Strouhal number varies rather smoothly across a large range of Reynolds number. When the Re increases from about 40 to 300, the St increases gradually from 0.1 to 0.2. The Strouhal number remains at around 0.2 throughout the subcritical range. When the Re increases through the critical range towards the supercritical range, the St increase suddenly from 0.2 to 0.4. As the Re is further increased, the St decreases slightly.

Recall that when the Re is in the critical range, the boundary layer separation point is changing from laminar to turbulent. The turbulent boundary layer separation location is in fact further downstream than the laminar one. This is illustrated in figure 2.4. In other words, the two boundary layer separation locations are closer to each other. Hence, more rapid interactions between the upper and lower vortex groups are now possible. As a result, the Strouhal number increases.

As the Strouhal number is rather steady for the Reynolds number below the critical range, it is therefore possible to express the Strouhal as a mathematical function of Reynolds number in a precise manner. Fey et $al.$ (1998) obtain such empirical formulas for the Reynolds number range $47 < Re < 2 \times 10^5$.
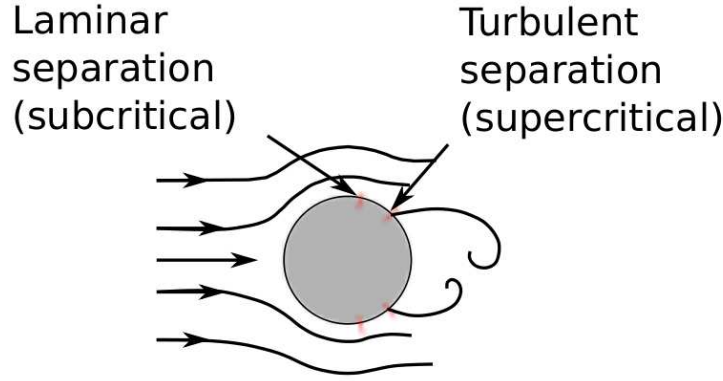
Figure 2.4 Separation locations behind a fixed circular cylinder (Sumer (2006)).

On Forces on the fixed cylinder

The fluid around the cylinder will exert a resultant force on the cylinder. The main contribution to the total force is due to the pressure. Typically, the total force is decomposed into the drag and the lift force components in the in-line and cross flow directions respectively.

For $Re > 40$, the flow becomes oscillatory and vortex shedding occurs. The pressure field around the cylinder undergoes periodic variation and as a consequence, the force components become periodic as well. The drag and the lift forces may be further decomposed into the mean and fluctuating components for analysis purposes.

For a circular cylinder, the mean drag force $\overline{C}_D$ has a definite value. The drag force generally fluctuate around its mean value. On the other hand, the mean lift force $\overline{C}_L$ is nil. In other words, the lift force simply fluctuates around zero.

The fluctuation frequency in the force components is directly related to the vortex shedding frequency. Typically, a vortex is shedded one at a time from each side in an alternative manner. The lift force fluctuating frequency is found to be generally the same as the vortex shedding frequency. Whereas that of the drag force fluctuation is usually double that of the vortex shedding frequency.

The mean drag $\overline{C}_D$ is a function of the Reynolds number Re (Sumer (2006)), and it is shown in figure 2.5. The $\overline{C}_D$ decreases steadily with Re until $Re \approx 300$. Then, $\overline{C}_D$ becomes almost a constant at around 1.2 at the Reynolds number range between 300 and 3×10^5. At $Re = 3 \times 10^5$, $\overline{C}_D$ decreases dramatically to a very low value of 0.25. The mean drag remains at around this low value throughout the supercritical range and then slowly increases after $Re > 1.25 \times 10^6$.

This abrupt fall of the mean drag is commonly referred to as the drag crisis. Recall that
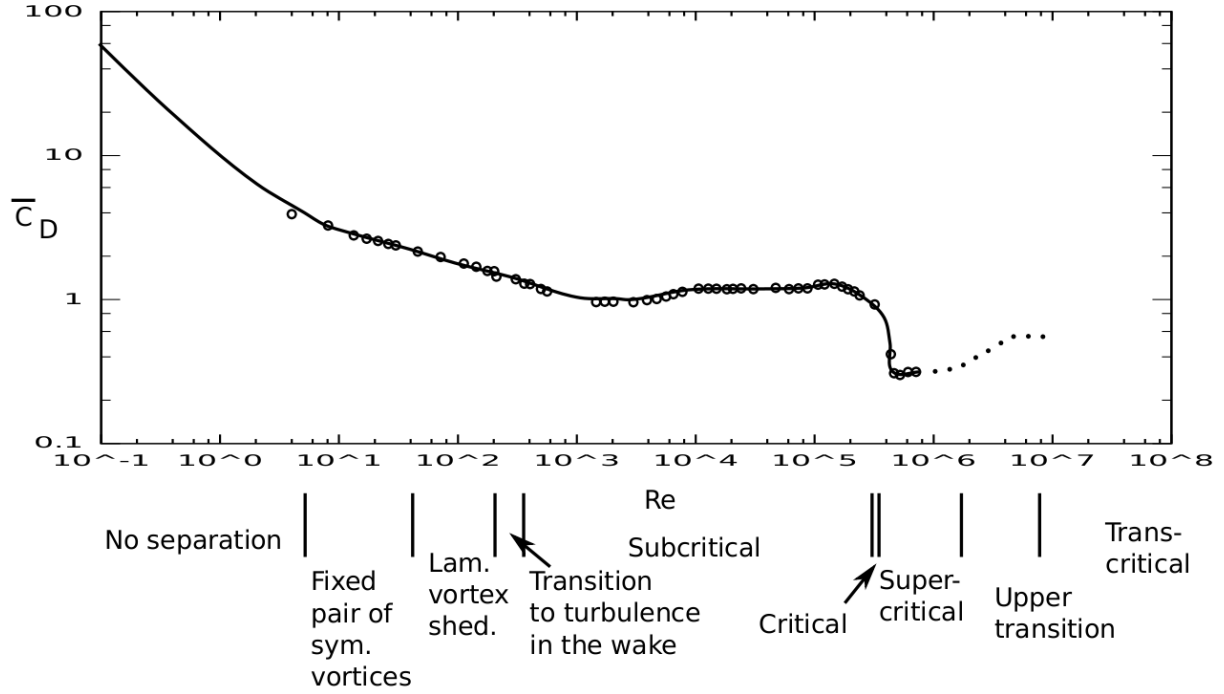
Figure 2.5 Mean drag for a fixed cylinder with respect to *Re*. (Sumer (2006))

when the flow regime changes from the subcritical to the supercritical regime, the separation points shift backward towards the wake. This has been illustrated in figure 2.4. This shift leads to a narrower wake region. In the wake region, the pressure on the cylinder is rather constant and it is smaller than that at the front of the cylinder. Hence, the overall pressure gradient across the cylinder in the streamwise direction decreases which results in a smaller drag force.

The fluctuating fluid forces can be analyzed statistically by examining the corresponding root mean square values. Experimental measurements collected by Hallam *et al.* (1977) showed that the fluctuating forces, especially the lift force, also decrease sharply when the flow regime changes from the subcritical to the supercritical regimes. The main reason is that in the supercritical flow regime, the interaction between the vortices in the wake region becomes weaker. As discussed above, the separation points are now much closer to each other and the vortices do not have as much opportunity to grow. Sumer (2006) also mentioned that this is due to the boundary layer separation becoming turbulent.

Recent findings on three dimensional flow features

For uniform flow passing a fixed cylinder, three dimensional flow features exist for Reynolds numbers above 190. To obtain accurate simulation results, it is essential to have 3-D flow

features properly considered. In particular, Williamson (1996) demonstrated that when there exists three dimensional flow features, two dimensional simulations may significantly over predict the forces and the amplitudes as compared with experimental data. On the other hand, two dimensional simulations remain highly valuable due to their much lower computational requirements to gain insights in particular for nominally two dimensional flow phenomena.

The principal three dimensional vortex structures for uniform flow passing over a fixed cylinder are summarized in table 2.2.

These results suggest that for investigations at low Reynolds numbers ($Re < 200$), even if three dimensional flow features may begin to exist, it should be reasonable to assume that they remain weak. In such cases, two dimensional simulations should be sufficiently accurate, but much more cost-effective than three dimensional simulations. For more details regarding three dimensional flow features for a fixed isolated cylinder in a uniform cross flow, we refer the interested reader to Williamson (1996).

Some factors influencing vortex shedding

Vortex shedding characteristics can be affected by many factors (Sumer (2006)). We highlight the main factors in table 2.3.

As expected, these factors can also affect the force coefficients. Since we limit our investigation to smooth circular cylinders, the above factors will not be considered in the present work. We refer the interested reader to Sumer (2006).

On effects of cylinder motion

When the cylinder is allowed to move, the alternating forces from the vortices will naturally cause cylinder body to oscillate. The motion of the cylinder in turns influences the vortex shedding patterns in the wake. This is especially so when the cylinder is oscillating at or near the vortex shedding frequency. Blevins (2000) summarized the effects as follows:

1. Increase vortex strength.

2. Increase spanwise correlation.

3. Synchronize the vortex shedding frequency with that of the cylinder motion (lock-in).

4. Increase mean drag.

5. Change the phase, sequence and pattern of vortices in the wake.

These effects are the basis of the vortex-induced vibration which will be reviewed in more details next.

Table 2.2 Three dimensional vortex structures for uniform flow passing over a fixed cylinder.

Re	Regime	Flow feature
$40 < Re < 190$	Laminar vortex street	Oblique vs Parallel shedding
$Re \sim 180 - 194$	Laminar vortex street	Mode A ($\lambda \sim 3D$ to $4D$) shedding
$230 < Re < 250$	Transition to turbulence in wake	Mode B ($\lambda \sim 1D$) shedding
$190 < Re < 260$	Laminar $\rightarrow$ Transition to turbulence in wake	Presence of Vortex Dislocations
$260 < Re < 1 \times 10^3$	Disorder $\Uparrow$ in fine-scale 3-D	Presence of fine-scale streamwise vortex structure
$1 \times 10^3 < Re < 2 \times 10^5$	Shear-Layer Transition	Kelvin-Helmholtz instabilities at the separating shear layers of the two sides of the body, Expect 3-D structures on the scale of shear layer and Kármán vortices.

Table 2.3 Key influencing factors for vortex shedding process

Factor	Key effect
Surface roughness	Rough surface promote earlier transition to turbulence response.
Cross section shape	Case by case.
Turbulence in incoming flow	Promote earlier transition to turbulence response.

2.1.2 Fundamentals of vortex-induced vibrations

Vortex-induced vibration is an important fluid-structure interaction phenomenon. The name of vortex-induced vibration highlights the underlying mechanism for the vibration responses. There have been extensive studies on vortex-induced vibrations in the past four decades (Sarpkaya (2010)). A set of important non-dimensional parameters have been identified. Generally, investigations attempt to examine the characteristics of the vibration responses (*e.g.* maximum amplitude, lift and drag forces, *etc.*) and flow patterns, and their changes when the non-dimensional parameters are varied. Sarpkaya (2010) remarks that the importance of the non-dimensional parameters change throughout the parameter space.

Some common non-dimensional parameters are listed in table 2.4. In the expressions, f_f is the vortex shedding frequency in the fluid. f_s is the natural frequency of the structure. For which, there are two common choices: $f_s = f_n = \sqrt{k/m_s}/(2\pi)$ the natural frequency in vacuum and $f_s = f_{n-w} = \sqrt{k/(m_s + m_a)}/(2\pi)$ the natural frequency in still water, where m_s is the mass of the structure, $m_a = C_A m_d$ the added mass and m_d the displaced fluid mass. Note that the added mass coefficient C_A for a circular cylinder is simply $C_A = 1$. The mass ratio may refer to two different expressions. Apart from what we listed in the table, some authors alternatively refer to the expression $m_s/(\rho_f D^2)$ as the mass ratio (Blevins (2000)). The mass ratio is sometimes called as the reduced mass (Paidoussis *et al.* (2011)).

Many different aspects of the vortex-induced vibration have been investigated. As mentioned in Williamson & Govardhan (2004) and Sarpkaya (2004), most studies focus on the fundamental behavior of the transverse vibrations (one degree of freedom) of an isolated cylinder in a uniform flow. One key characteristic is the "lock-in" effect, for which, there is a range of the reduced velocity such that the frequencies of the vortex-shedding and vibrations

Table 2.4 Common non-dimensional parameters for flow-induced vibrations.

Parameter	Symbol	Expression
Reynolds number	Re	$\frac{UD}{\nu}$
Strouhal number	St	$\frac{f_f D}{U}$
Reduced velocity	U_r	$\frac{U}{f_s D}$
Mass ratio	m^*	$\frac{\rho_s}{\rho_f}$
Amplitude ratio	A^*	$\frac{A}{D}$
Frequency ratio	f^*	$\frac{f}{f_s}$

are synchronized, and vibrations of large amplitudes are observed. Another key characteristic is that when the reduced velocity is varied in the "lock-in" range, the response is not smooth but exhibits "branches". Hysteresis is observed at the transitions between branches. The typical responses for an isolated cylinder under vortex-induced vibration are shown in figures 2.6 and 2.7.

Characteristics with respect to mass ratio

The shapes and appearances of the branches change with the mass-damping factor $m^*\zeta$. The damping ratio is often very small in actual applications. Hence, in practice, we can consider that the influence is principally due to the mass ratio m^*. For a large value of m^*, one can observe two branches: the initial and lower branches. Decreasing m^* to small values, the upper branch now appears between the initial and the lower branches. A smaller m^* also leads to a wider interval of lock-in reduced velocities and a larger maximum amplitude value. These variations can be observed in figure 2.6. Note that the influence of mass ratio are not the same for the maximum oscillation amplitude and the frequency responses. Comparing figures 2.6 and 2.7, we can see that while a mass ratio of $m^* = 10$ provokes a change in the response characteristics of the maximum oscillation amplitude, there is no observable difference in the corresponding oscillation frequency response with those of a larger mass ratio. A different pattern of oscillation frequency response appears when the mass ratio becomes smaller at $m^* = 2.4$ (see figure2.7). If we further decrease the mass ratio below a
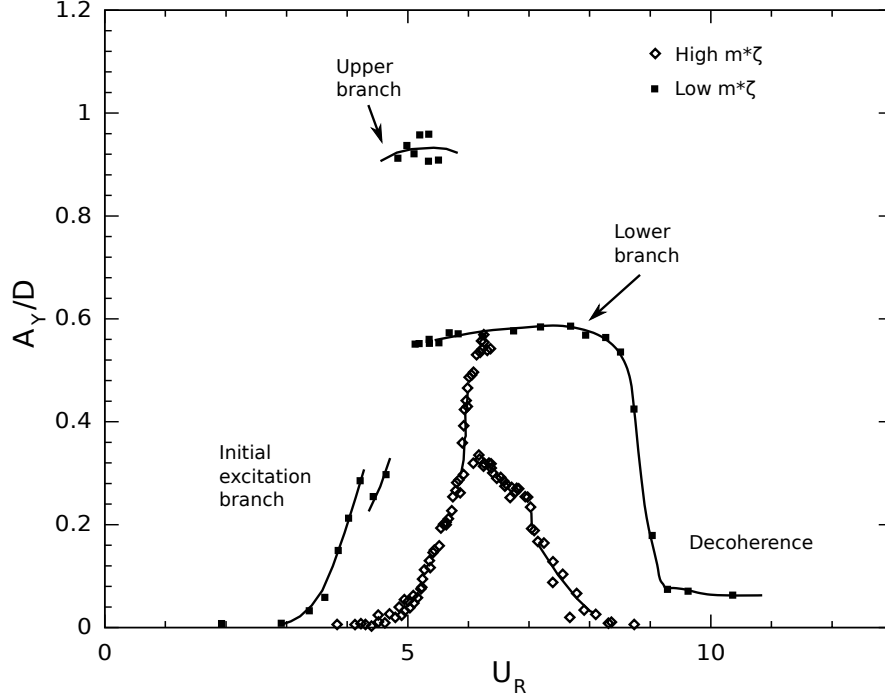
Figure 2.6 Typical peak oscillation amplitude response of an isolated cylinder under VIV (Khalak & Williamson (1999)). The high $m^*\zeta$ result is contributed by Feng (1968) with $m^*\zeta = 0.36$ and $m^* = 248$. The low $m^*\zeta$ result is contributed by Khalak & Williamson (1999) with $m^*\zeta = 0.013$ and $m^* = 10.3$. The natural frequency of the cylinder is that in still water.

certain "critical" value, the lower branch eventually disappears and merges with the upper branch. Govardhan & Williamson (2002) showed experimentally that a vibration amplitude of 0.8D can still be attained even at "infinite" reduced velocity, *e.g.* when the stiffness of the cylinder is very low. In other words, when the mass ratio is smaller than the critical value, there is no desynchronization. For the hysteresis responses, Prasanth *et al.* (2011) demonstrated numerically that the blockage and the mass ratios are two important factors for the hysteresis behavior between the initial and the lower branches in the laminar shedding regime. In particular, for certain combination of the two factors, the hysteresis between the initial and the lower branches may be completely suppressed.

Characteristics of vortex flow pattern

The corresponding flow field is generally described in terms of the observed vortex pattern. The change of vortex patterns is associated with a change of branches (Williamson & Govardhan (2004)). The major vortex patterns identified include {2S, 2P, 2C, 2T} which are illustrated in figure 2.8.
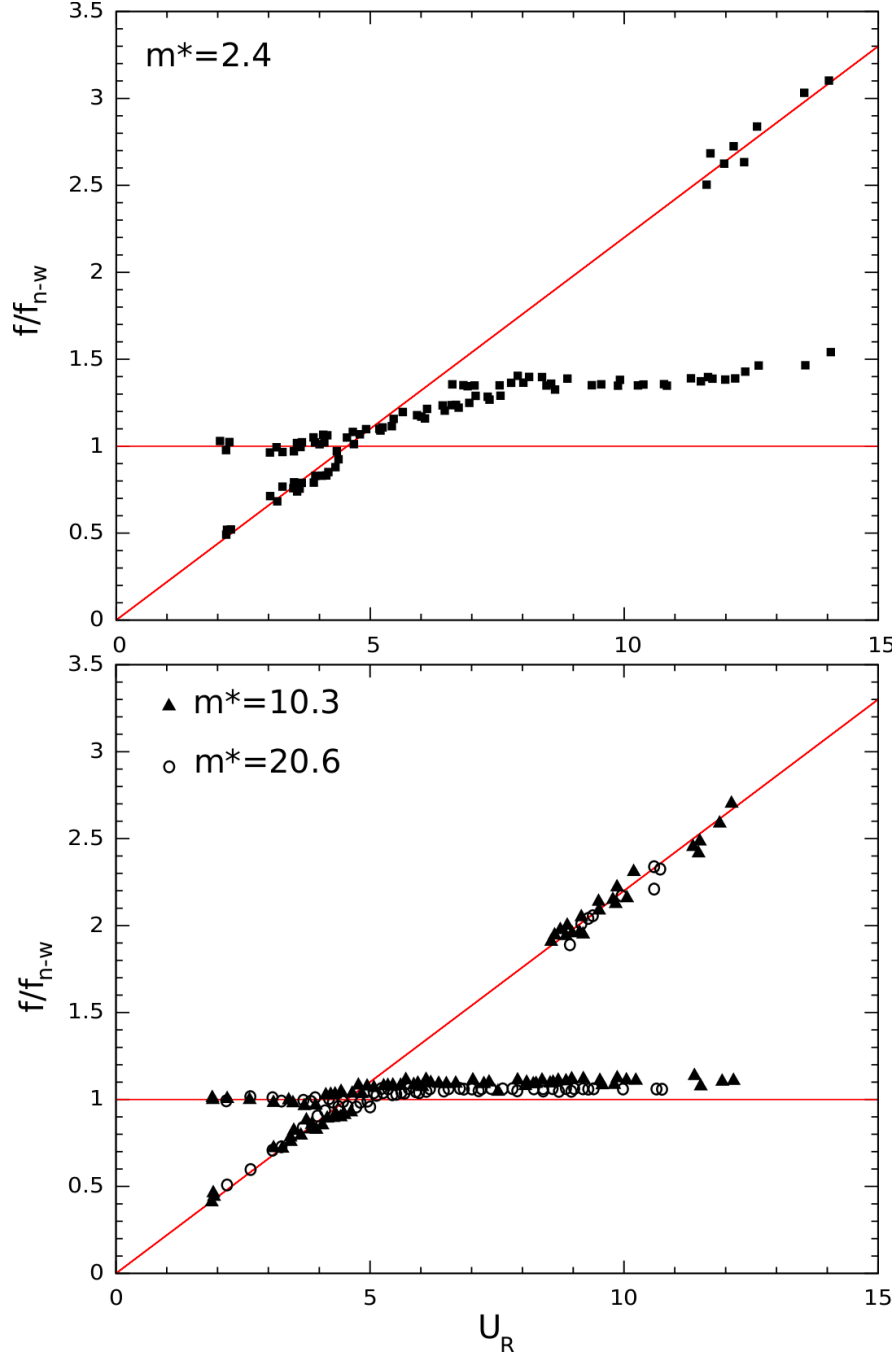
Figure 2.7 Typical frequency response of an isolated cylinder under VIV (Khalak & Williamson (1999)). Noted that the natural frequency of the cylinder is that in still water in this work.

Characteristics with two degrees of freedom

Recently, the importance of the streamwise vibration and its interactions with the transverse vibrations have been recognized (Aglen & Larsen (2011)). Streamwise vibrations generally

(a) 2S (Single)

(b) 2P (Pair)

(c) 2C (Co-rotating)

(d) 2T (Triplet)
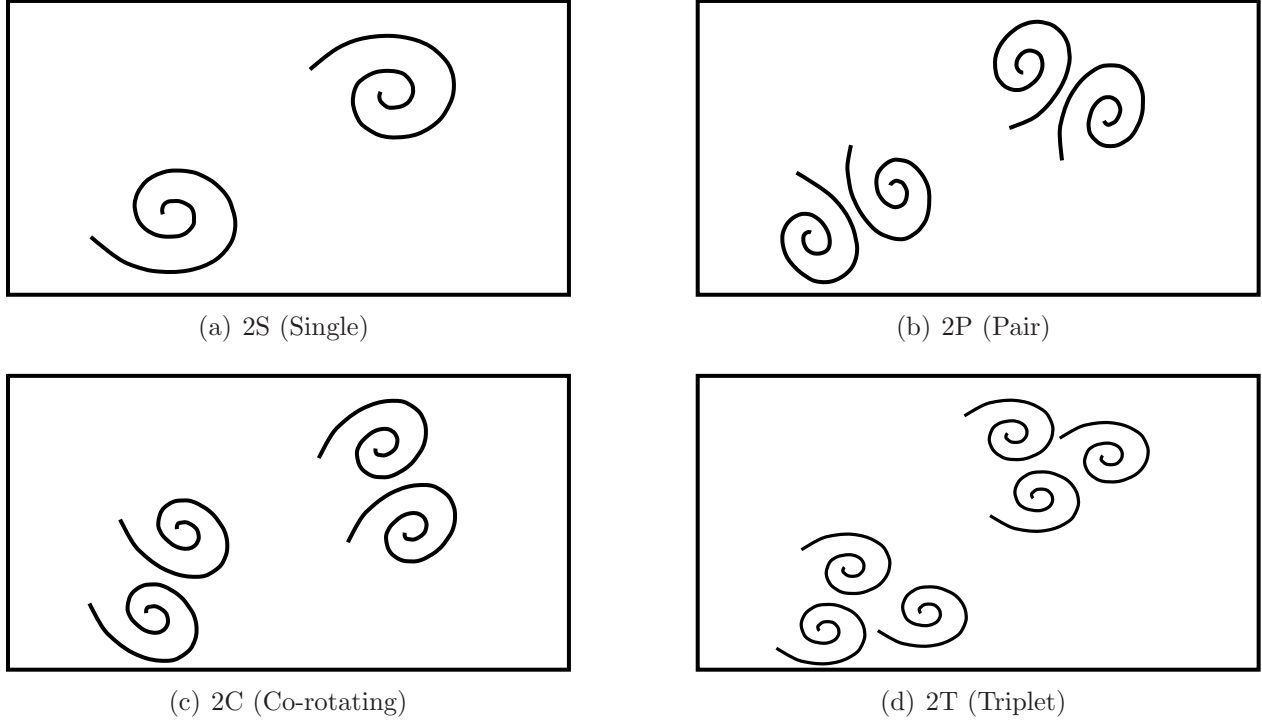
Figure 2.8 Vortex shedding patterns (Jauvtis & Williamson (2004)).

have smaller amplitude than transverse vibrations, and their lock-in range usually occurs at a frequency twice that of the transverse vibration. However, streamwise vibration can occur at very low ambient velocity. Thus, streamwise vibration can occur more often than the transverse vibration and hence, can have major impacts on equipment fatigue. Jauvtis & Williamson (2004) investigated the fundamental two degrees of freedom responses for vortex-induced vibrations at moderate values of the Reynolds number in the range of 1000 to 15000. For mass ratios above 5 or 6, the envelope of the transverse vibration amplitude for such cylinder resembles that of a cylinder that vibrates transversely only. When the mass ratio is reduced below 5, they discovered that the maximum transverse amplitude can be significantly greater than those (the upper branch) found in vortex-induced vibration response of transverse only oscillations. They describe this new branch of response as the super-upper branch. The vortex pattern (2T) is identified when the system is on the super-upper branch. The typical two degrees of freedom vortex-induced vibration responses are shown in figure 2.9.

Characteristics at low Reynolds number

Most of the vortex-induced vibration investigations were carried out in the moderate or high Reynolds number range ($Re > 10^3$). In the laminar shedding regime ($Re < 200$),
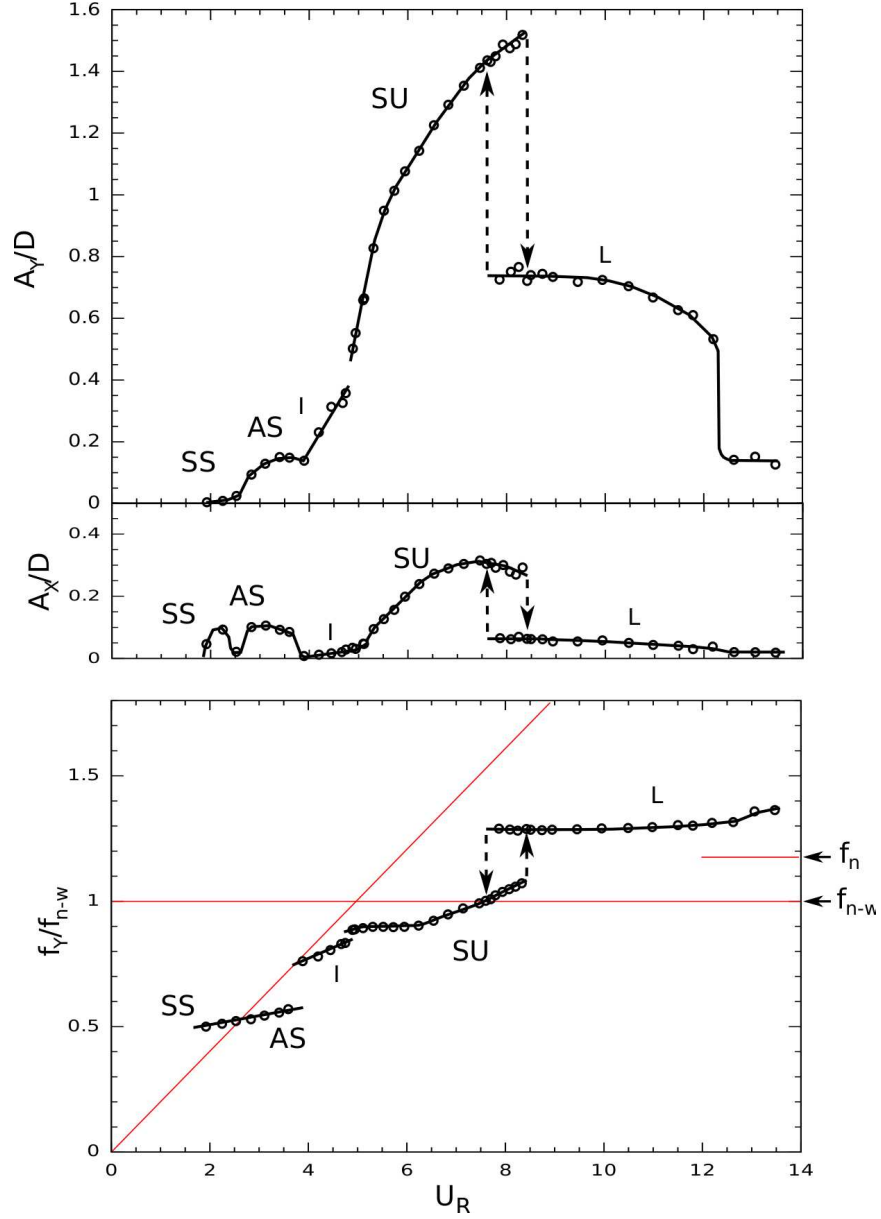
Figure 2.9 Typical XY oscillation response with low mass ratio (Jauvtis & Williamson (2004)).

there is only one experimental study and a handful of detailed numerical investigations. In most of these studies, the mass ratios of the cylinder considered are generally large. Anagnostopoulos & Bearman (1992) investigated experimentally the vortex-induced vibration response of a cylinder ($m^* = 149$) with transverse only oscillation for Reynolds numbers in the range of 90 to 150. The maximum amplitude is 0.55D. Shiels *et al.* (2001) studied this problem numerically with no damping and no structural mass ($m^* = 0$) at $Re = 100$. They obtained the maximum amplitude of 0.59D. Placzek *et al.* (2009) investigated forced and free vibrations for a cylinder that oscillates only transversely at $Re = 100$. The maximum

transverse amplitude was found to be 0.58D. However, the value of mass ratio employed was not evident as the simulation results were presented in terms of the "effective rigidity". Singh & Mittal (2005) studied computationally the two degrees of freedom vortex-induced vibration response for a cylinder with $m^* = 10$ with two settings. First, they investigated the problem at a fixed value of Reynolds number $Re = 100$ and varied the reduced velocity from 4 to 8.5. Then they examined the problem with a fixed reduced velocity ($U_r = 4.92$) and varied the Reynolds numbers between 50 and 500. The reduced velocity was chosen to be $U_r = 4.92$ because that is the location of the maximum peak for $Re = 100$. They assumed that the peaks for the other Reynolds numbers would also occur at the same reduced velocity. The maximum transverse amplitude response was about 0.6D in their investigations. Prasanth & Mittal (2008) investigated the two degrees of freedom vortex-induced vibration problem numerically for the range of Reynolds number: $60 < Re < 200$. In this work, the natural frequency of the cylinder with $m^* = 10$ is fixed and the free stream flow velocity is varied. The maximum transverse amplitude A_Y is found to be about 0.6D which is about 30 times larger than the maximum in line amplitude A_X. They found that there are only two branches of response: the initial and the lower branches. At the desynchronization range of the lower branch at higher Re, hysteresis is always observed. At the transition from the initial to the lower branch at the lower Re range, hysteresis may appear if the blockage ratio is larger than 5%. Note however that, $m^* = 10$ is considered large in the study of Jauvtis & Williamson (2004). In this case, the response is expected to be similar to that of the cylinder which oscillates transversely only. The maximum transverse amplitude A_Y of 0.6D is in accordance with the results compiled by Williamson & Govardhan (2004) for the vortex-induced vibration of a cylinder in the laminar shedding regime and the analysis from forced oscillation results.

Singh & Mittal (2005) observed that the vortex shedding modes in the laminar shedding region include the 2S mode and the C(2S) mode. In the 2S mode, a single vortex is shedded from each side of the cylinder in the vortex shedding cycle. The C(2S) mode is a variation of the 2S mode during which, the vortices "coalesce" in the wake region. Prasanth & Mittal (2008) noticed that when the mode switches from the 2S mode to the C(2S) mode, the oscillation amplitude can jump from a low value to a higher level. Note that the work of Prasanth & Mittal (2008) was executed with the cylinder spring stiffness fixed and the inlet flow velocity varied which simultaneously changes both the reduced velocity and the Reynolds number. Placzek *et al.* (2009) suggested that since there is no 2P mode for the laminar shedding regime, which is confirmed by the direct numerical simulation (DNS) results of Newman & Karniadakis (1997), the upper branch may not actually exist for the vortex-induced vibration response in this regime. The 2P mode is associated with the change from the initial branch to the upper branch at higher Reynolds number.

Remark on low mass ratio

For applications like piping in deep water oil exploration projects, the mass ratios can be small (*i.e.* order of one) (Stappenbelt & Lalji (2008)). Hence, there is a practical need to understand the effects of low mass ratio on vortex-induced vibrations to enhance design safety.

Despite the findings of Jauvtis & Williamson (2004), Sanchis *et al.* (2008) did not observe the super-upper branch, nor the regular upper branch for a cylinder with a low mass ratio $m^* = 1.04$ and a high mass-damping ratio $\alpha = (m^* + C_A)\zeta = 0.093$ at high Reynolds number $Re \approx 19000$. At low Reynolds number, the effect of low mass ratio on vortex-induced vibrations is yet to be systematically studied. Therefore, there is still much to understand regarding vortex-induced vibrations at low mass ratio, the limiting case being "zero" mass ratio.

On vortex-induced vibration model

Lastly, we briefly comment about modeling of vortex-induced vibration. The objective of modeling the vortex-induced vibration response is to be able to predict the physical behavior for those conditions that are not investigated by experiments. Various models have been proposed. They differ in their approaches to account for the effect of the flow field on the structure. Gabbai & Benaroya (2005) classify the models in two categories: semi-empirical and semi-analytical.

Semi-empirical models assume the form of the modeling equation of the fluid effects and generally require calibrations of model parameters with experimental data. The authors further classify the semi-empirical models into three groups: wake-oscillator coupled models, single degree of freedom models and force decomposition models. The wake-oscillator model employs an oscillator equation to represent the wake dynamics. A well known example is the use of a van der Pol type oscillator for the wake coupling with a rigid cylinder (Bishop & Hassan (1964), Hartlen & Currie (1970)). In other words, there is one equation for the fluid dynamics and one for the structure. On the other hand, both the single degree of freedom model and the force decomposition model only have one equation which represents the dynamics of the structure. These two models differ in the approaches to formulate the fluid force expression. For further details, please refer to the review by Gabbai & Benaroya (2005).

Benaroya & Wei (2000) have proposed a semi-analytical approach, based on the Hamilton's principle, for modeling vortex-induced vibration. In contrast to the models described above, their approach does not make any assumption about the form of the governing equa-

tion. However, the approach requires a detailed energy analysis around the selected control volume.

We remark that alternative classification exists. For example, Paidoussis *et al.* (2011) have proposed to classify the vortex-induced vibration models based on the nature of the fluidelastic force component. They suggest three categories:

- Forced system model - fluid force independent of structural dynamics,

- Fluidelastic system model - fluid force is a function of structural dynamics,

- Coupled system model - the fluid equation and the structural equations interacts with each other.

All the above models are particularly useful for providing the trends of the vortex-induced vibration response when the precise values of the responses (*e.g.* forces, amplitude, *etc.*) are not so important. An advantage is that these models are in general "applicable" even at very high Re. However, when it is necessary to obtain the responses precisely, we cannot rely on semi-empirical or semi-analytical models. With advances in computer technologies, we can determine the responses much more precisely by directly solving the governing equations, in particular for applications at low Reynolds number.

This concludes our review of vortex-induced vibrations. Next, we will look at the principal results of flow characteristics of uniform flow passing two fixed cylinders arranged in tandem.

2.1.3 Flow characteristics of a fixed tandem cylinder pair in uniform flow

The flow around two stationary cylinders in cross flow is highly dependent on the distance between the two cylinders, and the relative position with respect to the incoming flow. Zdravkovich & Pridden (1977) proposed a simple classification based on the arrangements of the two bodies into tandem, staggered and side-by-side configurations. Referring to figure 2.10, if we define α to be the angle between the line joining the centers of the two bodies and the incoming flow direction, then we will have $\alpha = 0^o$ for the tandem arrangement, $0^o < \alpha < \pm90^o$ for the stagger arrangement and finally, $\alpha = \pm90^o$ for the side-by-side arrangement.

Sumner (2010) provides a recent review of flow interference characteristics of two cylinders arrangement in cross flow. In figure 2.11, the most common classification of flow interference due to Zdravkovich (1985) is shown.

Wake-induced vibrations are strongest for the tandem (in-line) arrangement. For which, the second body is placed completely behind the first body in the streamwise direction. Lin *et al.* (2002) mentioned that the wake of the upstream cylinder modifies the incident vorticity
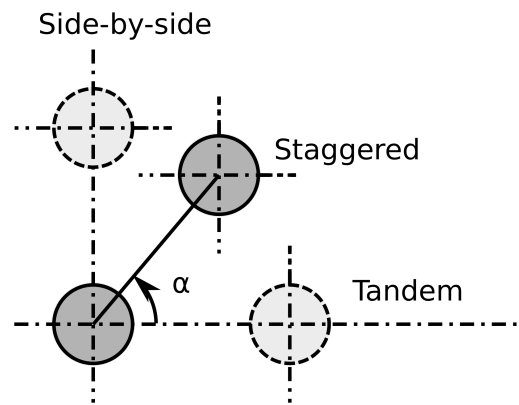
Figure 2.10 Classification of the arrangements of two cylinders.
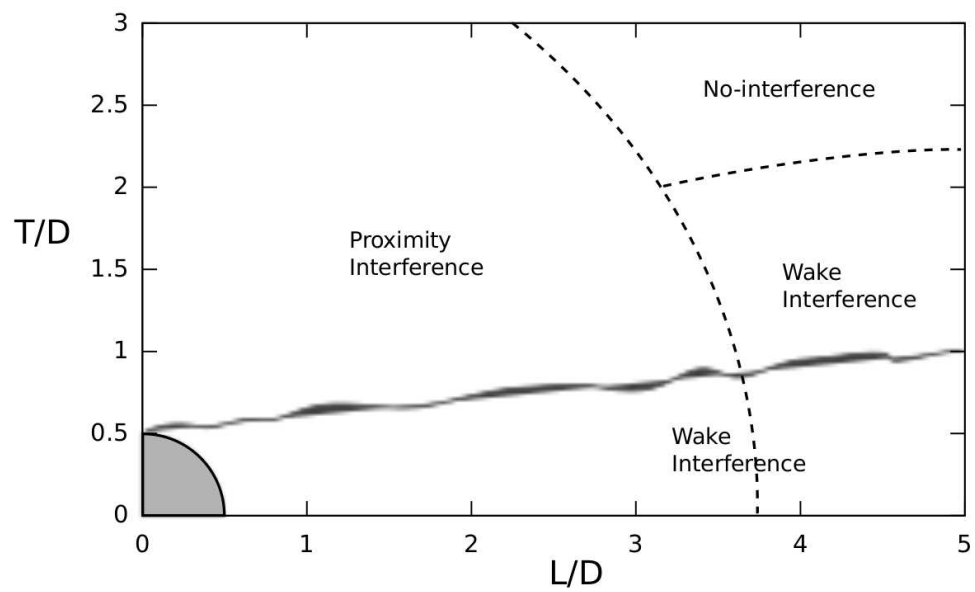
Figure 2.11 Classification of flow interference of two cylinders (Sumner (2010)).

field for the downstream cylinder. On the other hand, the downstream cylinder affects the wake dynamics and vortex formation region of the upstream cylinder. Lee & Basu (1997) commented that the upstream cylinder can be considered as a "turbulence generator" whereas the downstream cylinder can be considered as a drag-reduction device or wake stabilizer.

Sumner (2010) compiled a comprehensive list of the investigations of the tandem arrangement for various parameters in the literature. An important parameter for the tandem arrangement is the center to center separation ratio (L/D) where L is the distance between the centers of the two bodies and D is the characteristic diameter. The cylinders in tandem arrangement has been investigated experimentally at Reynolds number from as low as $Re = 100$ to the critical and post-critical regimes ($Re = 6.5 \times 10^5$) with two to five cylinders placed in-line at the separation ratio from $L/D = 1$ up to $L/D = 20$. The configuration has also been studied numerically, mostly at low Reynolds numbers.

The flow behavior of the tandem configuration is strongly influenced by the separation ratio L/D and the Reynolds number Re. Xu & Zhou (2004) and Zhou & Yiu (2006) classify the flow patterns loosely into three categories:

1. Extended-body regime ($1 < L/D < 2$)

2. Reattachment regime ($2 < L/D < 5$)

   - (I) Trailing end reattachment($L/D = 2$ to 3)
   - (II) Leading end reattachment($L/D = 3$ to 5)

3. Co-shedding regime ($L/D > 5$)

This is shown in figure 2.12. Note that these separation ratio marks above for the category division vary depending on the Reynolds numbers.

Extended-body regime

In the extended-body regime ($1 < L/D < 2$), the two cylinders are sufficiently close that they act as if they were a single bluff-body. Ishigai *et al.* (1972) observed that the downstream cylinder sits inside the vortex formation region of the upstream cylinder. The Kármán vortex shedding from the upstream cylinder is suppressed. The separated shear layers from the upstream cylinder become elongated and wrap around the downstream cylinder without any reattachment it. They continue to roll alternately into Kármán vortices behind the downstream cylinder.

Compared with an isolated cylinder, the Strouhal frequency is higher, especially at the beginning of the extended-body regime. This indicates that the vortex formation length for

(a) Extended-body regime.

(b) Reattachment regime (I).

(c) Reattachment regime (II).

(d) Co-shedding regime.
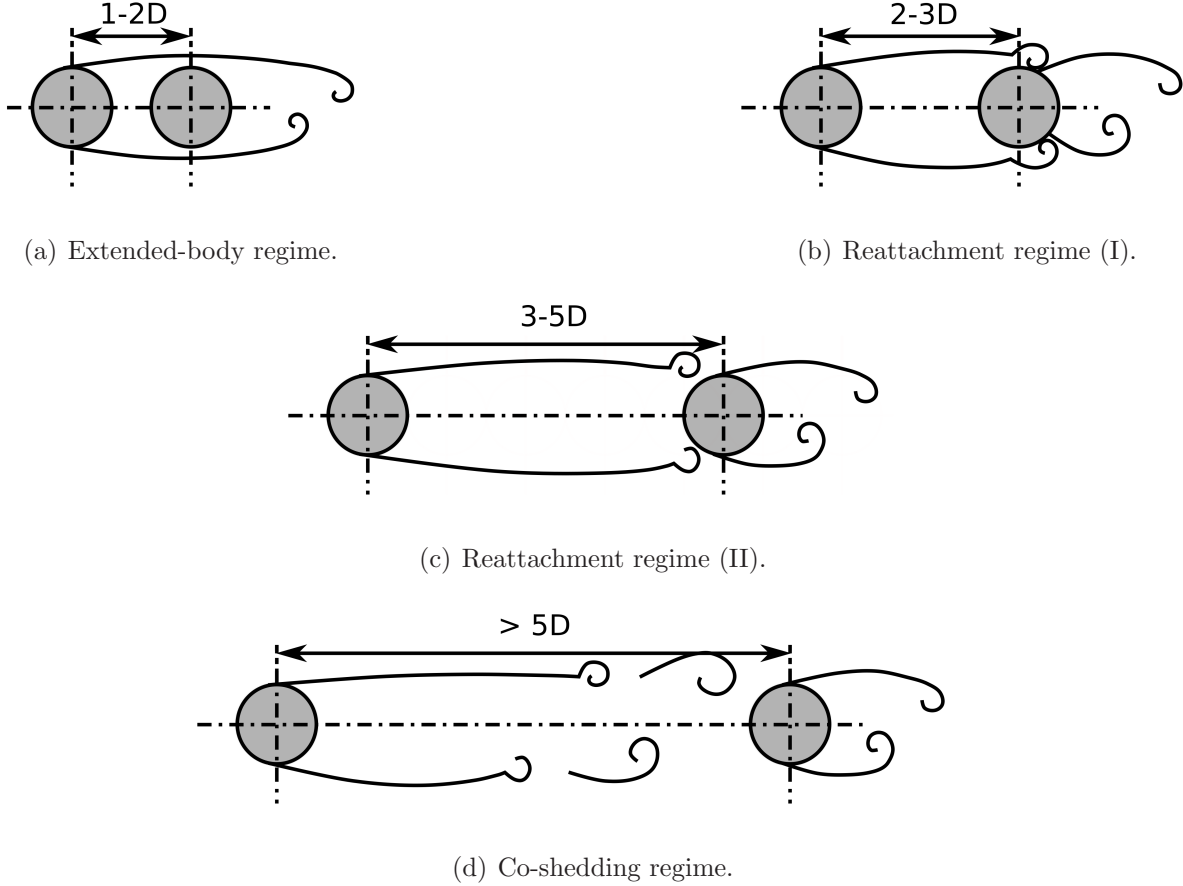
Figure 2.12 Classification of tandem flow regimes (Zhou & Yiu (2006)).

tandem cylinder pair is shorter than that of an isolated cylinder (Meneghini *et al.* (2001)). However the Strouhal frequency decreases rapidly as the separation ratio increases. Besides, the wake is also generally narrower (Lin *et al.* (2002)).

The downstream cylinder "acts" as a splitter plate for the upstream cylinder. This contributes to reduce the mean drag force of the upstream cylinder to be smaller than that of a fixed isolated cylinder Zhou & Yiu (2006). As for the downstream cylinder which is under the influences of the shear layers from the upstream cylinder, the mean drag coefficient of the downstream cylinder begins with a large negative value when the two cylinders are in contact. As the separation ratio increases from $L/D = 1$ to the boundary of this regime ($L/D \approx 2.4$), the mean drag coefficient gradually increases and reaches a "peak" of zero (Alam *et al.* (2003)).

For the upstream cylinder, there is only small unsteady force fluctuations. The downstream cylinder however experiences considerably larger force fluctuations for both drag and lift forces (Alam *et al.* (2003)).

Reattachment regime

In the reattachment regime ($2 < L/D < 5$), the separated free shear layers from the upstream cylinder reattach themselves onto the surface of the downstream cylinder, hence its name.

The regime can be further classified into two main sub-categories based on the reattachment location. For smaller separation ratio, the reattachment occurs more often at the back of the downstream cylinder. This disturbs the boundary layer development and separation on the downstream cylinder. As a result, the Kármán vortices formed behind the downstream cylinder are generally weak and small (Zhou & Yiu (2006)). Whereas for larger separation ratio, the vortices usually reattach themselves at the front of the downstream cylinder. The corresponding Kármán vortices from the downstream cylinder thus become stronger.

Inside the gap space between the two cylinders, the flow pattern becomes more complex and vortices may be formed. Notice that the shear layers enclosing the gap space can be oscillatory and may lead to shedding of vortices from the gap which interact with the vortices shedded from the downstream cylinder. The gap vortex shedding can be intermittent or periodic. The details of the complex gap flow dynamics are yet to be fully understood (Sumner (2010)).

When switching from the extended-body regime to the reattachment regime, the Strouhal frequency now decreases at a slower rate. The smaller Strouhal frequency, which is also lower than that of a fixed isolated cylinder, suggests that the downstream cylinder has a stabilizing effect to the overall flow dynamics (Sumner (2010)). Note that the transition from the extended-body regime to the reattachment regime is found to be bistable (Xu & Zhou (2004)).

In the reattachment regime, there is no streamwise vortical structure behind the upstream cylinder. The spanwise correlation in the wake of the downstream cylinder is also higher than that of an isolated cylinder. In other words, as compared with the isolated cylinder, three dimensional flow structures may only appear at higher values of the Reynolds number.

In this regime, the mean drag coefficients of both cylinders are still smaller than that of a fixed isolated cylinder. In particular, the mean drag coefficient of the upstream cylinder continues to decrease gradually as the separation ratio increases. That of the downstream cylinder also begins to decrease after the "peak" at $L/D \approx 2.4$ (Alam *et al.* (2003)).

As in the extended-body regime, the upstream cylinder is only subjected to small unsteady fluctuating forces. Whereas the downstream cylinders experience rather large unsteady fluctuating lift and drag forces (Alam *et al.* (2003)).

Interestingly, there are large peaks for both the drag and lift forces observed for the downstream cylinder at $L/D \approx 2.4$. Alam *et al.* (2003) experimentally found that the drag and lift fluctuation forces increase as "the position of reattachment proceeds forward (*i.e.*

towards the upstream cylinder) and vice versa." At $L/D \approx 2.4$, the reattachment position is the closest to the upstream cylinder.

Co-shedding regime

In the co-shedding regime ($L/D > 5$), the downstream cylinder is further away, in particular outside the vortex formation region of the upstream cylinder (Ishigai *et al.* (1972)), such that Kármán vortex shedding can now occur from both the upstream and downstream cylinders. Interestingly, the vortex shedding frequencies of both cylinders are identical. In particular, the Strouhal frequency is higher than those of the extended-body and reattachment regimes.

The Kármán vortices shedded from the upstream cylinder impinge onto the downstream cylinder periodically. Alam & Zhou (2007) comment that "the vortex shedding from the downstream cylinder is triggered by the arrival of the vortices generated from the upstream cylinder". As these vortices from the upstream cylinder impinge onto the downstream cylinder, they merge with those formed from the downstream cylinder. Meneghini *et al.* (2001) describes this merging of vortices as an "amalgamation process". The vortex impingement process directly affects the vortical structure behind the downstream cylinder. Zhou & Yiu (2006) commented that the vortex impingement process makes the Kármán vortices formed from the downstream cylinder weaker compared to those of the extended body and reattachment regimes. Lin *et al.* (2002) also noticed that the formation of the Kármán vortices behind the downstream cylinder is much closer to the cylinder base. Secondly, the vortex impingement process, together with the higher level of turbulence intensity and the streamwise vortical structures of the incoming flow, reduce the spanwise coherence behind the downstream cylinder. In other words, three dimensional flow structures can appear more easily in the wake of the downstream cylinder.

The co-shedding regime begins at the separation ratio for which the Kármán vortex shedding just starts to form from the upstream cylinder. This separation ratio is commonly referred to as the critical separation ratio. The critical separation ratio generally varies "inversely" with the Reynolds number. Note however that it is highly sensitive to both the Reynolds number and the free stream turbulence intensity (Sumner (2010)). The regime switching from and to the co-shedding regime is bistable. Hysteretic behavior can often be observed. Therefore, two dominant frequencies may be observed simultaneously (Sumner (2010)). For the separation ratios up to $L/D < 6$ to 8, synchronization between the vortex shedding processes and vortex streets of the upstream and downstream cylinder can still be observed. For larger distances ($L/D > 6$ to 8), vortex formation from the two cylinders may become independent (Sumner (2010)).

When the separation ratio surpasses the critical separation ratio, the mean drag force of

the downstream cylinder will suddenly change sign from negative to a positive value much closer to that of an isolated cylinder. Therefore, it is also referred to as the drag inversion separation ratio. On the other hand, the mean drag coefficient of the upstream cylinder reaches a minimum at this separation ratio (Zdravkovich & Pridden (1977)) and jumps to a higher value, close to that of an isolated cylinder, abruptly in an almost discontinuous fashion (Alam *et al.* (2003)). In the co-shedding regime, both the upstream and the downstream cylinders experience large unsteady fluctuating lift and drag forces (Alam *et al.* (2003)).

Next, we review the fundamentals results of wake-induced vibrations.

2.1.4 Fundamentals of wake-induced vibrations

Wake-induced vibration can occur when there are two (or more) circular cylinders (or any two slender bluff bodies) subjected to a cross flow with one of them placed downstream in the wake of the other. This setting can be found, for examples, in the cases of overhead electric power transmission lines subjected to the wind and in clustered offshore risers subjected to ocean currents. The knowledge of wake-induced vibrations is so limited that even in the recommended practice for riser interference from a world class leader in offshore engineering classification does not yet have a consistent way to incorporate the effects of wake-induced vibrations (Det Norske Veritas (2009)). As mentioned by Paidoussis *et al.* (2011), it has been observed that the body downstream can oscillate transversely with an amplitude as large as $10D$ peak-to-peak. Hence, these vibrations can cause significant and costly structural damages due to fatigue and they pose serious concerns in engineering applications.

The phenomenon of wake-induced vibration has been called differently in the literature. Ruscheweyh (1983) referred to it as "interference galloping". Bokaian & Geoola (1984) named it "wake-induced galloping". Zdravkovich (1988) called it "wake-displacement excitation". Brika & Laneville (1999) used the term "wake-galloping oscillation". More recently, Fontaine *et al.* (2006) described the phenomenon as "wake-induced oscillation" and Assi *et al.* (2013) suggested the name of "wake-induced vibration".

Unlike vortex-induced vibration, the complete mechanism of wake-induced vibration is not yet fully understood. Paidoussis *et al.* (2011) present an analysis using quasi-steady theory. They find that if the upstream body is fixed, the instabilities of the downstream body is due to fluid dynamic stiffness. This result seems to be supported by a recent experiment with two circular cylinders in a tandem arrangement by Assi *et al.* (2013). In their experiment, the upstream cylinder is fixed and the downstream cylinder is constrained to move only in the transverse direction with no damping nor spring. The downstream cylinder still experiences strong wake-induced vibrations. However, when the upstream body is also allowed to move, the flow pattern becomes more complicated and the flow may also induce instabilities due

to fluid dynamic damping as illustrated by Paidoussis *et al.* (2011). It certainly demands further research to shed more light on the complete mechanism of wake-induced vibrations.
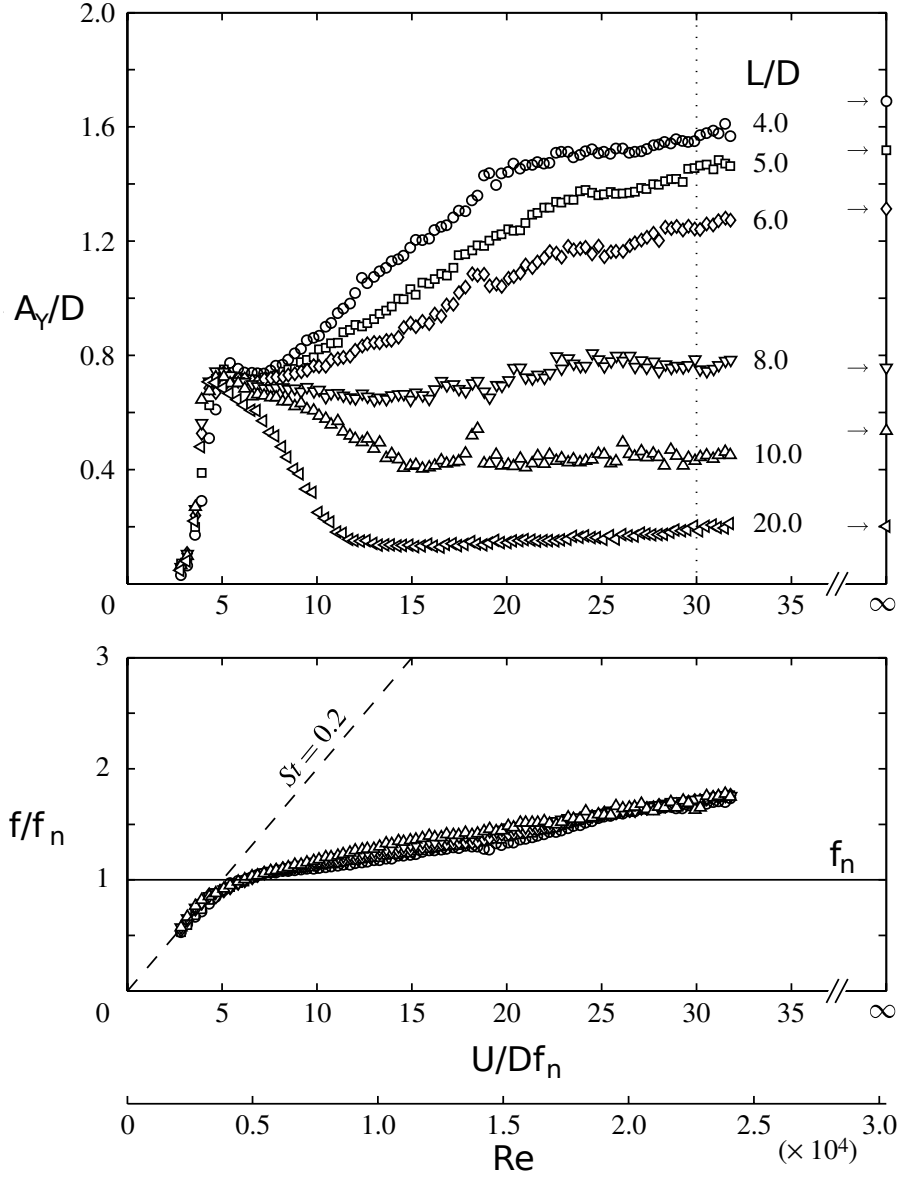
Figure 2.13 Typical response characteristics of wake-induced vibrations (Assi *et al.* (2013)). Note that the natural frequency is that of still air.

Some distinctive characteristics of wake-induced vibrations are however well-known. Figure 2.13 shows the oscillation responses of a tandem cylinder pair in a recent experiment by Assi *et al.* (2013). As mentioned above, in the experiment, the upstream cylinder is fixed and the downstream cylinder is allowed to move in the transverse direction only. The mass ratio

of the cylinder is $m^* = 2.6$. Under similar setting, an isolated cylinder can only develop a peak transverse oscillation amplitude of $A_Y = 0.8D$. We can see that the downstream cylinder can indeed develop very large transverse oscillations when it is "close" to the upstream cylinder.

Overall, the synchronization or the "locked-in" range of two cylinders in tandem arrangement is much wider than that of an isolated cylinder. As the reduced velocity increases, the upstream cylinder will generally synchronize first and then followed by the downstream one. Hence, at low reduced velocities (*e.g.* $U_r \leq 4$ to 5), the upstream cylinder can often have larger transverse oscillation amplitude than that of the downstream cylinder as shown by Borazjani & Sotiropoulos (2009) and Prasanth & Mittal (2009). At higher reduced velocities when the upstream cylinder often desynchronizes, the downstream cylinder can continue to oscillate with a transverse oscillation amplitude much larger than those of an isolated cylinder and the upstream cylinder.

Papaioannou *et al.* (2008) demonstrated that this increase in transverse oscillation amplitude of the downstream cylinder is more significant when the separation ratio is small. On the other hand, when the separation ratio is large, the synchronization range of the downstream cylinder can be even wider.

For the upstream cylinder, Prasanth & Mittal (2009) showed that when the separation ratio is large ($L/D \approx 5.5$), the transverse oscillation amplitude is similar to that of an isolated cylinder. However, Borazjani & Sotiropoulos (2009) illustrated, with a tandem cylinder pair ($m^* \approx 2.5$) which can only oscillate in the transverse direction, that when the separation ratio is reduced to a small value ($L/D \approx 1.5$), the transverse oscillation amplitude of the upstream cylinder can also notably exceed that of an isolated cylinder. When the separation ratio becomes very small, the vortex shedding of the upstream cylinder is now greatly disturbed. Vortices are mainly shedded from the downstream cylinder and they appear to be shedded from a single bluff body. Consequently, Borazjani & Sotiropoulos (2009) observed that the transverse oscillation amplitude of the downstream cylinder is generally larger than that of the upstream cylinder in this situation. When both cylinders are permitted to oscillate also in the streamwise direction, collisions can occur and the corresponding oscillation pattern becomes more complex.

Lastly, we mention an exceptional case regarding small separation ratio ($L/D \approx 1.5$). Normally, in this separation ratio range, the transverse oscillation amplitude of the upstream cylinder should be smaller than that of the downstream cylinder. Zdravkovich (1985) however observed the reverse in their experiments for cylinders with high mass ratios. The cylinders can move in both the streamwise and transverse directions. They noticed that the upstream cylinder is able to develop fully into regular vortex-induced vibrations. The vortices shedded

from the upstream cylinder however disrupt the vortex development behind the downstream cylinder, which in turn decreases the fluctuating forces and the resultant oscillation amplitude. Therefore, the downstream cylinder in this case is almost stationary. They suggested that most probably the process begins with a slight initial displacement of the downstream cylinder.

In summary, we see that a cylinder pair in tandem arrangement in cross flow can lead to very large transverse oscillations, primarily for the downstream cylinder. The phenomenon however is highly complex and involves many different parameters. A slight change of which can lead to very different responses.

On the effect of mass ratio

For vortex-induced vibrations, there are elaborate investigations regarding the mass ratio of the cylinder. In particular, it is well known that generally as the mass ratio decreases, the range of synchronization and the oscillation amplitude will both increase.

This aspect is not yet fully explored for wake-induced vibrations. In the literature, the investigated mass ratio values are rather scattered. The mass ratio value is often chosen based on the specific physical problem of interests.

However, it seems to be reasonable to expect the free oscillations of the tandem cylinder pair to have similar kind of characteristics with respect to the mass ratio as in the case of an isolated cylinder under vortex-induced vibrations.

On multiple collinear cylinders

There are only a few investigations that consider more than two bluff bodies placed in-line. Igarashi & Suzuki (1984) experimentally examined the flow characteristics of three stationary cylinders for a range of separation ratio ($1.0 \leq L/D \leq 4.0$) and Reynolds number ($1.1 \times 10^4 \leq Re \leq 3.9 \times 10^4$). The differences in the characteristics between the second and the third cylinders are reported. Interestingly, there are even certain different behaviors observed for the first cylinder as compared with that of the first cylinder of a fix tandem cylinder pair. Harichandan & Roy (2010) studied numerically the flow characteristics of three stationary cylinders in the in-line arrangement for two separation ratios of $L/D = 2$ and $L/D = 5$ at two Reynolds numbers $Re = 100$ and $Re = 200$. They observed that the flow characteristics is dependent on the Reynolds number even at such low Reynolds number range. In a brief investigation, Etienne *et al.* (2009) numerically showed that three freely oscillating cylinders arranged in-line, in a uniform flow at the Reynolds number of $Re = 200$ and at a fixed reduced velocity of $U_r = 8$, can develop significant vibrations.

More recently, Oviedo-Tolentino *et al.* (2013) investigated experimentally the two degrees of freedom vortex-induced vibrations responses of 10 collinear circular cylinders subject to uniform flow at low Reynolds numbers, with a moderately high mass-damping factor of $m^*\zeta = 0.13$ and a separation ratio of $L/D = 6$ between each adjacent cylinder pair. The maximum amplitude results in the streamwise and the transverse directions are shown in figure 2.14. They observed that the maximum oscillation amplitudes are in general greatly amplified, especially for cylinder 2 to 7. Their results clearly exhibit some characteristics of wake-induced vibrations. For example, the cylinders downstream show very large transverse oscillations at reduced velocities above the desynchronization of the first cylinder. Overall, we can see that the transverse oscillations for all 10 cylinders are always larger than the corresponding streamwise oscillations. In particular, the peak streamwise oscillations for all cylinders are on average only about $25 \sim 30\%$ of those in the transverse direction. The largest peak streamwise oscillation is $A_X/D \approx 0.65$ which is about 50% of the associated peak in the transverse oscillation of the same cylinder.
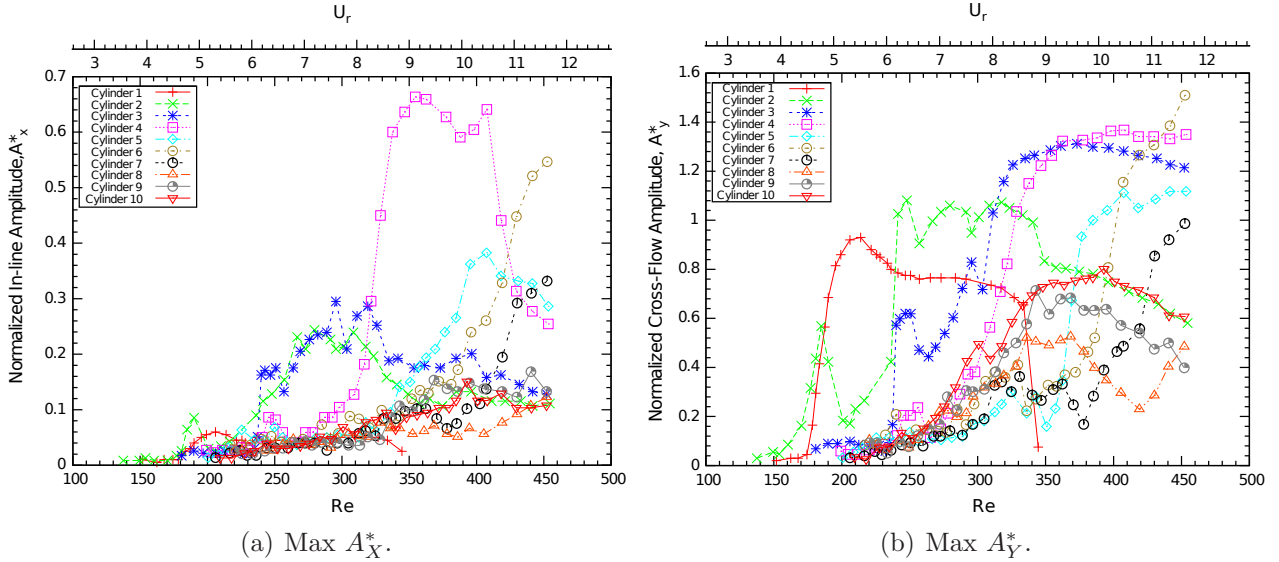
Figure 2.14 Maximum oscillation amplitude results of 10 in-line cylinders from Oviedo-Tolentino *et al.* (2013).

The investigation by Oviedo-Tolentino *et al.* (2013) clearly demonstrates that the general responses of multiple cylinders arranged in-line cannot be fully represented by the simple tandem cylinder pair. Many important aspects, *e.g.* low mass ratio, low mass-damping factor, the maximum amplitude, and effect of Reynolds number, *etc.*, deserve further investigation.

On three dimensional flow characteristics

Leontini *et al.* (2007) demonstrated that the wake of a transversely oscillating cylinder in uniform cross flow can effectively remain as two dimensional flows for $Re \leq 280$ which is markedly higher than that of a fixed isolated cylinder ($Re = 185$). The oscillation of the cylinder aids to increase the correlation length of the flow vortical structures in the spanwise direction. Carmo *et al.* (2010) reported that three dimensionality can exist at $Re \approx 163$ for two fixed cylinders in a tandem arrangement. However, it should be reasonable to assume that at low Reynolds numbers, three dimensionality should remain weak for freely oscillating cylinders arranged in-line.

These summarize our review of wake-induced vibrations. Next, we will review some aspects of numerical methods that are important for numerical investigations of fluid-structure interactions problems.

2.2   Numerical methods for fluid-structure interaction simulations

Numerical simulations are often employed to investigate fluid-structure interaction phenomena. They complement experimental studies and provides further insights into the physics of the problems. Especially, those aspects that are difficult to be studied experimentally (*e.g.* vorticity).

In this section, we first outline several essential elements of numerical fluid-structure interaction simulations, including the mathematical models, the treatments of the moving boundaries and the coupling strategies between the fluid and the structural domains. We limit our scopes only to those techniques that are relevant for vortex-induced vibrations and wake-induced vibrations. Two important considerations of numerical simulations are the correctness of the computational results and the efficiency of the numerical methods. We will overview standard procedures to ensure the correctness of the computational fluid dynamics (CFD) results, namely code verification, calculation verification and validation. Lastly, we will briefly survey the subject of parallel computing which is the de-facto approach to improve computational efficiency.

2.2.1   Essential elements of numerical FSI simulations

Numerical simulations of the fluid-structure interactions contain three essential elements: mathematical models, the treatment of the moving boundaries and the coupling strategies between the fluid and the structural domains. Depending on the intention of the investigations, each of the three elements can be approached in different ways, and each method is

associated with different advantages, disadvantages and computational cost. But all roads lead to Rome! They all provide a good "accurate enough" approximation.

Mathematical models of fluids and structures

The selection process typically begins by choosing appropriate mathematical models for the fluid and the structural domains. A proper selection is important since it has a direct impact on the efficiency of the computations.

There is a large group of fluid-structure interaction problems for which the fluid can be practically treated as incompressible and the structure can be effectively considered as a rigid body. These conditions occur naturally in many engineering applications. For example, risers in offshore engineering, tall slender building structures like chimneys, overhead transmission lines, tube bundles in steam generators, ship hull, *etc.* These models can also properly describe the experimental settings of many fundamental investigations of vortex-induced vibrations and wake-induced vibrations. This latter point, in particular, allows meaningful comparisons between experimental and these numerical results.

Therefore, in the present work, we consider flows governed by the incompressible Navier-Stokes equations, and solids undergoing rigid body vibrations governed by the classic mass-damper-spring ordinary differential equations (one for each coordinate direction). We refer this class of FSI problems equivalently to as fluid-solid interaction problems.

Numerical techniques for moving boundary problems

Numerical techniques for moving boundary problems can be generally classified under two main categories: 1) surface tracking or Lagrangian methods and 2) volume tracking or Eulerian methods (Shyy *et al.* (1996)). In the Lagrangian methods (see figure 2.15(a)), the grid conforms to the shape of the interface and it continuously follows the evolution of the interface. On the other hand, the Eulerian methods (see figure 2.15(b)) generally employ a fixed grid. The interface is not explicitly tracked but it is reconstructed based on certain fluid properties (*e.g.* fluid fraction). Due to this basic difference in the approach of the two classes of methods, they each have their own advantages and disadvantages.

Since the Lagrangian methods follow precisely the location of the interface, interfacial boundary conditions can be applied or extracted on the interface exactly naturally. This allows accurate calculations for the quantities of interests on the interface (*e.g.* force). However, this is at the expense of more complicated grid management. In particular, when the grid at the interface begins to skew or distort, it is generally necessary to re-mesh the domain (partially or completely) . This involves interpolation of the solution between the two grids

(a) Lagrangian method.
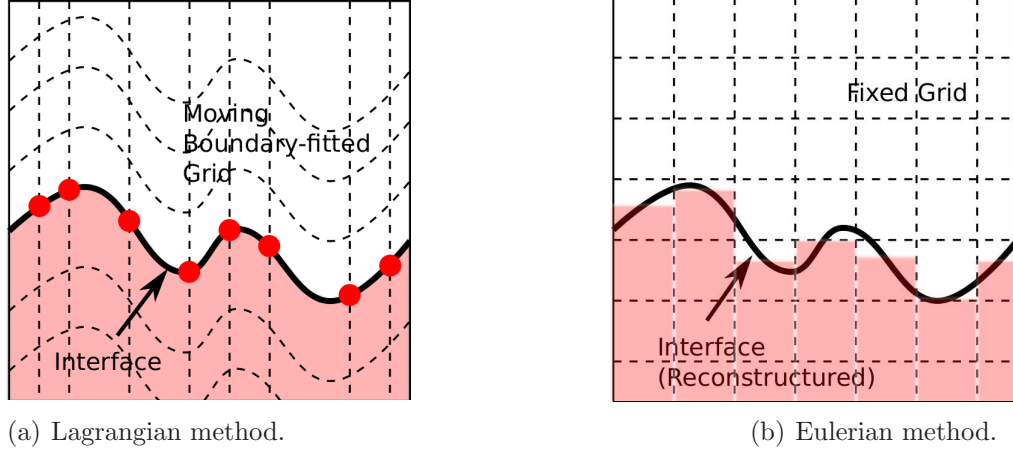
(b) Eulerian method.

Figure 2.15 Basic classification of numerical techniques for moving boundary problems.

which degrades the solution accuracy (Shyy *et al.* (1996)).

In contrast, for the Eulerian methods, topological changes of the interface (*e.g.* merging and splitting) do not bring additional challenges in the interface reconstruction scheme. However, the quality of the reconstructed interface depends on the underlying grid. Precise location of the interface can only be estimated within one cell. Improvement of the interface resolution at any specific location demands more complicated local grid refinements. Application of boundary conditions on the interface is achieved generally by modification of transport equation. This process however may induce smearing of the boundary condition (Shyy *et al.* (1996)).

For fluid-solid interaction problems, the movements of the structural boundary are usually "moderate". We are often interested in the magnitudes of the fluid force coefficients and the maximum amplitudes of the oscillations. This demands precise representations of the boundary surrounding the cylinders. For this reason, the class of Lagrangian methods is a more popular choice for the interface boundary arrangements for numerical fluid-structure interactions investigations.

Typically, the structural domain is described using a fully Lagrangian approach; whereas the fluid domain is formulated with the Arbitrary Lagrangian Eulerian (ALE) framework. In the Arbitrary Lagrangian Eulerian framework, the fluid domain at the immediate boundary of the structural body is treated in a Lagrangian (*i.e.* deforming) manner. Therefore, the mesh velocity of fluid interface node is equal to the velocity of the deforming structural boundary. The fluid domain at the far field boundary, which is not in direct contact with the structure, is described with the traditional Eulerian (*i.e.* fixed) framework. The corresponding mesh velocity is simply zero. For the fluid domain in between the deforming and the fixed boundaries, an appropriate mesh velocity is prescribed to bridge the mesh velocity

gap. The sole constraint for the mesh velocity selection is that the mesh velocity must always result in a proper (*i.e.* non-negative) volume (or area) of the element. We will also employ this approach in the present work.

On Coupling strategies between the fluid and structural domains

There are two main approaches regarding the coupling strategies between the numerical solvers of the fluid and the structure, namely the partitioned and the monolithical approaches.

In the partitioned approach, the degrees of freedom (*i.e.* the unknowns) of the fluid and the structural domains are solved separately in their own respective solvers. The fluid forces onto the structure and the displacement of the structure are exchanged with a third coupling program. The solutions from the fluid and the structural domains may be "strongly" coupled that the fluid forces and the displacement of the structure are iterated until they converge at each time step. In other words, the boundary conditions on the interface are satisfied to the iteration tolerance. Alternatively, the boundary condition constraints may be relaxed to be "weakly" coupled that the convergence of the fluid forces and the displacement of the structure obtained are not satisfied at each time step and the simulation proceeds to the next time step directly. The main advantage of this partitioned approach is that we can re-use existing flow and structural solvers to study fluid-structure interaction problems. In particular, the weakly coupled scheme requires much less computational resources. However, the disadvantage is that the stability of the scheme is highly dependent on the fluid-structure interaction problem. For highly coupled nonlinear problem, the partitioned approach may fail even with strongly coupled scheme.

In the monolithic approach, the degrees of freedom (or the unknowns) of the fluid and the structural domains are solved simultaneously in the same system. Hence, the resulting solutions automatically satisfy the constraints at the fluid structure interface at each time step. This ensures maximum stability. This advantage however comes at the expense of more involved code development and more expensive matrix solution.

From a point of view of getting accurate solution, it is not certain whether the partitioned or the monolithic approach is more efficient. Although the monolithical approach seems to be more demanding with respect to computational code and resources management, it can however provide the peace of mind in terms of the coupling stability. This feature is particularly important if we use the numerical solver to perform computational experiments and there is not much known about the expected response. Therefore, we will employ the monolithic approach.

2.2.2 Code verification, simulation verification and validation

If design or operations decision rely on simulation results, one must be able to guarantee the reliability and accuracy of predictions. In practice, and for historical reasons, this is accomplished in 3-steps:

1. Code verification

2. Simulation verification

3. Simulation validation

Verification attempts to answer the question: "Are we doing good numerical analysis?" It is thus a mathematical exercise. Code verification serves to establish the correctness of the implementation of the simulation algorithm (*i.e.* the partial differential equation solver). This can be achieved by systematic grid and time step refinement studies and involves computing the error (*i.e.* the difference between an exact solution and its numerical approximation). This is most effectively done together with the method of manufactured solution. Simulation or prediction verification establishes that the simulation program behaves according to theory on practical application problems. As no exact solutions are known, one must establish simulation verification based on error estimation. Finally, validation aims at answering the question: "Are we doing good engineering modeling?" This is achieved by comparing verified predictions with high quality measurements. For further details, we refer the reader to Roache (1998); Knupp & Salari (2003); Oberkampf (2010).

In essence, the method of manufactured solution is a generic approach to construct rich and complex enough test solutions for code verification. The method itself is not restricted to the partial differential equations of flow problems. It can also be applied to prepare test solutions for any partial differential equation solver. Manufactured solutions of many complex flow problems have been reported. For example compressible flow with invicid Euler equation and laminar Navier-Stokes equation (Roy *et al.* (2004)), incompressible turbulent flow modeled by the Reynolds Averaged Navier-Stokes (RANS) equations (Eca *et al.* (2007, 2012)), flow with heat transfer (Pelletier & Roache (2009)), *etc.* To the author's knowledge, there are only a few manufactured solutions for fluid-structure interaction problems (Etienne *et al.* (2012)).

There is a large group of fluid-structure interaction problems for which the structure can be effectively considered as a rigid body. The manufactured solution for fluid-structure interaction problem proposed by Etienne *et al.* (2012) however is not applicable for this modeling approach. Hence, there is a need to fill such a gap.

2.2.3   On Parallel computing

Parallel computing has long been applied to improve computational efficiency. Here, we will briefly overview the recent dominant trend.

Generally, there are two basic considerations if we wish to develop a numerical code to be run in parallel:

1. The architecture of the targeted computer system,

2. The "kinds" of parallelism permitted in the algorithm.

Classification of computer architectures

The majority of supercomputers nowadays follows a similar design principle: clusters of symmetric multi-processing (SMP) nodes connected by a fast network (van der Steen (2013)). Based on the relationships between the computing instruction and the data streams, Flynn suggested to classify the computers into four groups:

- Single-instruction-single-data (SISD) machines,

- Single-instruction-multiple-data (SIMD) machines,

- Multiple-instruction-single-data (MISD) machines,

- Multiple-instruction-multiple-data (MIMD) machines.

"Real" SISD machines now rarely exist. Even common workstations are now equipped with multi-core CPU and each may execute an instruction on data which can be non-related. One may argue that these workstations are each a group of SISD machines. As for MISD machines, there is no practical machine designed based on this architecture. The SIMD and MIMD frameworks are the two common computer architectures wildly adopted.

Alternatively based on the memory access arrangement, the computer can be classified into the shared-memory and the distributed-memory machines. In shared-memory machines, all processors can access/share the complete memory space. Whereas in distributed-memory machines, each CPU has its own associated memory address. The CPUs are connected by some networks and data may be exchanged on a per request basis. Note that there is no conflict between this classification and that proposed by Flynn. In particular, we can have shared-memory SIMD and shared-memory MIMD machines, and likewise distributed-memory SIMD and distributed-memory MIMD machines. For more details, we refer the readers to the up-to-date review by van der Steen (2013).

There is no single programming protocol that can be applied to and performs well for all these different computer architectures. For shared-memory machines, the dominant programming protocol is OpenMP; while that for distributed-memory machines is MPI. Depending on the actual computer design, the two protocols may need to be applied at the same time; for example, for a machine that is a cluster of multi-core workstations.

Parallelisms

We must also "identify" the kinds of parallelism permitted in the numerical algorithm. There are at large two classes of parallelism (Hager (2011)):

1. Data parallelism,

2. Functional parallelism.

Data parallelism exists when the problem contains a large set of data that can be "treated" simultaneously by different processors with either the same or different instructions. For example, in the domain decomposition procedure, the "N" worker processors subdivide the computational domain or the grid into "N" sections and each operates on a subdomain.

Functional parallelism exists when the problem can be split into "not related" tasks which can be executed at the same time. For example, in the master and worker scheme, the master processor distributes and manages workload among the worker processor. The functional nature of the master and the worker processors are "not related" to each other and can be executed at the same time.

Remark on parallel performance

The performance of a parallel code is typically measured by the "speed-up" factor S_N which is the execution time of the parallelized code (T_{PN}) with N processors over that of the sequential code T_S:

$$S_N = \frac{T_{PN}}{T_S} \tag{2.3}$$

The ideal speed up of $S_N = 1/N$ is not always possible to achieve for various reasons: including load imbalance, limitations of algorithm, bottlenecks in shared resources (*e.g.* the memory), communication, start-up overhead, *etc.* (Hager (2011)). Improvement of the parallel performance is a case by case exercise.

CHAPTER 3

METHODOLOGY

In this chapter, we discuss the research goal, objectives and methodology for the present work.

3.1   Summary of literature review

The literature review can be summarized as follows:

- Fluid-structure interaction is an important complex physical phenomenon which is typically investigated experimentally. Recently, numerical investigation have also begun to become popular, in particular for conditions at low Reynolds numbers.

- Wake-induced vibration (WIV) is a type of fluid-structure interaction that can result in severe oscillations. It may occur with arrangements of one or more elastically mounted bluff bodies subjected to a cross flow. For example, in offshore engineering applications, multiple risers may be subjected to such a condition depending on the incoming current direction. Accidents such as riser collisions or ruptures can be very costly.

- Many aspects of WIV still remain largely unknown. Even in the recommended practice for riser interference from a world class leader in offshore engineering classification does not know yet how to consistently incorporate the consideration of wake-induced vibrations (Det Norske Veritas (2009)).

- So far, most of the fundamental WIV investigations consider the configuration of a tandem cylinder pair in uniform cross flow. Very little is known for the case with more than two elastically mounted bodies.

- The results of fundamental WIV research are often compared with those of vortex-induced vibration (VIV). Recently, two research trends for VIV have emerged: the responses of an elastically mounted body freely oscillating in both the streamwise and transverse directions, and the VIV responses of a cylinder with low mass ratio. However, results for these configurations at low Reynolds numbers are rather scattered.

- In a brief investigation, Etienne *et al.* (2009) showed that three freely oscillating cylinders arranged in-line in a uniform flow at a fixed reduced velocity of $U_r = 8$ can develop significant vibrations caused by wake-induced vibrations.

- More recently, Oviedo-Tolentino *et al.* (2013) performed an experiment with ten collinear cylinders with a medium large mass-damping factor ($m^*\zeta = 0.13$) placed in a uniform flow. They confirmed that the cylinders behind the second one can develop transverse oscillations that are actually larger than those of the second cylinder.

- Consequently, multiple cylinders arranged in-line placed in cross flow can potentially have much higher chances for collisions.

Based on the evidence from the recent findings, it is therefore important to take a closer look at the behavior of multiple elastically mounted bodies in an in-line arrangement placed in cross flow. The results will contribute to advancements in fundamental engineering knowledge. This is important because such work may trigger revisions of the safety best practice for offshore engineering riser interference. The current recommendation from Det Norske Veritas (2009) simply suggests to maintain a minimum separation distance of two diameters between the circumferences of the two adjacent cylinders. This guideline is primarily based on the results of vortex-induced vibration responses of an isolated cylinder.

The response characteristics of multiple elastically mounted bodies arranged in-line placed in cross flow are limited in the literature. We may obtain valuable information about the largely unexplored phenomenon from numerical simulations at low Reynolds numbers.

3.2   Research goal

Our goal is to numerically explore wake-induced vibration responses of three circular cylinders with low mass ratio and zero damping arranged in-line at low Reynolds numbers in order to advance the fundamental engineering knowledge regarding multiple elastically mounted bodies arranged in-line placed in cross flow.

3.3   Objectives

To reach this research goal, we have identified the following specific objectives:

1. Verify the correctness of the numerical code for the class of fluid-solid interaction problems.

2. Apply the tool to establish the limiting two degrees of freedom vortex-induced vibration response characteristics of an isolated cylinder with zero mass ratio at low Reynolds numbers.

3. Apply the tool to examine the two degrees of freedom free oscillation responses of three circular cylinders with low mass ratio and zero damping arranged in-line at low Reynolds numbers.

3.4 Methodology

3.4.0 General consideration and approach

We carry out the numerical simulations using a finite element method since it has an excellent track record in simulating fluid-structure interaction problems. All cylinders are modeled as rigid bodies and are permitted to oscillate in both the streamwise and transverse directions. We consider a low mass ratio which is an important factor in offshore engineering applications; in particular those in the deep sea. Zero damping is prescribed to promote stronger oscillations. The fluid is modeled as incompressible. The flow and the solid body motions are fully coupled together. The nonlinear system of equations is linearized with Newton-Raphson method. The system is then solved using a direct solver.

We limit ourselves to consider only flows at low Reynolds numbers. Unlike the flow conditions at higher Reynolds numbers, there is no need to consider turbulence models which may introduce modeling errors into the solution. Besides, the vortex-induced vibrations and wake-induced vibrations at low Reynolds numbers are also known to be essentially two dimensional phenomena. Two dimensional simulations at low Reynolds numbers require much less computational resources than three dimensional ones. As it is nicely described by Borazjani & Sotiropoulos (2009), while the Reynolds numbers are typically significantly higher in many practical applications, simulations at low Reynolds number can often adequately capture the essential characteristics of the phenomena. It is therefore an ideal setting as a first step to extract physical insight underneath complex flow phenomena for our purpose.

3.4.1 Verification of the correctness of the numerical code (Article 1)

For the simulation results to be useful, one must be able to guarantee the reliability and accuracy of predictions. This begins with establishing the correctness of the implementation of the simulation algorithm. As mentioned, code verification is most effectively accomplished using the method of manufactured solution. We propose to perform the code verification in space and time in a decoupled manner. The verification of spatial discretization of the flow solver is verified with a steady case solution that is properly constructed with polynomials. For the verification of temporal correctness, we propose a two-step approach to construct an unsteady manufactured solution for a solid body coupled with the flow solver. First, we develop a baseline solution by combining applicable one dimensional exact solutions together.

Then, the base solution is transformed to a properly rotated coordinate to ensure that all the necessary components are activated in the governing equations. We examine the feasibility of this two-step construction process first with a two dimensional case, followed by a three dimensional case.

3.4.2 Establishment of the limiting VIV responses of a cylinder with zero mass ratio (Article 2)

As mentioned, the response of wake-induced vibrations are often compared with those of vortex-induced vibrations. However, there are very few results in the literature for the two degrees of freedom vortex-induced vibration responses of an isolated cylinder with low mass ratio at low Reynolds numbers. Therefore, we proceed to fill this gap in our knowledge.

We investigate the benchmarking two degrees of freedom vortex-induced vibration responses in the following parameter space: Reynolds number ($75 \leq Re \leq 175$) and reduced velocity ($5.0 \leq U_{r_{n-w}} \leq 11.0$), where $U_{r_{n-w}}$ is the reduced velocity defined with the natural frequency of the cylinder in still water. For each simulation, the Reynolds number is fixed and the reduced velocity is varied slowly by adjusting the stiffness of the spring in a continuous manner. The approach has been demonstrated by Etienne & Pelletier (2012) to be a convenient method to examine the peak maximum oscillation amplitude as a function of the reduced velocity.

To determine the theoretical maximum amplitude response, we consider the limiting mass ratio of $m^* = 0$. Note that the reduced velocity, defined with the natural frequency of the cylinder in still water, remains a finite value even for a cylinder with a zero mass ratio. Details of the definition of these non dimensional parameters will be discussed in latter section. The damping is set to zero. For better comparisons, we also determine the two degrees of freedom vortex-induced vibration responses for the case with $m^* = 1$ and those of transverse only oscillation in a similar fashion. Lastly, we also compare the free oscillation result with that of the forced oscillation at $Re = 100$.

3.4.3 Examination of the WIV responses of three circular cylinders with low mass ratio arranged in-line at low Re (Article 3)

For the exploration of the wake-induced vibration responses of three in-line cylinders, we again carry out a parametric study with respect to the Reynolds number $Re = \{100, 150, 200\}$ and the reduced velocity ($2.0 \leq U_{r_n} \leq 13.0$). We consider three identical cylinders of low mass ratio ($m^* = 4/\pi$) with zero damping. The separation ratio is kept constant at $L/D = 4$ which is at the boundary between the proximity and wake interference regions for a tandem

cylinder pair, to provoke richer fluid dynamic interactions. Here, since the mass ratio is non zero, the reduced velocity U_{r_n} can now be defined with the natural frequency of the cylinder in air. Again, the details of the definition of the non dimensional parameters will be discussed in latter section.

We compare the responses of three freely oscillating cylinders arranged in-line with those of a tandem cylinder pair and those of an isolated cylinder under the same conditions. Upon preliminary studies, we observe that the dynamics of the wake-induced vibration responses are very rich. Hence, we opt to set the reduced velocity fixed at each simulation run to closer examine the response characteristics.

CHAPTER 4

ARTICLE 1: Code verification for unsteady 3-D fluid-structure interaction problems

Kintak Raymond Yu, Stéphane Étienne, Alexander Hay, Dominique Pelletier (2014). Submitted to: *Theoretical and Computational Fluid Dynamics.*

Abstract

This paper describes a procedure to synthesize manufactured solutions for code verification of fluid-structure interaction (FSI) problems. The methodology can be utilized to develop manufactured solutions for both 2-D and 3-D problems. We demonstrate the procedure with our flow solver. We consider flows governed by the incompressible Navier-Stokes equations and focus on a class of FSI problems involving solids undergoing rigid body vibrations governed by the classic mass-damper-spring ordinary differential equations. We present details of the formulation and methodology. We also discuss some practical issues of the proposed approach. Results from grid and time step refinement studies confirm the verification of our solver and demonstrate the versatility of the simple synthesis procedure. In addition, the results also demonstrate that the modified decoupled approach to verify flow problems with high order time-stepping schemes can be employed equally well to verify code for multi-physics problems (here, those of the fluid-structure interactions) when the numerical discretization is based on the method of lines.

4.1 Introduction

Fluid-structure interaction (FSI) phenomena occur in many natural and man-made environments. Better understanding of these phenomena will lead to engineering improvement: such as reducing cost, improving performance, reducing failures, or even avoiding loss of life. The advancement of computational capabilities has provided effective means to gain insights into these complex physical problems.

However, if design or operations decision rely on simulation results, one must be able to guarantee the reliability and accuracy of predictions. In practice, and for historical reasons, this is accomplished in 3-steps:

1. Code verification

2. Simulation verification

3. Simulation validation

Verification answers the question: "Are we doing good numerical analysis?" It is thus a mathematical exercise. Code verification serves to establish the correctness of the implementation of the simulation algorithm (*i.e.* the partial differential equation solver). This can be achieved by systematic grid and time step refinement studies and involves computing the error (*i.e.* the difference between an exact solution and its numerical approximation). This is most effectively done together with the method of manufactured solution. Simulation or prediction verification establishes that the simulation program behaves according to theory on practical application problems. As no exact solutions are known, one must establish simulation verification based on error estimation. Finally, validation aims at answering the question: "Are we doing good engineering modeling?" This is achieved by comparing verified predictions with high quality measurements. For further details, we refer the reader to Roache (1998); Knupp & Salari (2003); Oberkampf (2010).

As described in the AIAA CFD code verification project summary, the method of manufactured solution is a very powerful method for testing numerical codes and algorithms, as "Manufactured solutions do not suffer from numerical accuracy issues that commonly occur with analytical asymptotic solutions" (Ghia *et al.* (2010)). In essence, the method of manufactured solution is a generic approach to construct rich and complex enough test solutions for code verification. The method itself is not restricted to the partial differential equations that arise in fluid dynamics. It can also be applied to prepare test solutions for any partial differential equation solver. We can apply this approach to verify any code using a consistent discretization (e.g. finite difference method, finite volume method, finite element method, etc.) on both structured and unstructured meshes. Recall that a discretization scheme is consistent if the associated truncation (consistency) error tends to zero as the characteristic grid size is reduced. Manufactured solutions of many complex flow problems have been reported. For example compressible flow with invicid Euler equation and laminar Navier-Stokes equation (Roy *et al.* (2004)), incompressible turbulent flow modeled by the Reynolds Averaged Navier-Stokes equations (Eca *et al.* (2007, 2012)), flow with heat transfer (Pelletier & Roache (2009)), etc. To the authors' knowledge, there are only a few manufactured solutions for fluid-structure interaction problems (Etienne *et al.* (2012)).

There is a large group of fluid-structure interaction problems for which the structure can be effectively considered as a rigid body. This condition occurs in many engineering applications. For example, risers in offshore engineering, tall slender building structures

like chimneys, overhead transmission line section, tube bundles in steam generators, ship hull, etc. The simplification allows considerable cost-saving in computational resources. The manufactured solution for fluid-structure interaction problem proposed by Etienne *et al.* (2012) however is not applicable for this modeling approach. Hence, there is a need to fill such a gap.

The present paper describes a procedure to synthesize manufactured solutions for code verification of fluid-structure interaction (FSI) problems for which the structure can be modeled by a rigid body. The methodology can be utilized to develop manufactured solutions for both 2-D and 3-D problems. We demonstrate the procedure with our numerical solver. We consider flows governed by the incompressible Navier-Stokes equations, and solids undergoing rigid body vibrations governed by the classic mass-damper-spring ordinary differential equations (one for each coordinate direction). We refer this class of FSI problems as fluid-solid interaction problems. We present details of the formulation and methodology. We also discuss some practical issues of the proposed approach. In addition, the results demonstrate that the modified decoupled approach to verify flow problems with high order time-stepping schemes can be employed equally well to verify code for multi-physics problems (here, those of the fluid-structure interaction) when the numerical discretization approach is based on the method of lines.

The paper is organized as follows. First, we present our mathematical models for the problem of unsteady fluid-solid interactions. We then review the subject of code verification. In particular, we review the method of manufactured solution (MMS) and practical considerations when it is used to verify an unsteady numerical solver. The proposed code verification procedures for unsteady FSI problems are then outlined, followed by a description of our finite element solver: CADYF. We then present the methodology to synthesize the manufactured solutions for unsteady FSI problems and provide the corresponding results from code verification of CADYF. We close the paper with a conclusion.

4.2 Governing equations

Here, we describe the governing equations for the fluid-solid interaction problems.

4.2.1 Fluid model

We model the fluid as a Newtonian incompressible fluid, for which, the flow field can be described in an Arbitrary Lagrangian Eulerian (ALE) framework with the following continuity

and momentum equations (Schlichting & Gersten (2000)):

$$\boldsymbol{\nabla} \cdot \mathbf{u} = 0, \tag{4.1}$$

$$\rho_f \mathbf{u}_{,t} + \rho_f [(\mathbf{u} - \mathbf{v}) \cdot \boldsymbol{\nabla}]\mathbf{u} = \boldsymbol{\nabla} \cdot \boldsymbol{\sigma}. \tag{4.2}$$

where ρ_f is the fluid density, $\mathbf{u}$ the fluid velocity, $\boldsymbol{\sigma}$ the total fluid stress tensor (pressure and viscous forces), and $\mathbf{v}$ the velocity of the moving reference frame. More details of its development may be found in Lacroix & Garon (1992). The associated constitutive equation is given by:

$$\boldsymbol{\sigma} = \boldsymbol{\tau} - p\mathbf{I} \quad \text{with} \quad \boldsymbol{\tau} = \mu[\boldsymbol{\nabla}\mathbf{u} + (\boldsymbol{\nabla}\mathbf{u})^{\mathrm{T}}].$$

where μ is the dynamic viscosity and p the fluid pressure. The fluid equations are closed with the following boundary conditions,

$$\boldsymbol{\sigma} \cdot \hat{\mathbf{n}} = \overline{\mathbf{t}} \text{ on } \Gamma_N, \tag{4.3}$$

$$\mathbf{u} = \overline{\mathbf{u}} \text{ on } \Gamma_D. \tag{4.4}$$

where Γ_N denotes a boundary on which Neumann boundary conditions are applied in the form of prescribed surface forces (tractions) $\overline{\mathbf{t}}$ with $\hat{\mathbf{n}}$ the unit normal vector, and Γ_D corresponds to a Dirichlet boundary on which the velocity, $\overline{\mathbf{u}}$, is imposed.

4.2.2 Solid model

The solid is modeled as a rigid body and it is supported by constant stiffness springs and dampers in all directions. Hence, there are three translational degrees of freedom (two for 2-D). The equations of motion for the rigid body are given by the non-dimensional mass-damper-spring equations:

$$\ddot{\mathbf{x}}^* + 2\zeta\left(\frac{2\pi}{\mathrm{Ur}}\right)\dot{\mathbf{x}}^* + \left(\frac{2\pi}{\mathrm{Ur}}\right)^2 \mathbf{x}^* = \frac{2}{m^*\pi}[C_d, C_l, C_s]^{\mathrm{T}}. \tag{4.5}$$

where $m^* = \rho_s/\rho_f$ is the mass ratio, $\mathbf{x}^* = [x^*, y^*, z^*]^{\mathrm{T}} = \mathbf{x}/D$ the vector of non-dimensional solid displacements in x, y and z, C_d, C_l and C_s the fluid loading coefficients in each direction (drag, lift and slip). These force coefficients are written as functions of $\mathbf{F} = [F_x, F_y, F_z]^{\mathrm{T}}$ for each direction as follows:

$$C_d = \frac{F_x}{\frac{1}{2}\rho_f U^2 A}, \quad C_l = \frac{F_y}{\frac{1}{2}\rho_f U^2 A}, \quad C_s = \frac{F_z}{\frac{1}{2}\rho_f U^2 A}. \tag{4.6}$$

where A is the projected area. Time is non dimensionalized as $t^* = Ut/D$. The following constraints are applied on the surface of the rigid body:

$$\mathbf{u} = \dot{\mathbf{x}}^*, \tag{4.7}$$

$$\bar{\mathbf{t}} = \mathbf{F}_R, \tag{4.8}$$

$$\mathbf{F}_R + \mathbf{F}' = \mathbf{F} \tag{4.9}$$

where $\mathbf{F}_R$ is the reaction force and $\mathbf{F}'$ represents the sum of all the other forces applied onto the solid body.

4.3 Code verification

The goal of code verification is to establish the correctness of the implementation of the numerical algorithm to solve the partial differential equations. This can be achieved by systematic grid and time step refinement studies and involves computing the error (*i.e.* the difference between a closed form solution and its numerical approximation). This is most effectively done together with the method of manufactured solution.

4.3.1 Method of manufactured solution (MMS)

In essence, the method of manufactured solution (MMS) is a generic approach to construct rich and complex enough test solutions for code verification of a partial differential equation solver. The procedure systematically formulates the expressions for the test solution of the partial differential equations, the corresponding boundary conditions and initial conditions, and also the associated balancing source terms.

We begin by first "choosing" a continuum solution. In general, this solution will not satisfy the governing equations because of the arbitrary nature of our choice. The apparent conflict can be easily resolved by introducing an appropriate source term to cancel out any imbalance in the partial differential equation caused by our choice of the continuum solution. We remark that this solution choice can often be made independently of the code or of the governing equations considered. That is, we can use the same solution to verify an incompressible Navier-Stokes code, a Darcy flow model, a heat equation, etc.

The solution should be non-trivial in the sense that it exercises all derivatives and terms in the partial differential equation. The solution also defines the boundary conditions in all forms be they Dirichlet, Neumann or Robin and the initial condition. We illustrate the process with a simple example.

Consider the following 1-D transient solution:

$$u_m(x, t) = a + \sin(x + ct) \tag{4.10}$$

where a and c are constants.

We can apply the above solution to verify a solver for the nonlinear Burger's equation:

$$L(u) = u_t + uu_x - \alpha u_{xx} = 0 \tag{4.11}$$

where α is a constant.

Note that the selected solution does not satisfy the Burger's equation (*i.e.* $L(u_m) \neq 0$)! The corresponding balancing source term s can be determined from:

$$s = L(u_m) = (u_m)_t + (u_m)(u_m)_x - \alpha(u_m)_{xx} \tag{4.12}$$

which yields:

$$s = c \, \cos(x + ct) + [a + \sin(x + ct)] \cos(x + ct) + \alpha \, \sin(x + ct) \tag{4.13}$$

The expressions for the different type of boundary conditions are obtained directly from the solution (*i.e.* equation 4.10) once the domain of the problem is specified. For example, the Dirichlet condition at $x = 0$ is just $u_m(0, t) = a + \sin(ct)$. The initial condition can be obtained similarly as $u_m(x, 0) = a + \sin(x)$.

With every aspect of the test solution now known, we can proceed to perform grid and time step convergence studies to examine the order of convergence of the code by solving the following augmented partial differential equation:

$$L(u) = u_t + uu_x - \alpha u_{xx} = s \tag{4.14}$$

The principle of grid convergence study is based on the behavior of the error e as the grid size h is reduced:

$$e = \|u_h - u_{ex}\| = Ch^p + H.O.T. \tag{4.15}$$

where u_h is the discrete solution, u_{ex} the exact solution, h a measure of the discretization and p the convergence rate of the numerical scheme. This behavior applies to every consistent methodology (*e.g.* finite difference method, finite volume method, finite element method, etc). The idea is to monitor the behavior of the error e as the grid is refined. Grid doubling

is not necessary, just refinement. However, thorough iterative convergence (*e.g.* that of the Newton's method for the nonlinear system, or the conjugate gradient method for the symmetric matrix, etc.) is required. Theoretically, the values of $C = e/h^p$ should become constant as the grid is refined.

A grid convergence study via the MMS will detect all ordered errors (interior discretization, boundary condition discretization, etc.). It will not evaluate the adequacy of non-ordered approximation such as the distance to an outflow boundary or $\frac{\partial p}{\partial n} = 0$ at a wall. The errors of such approximations do not vanish as $h \to 0$, therefore they are non-ordered approximation. However, if the solver uses a second order approximation of $\frac{\partial p}{\partial n} = 0$ at a wall and the grid convergence study shows that it is indeed second order accurate, then the code is verified on this point. The method will not detect coding mistakes that slow down the iterative solver while leaving the answer unaffected. See Roache (1998); Knupp & Salari (2003); Oberkampf (2010) for further discussion.

When the grid convergence test is completed satisfactorily, we have verified: any equation transformation used (body fitted grids), the order of the discretization, the coding of the discretization and the matrix solution procedure. The technique is simple, yet very powerful. Users sometimes say that the method is too sensitive and reveal minor inconsistencies in the special treatment of a single grid point that may corrupt the convergence rate of the method everywhere (Roache (1998)). The algebraic complexity may be something of a challenge. However, symbolic manipulation can easily deal with it.

Code verification guarantees that the numerical algorithm implementation is correct. However, when applying a verified code to a practical case, one must also perform simulation verification to ensure that the code is used properly. Error estimates may be computed using classical Richardson extrapolation (Roache (1998)) or any unstructured mesh error estimator (Pelletier (1999)).

4.3.2 Code verification of an unsteady solver

An unsteady solver involves both spatial and temporal errors.

$$e = C_h h^p + C_{\delta t} \delta t^q \tag{4.16}$$

where C_h and $C_{\delta t}$ are constants, and h and δt are the spatial and temporal characteristics sizes respectively. There are three fundamental approaches to exercise code verification for flow solver (Etienne *et al.* (2009)).

The first approach, referred as the direct approach, is to refine grid and the time step simultaneously in such a way that the temporal and spatial errors will be decreased by the

same factor. This approach closely follows the procedure of code verification for steady cases. For a code which is second order accurate in space and first order accurate in time, halving the grid size decreases the spatial error by a factor of 4. To maintain the same error reduction ratio in time, we will need to refine the time step also by a factor of 4 as well. In practice, halving the grid size increases the number of grid points by a factor of 4 in 2-D and 8 in 3-D. Simultaneous refinement of h and δt thus increases the cost by a factor of 16 in 2-D and 32 in 3-D at each refinement.

This approach can be computationally expensive in practice, especially for higher order time stepping methods (Knupp & Salari (2003); Etienne et $al.$ (2009)). For example, consider a numerical scheme which is second order accurate in space and fifth order accurate in time. Halving the time step reduces the error in time by a factor of $2^5 = 32$. To maintain the same error reduction ratio in space, the grid size has to be refined by a factor of $2^{\frac{q}{p}} = 2^{\frac{5}{2}} = 4\sqrt{2} \approx$ 5.66. This amounts to increasing the number of nodes by a factor of $(4\sqrt{2})^2 = 32$ in 2-D and a factor of $(4\sqrt{2})^3 \approx 181$ in 3-D! The high order of the temporal scheme becomes the bottle neck of the verification process. Also, when the observed order of accuracy does not match the theoretical one, we would have to search into both the spatial and the temporal codes to hunt for mistakes (Knupp & Salari (2003)).

The second approach, referred as the decoupled approach, is to separate the process of spatial and temporal code verification. We can investigate the spatial error simply with a steady case. For temporal error, the approach proposes to use a very fine grid to "eliminate" the spatial error (Knupp & Salari (2003)). This approach can be risky because the chosen grid may be fine enough for steady problem but may not be fine enough for unsteady problem (Knupp & Salari (2003)). In practice, this approach can still be rather computationally expensive (Etienne et $al.$ (2009)).

The third approach may be referred to as a modified decoupled approach. Similar to the decoupled approach, the spatial error is first investigated with a steady case. For the temporal error code verification, the modified decoupled approach proposes to use any "reasonable" grid. The spatial error of the employed grid is evaluated and subtracted from the total error. Etienne and Pelletier propose to measure the error with iterated Richardson extrapolation (Etienne et $al.$ (2009)). Alternatively, we can measure the spatial error with a higher order time integrator or the same time integrator with a much finer time step. We can even construct a manufactured solution with only temporal error and "no" spatial error. The modified decoupled approach is a cost-effective method to exercise code verification for flow solver with high order time stepping scheme (Etienne et $al.$ (2009)).

The application of the modified decoupled approach for multi-physics problem, though possible in principle, has yet to be demonstrated. We will employ the modified decoupled

approach in our code verification for temporal error of fluid-structure interaction problems and examine if there is any restriction to its application.

4.3.3 Procedure to verify code for unsteady FSI problems

As mentioned in the previous section, we employ the modified decoupled approach to verify the fluid-solid interaction code. Obviously, we must first complete separate verification of the flow and rigid body dynamics solvers. Based on these, the main focus of fluid-solid interaction code verification is in fact to examine the coupling between the fluid and solid body.

We summarize our procedure for code verification in unsteady fluid-solid interaction problems below:

1. Verify the flow solver (steady and unsteady)

2. Verify the solid body dynamics solver (steady and unsteady)

3. Verify the coupling of fluid solid interface (steady and unsteady)

In the following, we will assume that the first two steps have been completed and we will concentrate on the third step.

4.4 A Note on the numerical solver

In this section, we briefly describe the numerical solver: CADYF.

CADYF was originally a flow solver. However, it now also includes fluid flows interacting with elastic or rigid solid bodies. For example, for fluid-structure interaction problems or heat transfer problems. It employs the classical semi-discrete approach (method of lines) to discretize the governing partial differential equations. The finite element method is used to discretize space. For solving the resulting ordinary differential equations, CADYF offers several time stepping schemes including simple backward Euler scheme, implicit Runge-Kutta schemes and backward difference formula schemes. The nonlinear equations are linearized using Newton's method. The principal feature of the computational framework is that all the discretized governing equations are solved in a monolithic or a fully coupled manner using a direct solver. This ensures maximum overall numerical stability of the solver.

For steady state problems, CADYF provides an adaptive mesh refinement feature based on the Zhu-Zienkiewski error estimation algorithm. Although, CADYF can consider both structured and unstructured grids, the adaptive mesh refinement feature makes the unstructured grids option more cost-effective for general application.

For the demonstration below, we employ the Taylor-Hood element in the spatial domain which interpolates the velocity quadratically and the pressure linearly. Hence, it will be third order accurate for velocity and second order for pressure. As for the temporal domain, it will depend on the time stepping scheme employed.

4.4.1 Coupling of the fluid and solid models

The coupling between the fluid and solid model is achieved as follows. On the fluid side of the interface between the fluid and the solid domain, the nodal forces acting on the fluid due to the solid node are determined by the implicit method of reaction (Dhatt (1984)). The interface forces acting on the solid body are set to be the opposite of the fluid reaction force. The total fluid force on the solid are added up and used in the mass-damper-spring equation. The displacement and velocity of the rigid body can be evaluated. In the fluid domain, the displacements and velocities of the nodes on the fluid solid boundary are set equal to the solid rigid body displacement and velocity. A pseudo-solid approach is employed to manage the mesh deformation of the nodes inside the fluid domain (Étienne & Pelletier (2005)). These coupling relations are computed simultaneously. In other words, the fluid and solid domains are fully coupled in CADYF.

However, we remark that the proposed manufactured solution synthesis procedure and the manufactured solutions developed in the following are also applicable to solvers that are not fully coupled.

4.5 Manufactured solution for code verification

A challenge of manufacturing a solution for code verification in the present case arises from the coupling between the fluid and the solid equations of motion. First, the manufactured solution field for the flow (u_{mf}) should result in non zero components of the viscous stress tensor such that the verification of the resulting reaction force is complete. Secondly, u_{mf} needs to respect the constraints on the interface between the fluid and the solid domain. Lastly, u_{mf} must also be chosen to be compatible with that of the solid (u_{ms}) induced by the fluid-solid interaction. In other words, u_{mf} must account for the solid body dynamics in order to provide the correct forces on the solid.

There is no unique way to construct such a solution which satisfies all these requirements. We begin our construction in the fluid domain. We then specify a suitable solution for the solid body. Finally, we ensure that the two solutions interact "nicely" together through a simple coupling scheme.

4.5.1 Couette flow in a rotated frame

We seek a simple solution that can provide non-trivial traction forces on the boundaries of the fluid domain. This can be naturally achieved if the solution exercises all terms in the Navier-Stokes equations.

In general, a Couette flow will not exercise all terms in the Navier-Stokes equations in the Cartesian coordinate ($\boldsymbol{x}$). However, if we consider a Couette flow in a rotated coordinate system ($\boldsymbol{x}'$), all terms in the non-rotated coordinate $\boldsymbol{x}$ will be non zero! We now examine the stress tensor for the Couette flow in the rotated coordinate in more details through a two dimensional case.

(a) A rotated 2-D domain.   (b) Couette flow.
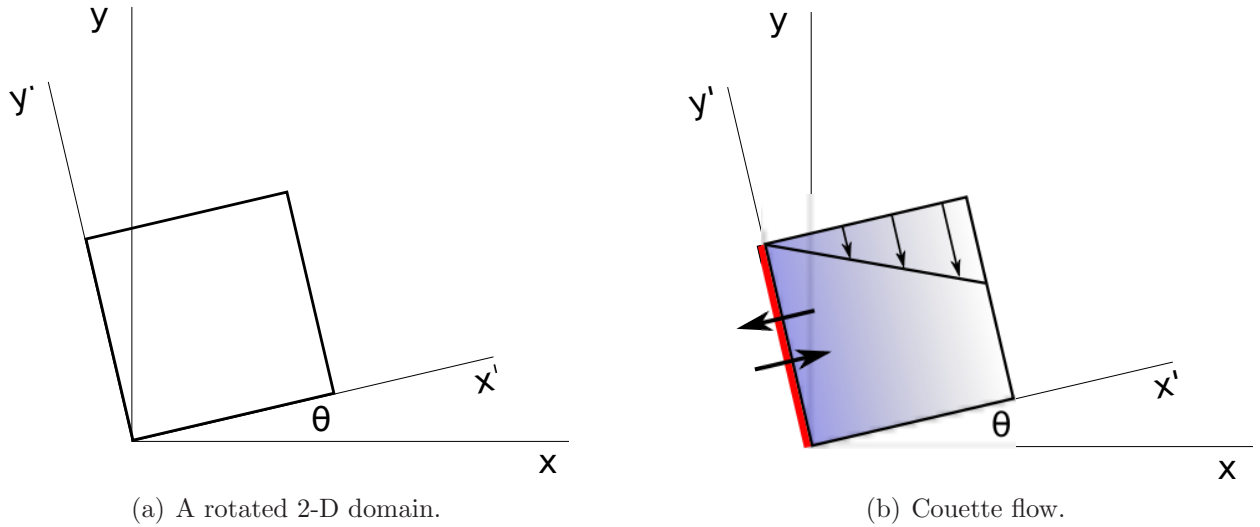
Figure 4.1 A rotated two dimensional coordinate system.

Let $\boldsymbol{x}'$ be the coordinate of a point in a frame rigidly rotated counterclockwise by an angle θ from the original Cartesian frame $\boldsymbol{x}$. See figure 4.1(a).

The relationship between $\boldsymbol{x}'$ and $\boldsymbol{x}$ is:

$$\boldsymbol{x}' = L^{-1} \cdot \boldsymbol{x}, \tag{4.17}$$

$$L^{-1} = \begin{bmatrix} \cos(\theta) & \sin(\theta) \\ -\sin(\theta) & \cos(\theta) \end{bmatrix} \tag{4.18}$$

where L is the matrix of direction cosines (a rotation matrix) (Aris (1989)). With which, we can obtain the expression of any vector $\boldsymbol{v}'$ and any second order tensor $\boldsymbol{T}'$ in the rotated

frame back in the non-rotated frame with:

$$\boldsymbol{v} = L \, . \, \boldsymbol{v}^{'}, \tag{4.19}$$

$$\boldsymbol{T} = L \, . \, \boldsymbol{T}^{'} \, . \, L^{-1} \tag{4.20}$$

The solution of the Couette flow is:

$$u = 0, \quad v = -ax, \quad p = 0 \tag{4.21}$$

where a is a constant. Hence, we have:

$$\boldsymbol{\nabla u} = \begin{bmatrix} u_{,x} & v_{,x} \\ u_{,y} & v_{,y} \end{bmatrix} = \begin{bmatrix} 0 & -a \\ 0 & 0 \end{bmatrix} \tag{4.22}$$

These lead us to have the viscous stress tensor as:

$$\boldsymbol{\tau} = \mu \begin{bmatrix} u_{,x} + u_{,x} & u_{,y} + v_{,x} \\ v_{,x} + u_{,y} & v_{,y} + v_{,y} \end{bmatrix} = \mu \begin{bmatrix} 0 & -a \\ -a & 0 \end{bmatrix} \tag{4.23}$$

Now consider that we use this solution in the rotated frame $\boldsymbol{x}^{'}$. In the original non-rotated frame, the velocity gradient will be:

$$\boldsymbol{\nabla u} = L \, . \, \boldsymbol{\nabla}^{'} \boldsymbol{u}^{'} \, . \, L^{-1} \tag{4.24}$$

$$= \begin{bmatrix} \cos(\theta) & -\sin(\theta) \\ \sin(\theta) & \cos(\theta) \end{bmatrix} \begin{bmatrix} 0 & -a \\ 0 & 0 \end{bmatrix} \begin{bmatrix} \cos(\theta) & \sin(\theta) \\ -\sin(\theta) & \cos(\theta) \end{bmatrix} \tag{4.25}$$

$$= \begin{bmatrix} a \, \cos(\theta) \, \sin(\theta) & -a \, \cos^2(\theta) \\ a \, \sin^2(\theta) & -a \, \cos(\theta) \, \sin(\theta) \end{bmatrix} \tag{4.26}$$

Hence, the corresponding viscous stress tensor is non-trivial (except for $\theta = \pi/4$). The viscous force components in each direction can also be readily computed. As for the pressure, since it does not come into play directly in the continuity equation, nor in the boundary conditions, it can in fact be chosen freely. For example, $p = x + y$.

We see that the "rotated" Couette flow with an appropriately chosen pressure distribution will exercise all terms in the Navier-Stokes equations. This simple problem provides the necessary non-trivial viscous forces in the domain and on the boundaries. Therefore, it is an appropriate solution for the fluid domain. In particular, there is no imbalance in the expressions and thus, the problem does not require any additional source term. We remark that we can "complexify" the rotated Couette flow solution as needed with polynomial, trigonomet-

ric and exponential functions to satisfy other verification goals, such as, to introduce extra spatial and/or temporal errors.

The aforementioned rotation procedure is directly applicable to 3-D. For example, suppose that we first rotate the coordinate along the z axis by an angle of θ to an intermediate coordinate, and then along the y axis of the intermediate coordinate by an angle of α, we will arrive with the following direction cosine matrix:

$$
L^{-1} = \begin{bmatrix} \cos(\alpha)\cos(\theta) & \cos(\alpha)\sin(\theta) & \sin(\alpha) \\ -\sin(\theta) & \cos(\theta) & 0 \\ -\sin(\alpha)\sin(\theta) & -\sin(\alpha)\sin(\theta) & \cos(\alpha) \end{bmatrix} \tag{4.27}
$$

Now that the flow solution is specified, we can choose a boundary to act as a solid flat plate. We select the boundary $\boldsymbol{x}' = 0$ to be our solid body surface as depicted in figure 4.1(b).

4.5.2   Rigid body dynamics

The dynamics of the solid body is governed by the mass-damper-spring equation. Some exact analytical solutions for a single degree of freedom (DOF) system are available in many standard vibration textbooks (den Hartog (1985); Meirovitch (2010)). For a damped single DOF system under periodic harmonic excitation:

$$
m\ddot{x}^* + c\dot{x}^* + kx^* = F = kf_0\cos(\omega_f t), \tag{4.28}
$$

the position is given by:

$$
x^* = e^{-\zeta\omega_n t}[x_i^*\cos(\omega_d t) + \frac{v_i^* + \zeta\omega_n x_i^*}{\omega_d}\sin(\omega_d t)] \tag{4.29}
$$

$$
+ \frac{f_0}{[(1 - \frac{\omega_f^2}{\omega_n^2})^2 + (2\zeta\frac{\omega_f}{\omega_n})^2]}\{2\zeta\frac{\omega_f}{\omega_n}\sin(\omega_f t) + [1 - \frac{\omega_f^2}{\omega_n^2}]\cos(\omega_f t)\}
$$

where x_i^* and v_i^* are the initial position and velocity of the homogeneous solution, and ω_n, ω_d and ω_f are the natural, damped and forcing frequencies respectively. The velocity and acceleration can be obtained by taking the time derivative of the position above. The position, velocity and acceleration all contain trigonometric functions which provide the necessary non trivial expressions to verify the mass-damper-spring equation.

4.5.3 Treatment of force imbalances

The manufactured solutions for the flow and the solid body were selected independently. Hence, the forces acting at the interface between the fluid and the solid will not match. There will be an imbalance disturbing the solid body dynamics and the flow solutions.

For the solid body dynamics, we can circumvent the imbalance by introducing an interface force ($\mathbf{F}'$) (a source term) such that Newton's second law is satisfied at the interface. This can be easily formulated since the exact reaction force is known from the manufactured flow solution. In particular, we set $\mathbf{F}' = -\mathbf{F}_R$.

As for the flow solution, we can resolve the disturbance by simply requiring the fluid domain to "follow" the solid body and behaving as if they were a single rigid body. We only need to apply the same body acceleration onto the fluid domain as that of the solid body.

To illustrate this, consider the simple two dimensional Couette flow discussed above. If the acceleration of the solid body is known, says in the x-direction, we apply the same acceleration to the flow solution in u. The "moving" Couette flow solution is as follows:

$$u = \dot{x}^*, \quad v = -a(x - x^*), \quad p = (x - x^*) + y \tag{4.30}$$

where x^* is the solid body displacement. Note that if we impose the acceleration along the x axis in the rotated frame, all components of the acceleration vector will be non zero in the non-rotated frame.

Lastly, we make a comment about the treatment of mesh displacement in the fluid domain for the ALE formulation. Given the motion of the solid body in the fluid domain, there is no unique way to specify the mesh displacement throughout the domain. We can utilize the ALE formulation in the traditional way and design a mesh displacement scheme following the solid body dynamics at the interface while respecting the fixed boundary at the "far-field". Alternatively, in the present case, we can simply require the pseudo-solid mesh to also "follow" the solid body motion. This last approach results in a much simpler treatment of the mesh displacements. We only need to set the corresponding mesh displacement to x^*. Hence, it will be employed in the following.

By combining all these ideas, we obtain a systematic procedure to construct manufactured solutions for code verification of fluid-solid interaction problems in 2-D and 3-D based on simple 1-D solutions. Note that this methodology of synthesis does not impose any constraint to, nor is it limited by the underlying governing equations. Therefore, it can be applied equally well to construct solution for any general fluid-structure interaction problem. Next, we present the results from the present code verification.

4.6 Results

We present the results of code verification with the manufactured solutions developed in the previous sections for both 2-D and 3-D problems. We measure all errors with the L_2 norm which is defined as:

$$\|e\|_{L_2}^2 = \|u_{ex} - u_h\|_{L_2}^2 = \int\limits_{\Omega} (u_{ex} - u_h)^2 d\Omega \tag{4.31}$$

where e is the error, u_{ex} the exact solution and u_h the numerical solution.

In the following, we first verify the computation of the reaction forces on the solid body with a steady case. Then, we present the time step refinement results of the rotated Couette flow problem for several time integrators.

4.6.1 MMS for steady fluid only case

We first present the results for the 2-D case. To verify the implementation of the reaction force computation, we use the following steady manufactured solution:

$$u = 1 + 2x + y + x^2 - 2xy + y^2 + y^3 \tag{4.32}$$

$$v = 1 + x - 2y + x^2 - 2xy + y^2 + x^3 \tag{4.33}$$

$$p = x^2 + 2y^2 \tag{4.34}$$

We impose this base solution in the rotated square domain as illustrated in figure 4.1(a). In particular, the rotated square domain is bounded in $x' \in (0,1)$ and $y' \in (0,1)$ where the rotated coordinate system $\boldsymbol{x}'$ is rotated counterclockwise by an angle $\theta = \pi/6$. On the boundary $x' = 0$, the exact reaction force is given by:

$$\mathbf{F}'_R = \int\limits_0^1 (\boldsymbol{\sigma} \cdot \text{-}\hat{\mathbf{n}}) dy \tag{4.35}$$

where $\hat{\mathbf{n}}$ is the outward normal unit vector. On the boundary $x' = 0$, $\hat{\mathbf{n}}^T = \{-1, 0\}$. The exact reaction force is then found to be $\mathbf{F}'_R = \{\frac{4}{3}, 3\}$. The corresponding exact reaction force value in the non-rotated coordinate system $\boldsymbol{x}$ can be retrieved using the matrix of direction cosine as described in section 4.5.1. In particular, the reaction force in the non-rotated frame amounts to $\mathbf{F}_R = L \cdot \mathbf{F}'_R = \{\frac{2}{\sqrt{3}} - \frac{3}{2}, \frac{3^{\frac{3}{2}}}{2} + \frac{2}{3}\} \approx \{-0.3453,\ 3.2647\}$.

The grid refinement results for the reaction force are summarized in table 4.1. The grid number in the first column indicates the refinement ratio with respect to the initial grid.

Table 4.1 Grid refinement results in 2-D reaction forces.

Grid	# Node	# Elem	F_{Rx}	F_{Ry}
1	399	180	-0.3749	3.2049
2	1599	760	-0.3593	3.2364
4	6399	3120	-0.3521	3.2509
8	25599	12640	-0.3487	3.2579
16	102399	50880	-0.3470	3.2614
32	409599	204160	-0.3461	3.2631
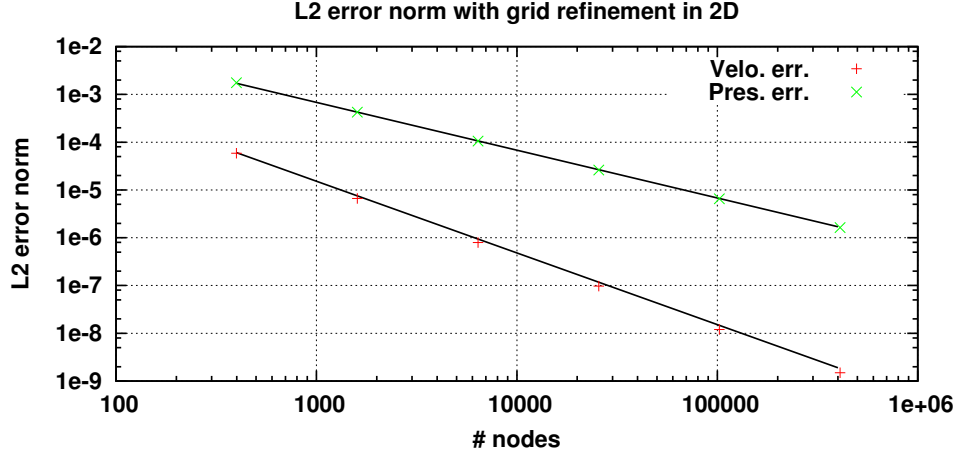
Figure 4.2 L_2 error norms of grid refinement for 2-D reaction force.

Here, we reduce the grid size by a factor of 2 for each refinement. The obtained reaction forces shown in the last two columns approach the exact values as the grids are refined.

Figure 4.2 shows the trajectory of the L_2 error norm as a function of the number of grid points. We can see that the two L_2 error norms decrease linearly as the grid is refined. The order of convergence of the numerical solver $O(k)$ can be obtained from the slope m of the line. In particular, $m = -k/D$ where D is the dimension of the problem being 2 here. For example, if $m = -1$, then the order of convergence is $O(2)$. The observed slopes indicate that the orders of convergence are $O(h^3)$ for the velocity and $O(h^2)$ for the pressure. These match the theoretical results of the Taylor-Hood element.

In a similar manner, we use the following steady manufactured solution as the base solu-

tion to verify the reaction force computation in 3-D:

$$u = 1 + x + y + z + x^2 - 2xy + y^2 + yz + z^2 - xz - y^3 - 4z^3 \qquad (4.36)$$

$$v = 1 + x - 0.5y + z + x^2 - 2xy + y^2 - yz + z^2 + xz + 2z^3 + 3x^3 \qquad (4.37)$$

$$w = 1 + x + y - 0.5z + x^2 + xy + y^2 + z^2 + 2x^3 + y^3 \qquad (4.38)$$

$$p = 3x^2 + 2y^2 + z^2 \qquad (4.39)$$

We impose this base solution in a rotated cube domain bounded in $x^{'} \in (0,1)$, $y^{'} \in (0,1)$ and $z^{'} \in (0,1)$ where the rotated coordinated system $\boldsymbol{x}^{'}$ is first rotated counterclockwise to an intermediate coordinate by an angle of $\theta = \pi/6$ around the z axis, and then rotated again counterclockwise by an angle of $\alpha = \pi/3$ around the y axis of the intermediate coordinate. This gives an exact force $\mathbf{F}^{'}_R = \{-2,\ 2,\ 0\}$ on $x^{'} = 0$. In the non-rotated coordinated system $\boldsymbol{x}$, the exact reaction force becomes $\mathbf{F}_R = L \ . \ \mathbf{F}^{'}_R = \{-\frac{\sqrt{3}}{2} - 1, -\frac{1}{2} + \sqrt{3}, -\sqrt{3}\} \approx \{-1.866,\ 1.232,\ -1.732\}$.

Table 4.2 Grid refinement results in 3-D reaction forces.

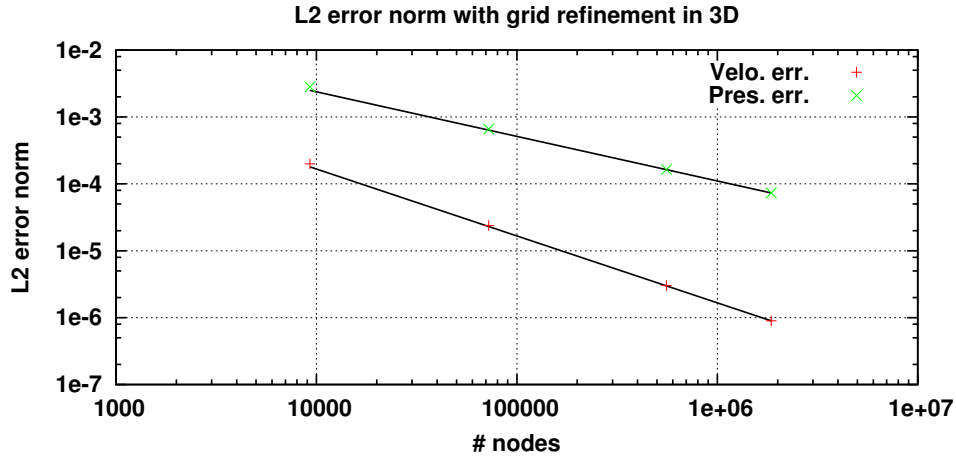| Grid	# Node	# Elem	F_{Rx}	F_{Ry}	F_{Rz}
1	9271	6006	-1.601	1.192	-1.693
2	72293	50406	-1.740	1.213	-1.713
4	557695	403206	-1.803	1.223	-1.723
6	1859417	1360806	-1.824	1.226	-1.726

Figure 4.3 L_2 error norms of grid refinement for 3-D reaction force.

The grid refinement results of the 3-D case are summarized in table 4.2. As expected, the reaction forces shown in the last three columns approach the exact values as the grid is

refined.

In figure 4.3, the L_2 error norms of the flow velocity and the pressure with respect to the corresponding number of nodes of each grid are shown. The dimension of the problem is now 3. The theoretical orders of convergence for the velocity $O(h^3)$ and the pressure $O(h^2)$ are again observed. These results demonstrate that the reaction forces are computed properly in both 2-D and 3-D by the numerical solver.

4.6.2   MMS for unsteady fluid-solid interaction

Here, we illustrate the application of the combined 1-D manufactured solution outlined in section 4.5 to verify the fluid-solid interaction module for unsteady case. We first specify the parameters of the manufactured solution. We then present the two dimensional results followed by those of the three dimensional problem.

To specify the manufactured solution, we impose a periodic excitation to the damped single DOF system with the following parameters: $m = 1$, $c = 0.01$, $k = 4$, $x_i^* = v_i^* = 0$ and $f_0 = 0.025$. We also fix the moving Couette flow solution with $a = 1$, and we further simplify the solution by setting the fluid pressure to zero. In particular, the two dimensional moving Couette flow solution now becomes:

$$u = \dot{x}^*, \quad v = -1(x - x^*), \quad p = 0 \tag{4.40}$$

where x^* is the solid body displacement again. Whereas, the three dimensional moving Couette flow solution is:

$$u = \dot{x}^*, \quad v = 0, \quad w = -1(x - x^*), \quad p = 0 \tag{4.41}$$

The spatial variations of these two manufactured solutions are represented exactly by the Taylor-Hood element. Hence, the observed error is solely due to how well the time integrators capture the rigid body dynamics. This further facilitates the time step refinement studies via the modified decoupled approach. Indeed, we can perform the time step refinement with any grid, even a coarse one. For the time refinement study, we consider three time stepping schemes, namely IRK11, IRK32 and IRK53, from the implicit Runge-Kutta method of the Radau IIA family. The corresponding theoretical global orders of convergence for the time stepping schemes are summarized in table 4.3 (Hairer (2010)). The fluid-structure interaction module will be properly verified if these theoretical orders of convergence are observed.

As described in section 4.5 and in the steady reaction force verification problems above, the baseline manufactured solution is imposed in the rotated coordinate $\boldsymbol{x}'$. The error is,

(a) 2-D IRK11

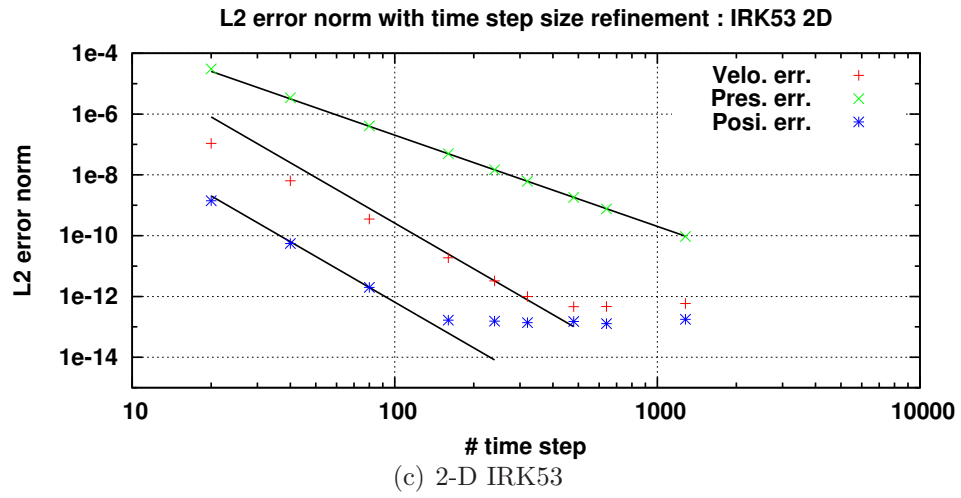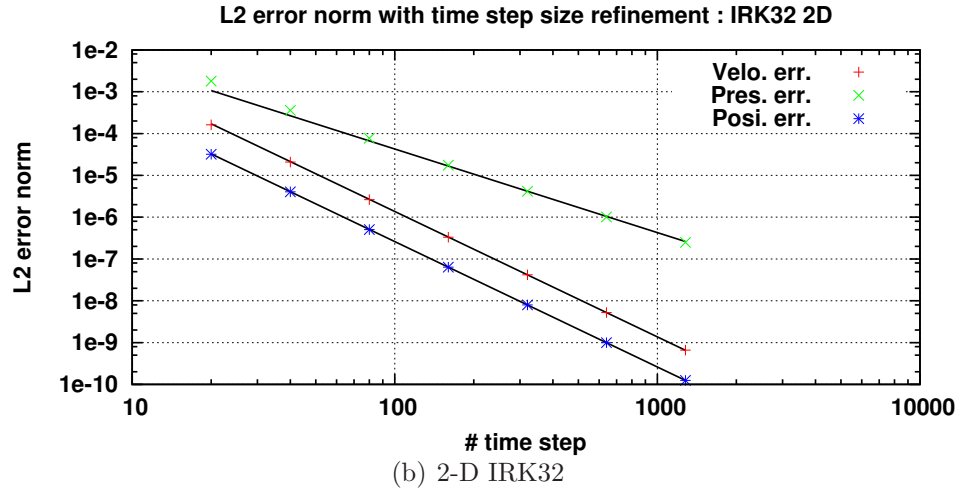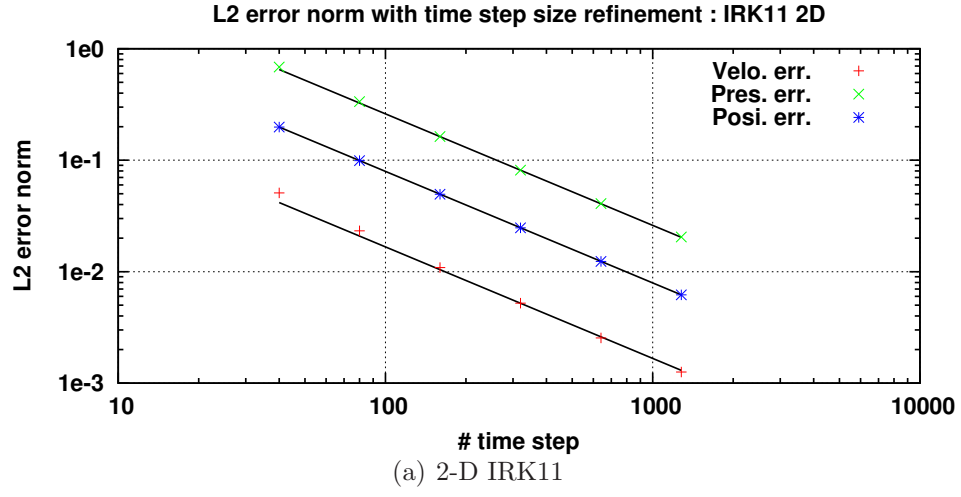
(b) 2-D IRK32

(c) 2-D IRK53

Figure 4.4 L_2 error norms of the time step refinement in 2-D.

on the other hand, measured in the non-rotated coordinate $\boldsymbol{x}$. We employ the same rotated square and cube domains used in the steady reaction force verification. And we choose the boundary $\boldsymbol{x}' = 0$ in the rotated coordinate to be the solid boundary. Here, the temporal error is measured at the end of each simulation run. In particular, we quantify the error with the L_2 norms of the velocity and pressure of the fluid domain and the position of the center of mass of the solid body.

We now examine the time step refinement results for the two dimensional problem. From the manufactured solution, the reaction forces in the non-rotated coordinate are $\mathbf{F}_R = \{\sin(\theta), -\cos(\theta)\} \approx \{0.5, -0.866\}$ on the solid surface ($\boldsymbol{x}' = 0$). The L_2 error norms of the velocity, the pressure and the solid position of the time step refinement are shown in figure 4.4 in log-log scale. Recall that the order of convergence of the numerical scheme $O(k)$ can be obtained from the slope m via the relation: $m = -k/D$. Note however that the dimension D for time is simply 1. The theoretical error orders are generally observed for all three time integrators.

We remark that for the IRK53 scheme, although the proper order of convergence is observed for the pressure and position, the order of convergence for the velocity error with small number of time steps (from 20 to 160) is somewhat below $O(\delta t^5)$. At this range, the problem may not yet be in the asymptotic range of the time integration scheme. The computations of velocity may possibly be "polluted" by those of the pressure since the accuracy in pressure $\|p_{ex} - p_h\|_{L_2} = O(\delta t^3)$ is 2 orders lower than that of the velocity $\|u_{ex} - u_h\|_{L_2} = O(\delta t^5)$. As we increase the number of time steps to about 300, the order of convergence of the velocity becomes very close to its theoretical value. However, when we further increase the number of time step, the error reaches a floor value close to machine zero. And it is not possible to measure the temporal error properly. This limit for machine precision is also encountered in the position error of the solid body with large number of time steps. Therefore, to determine the order of convergence of the IRK53 scheme more rigorously, we would need to consider finer precision computation.

We next present the time step refinement results for the three dimensional problems. From the 3-D manufactured solution, the reaction forces in the non-rotated coordinate are $\mathbf{F}_R = \{\sin(\alpha)\cos(\theta), \sin(\alpha)\sin(\theta), -\cos(\alpha)\}$ which is about $\mathbf{F}_R \approx \{0.75, 0.433, -0.5\}$ on

Table 4.3 Theoretical global order of convergence of time integrator.

Scheme	Velocity	Pressure	Position
IRK11	$O(\delta t^1)$	$O(\delta t^1)$	$O(\delta t^1)$
IRK32	$O(\delta t^3)$	$O(\delta t^2)$	$O(\delta t^3)$
IRK53	$O(\delta t^5)$	$O(\delta t^3)$	$O(\delta t^5)$

the solid surface ($\boldsymbol{x}' = 0$). The corresponding L_2 error norms of the velocity, the pressure and the solid position of the time step refinement are shown in figure 4.5. There is no change for the dimension D of time for the 3-D problem (*i.e.* $D = 1$). Once again, the theoretical error orders are generally observed and similar trend is observed for the IRK53 scheme.

We finalize our discussion with a closer look at the time evolution of the reaction forces. In figure 4.6, the time evolutions of the two dimensional reaction force F_R on the solid boundary ($\boldsymbol{x}' = 0$) in the x direction in the non-rotated coordinate for the three IRK schemes with various time steps are shown. Those of the 3-D problem are shown in figure 4.7. Recall that the manufactured solutions are spatially exact. There is however temporal error arising from imposing the fluid domain to follow the acceleration of the solid body which contains non trivial expressions in time. In the absence of any temporal error, the obtained reaction force should remain basically a constant value as prescribed by the spatial part (*i.e.* Couette flow) of the base manufactured solution throughout the entire simulation. From the figures, we see that generally for all cases, as the number of time step increases, the obtained reaction forces indeed approach steadily towards the exact values of $F_{R_x} = 0.5$ for 2-D and $F_{R_x} = 0.75$ for 3-D as prescribed by the base Couette flow solution.

Two additional observations can be made regarding the order of time stepping scheme. First, we can observe that the maximum error magnitudes are much smaller for higher order schemes (*e.g.* IRK53) as compared with those for the lower order scheme (*e.g.* IRK11). More specifically, For both the 2-D IRK53 and 3-D IRK53 cases, the variations in the reaction force magnitude throughout the simulation are less than 1.0×10^{-4} for all time step sizes. Secondly, it is evident that the higher order scheme requires much less refinement to improve its computations. In other words, the time step refinement of the higher order scheme is more effective than the lower order ones. These results demonstrate the efficiency of employing higher order time stepping schemes.

From the above results, we have successfully verified the fluid-solid interaction code module. We have shown that the simple procedure presented here is an effective methodology to construct manufactured solutions for code verification of fluid-structure interaction problems. Although we illustrate the procedure here using the Taylor-Hood element for spatial discretization and the family of implicit Runge Kutta method (Radau IIA) for temporal discretization, we stress however that the procedure does not impose any restriction to the choice of spatial discretization method, nor time integration schemes. Lastly, the modified decoupled approach proposed to verify unsteady flow problems with high order time stepping schemes is shown to be applicable equally well for code verification of multi-physics problems.

4.7 Conclusion

In this paper, we presented a simple procedure to synthesize manufactured solutions of fluid-structure interaction problems in 2-D and 3-D for code verification. In essence, the methodology first constructs a base solution by combining applicable 1-D exact solutions together. To satisfy the involvement of all the necessary components in the governing equations, the base solution is imposed in a properly rotated coordinate, whereas the numerical error is examined in the non-rotated coordinate. We apply the outlined procedure to verify our numerical code for 2-D and 3-D fluid-solid interaction problems. The results demonstrate the applicability and versatility of the procedure to construct manufactured solutions for fluid-solid interaction problems. Note that this methodology of synthesis does not impose any constraint to, nor is it limited by the underlying governing equations. Therefore, it can be applied equally well to construct solutions for any general fluid-structure interaction problem. Moreover, the results also demonstrate that the modified decoupled approach proposed to verify flow problems with high order time-stepping schemes can be employed equally well to verify code for multi-physics problems when the numerical discretization approach is based on the method of lines.

L2 error norm with time step size refinement : IRK11 3D

(a) 3-D IRK11

L2 error norm with time step size refinement : IRK32 3D

(b) 3-D IRK32

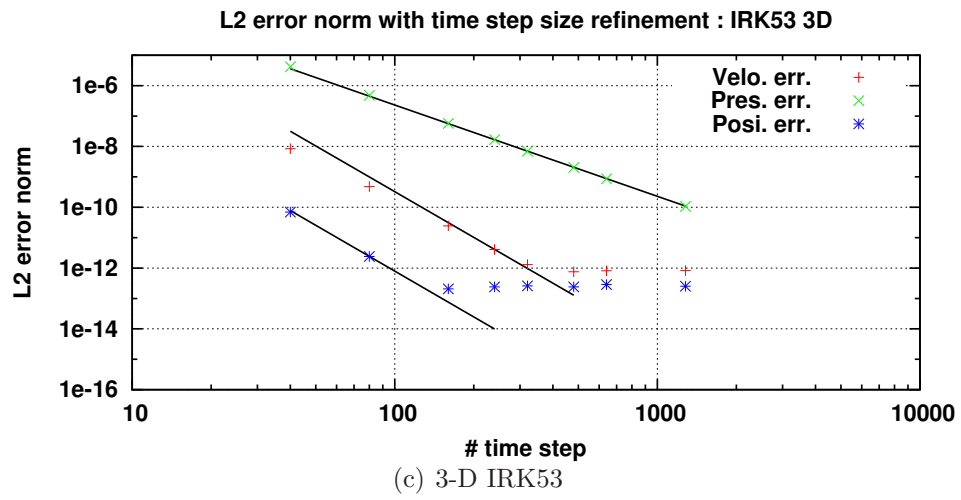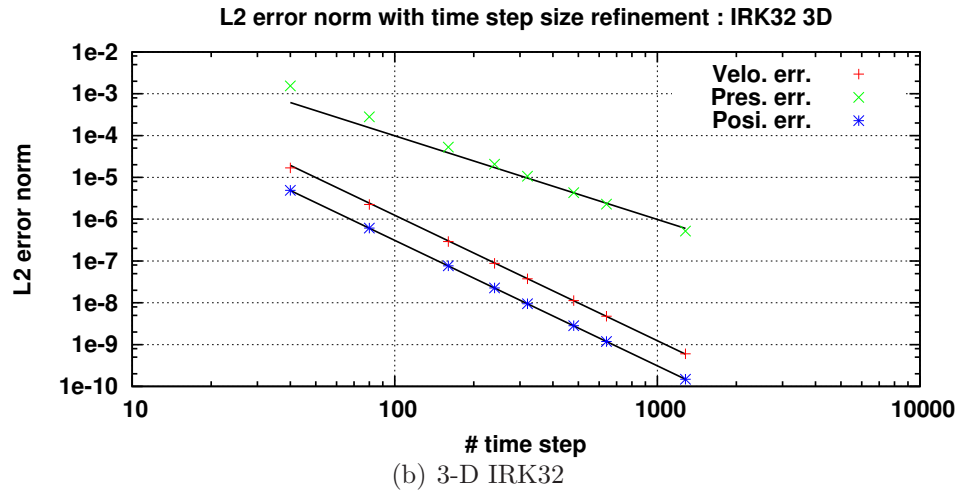**L2 error norm with time step size refinement : IRK53 3D**

(c) 3-D IRK53
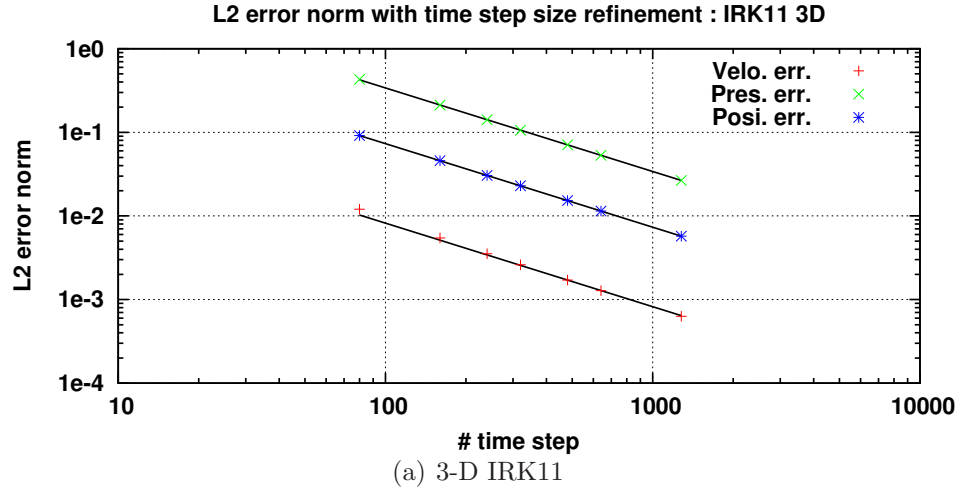
Figure 4.5 L_2 error norms of the time step refinement in 3-D.
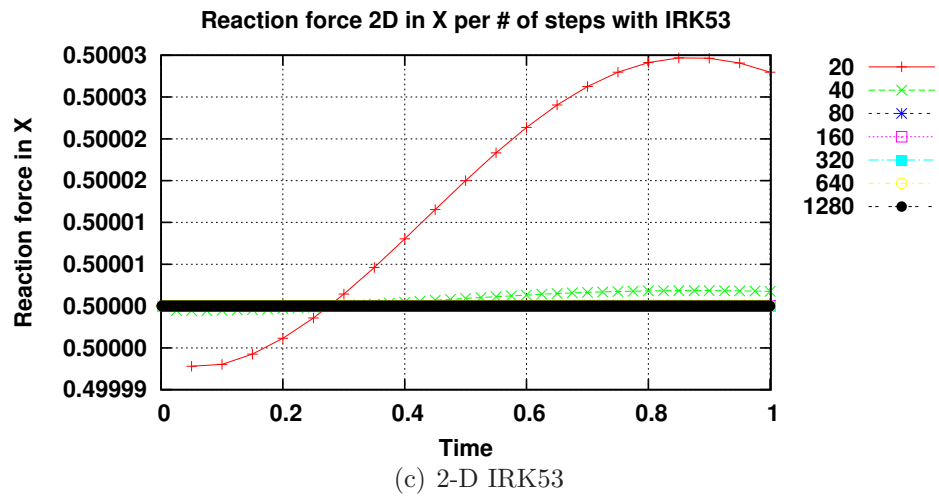
(a) 2-D IRK11

(b) 2-D IRK32

(c) 2-D IRK53
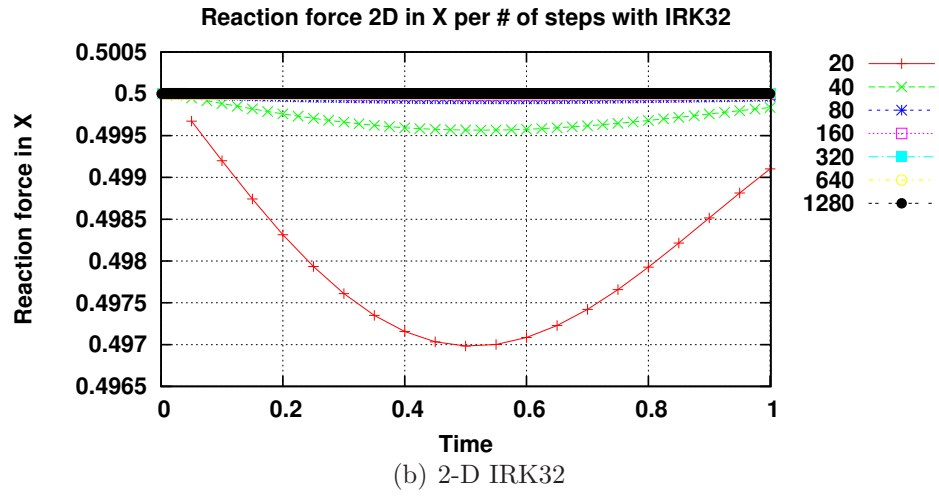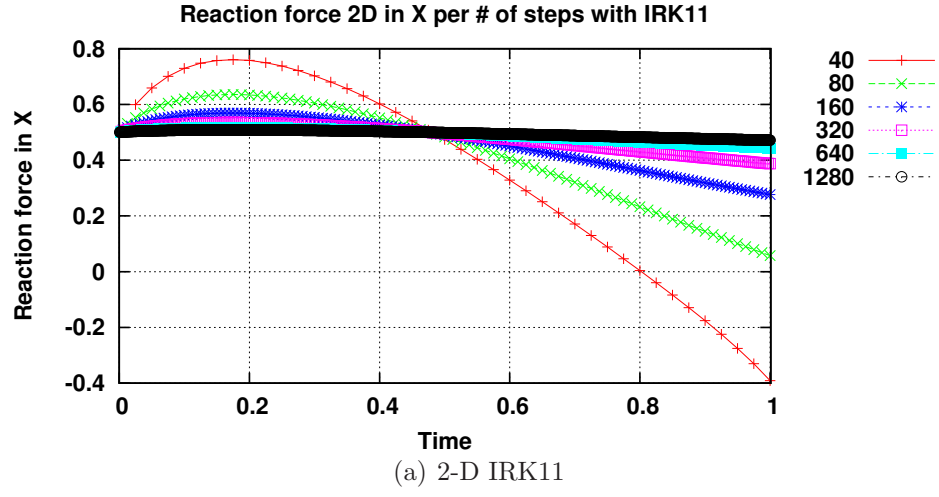
Figure 4.6 Time evolution of F_{Rx} for time step refinement in 2-D.

(a) 3-D IRK11

(b) 3-D IRK32

(c) 3-D IRK53
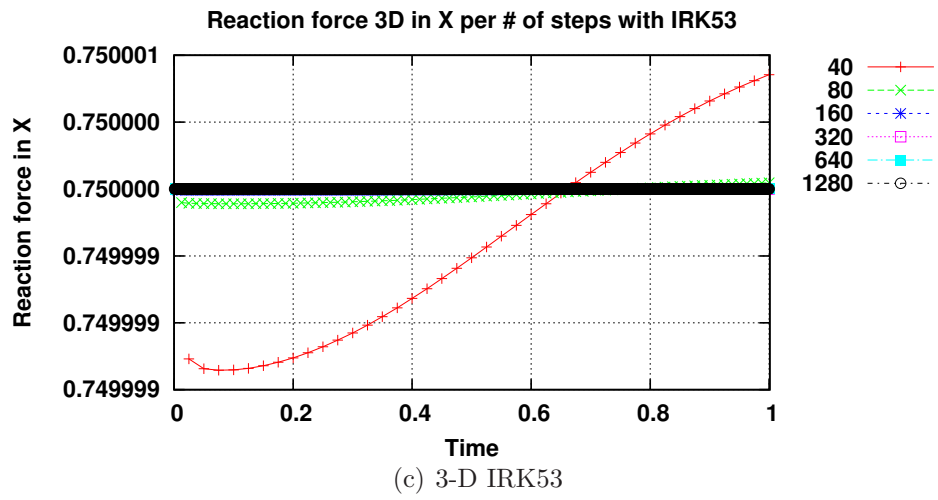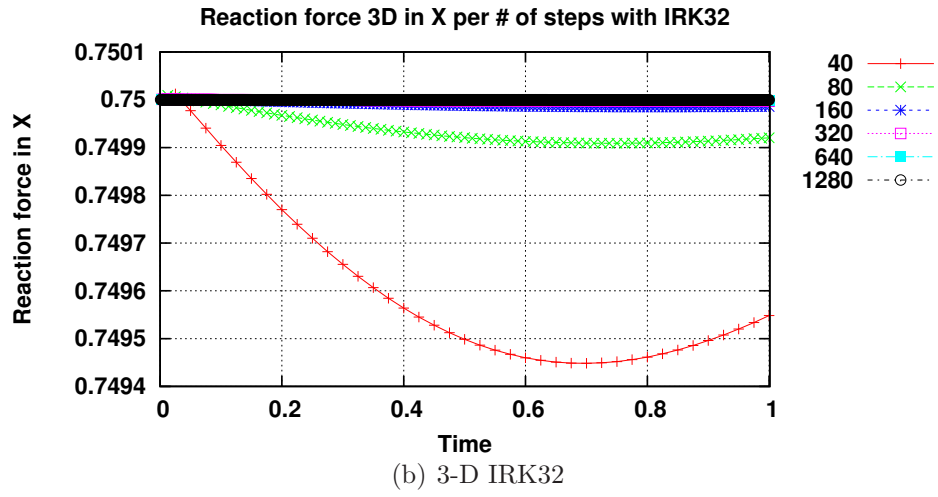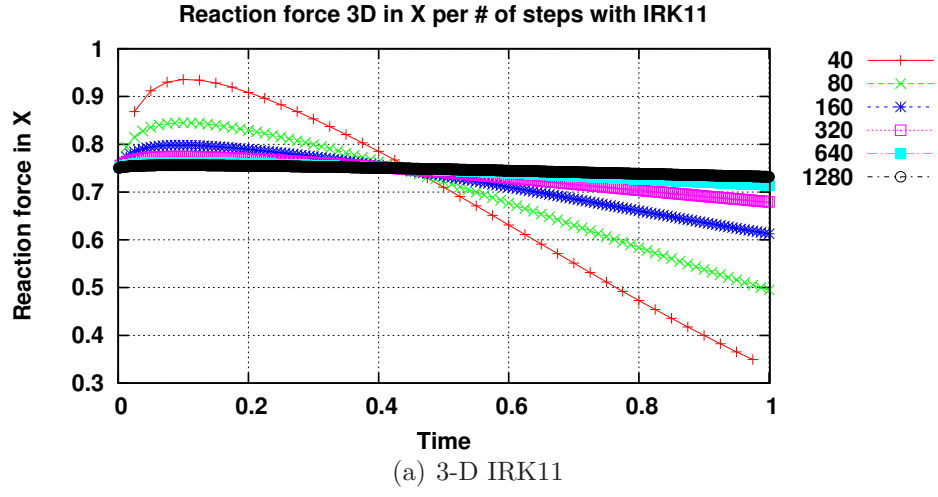
Figure 4.7 Time evolution of F_{Rx} for time step refinement in 3-D.

REFERENCE

ARIS, R. (1989). *Vectors, tensors, and the basic equations of fluid mechanics.* Dover publications, New York.

DEN HARTOG, J. P. (1985). *Mechanical vibrations.* Dover books on engineering. Dover publications, New York.

DHATT, G. (1984). *The finite element method displayed.* Wiley, Chichester [West Sussex] ; New York.

ECA, L., HOEKSTRA, M., HAY, A. & PELLETIER, D. (2007). On the construction of manufactured solutions for one- and two-equation eddy-viscosity models. *International Journal for Numerical Methods in Fluids*, 54, 119 – 54.

ECA, L., HOEKSTRA, M. & VAZ, G. (2012). Manufactured solutions for steady-flow reynolds-averaged navier-stokes solvers. *International Journal of Computational Fluid Dynamics*, 26, 313 – 332.

ETIENNE, S., GARON, A. & PELLETIER, D. (2009). Code verification for unsteady flow simulations with high order time-stepping schemes. *47th aiaa aerospace sciences meeting including the new horizons forum and aerospace exposition*, 1–11.

ETIENNE, S., GARON, A. & PELLETIER, D. (2012). Some manufactured solutions for verification of fluid-structure interaction codes. *Computers and Structures*, 106-107, 56 – 67.

ÉTIENNE, S. & PELLETIER, D. (2005). A general approach to sensitivity analysis of fluid–structure interactions. *Journal of Fluids and Structures*, 21, 169 – 186.

GHIA, U., BAYYUK, S., HABCHI, S., ROY, C., SHIH, T., CONLISK, T., HIRSCH, C. & POWERS, J. M. (2010). The AIAA code verification project - test cases for CFD code verification. *48th AIAA Aerospace Sciences Meeting Including the New Horizons Forum and Aerospace Exposition.* Orlando, FL, United states.

HAIRER, E. (2010). *Stiff and differential-algebraic problems.* Springer, Berlin.

KNUPP, P. M. & SALARI, K. (2003). *Verification of computer codes in computational science and engineering.* Discrete mathematics and its applications. Chapman & Hall/CRC, Boca Raton, Fla.

LACROIX, M. & GARON, A. (1992). Numerical solution of phase change problems. an eulerian-lagrangian approach. *Numerical Heat Transfer, Part B: Fundamentals*, 21, 57 – 78.

MEIROVITCH, L. (2010). *Fundamentals of vibrations*. Waveland press, Long grove, Illinois.

OBERKAMPF, W. L. (2010). *Verification and validation in scientific computing.* Cambridge University Press, New York.

PELLETIER, D. (1999). Adaptive finite element computations of complex flows. *International Journal for Numerical Methods in Fluids.* UK, vol. 31, 189 – 202.

PELLETIER, D. & ROACHE, P. J. (2009). Verification and validation of computational heat transfer. *Handbook of Numerical Heat Transfer*, John Wiley & Sons, Inc. 417–442.

ROACHE, P. J. (1998). *Verification and validation in computational science and engineering.* Hermosapublishers, Albuquerque, N.M.

ROY, C., NELSON, C., SMITH, T. & OBER, C. (2004). Verification of Euler/Navier-Stokes codes using the method of manufactured solutions. *International Journal for Numerical Methods in Fluids*, 44, 599 – 620.

SCHLICHTING, H. & GERSTEN, K. (2000). *Boundary-layer Theory.* Springer, Berlin.

CHAPTER 5

ARTICLE 2: Two degrees of freedom vortex-induced vibration responses with zero mass and damping at low Reynolds number

Kintak Raymond Yu, Alexander Hay, Dominique Pelletier, Stéphane Étienne (2014).
Submitted to: *Journal of Fluid Mechanics.*

Abstract

This work aims to characterize the two degrees of freedom (transverse and streamwise) responses of vortex-induced vibrations of a cylinder at low Reynolds number for the limiting case of zero mass ratio and zero damping. We focus on determining the maximum amplitude values. We numerically investigate the responses in the following parameter space: Reynolds number ($75 \leq Re \leq 175$), reduced velocity ($5.0 \leq U_r \leq 11.0$) and mass ratio ($m^* = 0$). For comparison, we also investigate the XY oscillation with $m^* = 1$ and those of transverse only oscillation. The effect of Re and m^* on the oscillation responses are examined. We also compare the free oscillation results with those of the forced oscillation at $Re = 100$. The overall maximum transverse amplitude (A_Y) is $0.9D$ for the XY oscillation with $m^* = 0$, a significant 50% increase from $0.6D$ previously reported in the low Re regime. The peak A_Y occurs at different U_r when the Reynolds number varies. This is in contrast to the results of Etienne & Pelletier (2012) who found that the maximum A_Y always occurs at the same U_r for $Re < 50$. Furthermore, the maximum A_Y increases with Re. This is most evident for the XY oscillation with $m^* = 0$. This behavior differs markedly from what was suggested by Williamson & Govardhan (2006) that the maximum A_Y is unaffected by Re in the laminar range. The critical mass ratios are 0.106 for XY oscillation and 0.117 for transverse only oscillation respectively.

5.1 Introduction

Vortex-induced vibration (VIV) is an important fluid-structure interaction phenomenon in offshore engineering. When flow passes over a bluff body (e.g. a cylinder), the flow field is disturbed and vortices can form behind the body. The shedded vortices can impose forces onto

the bluff body and become a source of excitation forces for the structure. The motion of the structure will affect the patterns of vortices generated, which in turn alter the characteristics of the excitation forces. However, under the right conditions, the induced vibrations can become so significant that they pose concern in terms of engineering design safety.

There have been extensive studies in vortex-induced vibrations in the past four decades (Sarpkaya (2010)). A set of important non-dimensional parameters, e.g. amplitude ratio A^*, Reynolds number Re, reduced velocity U_r, mass ratio m^*, etc., have been identified (Sarpkaya (2010)). Generally, investigations attempt to examine the characteristics of the vibration responses (e.g. maximum amplitude, lift and drag forces, etc) and flow patterns, and their changes when the non-dimensional parameters are varied. It is noted that the importance of the non-dimensional parameters change throughout the parameter space (Sarpkaya (2010)).

Many different aspects of the vortex-induced vibration have been investigated. Most studies focus on the fundamental behavior of the transverse vibrations (one degree of freedom) of an isolated cylinder in a uniform flow (Williamson & Govardhan (2004); Sarpkaya (2004)). One key characteristic is the "lock-in" effect, for which, there is a range of reduced velocity such that the frequencies of vortex-shedding and vibrations are synchronized, and vibrations of large amplitudes are observed (Sarpkaya (2004)). Another key characteristic is that when the reduced velocity is varied in the "lock-in" range, the response is not smooth but exhibits "branches" (Sarpkaya (2004)). Hysteresis is observed at the transitions between branches (Sarpkaya (2004)). The shapes and appearances of the branches change with mass-damping factor $m^*\zeta$. The damping ratio is often very small. Hence, we can practically consider that the influence is principally due to the mass ratio m^*. For a large value of m^*, one can observe two branches: the initial and lower branches. Decreasing m^* to small values, the upper branch now appears between the initial and the lower branches. A smaller m^* also leads to a wider interval of lock-in reduced velocities and a larger maximum amplitude. The typical characteristic of the maximum transverse amplitude with respect to the mass ratio is illustrated in figure 5.1(a). If we further decrease the mass ratio below a certain "critical" value, the lower branch eventually disappears and merges with the upper branch. Govardhan & Williamson (2002) showed experimentally that a vibration amplitude of 0.8D can still be attained even for an "infinite" value of the reduced velocity. In other words, when the mass ratio is smaller than the critical value, there is no desynchronization. Note that for the hysteresis responses, Prasanth et al. (2011) demonstrated numerically that the blockage and the mass ratios are two important factors for the hysteresis behavior between the initial and the lower branches in the laminar shedding regime. In particular, for certain combination of the two factors, the hysteresis between the initial and the lower branches may be completely suppressed.

(a) Max amplitude.
(b) Frequency.
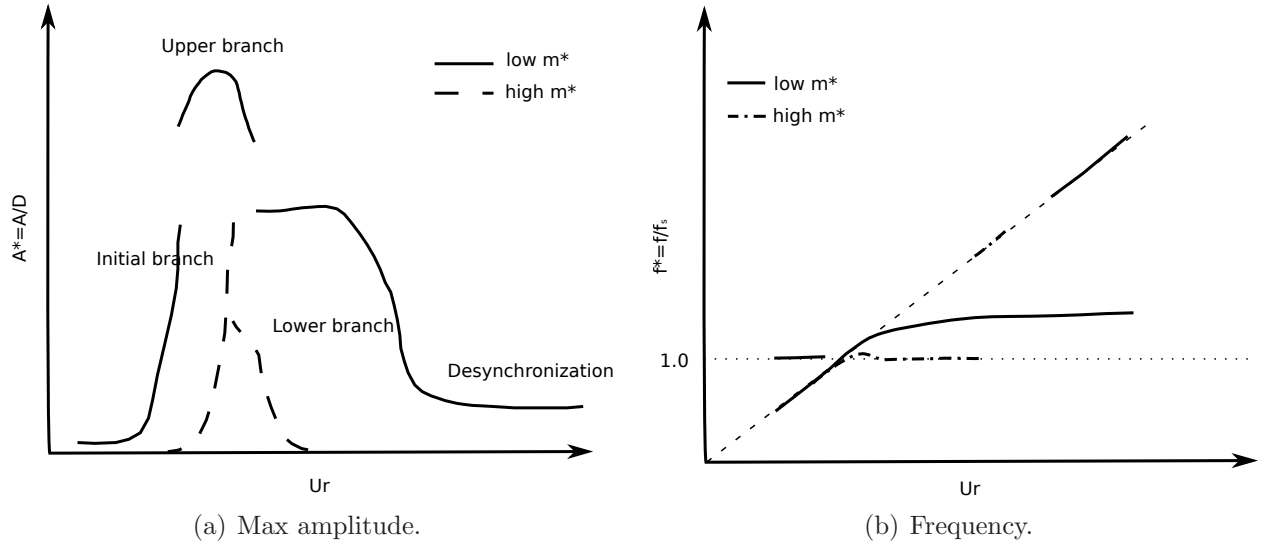
Figure 5.1 Illustrations of typical VIV responses (small ζ).

Inside the "lock-in" range, the frequency of oscillation varies rather smoothly. However, a jump in frequency can be observed when we shift from one branch to another (Khalak & Williamson (1999)). The typical frequency response is illustrated in figure 5.1(b). If the mass ratio is large, the frequency of oscillation will be close to the natural frequency of the cylinder. With low mass ratio, the frequency of oscillation is generally larger than the natural frequency of the cylinder but smaller than the vortex-shedding frequency of a fixed cylinder (Williamson & Govardhan (2004)). However, with a small mass ratio, the oscillation frequency can even be above the vortex-shedding frequency in some reduced velocity ranges (Govardhan & Williamson (2002); Khalak & Williamson (1999)).

The corresponding flow field is generally described in terms of the observed vortex pattern. The change of vortex patterns is associated with a change of branches. The major vortex patterns identified include 2P, 2S, 2C, 2T (Williamson & Govardhan (2004)).

For further details regarding the phenomena of vortex-induced vibrations, we refer the readers to the excellent reviews by Williamson & Govardhan (2004) and by Sarpkaya (2004).

Recently, the importance of the streamwise vibration and its interactions with the transverse vibrations have been recognized (Aglen & Larsen (2011)). Streamwise vibrations generally have smaller amplitude than transverse vibrations, and "lock-in" usually occurs at a frequency twice that of the transverse vibration. However, streamwise vibration can occur at very low ambient velocity. Thus, streamwise vibration can occur more often than the transverse vibration and hence, can have major impacts on equipment fatigue (Aglen & Larsen (2011)). Jauvtis & Williamson (2004) investigated the fundamental two degrees of freedom responses for vortex-induced vibrations for Reynolds number in the range of 1000 to 15000.

For mass ratios above 5 or 6, the envelope of the transverse vibration amplitude resembles that of a cylinder vibrating transversely only (Jauvtis & Williamson (2004)). When the mass ratio is reduced below 5, they discovered that the maximum transverse amplitude can be significantly greater than those (the upper branch) found in vortex-induced vibration responses of transverse only oscillations. They describe this new branch of response as the super-upper branch. The vortex pattern (2T) is identified when the system is on the super-upper branch.

Williamson & Govardhan (2006) observed that the Reynolds number can affect the maximum amplitude. At Reynolds number greater than 500, a larger Re results in a larger maximum amplitude for the initial and the upper branches for a cylinder oscillating transversely only. This relationship however is not observed for the lower branch response and for responses at Reynolds numbers Re smaller than 200.

Most of the vortex-induced vibration investigations were carried out in the moderate or high Reynolds number range ($Re > 10^3$). In the laminar shedding regime ($Re < 200$), there is only one experimental study and a handful of detailed numerical investigations. Anagnostopoulos & Bearman (1992) investigated experimentally the vortex-induced vibration response of a cylinder ($m^* = 149$) with transverse only oscillation for Reynolds numbers in the range of 90 to 150. The maximum observed amplitude is 0.55D. Shiels et $al.$ (2001) studied this problem numerically with no damping and no structural mass ($m^* = 0$) at $Re = 100$. They obtained a maximum amplitude of 0.59D. Placzek et $al.$ (2009) investigated forced and free vibrations for a cylinder oscillating only transversely at $Re = 100$. The maximum transverse amplitude is found to be 0.58D. However, the value of mass ratio employed is not evident as the simulation results are presented in terms of the "effective rigidity" (Placzek et $al.$ (2009)). Singh & Mittal (2005) studied computationally the two degrees of freedom vortex-induced vibration response for a cylinder with $m^* = 10$ with two settings. First, they investigated the problem at a fixed value of Reynolds number $Re = 100$ and varied the reduced velocity from 4 to 8.5. Then they examined the problem with a fixed reduced velocity ($U_r = 4.92$) and varied the Reynolds numbers between 50 and 500. The reduced velocity was chosen to be $U_r = 4.92$ because that is the location of the maximum peak for $Re = 100$. They assumed that the peaks for the other Reynolds numbers would also occur at the same reduced velocity. The maximum transverse amplitude response was about 0.6D in their investigations. Prasanth & Mittal (2008) investigated the two degrees of freedom vortex-induced vibration problem numerically for the range of Reynolds number: $60 < Re < 200$. In their work, the natural frequency of the cylinder is fixed and the free stream flow velocity is varied. The maximum transverse amplitude A_Y is found to be about 0.6D which is about 30 times larger than the maximum in line amplitude A_X. They found that there are only two branches of response: the initial and the lower branches. In the desynchronization range of the lower

branch at higher Re, hysteresis is always observed. Near the transition from the initial to the lower branch at lower Re, hysteresis may appear if the blockage ratio (*i.e.* the diameter of the cylinder over the width of the domain) is larger than 5%. Note however that, $m^* = 10$ is considered large in the study of Jauvtis & Williamson (2004). In this case, the response is expected to be similar to that of the cylinder oscillating transversely only. The maximum transverse amplitude A_Y of 0.6D is in accordance with the results compiled by Williamson & Govardhan (2004) for the vortex-induced vibration of a cylinder in the laminar shedding regime and the analysis of forced oscillation results.

Singh & Mittal (2005) observed that the vortex shedding modes in the laminar shedding region include the 2S and the C(2S) modes. In the 2S mode, a single vortex is shed from each side of the cylinder during one cycle of vortex shedding. The C(2S) mode is a variation of the 2S mode during which, the vortices "coalesce" in the wake region. Prasanth & Mittal (2008) noticed that when the mode switches from the 2S mode to the C(2S) mode, the oscillation amplitude can jump from a low value to a higher level. Note that the work of Prasanth & Mittal (2008) was executed for a fixed value of the cylinder spring stiffness. The inlet flow velocity is varied which simultaneously changes both the reduced velocity and the Reynolds number. Placzek *et al.* (2009) suggested that since there is no 2P mode for the laminar shedding regime, which is confirmed by the Direct Numerical Simulation (DNS) results of Newman & Karniadakis (1997), the upper branch may not actually exist for the vortex-induced vibration response in this regime. The 2P mode is associated with the change from the initial branch to the upper branch at higher Reynolds number.

For applications like piping in deep water oil exploration projects, the mass ratio can be small (*i.e.* order of one) (Stappenbelt & Lalji (2008)). Hence, there is a practical need to understand the effects of low mass ratio on vortex-induced vibrations to enhance design safety. Despite the findings of Jauvtis & Williamson (2004), Sanchis *et al.* (2008) did not observe the super-upper branch, nor the regular upper branch for a cylinder with a low mass ratio $m^* = 1.04$ and a "high" mass-damping ratio $\alpha = (m^* + C_A)\zeta = 0.093$ at high Reynolds number $Re \approx 19000$. Hence, there is still much to understand regarding vortex-induced vibrations at low mass ratio, the limiting case being "zero" mass ratio.

Etienne & Pelletier (2012) numerically investigated the instability boundary of the two degrees of freedom (transverse and streamwise) responses of vortex-induced vibrations of a rigid cylinder with zero mass ratio and zero damping for very low Reynolds number (< 50). Here, we extend their work and explore the problem for Reynolds number values between 75 and 175, just below the appearance of Mode A three dimensional instability (Williamson (1996)). In particular, we study the following parametric space: Reynolds number $\{Re = UD/\nu : 75 \leq Re \leq 175\}$, reduced velocity $\{U_r = U/(f_{n-w}D) : 5.0 \leq U_r \leq 11.0\}$ and mass

ratio $\{m^* = \rho_s/\rho_f : m^* = 0\}$. We aim to characterize the responses and focus especially on the maximum amplitude. To better contrast the results, we also investigate the two degrees of freedom response with $m^* = 1$ and the response of transverse only oscillation.

We demonstrate for the first time that the maximum transverse amplitude $A_Y^* = A_Y/D$ can also be affected by the Reynolds number in the laminar shedding regime. We report that there is an effect of Reynolds number on the location of the jump of the total phase angle between the lift force and transverse displacement. We also report the critical mass ratio for transverse only and two degrees of freedom oscillations at $Re = 100$.

Here, U is the uniform flow velocity, f_{n-w} the natural frequency of the cylinder in a still fluid medium $[f_{n-w} = \sqrt{k/(m_s + m_a)}/(2\pi)]$, D its diameter and ν the fluid kinematic viscosity, k is the rigidity of the spring that supports a unit length cylinder in the 3rd direction, m_s is its mass per unit length and the added mass due to surrounding fluid is $m_a = \rho_f \pi D^2/4$. For zero mass cylinders, the mass ratio is null as well. Note that the natural frequency f_{n-w} previously defined is non singular even with a zero mass cylinder. For which, we have $f_{n-w} = \sqrt{k/m_a}/(2\pi)$, and hence a reduced velocity $U_r = \pi U \sqrt{\rho_f \pi/k}$.

The paper is organized as follows. First the modeling equations are presented. Then, we describe our numerical methodology, and its validation. After, we will present our simulation results for the parameter space studied.

5.2 Numerical method

This section briefly describes the numerical method that is used for all computations reported here.

5.2.1 Governing equations

We model the fluid as a Newtonian incompressible fluid, for which, the flow field can be described with the following continuity and momentum equations (Schlichting & Gersten (2000)):

$$\boldsymbol{\nabla} \cdot \boldsymbol{u} = \boldsymbol{0}, \tag{5.1}$$

$$\rho_f \boldsymbol{u}_{,t} + \rho_f[(\boldsymbol{u}) \cdot \boldsymbol{\nabla}]\boldsymbol{u} = \boldsymbol{\nabla} \cdot \boldsymbol{\sigma}. \tag{5.2}$$

where ρ_f the fluid density, $\boldsymbol{u}$ the fluid velocity, and $\boldsymbol{\sigma}$ the total fluid stress tensor (pressure and viscous forces). The associated constitutive equation is given by:

$$\boldsymbol{\sigma} = \boldsymbol{\tau} - p\boldsymbol{I} \quad \text{with} \quad \boldsymbol{\tau} = \mu[\boldsymbol{\nabla}\boldsymbol{u} + (\boldsymbol{\nabla}\boldsymbol{u})^{\mathrm{T}}].$$

where μ is the dynamic viscosity and p is the fluid pressure. The fluid equations are closed with the following boundary conditions,

$$\boldsymbol{\sigma} \cdot \hat{\boldsymbol{n}} = \bar{\boldsymbol{t}} \text{ on } \Gamma_N, \tag{5.3}$$

$$\boldsymbol{u} = \overline{\boldsymbol{u}} \text{ on } \Gamma_D. \tag{5.4}$$

where Γ_N denotes a boundary on which Neumann boundary conditions are applied in the form of prescribed surface forces (tractions) $\bar{\boldsymbol{t}}$ with $\hat{\boldsymbol{n}}$ the outward normal unit vector, and Γ_D corresponds to a Dirichlet boundary on which the velocity, $\overline{\boldsymbol{u}}$, is imposed.

The rigid cylinder is supported by constant rigidity springs and dampers in the transverse and streamwise directions. The equations of motion for the cylinder are given by the non-dimensional mass-damper-spring equations:

$$m^* \ddot{\boldsymbol{x}}^* + 2\zeta \left(1 + m^*\right) \left(\frac{2\pi}{U_r}\right) \dot{\boldsymbol{x}}^* + \left(1 + m^*\right) \left(\frac{2\pi}{U_r}\right)^2 \boldsymbol{x}^* = \frac{2}{\pi} [C_D, C_L]^{\mathrm{T}}. \tag{5.5}$$

with $m^* = \rho_s/\rho_f$ the mass ratio, $\zeta = c/(2\sqrt{k(m_s + m_a)})$ the damping ratio, $\boldsymbol{x}^* = [x^*, y^*]^{\mathrm{T}} = \boldsymbol{x}/D$ the vector of x and y displacements, C_D and C_L the fluid loading coefficients in each direction (drag and lift). These force coefficients are written as functions of F_x and F_y the fluid loading for each direction as follows:

$$C_D = \frac{F_x}{\frac{1}{2}\rho_f D U^2}, \tag{5.6}$$

$$C_L = \frac{F_y}{\frac{1}{2}\rho_f D U^2}. \tag{5.7}$$

Time is non dimensionalized as $t^* = Ut/D$. The following constraints are applied on the surface of the cylinder:

$$\boldsymbol{u} = \dot{\boldsymbol{x}}^*, \tag{5.8}$$

$$\bar{\boldsymbol{t}} = \boldsymbol{F} \tag{5.9}$$

Simulation of vortex-induced vibration requires a numerical solver capable of handling the moving boundary of the cylinder. Numerical schemes for moving boundary problems generally fall into two categories: interface tracking and interface capturing methods (Shyy *et al.* (1996); Loon *et al.* (2007); Kajishima & Takeuchi (2011)). Both classes have their own advantages and disadvantages. For an isolated cylinder, there is a third alternative which consists of solving the governing equations with respect to a moving frame of reference

attached to the center of the cylinder (Li *et al.* (2002)). This approach frees us from the need for handling the interface movements. Hence, it is a more efficient method.

We define the following coordinate transformation with a simple translation that only varies in time:

$$\boldsymbol{r}_{ab} = \boldsymbol{r}_{mo} + \boldsymbol{r}_{mo/ab} \tag{5.10}$$

Here, the subscript ab denotes the absolute (fixed) frame and mo the moving frame respectively. Rewriting the governing equation for the fluid domain, we have:

$$\boldsymbol{\nabla} \cdot \boldsymbol{u}_{mo} = \boldsymbol{0}, \tag{5.11}$$

$$\rho_f \boldsymbol{u}_{mo,t} + \rho_f[(\boldsymbol{u}_{mo}) \cdot \boldsymbol{\nabla}]\boldsymbol{u}_{mo} = \boldsymbol{\nabla} \cdot \boldsymbol{\sigma}_{mo}. \tag{5.12}$$

The associated constitutive equation now becomes:

$$\boldsymbol{\sigma}_{mo} = \boldsymbol{\tau}_{mo} - [p_{mo} + \rho_f(x\hat{\boldsymbol{i}} + y\hat{\boldsymbol{j}}) \cdot \ddot{\boldsymbol{r}}_{mo/ab}]\boldsymbol{I} \quad \text{with} \quad \boldsymbol{\tau}_{mo} = \mu[\boldsymbol{\nabla}\boldsymbol{u}_{mo} + (\boldsymbol{\nabla}\boldsymbol{u}_{mo})^{\mathrm{T}}].$$

We see that the coordinate transformation simply adds to the fluid governing equations an additional force term $-\rho_f\ddot{\boldsymbol{r}}_{mo/ab}$ which can be absorbed into the pressure term. Thus we must post-process the fluid forces when we couple the fluid equations with the equations for the dynamics of the cylinder. Since $\ddot{\boldsymbol{r}}_{mo/ab} = \ddot{\boldsymbol{x}}^*$, the additional force is simply $-\rho_f V_{cyl}\ddot{\boldsymbol{x}}^*$ where V_{cyl} is the volume of the cylinder.

5.2.2 Solution strategy

We use a finite element method to solve the governing equations in a monolithic manner. The degrees of freedom for the flow, the velocity and the pressure, are fully coupled to the point mass displacements of the cylinder. We use the 3rd order Radau IIA Implicit Runge-Kutta (IRK) time stepping scheme which has 3rd order temporal accuracy for velocity and 2nd order accuracy for the pressure (Hairer & Wanner (2002)). The nonlinear system of equations is linearized by the Newton-Raphson method using the numerical Jacobians. The sparse system is resolved with a direct solver.

We note that this methodology is not only applicable to problems of flows with rigid body motion, but also to the general unsteady fluid-structure interaction problems. Further details of the finite element flow solver and the verification of its space and time accuracy can be found in Etienne *et al.* (2009).

5.3 Numerical details, verification and validation

For efficiency reasons, we opt for solving the governing equations in a moving frame of reference. We employ a spatial discretization that has been previously verified. Here, we verify the time step size on two vortex-induced vibration problems. To validate our computational scheme, we compare our solutions to the results from the literature and those from a validated reference numerical scheme on a well documented problem (Etienne & Pelletier (2012)). The benchmark numerical scheme solves the governing equations in the absolute (fixed) reference frame and employs the Arbitrary Lagrangian Eulerian (ALE) formulation for interface movement management (Etienne & Pelletier (2012)).

5.3.1 Description of the computational problem

The domain for our simulations is summarized in figure 5.2. We impose a uniform unit flow ($u = 1, v = 0$) on all external boundaries (inflow, outflow, upper and lower sides). One node inside the fluid domain is prescribed with zero pressure. On the cylinder, we require the fluid velocity to be equal to the solid velocity which is zero in the moving frame.

Figure 5.2 Geometry and boundaries.
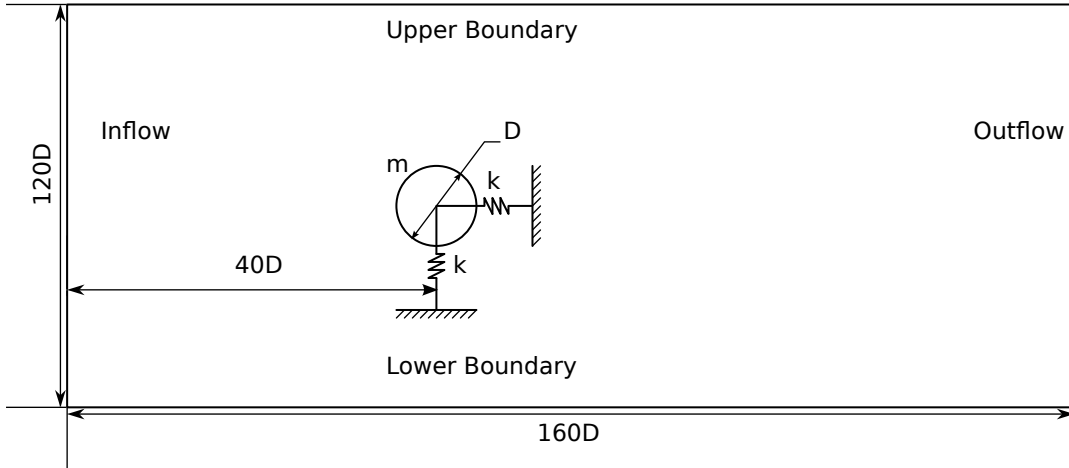
5.3.2 Verification

We employ the same dimensions and mesh data as in Etienne & Pelletier (2012). As noted in Etienne & Pelletier (2012), the domain dimensions were chosen so as to minimize the blockage effect due to the cylinder. The blockage ratio is 0.83% and only a small amount of induced response hysteresis is expected (Prasanth *et al.* (2011)). With the same mesh data,

we are assured that our simulations have three significant digits for the force coefficients (Etienne & Pelletier (2012)).

Here, we verify the time step size on two vortex-induced vibration problems. First, we consider a cylinder that can oscillate in both the transverse and streamwise directions at $Re = 175$ and $U_r = 11$ with $m^* = 1$ and zero damping. Then, we examine a cylinder with $m^* = 0$ that can only oscillate in the transverse direction while keeping the rest of the parameters the same. These correspond to the conditions with higher flow energies and softer cylinder springs in the investigated parametric space. Three time step sizes are compared: $\Delta t = 0.2$, $\Delta t = 0.1$ and $\Delta t = 0.05$. The simulation results are listed in tables 5.1 and 5.2. We see that for both cases, the maximum differences between the results with $\Delta t = 0.05$ and $\Delta t = 0.1$ are less than 2%. Hence, we will employ $\Delta t = 0.1$ for this work.

Table 5.1 XY: $m^* = 1$, at $Re = 175$ and $U_r = 11$.

Δt	RMS A_X^*	Max A_X^*	RMS A_Y^*	Max A_Y^*
0.2	0.01475	0.02170	0.33485	0.46866
0.1	0.01477	0.02168	0.33484	0.46843
0.05	0.01478	0.02172	0.33482	0.46837

Δt	RMS C_D	Mean C_D	RMS C_L	Max C_L
0.2	0.04307	1.31337	0.01108	0.01996
0.1	0.04394	1.31366	0.01017	0.01880
0.05	0.04415	1.31369	0.00998	0.01851

Table 5.2 Y: $m^* = 0$, at $Re = 175$ and $U_r = 11$.

Δt	RMS A_Y^*	Max A_Y^*	RMS C_D	Mean C_D	RMS C_L	Max C_L
0.2	0.39060	0.55107	0.47636	1.95755	0.20958	0.29509
0.1	0.39019	0.54513	0.48603	1.96889	0.20232	0.28240
0.05	0.38996	0.54476	0.48815	1.97361	0.20027	0.27994

5.3.3 Validation

Following Etienne & Pelletier (2012), we also validate our results with the problem of an isolated cylinder mounted on springs in a cross flow. The problem has the following parameters: Reynolds number $Re = 200$, damping ratio $\zeta = 0.01$, reduced velocity $U_{r-n} = U/(f_n D) = 2\pi U/(\sqrt{k/m}D) = 5$ where f_n is the natural frequency of the cylinder in still air, and mass ratio $m^* = 4/\pi$.

Our benchmark reference simulation uses the absolute frame of reference and requires a different set of boundary conditions. We impose a unit velocity ($u = 1$, $v = 0$) at the inflow boundary, zero normal and shear forces at the outflow, and symmetry on the top and bottom boundaries. Our results are compared with those from Blackburn & Karniadakis (1993) and Yang *et al.* (2008). We note that there are differences in the chosen computational domain sizes and boundary conditions. The results are shown in figure 5.3.
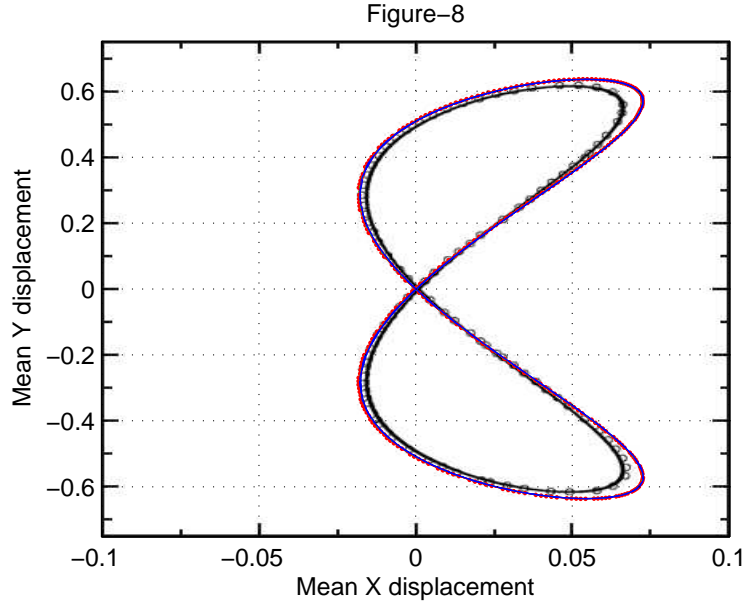

Figure 5.3 Validation: Figure-8.

In figure 5.3, the results from the present work are overlaid on top of figure 8a from Yang *et al.* (2008). The results from Blackburn & Karniadakis (1993) are shown with "o"; results from Yang *et al.* (2008) are shown with the solid line (black); our benchmark scheme with symmetry boundary conditions are shown with the dotted-dashed line (red); and the moving frame results with the dashed line (blue). For comparison, we also include the results of the benchmark scheme with all unit flow boundary condition with the dotted line (green).

First, we note that the trajectories of the benchmark scheme with different boundary conditions are identical which confirms that our computational domain indeed has a very small blockage ratio as expected. The results from the moving frame of reference are essentially indistinguishable from those of the benchmark scheme using the fixed frame of reference.

Comparing with the other results, we see that all trajectories are quite similar. Blackburn & Karniadakis (1993) report a mean streamwise displacement of 0.62D; whereas it is 0.64D for Yang *et al.* (2008). We find a value of 0.59D.

With these results, and knowing that our results are accurate to three significant figures, we have validated that the numerical scheme with a moving frame of reference is suitable to study the problem of an isolated cylinder in uniform cross flow.

5.3.4 Parametric Study

We explore the following parameter spaces:

- Reynolds number ($75 \leq Re \leq 175$),
- Reduced velocity ($5.0 \leq U_r \leq 11.0$),
- Mass ratio ($m^* = \{0, 1\}$)

with zero structural damping. We compare the vortex-induced vibration responses of a cylinder which freely oscillates in both the transverse and streamwise directions to those of a cylinder oscillating only transversely. In what follows, we refer to these results as the XY oscillation response and the Y-only oscillation response respectively. For each simulation run, we fix both the Reynolds number and the mass ratio, and then alter the reduced velocity continuously within the range of interests by varying the spring stiffness. We span the range of reduced velocity in two directions. First, we increase it from its lower bound to its upper bound. Then, we reduce it from the upper bound to the lower bound. In addition, we also carry several simulations with fixed Reynolds number and reduced velocity to compare with the results from both the reduced velocity variation directions. For all cases, both the flow and cylinder are at rest initially.

We first characterize the impact of the variation rate of the reduced velocity with a vortex-induced vibration problem at $Re = 175$. Both XY and Y-only oscillations are considered. The mass ratio of both $m^* = 0$ and $m^* = 1$ are investigated. We have considered three variation rates: $\Delta U_r = 1/300$ (*i.e.* 300 non dimensional time unit), $\Delta U_r = 1/600$ and $\Delta U_r = 1/900$. A slower variation rate provides more accurate results at a higher computational cost. We examine the maximum amplitudes and the frequency responses in the transverse direction. Sample results are shown in figures 5.4 and 5.5. We observe that the variation rate of U_r does not have a large influence on the maximum amplitude values. For example, the $\Delta U_r = 1/300$ result can already capture the peak value rather successfully. However, they may induce a delay into the sudden response changes. For example, at the onset of synchronization close to the peak (see figure 5.5(a)). Among the 3 variation rates considered, the $\Delta U_r = 1/600$ result provides sufficient details in the responses at a moderate cost. Comparing with the $\Delta U_r = 1/900$ result, it differs at most by 2.5%. In particular, the maximum amplitude peak values differ by less than 0.5%. Hence, we choose the variation rate of $\Delta U_r = 1/600$ as our limit for all our simulations below.
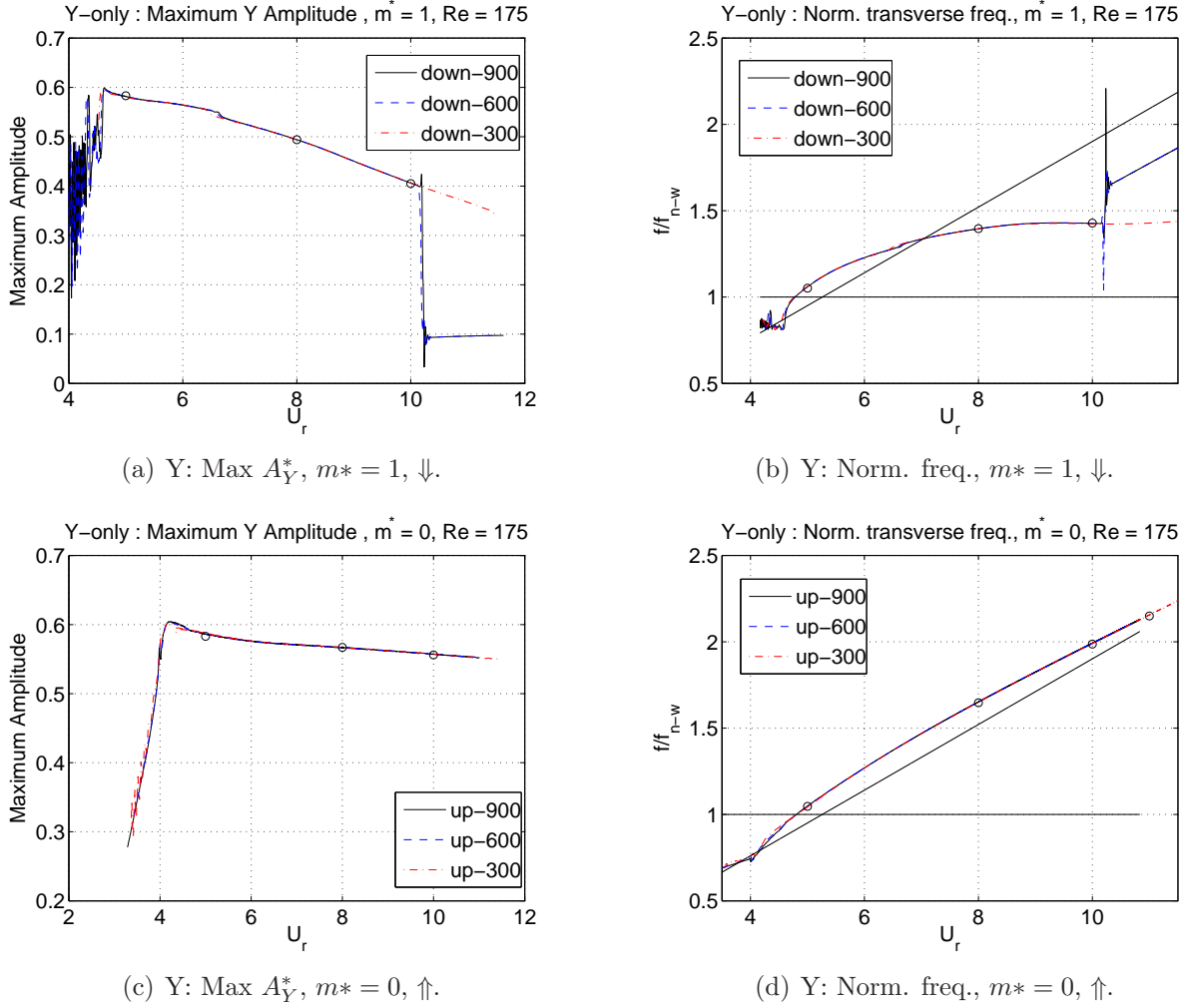
Figure 5.4 Verification: Variation rate : Y-only.

5.4 Results

In general, both of the Y-only and XY results are in accordance with previous works. At fixed values of the Reynolds number and the mass ratio, as we increase the reduced velocity, the maximum transverse amplitude first climbs to its peak value and then decreases. However when we increase the Reynolds number, the maximum transverse amplitude also increases in various degrees. More specifically, the increases are more significant for the XY oscillations than the Y-only oscillations. This is in contrast to the observations from Williamson & Govardhan (2006) based on previous numerical investigations. This will be discussed in more details in the sequel.

We first look at the maximum amplitude and frequency responses. Then, we inspect the displacement trajectories and the force phase diagrams. After, we examine the change of

(a) XY: Max A_Y^*, $m* = 1$, $\Uparrow$.

(b) XY: Norm. freq., $m* = 1$, $\Uparrow$.

(c) XY: Max A_Y^*, $m* = 0$, $\Downarrow$.

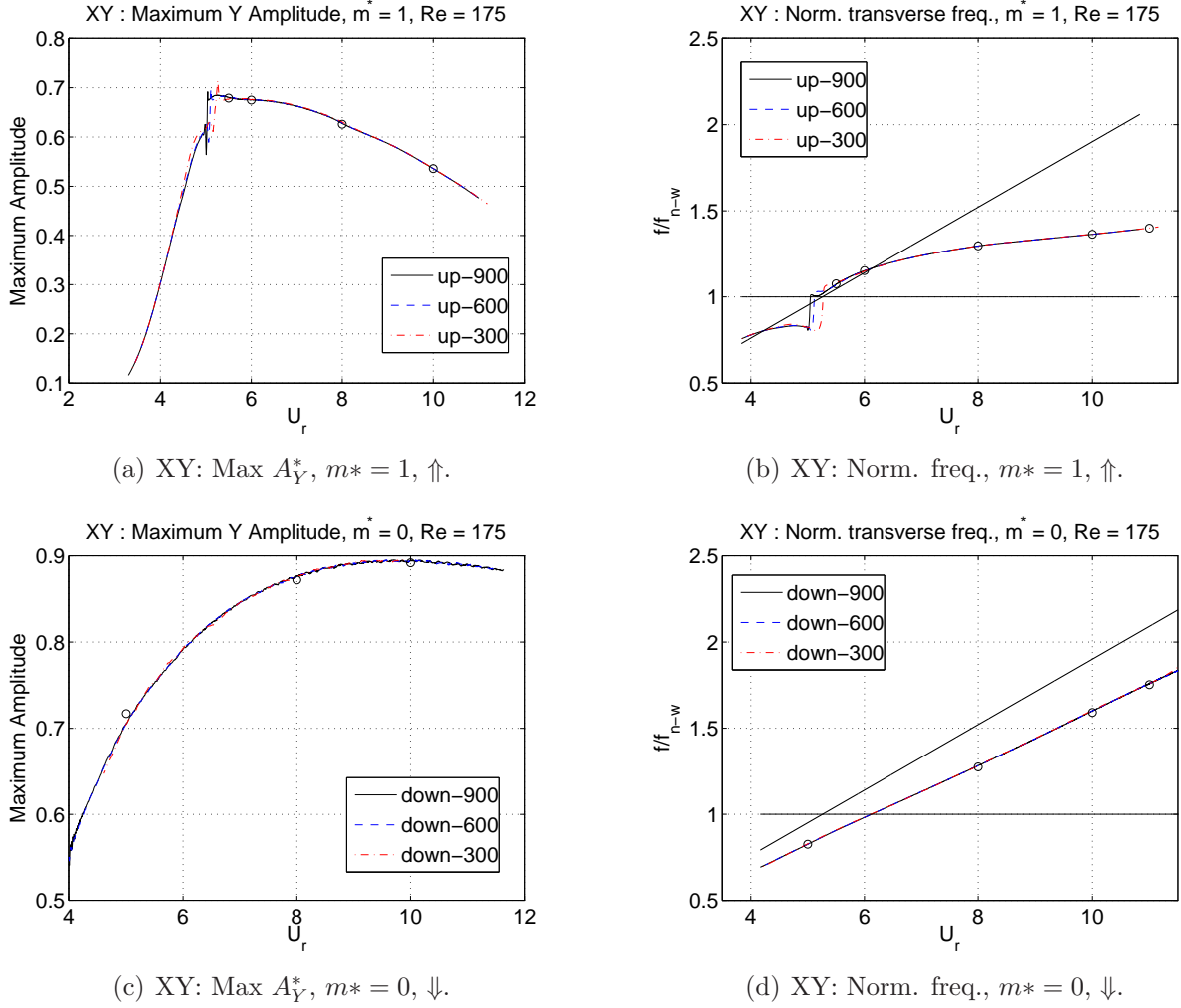(d) XY: Norm. freq., $m* = 0$, $\Downarrow$.

Figure 5.5 Verification: Variation rate : XY.

total phase angle between the lift force and the transverse displacement. This is followed by the vortical structure pattern. We also compare our results with those of forced vibrations. Lastly, we discuss the critical mass ratios and branching.

5.4.1   Maximum amplitudes

The maximum amplitude responses obtained by increasing and decreasing the reduced velocity generally correspond well to each other. Both sets of responses agree well with the results of the fixed reduced velocity simulations. As expected, there is a narrow range of hysteresis at low reduced velocity (around $U_r = 4.0$ to 5.0) for most cases. Hysteresis can also be clearly observed at a higher value of reduced velocity $U_r > 10.0$ for some conditions. At the central range where the peak maximum amplitudes occur, there is no hysteresis.

The maximum transverse amplitude with respect to the Reynolds number and reduced

velocity for $m^* = 1$ of the Y-only oscillation response is shown in figure 5.6. The peak amplitudes is close to $0.597D$ at a reduced velocity of about 5. This is in good agreement with the results from other studies of Y-only oscillation response (Anagnostopoulos & Bearman (1992); Shiels et $al.$ (2001); Placzek et $al.$ (2009)). When the Reynolds number is increased, the maximum amplitude only marginally increases and the location of the peak shifts slightly towards the lower reduced velocity end. This seems to agree with the suggestion of Williamson & Govardhan (2006) that the Reynolds number does not significantly affect the maximum transverse amplitude in the laminar regime.

At $Re = 150$ and $Re = 175$, hysteresis can be clearly seen at the higher reduced velocity range. Synchronizations do not occur for $U_r > 10$ in the decreasing direction. However, in the increasing direction, the responses remain synchronized beyond $U_r > 11$. Besides, at these Reynolds numbers, a hysteretic bump can also be observed at reduced velocities between $U_r = 6$ and 7.

At lower reduced velocity ($U_r < 5$), we observe hysteretic responses for all the investigated values of the Reynolds numbers. The responses are generally smoother in the increasing direction. At lower Reynolds number, a clear soft "jump" in the amplitude can be seen. At higher Reynolds number, some "instabilities" at moderate frequency can be observed. Whereas in the decreasing direction, the "instabilities" are more evident and they also become stronger at higher Reynolds number. We have carried several simulations with slower variation rates of the reduced velocity to ensure that the observed instabilities are not due to an insufficiently slow variation rate. The amplitude response at $Re = 100$ for $U_r < 5$ in the decreasing direction is shown in figure 5.7. It resembles the quasi-periodic (beating) phenomenon observed by Khalak & Williamson (1999) for low mass-damping systems. Placzek et $al.$ (2009) commented that "quasi-periodic (beating) phenomenon can be understood as a desynchronization phenomenon". Intuitively, the spring is softened in the increasing direction (towards synchronization). This favours lower frequency response content. On the other hand, the spring is stiffened in the decreasing direction (towards desynchronization); which in turn promotes higher frequency response content. The observed hysteretic patterns therefore agree with our expectation. We will show later that the hysteretic responses in the two directions are associated with the differences in the vortex shedding patterns.

The results for $m^* = 0$ of the Y-only oscillation response is shown in figure 5.8. The variation of the maximum amplitude is much smoother in the studied parameter space. Instability is absent in the lower reduced velocity range. However, the soft amplitude jumps in the increasing direction at $U_r \approx 4$, which can be observed more clearly in figure 5.8(a) for higher values of Reynolds number, are always present. There is no hysteretic response in the higher reduced velocity range. When the Reynolds number is increased, the increase in
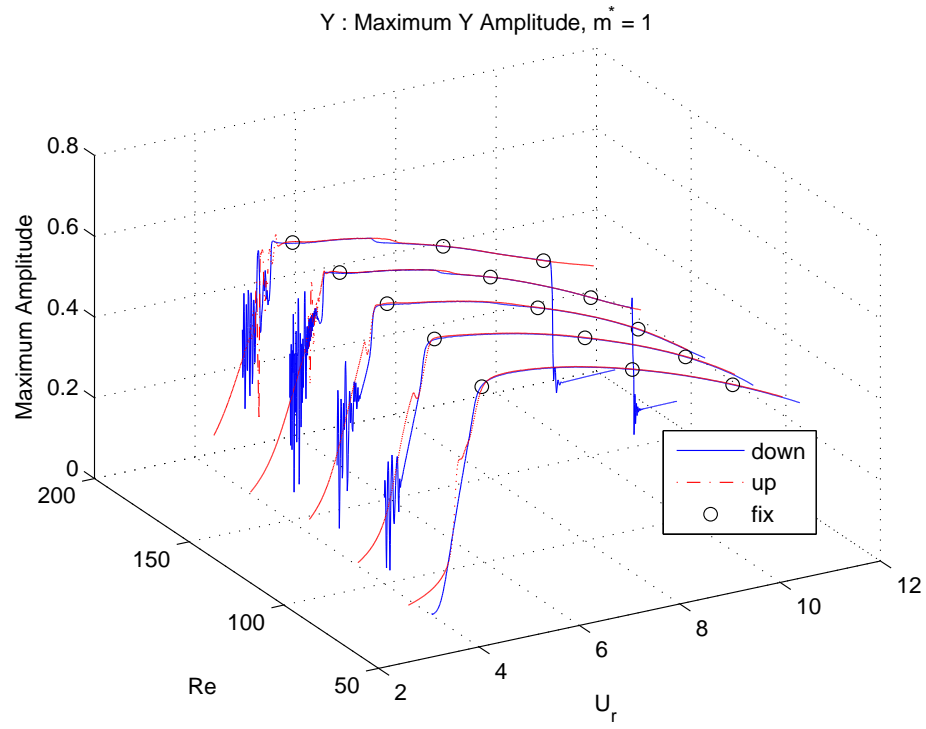
(a) Response surface.
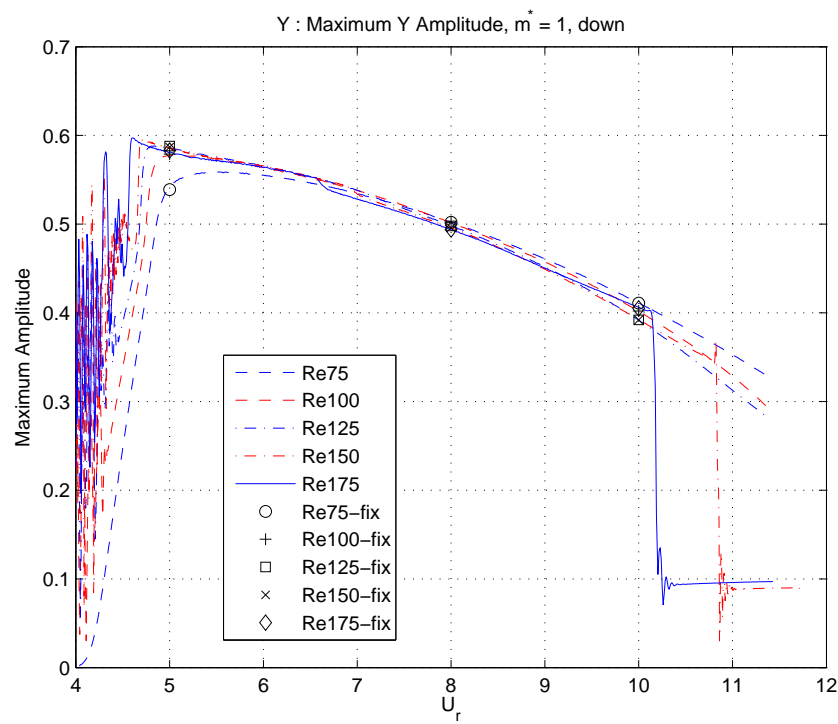
(b) Reduced velocity view.
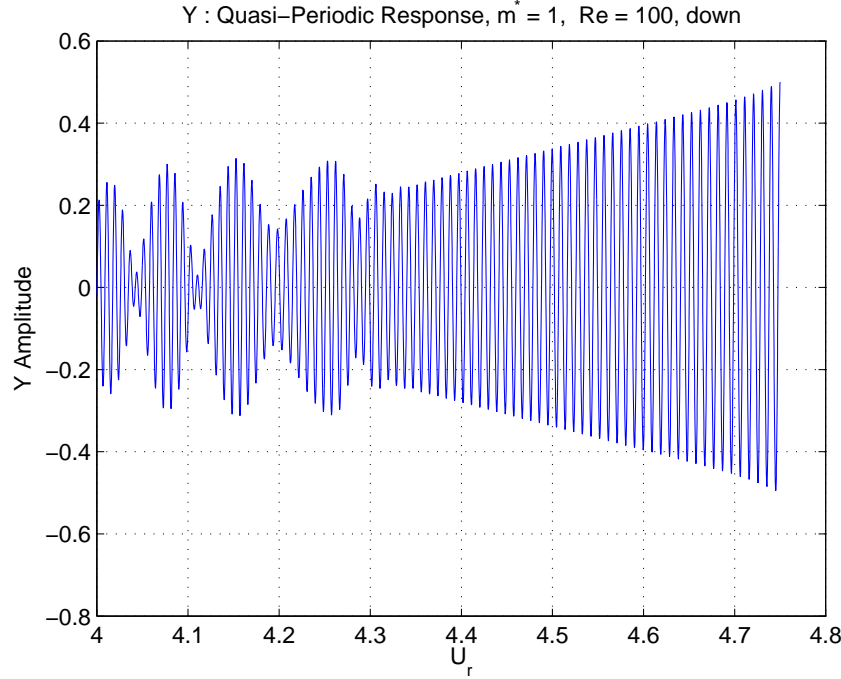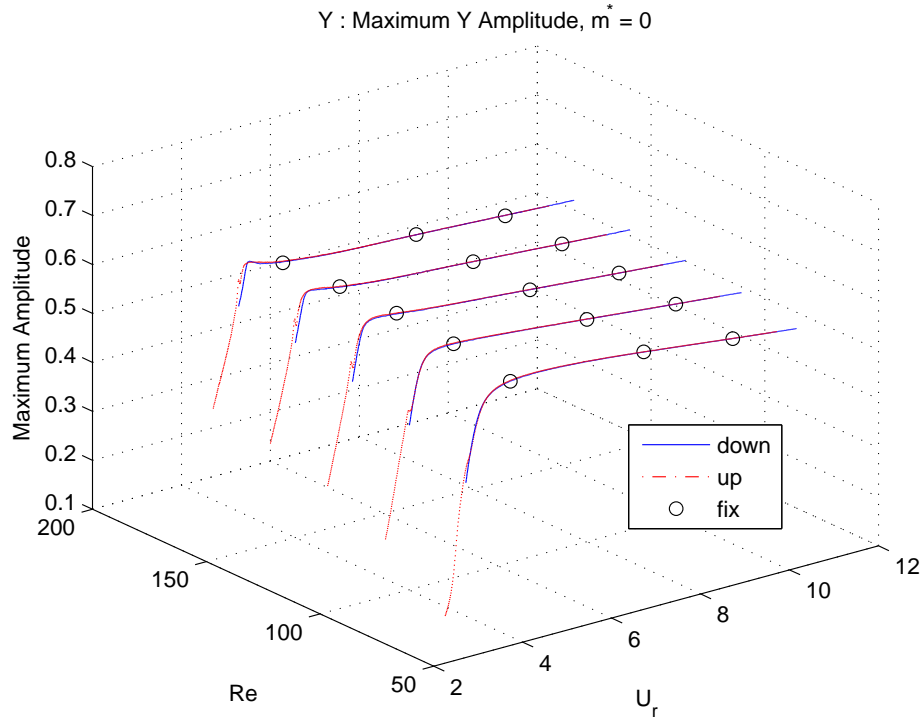
Figure 5.6 Y: Max amplitude with $m^* = 1$.

Figure 5.7 Y: Quasi-periodic response with $m^* = 1$ at $Re = 100$.

the maximum amplitude becomes slightly more evident. The overall peak value is $0.604D$ at $Re = 175$. At the other Re, the peak value is essentially identical to the results from $m^* = 1$. At $Re = 100$, we observe a maximum amplitude of $0.578D$ which is comparable to the $0.59D$ from Shiels *et al.* (2001). Similar to the $m^* = 1$ case, the location of the peak shifts slightly towards lower values of the reduced velocity end when the Reynolds number is increased. However, the maximum amplitude only gently decreases in the higher reduced velocity range in contrast to the $m^* = 1$ results. No desynchronization is observed.

The results for $m^* = 1$ of the XY oscillation response are shown in figure 5.9. Comparing with the results for $m^* = 1$ of the Y-only oscillation results, we can see four major differences. First, the peak maximum amplitude now jumps to $0.682D$ for $Re = 175$. Secondly, the maximum amplitude is more strongly influenced by the Reynolds number. A higher Re leads to a higher maximum amplitude peak. Thirdly, the maximum amplitudes for the five different values of Reynolds numbers occur over a broader range of U_r from 5.5 to 6.5. Lastly, as the Reynolds number increases, the location of the peak amplitude shifts towards the lower reduced velocity at a slower pace. The maximum amplitudes seems to have similar decreasing rates in the higher U_r range as those of Y-only oscillation with $m^* = 1$.

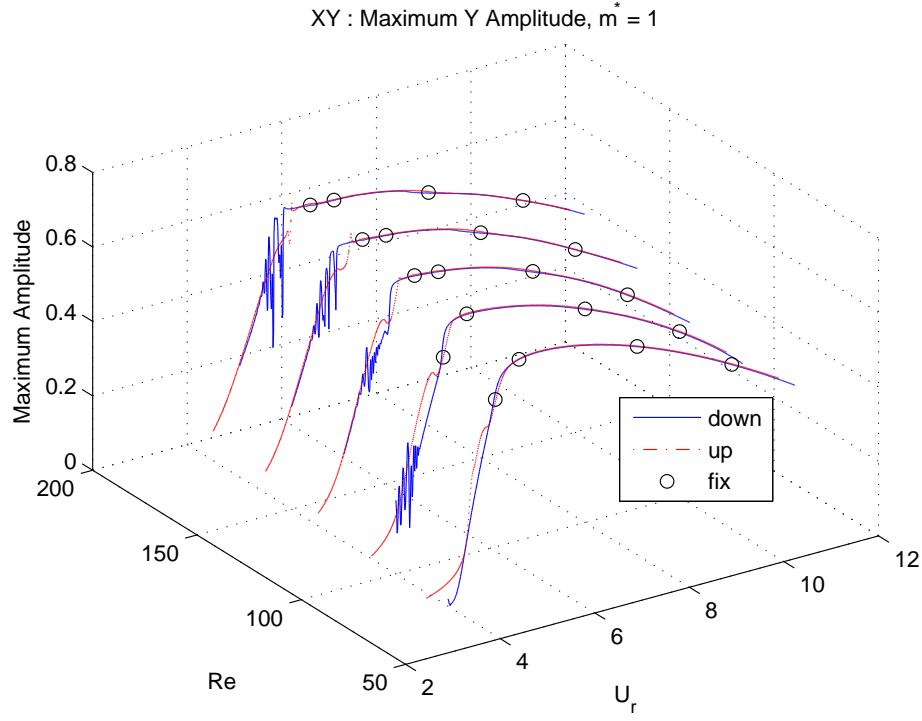From the literature, several maximum amplitudes of XY oscillation at around $Re = 100$
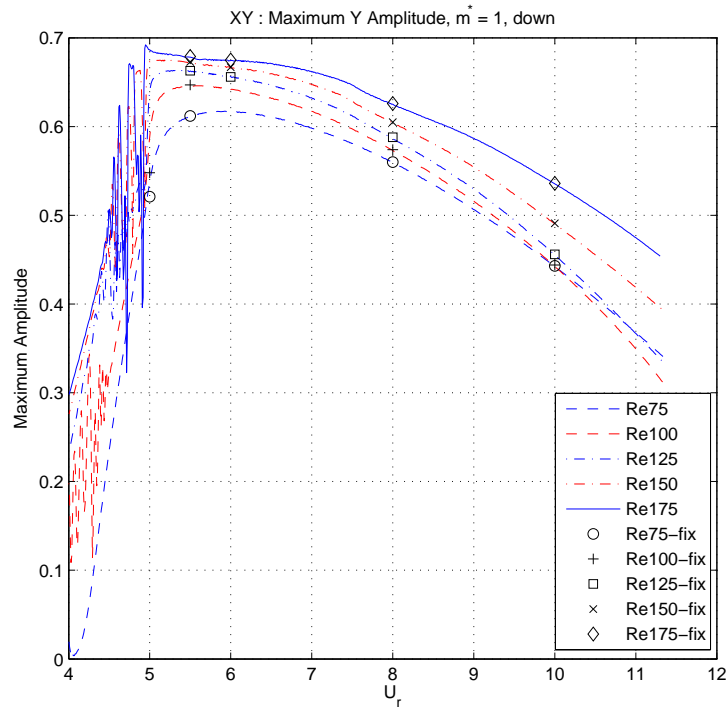
(a) Response surface.
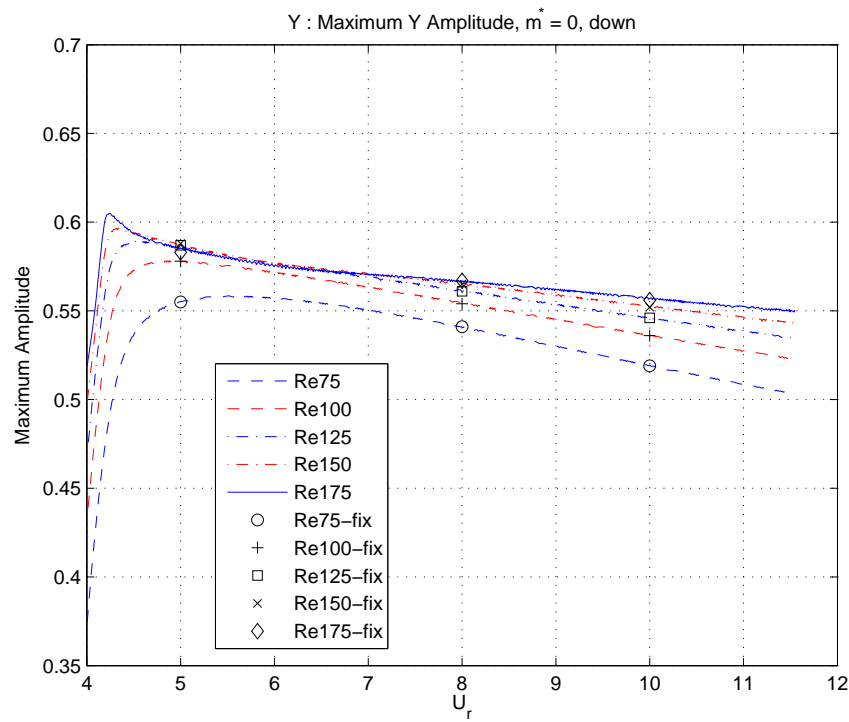
(b) Reduced velocity view.

Figure 5.8 Y: Max amplitude with $m^* = 0$.
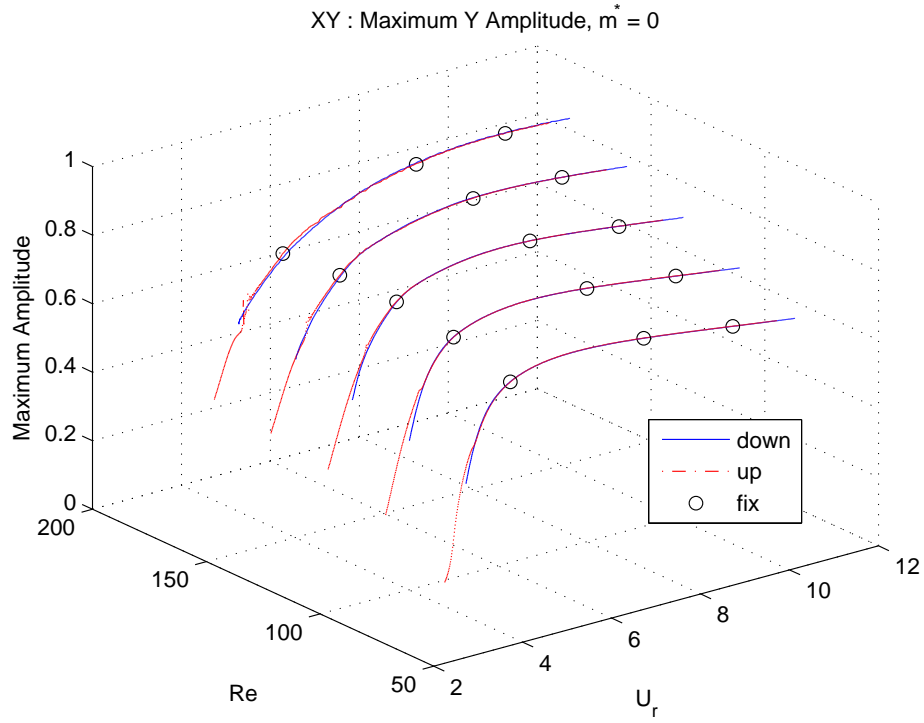
(a) Response surface.

(b) Reduced velocity view.
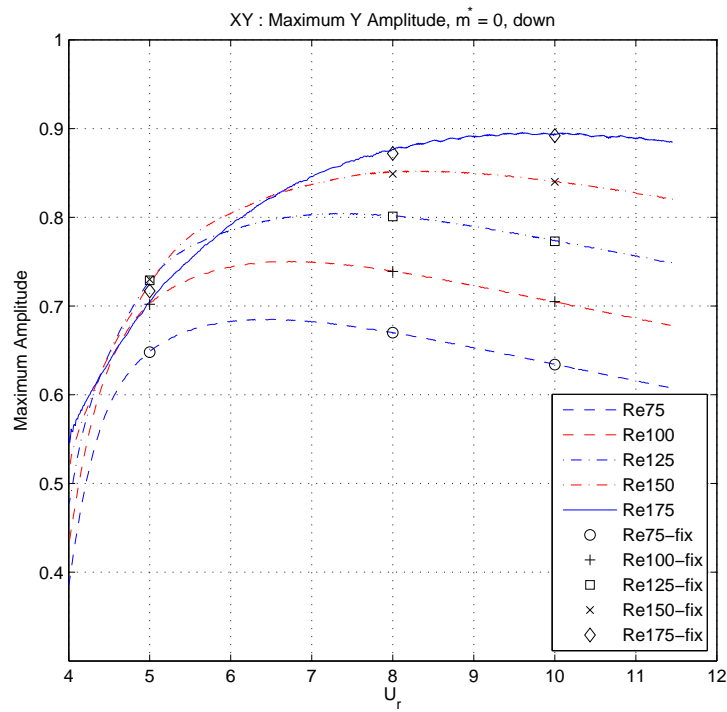
Figure 5.9 XY: Max amplitude with $m^* = 1$.

have been reported. Newman (1996) studied the XY oscillation response of a flexible cable at $Re = 100$ with $m^* = 2$, zero damping and a blockage ratio of 3.33%. He found a maximum transverse amplitude of about $0.59D$. Prasanth & Mittal (2008) investigated the XY oscillation response of a circular cylinder with $m^* = 10$ numerically and they found the maximum transverse amplitude to be about $0.56D$ at $U_r = 5.1$ and $Re = 85$. Prasanth *et al.* (2011) later investigated the hysteresis in the two degrees of freedom vortex-induced vibrations response for a cylinder. With $m^* = 2$ and a blockage ratio of 5.0%, the maximum transverse amplitude is observed to be $0.58D$ at around $U_r = 4.75$ and $Re = 78$. We find the maximum transverse amplitude to be $0.647D$ at $Re = 100$ with $m^* = 1$.

The results for $m^* = 0$ of the XY oscillation response are shown in figure 5.10. The overall peak value is now found to be around $0.890D$, a significant 50% increase compared to the Y-only oscillation response. At higher reduced velocities, the maximum amplitude only decreases gently. The location of the peak transverse amplitude now shifts towards higher values of the reduced velocity as the Reynolds number is increased from 75 to 175. This is in sharp contrast to both the responses observed for the Y-only responses with the same values of parameters and also to the observation of the XY oscillation responses of a cylinder with $m^* = 0$ by Etienne & Pelletier (2012) who found the maximum transverse amplitude almost always occurs at $U_r = 6.5$ for very low Reynolds number ($Re < 50$). The maximum transverse amplitude also increases more rapidly when the Reynolds number increases. This behavior markedly differs from what was suggested by Williamson & Govardhan (2006) who found that the maximum transverse amplitude response is not influenced by the Reynolds number in the laminar shedding range. We note however that the data available to Govardhan and Williamson back in 2006 were mostly reported for $Re = 100$ and $Re = 200$. Also, the data on maximum amplitude are typically presented using log-log scales which complicates the precise interpretation of information. Thus, it is very probable that this trend with Reynolds number was not possible to be identified previously.

Singh & Mittal (2005) determined the maximum amplitudes of XY oscillation responses of a cylinder with $m^* = 10$ for a range of Reynolds number ($85 < Re < 200$) at a fixed reduced velocity of $U_r = 4.92$. They expected that the maximum amplitudes would occur at the same reduced velocity independent of the Reynolds number. Their choice of $U_r = 4.92$ corresponds to the peak location at $Re = 100$. While the Y-only oscillation response for $m^* = 1$ shows that this can be a reasonable assumption when the mass ratio is very large, the XY oscillation response for $m^* = 0$ clearly shows that this condition is not always true. Consequently, to numerically determine the peak value of the maximum amplitude at a given Reynolds number, it is more effective to fix the inlet flow velocity and vary the spring stiffness of the cylinder.

(a) Response surface.

(b) Reduced velocity view.

Figure 5.10 XY: Max amplitude with $m^* = 0$.

In both the XY oscillation cases above, the streamwise amplitudes are much smaller than the transverse amplitudes. The largest maximum streamwise amplitude is about 25% of the maximum transverse amplitude and it is generally under 20%.

We summarize the effect of Reynolds number on the peak maximum transverse amplitude in figure 5.11. Our data is presented together with those compiled by Morse & Williamson (2009a). The symbols for the compiled data are described in table 3 in Williamson & Govardhan (2006) and Morse & Williamson (2009a). We also show in the figure the results at very low Re from Etienne & Pelletier (2012). In particular, we see that the peak maximum amplitude of Y-only oscillation with $m^* = 0$ and $m^* = 1$ are essentially identical. Hence, they are on top of each other, especially for lower values of the Reynolds number. More distinguishable difference in the two maximum amplitude results can only be observed at $Re = 175$.
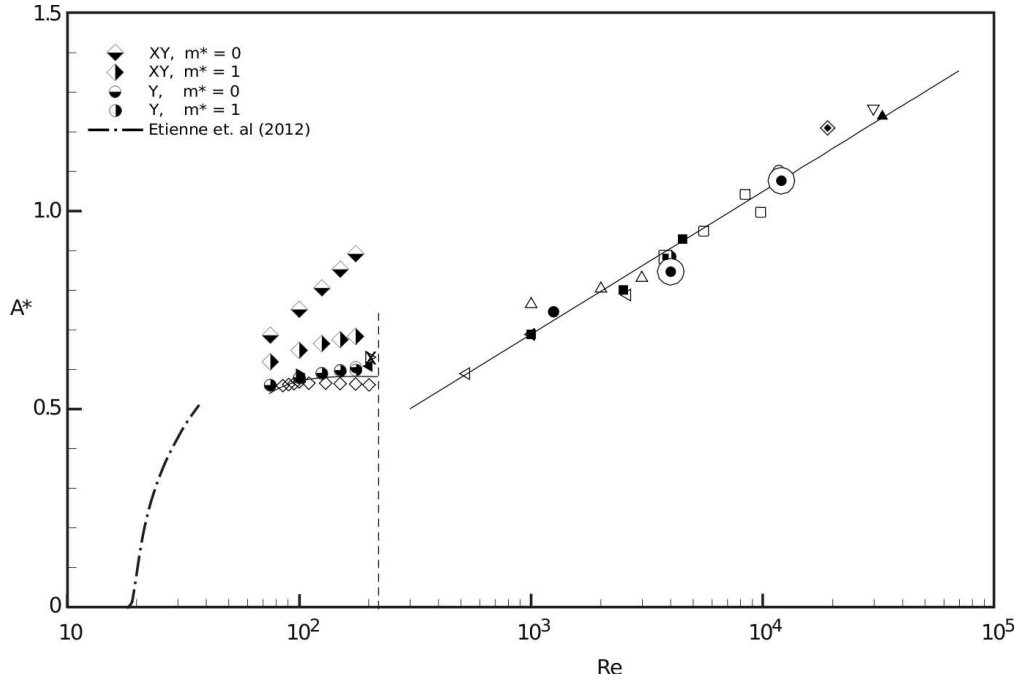
Figure 5.11 Effect of Re on max amplitude.

Jauvtis & Williamson (2004) discovered experimentally that when the mass ratio is "large", the XY oscillation responses resemble those of the Y-only oscillation. At low Reynolds numbers, Prasanth *et al.* (2011) reported that the maximum amplitudes for the XY and Y-only oscillation responses are "almost the same" for a cylinder with $m^* = 10$. We examine the effect of mass ratio on the peak maximum transverse amplitude of the XY and Y-only oscillations at $Re = 175$. This is the highest Reynolds number in our parametric space

corresponding to the case with the largest upstream flow energy. From figure 5.12, we see that the maximum transverse amplitude of the XY oscillation is larger than that of the Y-only oscillation for all m^* considered. As the mass ratio is increased, the maximum amplitudes decrease for both the XY and Y-only oscillations. The maximum amplitude of the XY oscillation reduces more rapidly than that of the Y-only oscillation. The maximum amplitude of the XY oscillation with $m^* = 0$ is 50% larger than the Y-only peak amplitude. When m^* is increased to 5, it is only about 5% larger than that of the Y-only oscillation.
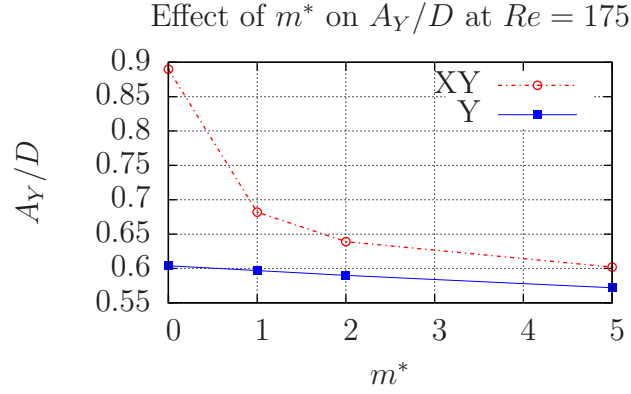

Figure 5.12 Effect of mass ratio on max amplitude.

5.4.2   Frequency responses

The transverse frequency responses for our parameter space are shown in figures 5.13 and 5.14. The responses from the increasing and decreasing of the reduced velocities do not differ significantly. The profile for the Y-only oscillation and the XY oscillation are also rather similar. Overall, the Y-only oscillation frequencies are consistently higher than those of the XY oscillation. Intuitively, this is reasonable because the XY oscillation has an additional degree of freedom for movement. Hence, the XY oscillation can achieve larger displacements. The energy input for the cylinder oscillation comes from the flow. With a fixed inlet flow, the amount of overall energy input is the same, and hence the amount of available work done should be comparable. A larger displacement demands a smaller oscillation frequency, and vice versa. Consequently, the frequency of the XY oscillation is lower than that of the Y-only oscillation. This can also be observed from the frequency characteristics in the original work of Jauvtis & Williamson (2004).

Generally, the higher the reduced velocities, the higher the oscillation frequencies (f). We can observe two main trends: one corresponds to the Reynolds number, the other to the

mass ratio.

The Reynolds numbers investigated are all within the "laminar parallel shedding" regime (Fey *et al.* (1998)). For which, the Strouhal number (St_{fix}) increases linearly with the Reynolds number. Thus, a higher Reynolds number leads to an increase in the slope of the vortex shedding frequency line. Also, with a higher Reynolds number, the vortex shedding frequency intercepts the cylinder natural frequency (f_{n-w}) at a lower reduced velocity.

For both the Y-only and XY oscillation responses, the oscillation frequency generally increases as the Reynolds number is increased. For small Reynolds numbers, there can be a large range of reduced velocities, typically in the lower range, where the oscillation frequencies are above the vortex shedding frequencies. For larger Reynolds numbers, the oscillation frequencies generally shift under the vortex shedding frequency lines, except for the Y-only oscillation frequency with $m^* = 0$. Although it also shifts towards the vortex shedding frequency lines when the Reynolds number is increased, the response remains entirely above the vortex shedding frequencies for all investigated values of the Reynolds number.

We can observe two main characteristics with respect to the mass ratio values. For $m^* = 0$, the oscillation frequency lines are rather close to and in fact almost parallel to the vortex shedding frequency line. Again, we notice the gentle increase in the slopes for the oscillation frequencies with an increase in the Reynolds numbers. For the XY oscillation, the oscillation frequency line seems to always intercept the natural frequency line at a value of the reduced velocity of about 6.0 for all Reynolds numbers. However, we do not observe any similar pattern for the Y-only oscillation. The general profiles of the oscillation frequency resemble closely those observed by Govardhan & Williamson (2002) for a cylinder with $m^* < m^*_{critical}$ subjected to transverse vibrations only.

For $m^* = 1$, the responses are less sensitive to the changes in the Reynolds number for both the Y-only and XY oscillations. The general profiles of the oscillation frequency lines of $m^* = 1$ are rather similar to each other. At low reduced velocity, the slope of the oscillation frequency is closer to the vortex-shedding frequency. As the reduced velocity increases, the slope approaches that of the cylinder's natural frequency. Also, increasing the Reynolds number will shift the intercepts with the natural frequency lines towards lower values of the reduced velocities. At a reduced velocity of 11, the oscillation frequencies for the various Reynolds numbers all occur at $f/f_{n-w} = 1.4$ for both the Y-only and XY oscillations. This value is comparable to $f/f_{n-w} = 1.4$ for a cylinder with Y-only vibrations with $m^* = 2.4$ (Khalak & Williamson (1999)), $f/f_{n-w} = 1.3$ on the lower branch for a cylinder having XY oscillations with $m^* = 2.6$ (Jauvtis & Williamson (2004)) and $f/f_{n-w} = 1.5$ on the lower branch for a pivoted cylinder having XY vibrations with $I^* = I/I_d = 1.03$ (where I is the inertia for the cylinder and I_d is the inertia of the displaced fluid with respect to the
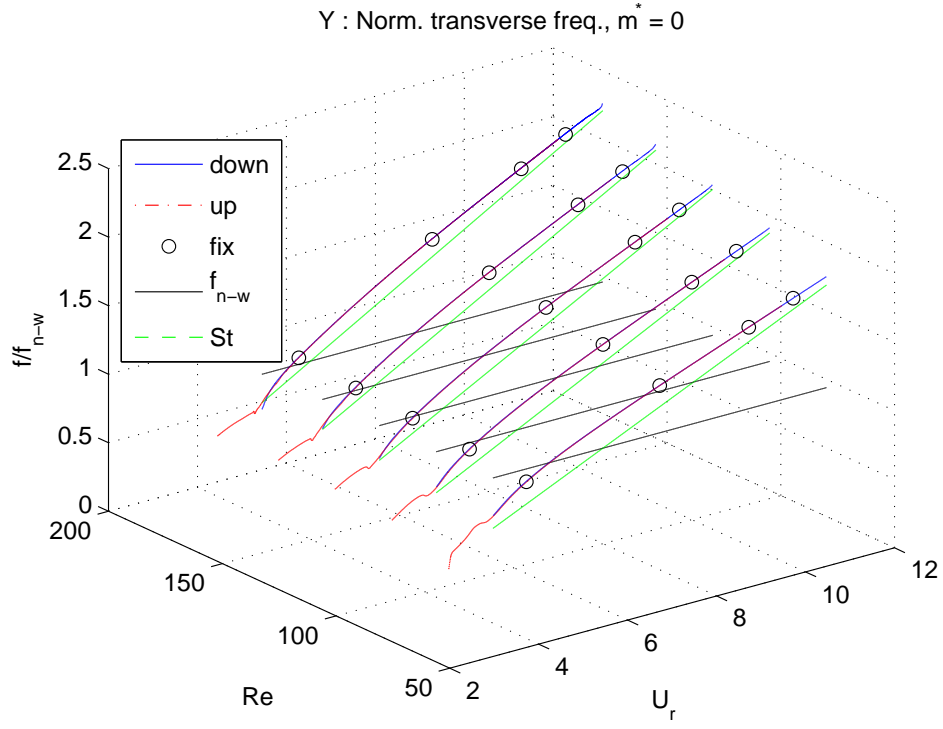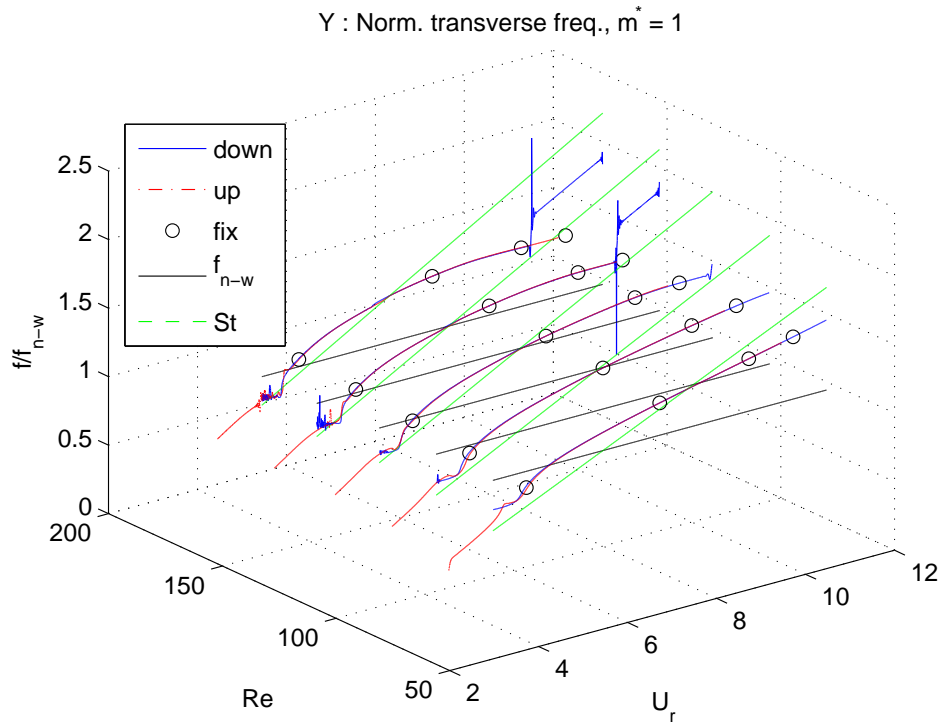
(a) $m^* = 0$.

(b) $m^* = 1$.
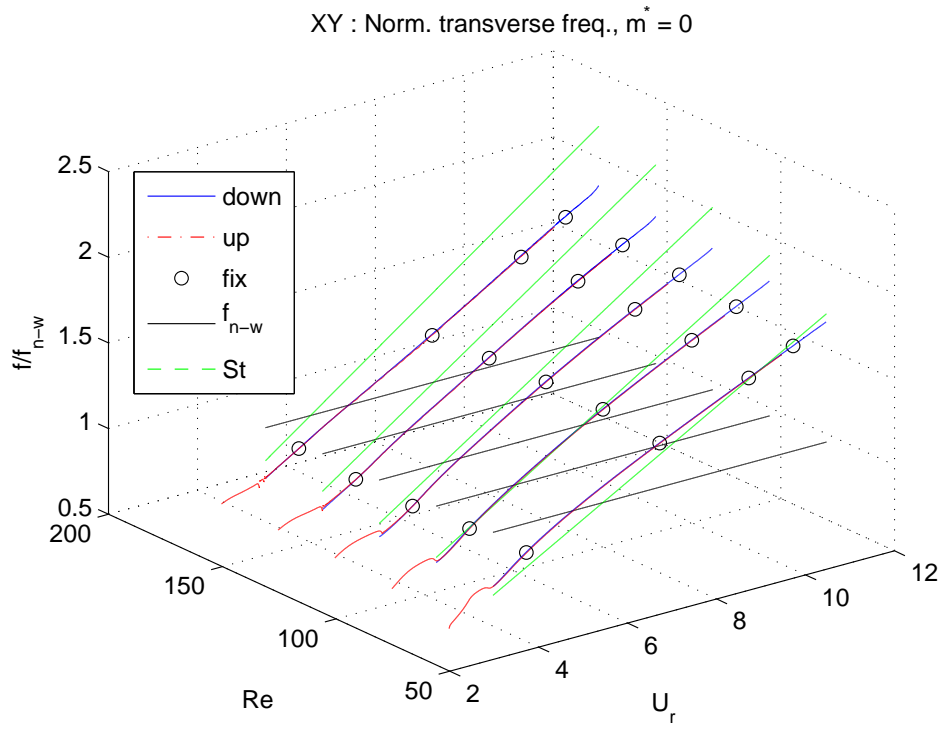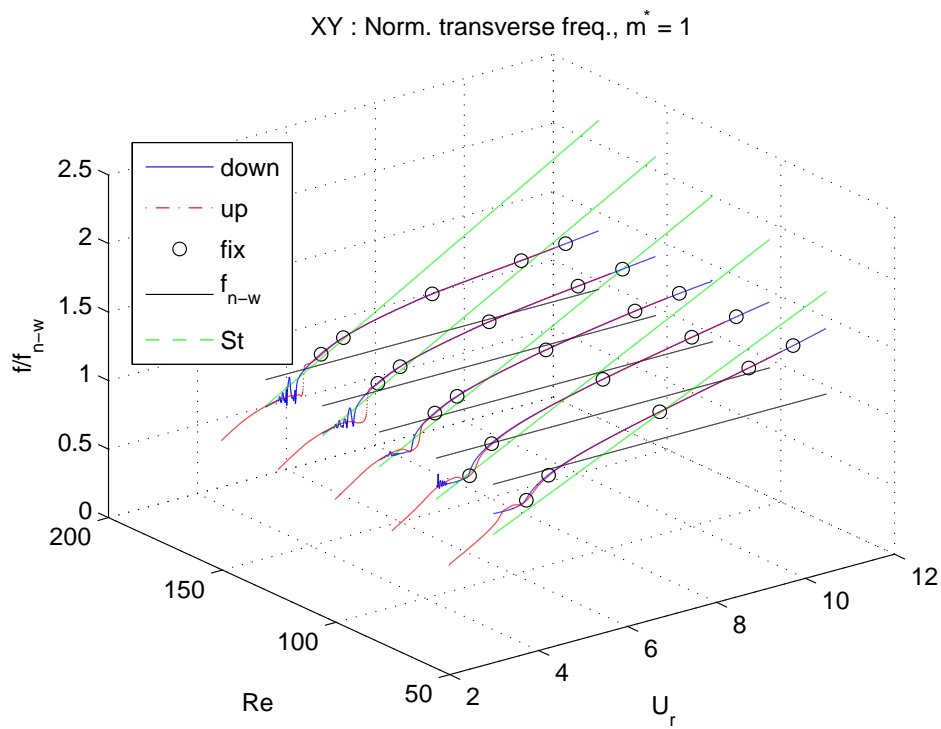
Figure 5.13 Y: Normalized frequency of oscillation.

(a) $m^* = 0$.

(b) $m^* = 1$.

Figure 5.14 XY: Normalized frequency of oscillation.

pivot point) (Flemming & Williamson (2005)) all at the reduced velocity of 11. The general profile of the oscillation frequency line however does not resemble those presented in these works which all contain branching in their responses. We note that the results reported in the aforementioned references were obtained for flows at much higher Reynolds number ($Re > 1000$), compared to the values used in the present work $75 < Re < 175$. We also highlight the fact that the variation of reduced velocities in the present work is achieved by adjusting the spring stiffness value while keeping the Reynolds number fixed; whereas in the experiments, the reduced velocity is usually changed by adjusting the flow rate, which will also simultaneously alters the Reynolds number. One should take these differences into consideration before drawing conclusions about the results, as also observed by Wanderley *et al.* (2011).

Lastly, we note that for Y-only oscillation with $m^* = 1$, similar to the maximum amplitude response, hysteresis is observed for the cases at higher Reynolds number. At $Re = 150$ (figure 5.15(a)), the hysteretic response is located at about $U_r = 7.0$. At $Re = 175$ (figure 5.15(b)), it is found at about $U_r = 6.5$.

5.4.3 Displacement trajectories

Here, we only report the displacement trajectories of the cylinder for the XY oscillation response. The displacement trajectories for the results of the increasing and decreasing reduced velocity directions are essentially identical. Hence, we here present only the results in the decreasing direction for clarity.

We first examine the results for $m^* = 0$. Figure 5.16(a) shows the displacement trajectories at $Re = 125$. At high reduced velocity (*i.e.* low spring stiffness), there is a large streamwise displacement (about 4.5) due to the drag force. As the reduced velocity decreases (*i.e.* larger spring stiffness), the streamwise displacement decreases. The shape of the trajectory generally resembles the classical figure-8 except for low values of the reduced velocity. In this range, it becomes a parabolic-like shape. At other Reynolds numbers, the displacement responses are very similar. Besides the differences in the maximum transverse magnitude reported in the previous section, they differ mainly in the initial streamwise displacement: a higher Reynolds number leads to higher streamwise displacements at high reduced velocity (low spring stiffness) values. For low reduced velocities, the trajectories for all cases center at around $x = 0.5$.

The trajectory responses for $m^* = 1$ are shown in figure 5.16(b) for $Re = 75$ and figure 5.16(c) for $Re = 175$. At high reduced velocities, they have significantly smaller streamwise displacements compared to the zero mass ratio results. The trajectory shapes still resemble those of the zero mass ratio for low Reynolds number cases as in figure 5.16(b). At

(a) $Re = 150$, $m^* = 1$.
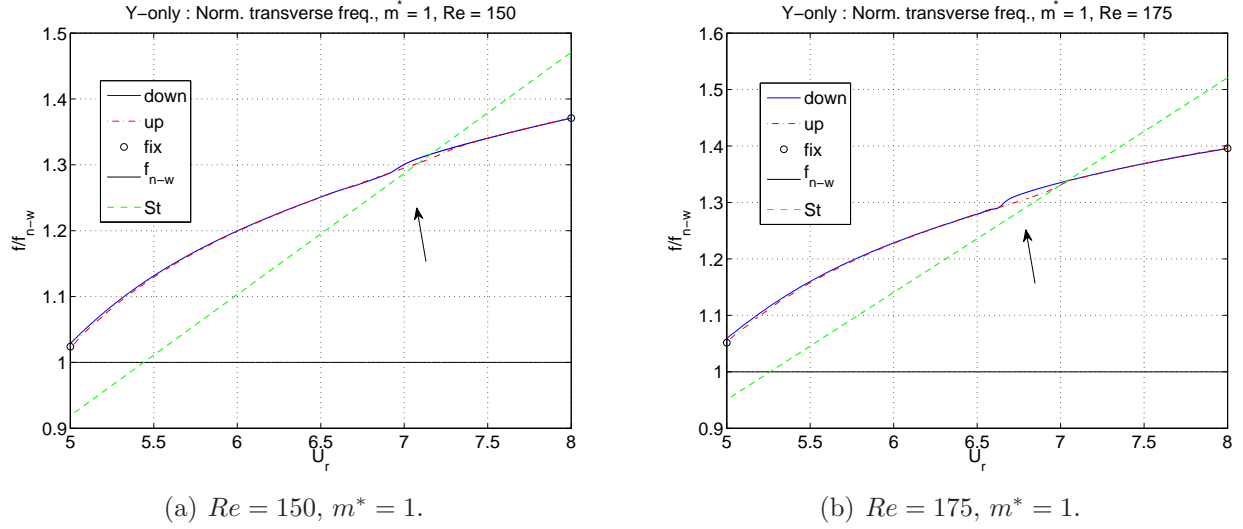
(b) $Re = 175$, $m^* = 1$.

Figure 5.15 Y : Hysteresis in the normalized frequency response.

high Reynolds number as in figure 5.16(c), the parabolic shape is not present at low reduced velocity. The trajectory becomes a figure-8 and the transverse amplitudes are rather "chaotic" presenting a "quasi-periodic" response.

5.4.4 Drag and lift coefficients

The force coefficients for the XY and Y-only oscillations exhibit very different trends. Results of the XY oscillations for the lift and drag coefficients are shown in figure 5.17(a) for $m^* = 0$ and figures 5.17(b) and 5.17(c) for $m^* = 1$. We observe that for the zero mass ratio case, the phase diagrams at different Reynolds numbers all exhibit similar profiles that resemble those of the displacement trajectories: at high to moderate reduced velocities, the shapes form a figure-8; at low reduced velocities, the shapes become parabolic, convex backward relative to the flow direction. This is reasonable as there is no mass, nor damping to introduce any delay in the response between the forces and displacements. In other words, the displacement profiles should only differ from those of the forces scaled by the spring stiffness coefficients.

For the cases with $m^* = 1$, with the inertial effect, the force coefficient profiles of low Reynolds number are less similar to those of the higher Reynolds number. The shapes of figure-8 are now stretched and the parabolic shapes are replaced by an almost vertical line in the low reduced velocity region.

Results of the Y-only oscillation for the lift and drag coefficients are shown in figure 5.18(a) for $m^* = 0$ and figure 5.18(b) for $m^* = 1$. The force coefficient profiles for $m^* = 0$ and $m^* = 1$ are much more similar to each other. And compared to the XY oscillation, the drag coefficients of the Y-only oscillation are generally much larger.
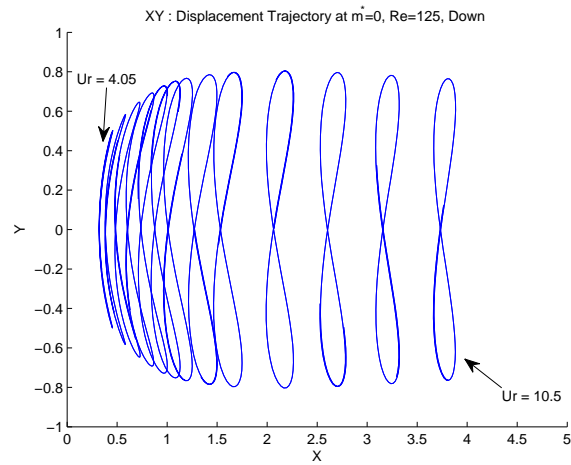
(a) $m^* = 0$ and $Re = 125$.
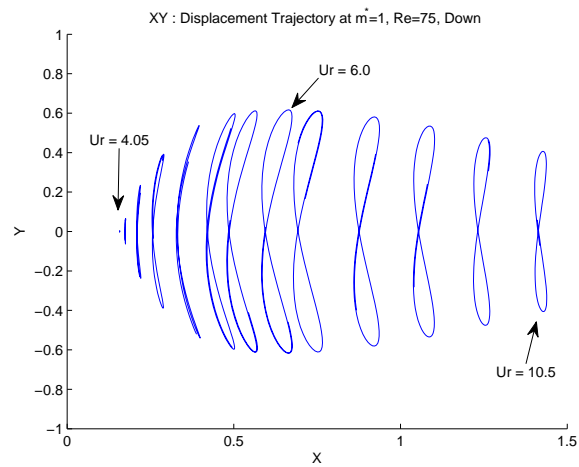
(b) $m^* = 1$ and $Re = 75$.
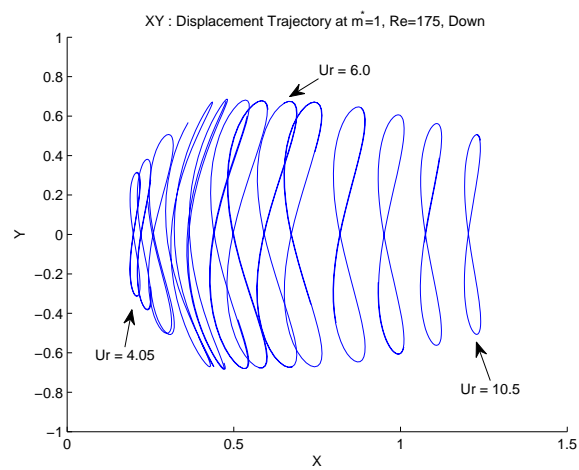
(c) $m^* = 1$ and $Re = 175$.

Figure 5.16 XY: Displacement trajectories.
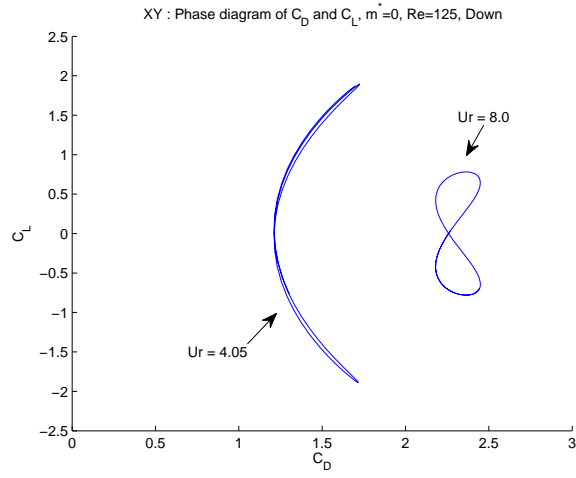
(a) $m^* = 0$ and $Re = 125$.
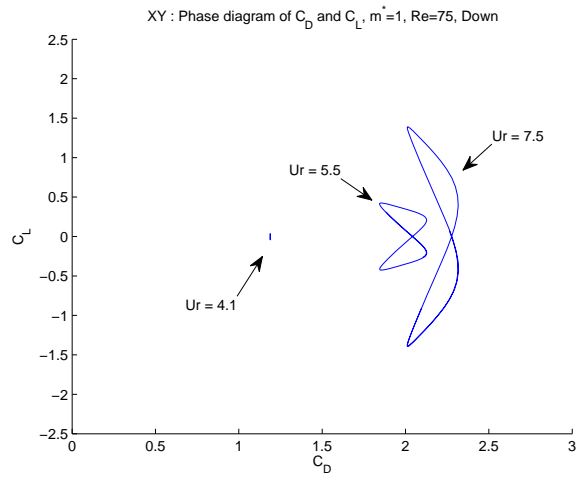
(b) $m^* = 1$ and $Re = 75$.
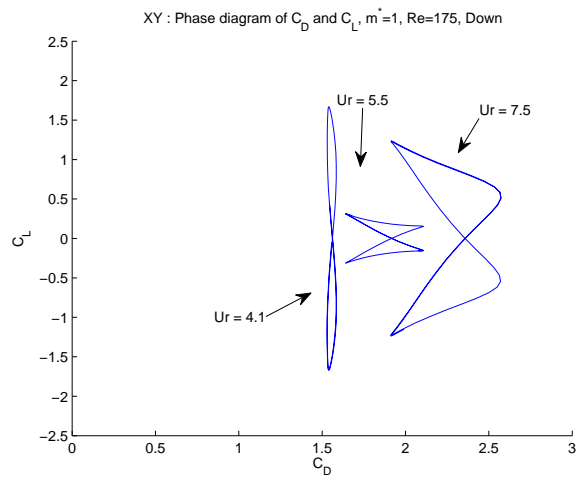
(c) $m^* = 1$ and $Re = 175$.

Figure 5.17 XY: Phase diagram with C_D and C_L.
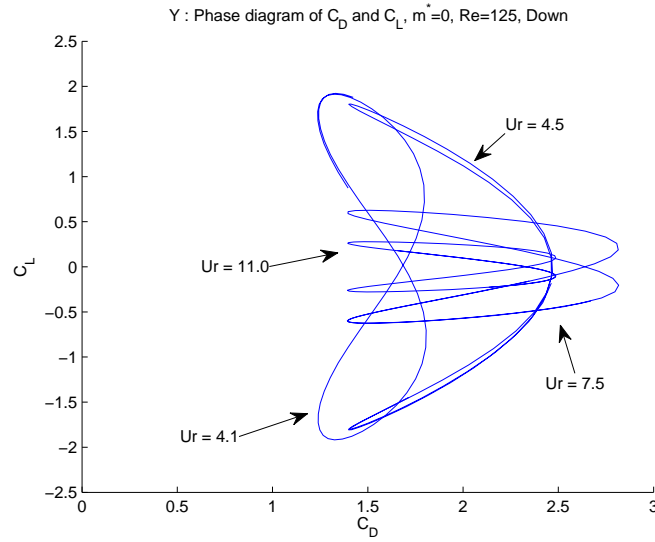
(a) $m^* = 0$ and $Re = 125$.
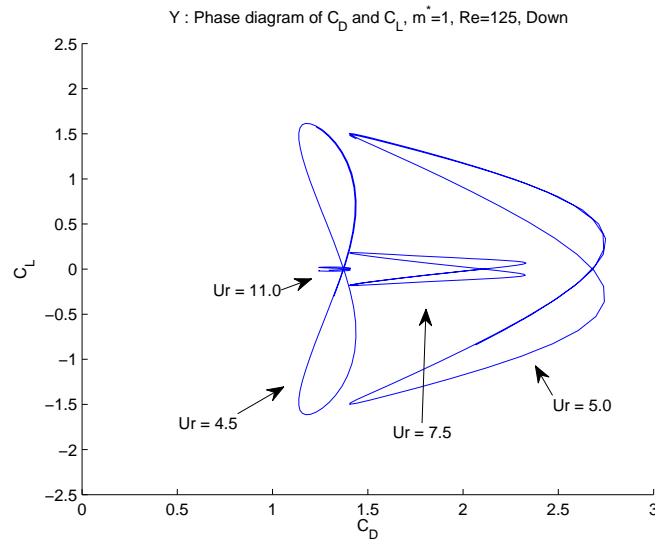
(b) $m^* = 1$ and $Re = 125$.

Figure 5.18 Y: Phase diagram with C_D and C_L.

We first take a closer look at the response for $m^* = 0$. At high reduced velocities, the profile is a stretched figure-8. The profile takes a parabolic shape at lower reduced velocity and at very low reduced velocity, the profile becomes a more regular figure-8.

The $m^* = 1$ results generally have similar shapes which seem to be slightly stretched due to inertia effects. The magnitudes of the $m^* = 1$ results are also smaller than those with $m^* = 0$ which agree with what is expected.

5.4.5   Phase angle between lift and transverse displacement

In this section, we examine the change of the phase angle between the lift and the transverse displacement. With $m^* = 0$ for both Y-only and XY motions, there is no change in the phase angle observed. This is expected. As it is mentioned in the force coefficient section, there is no inertia nor damping term to introduce any delay in the responses between the forces and the displacement.

With $m^* = 1$, we observe a 180° phase angle change for both Y-only and XY motions. In figure 5.19, we show the phase angle portrait for XY oscillation with $Re = 100$ before and after the change. The approximate locations of the phase angle change are summarized in table 5.3. We can see that there is an effect of Re to the location of the change. For Y-only oscillation, an increase in the Reynolds number will shift the phase angle change towards smaller values of the reduced velocity. The opposite is generally true for the XY oscillation with the exception at $Re = 75$. It will be illustrated in the next section that across this jump in phase angle, the vortex pattern does not have any significant modification.
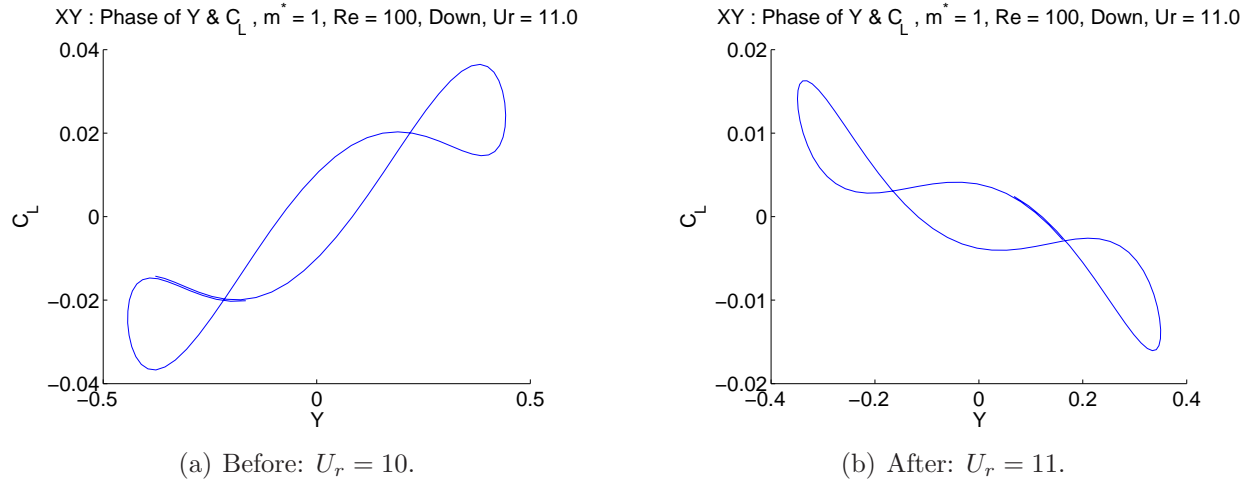

(a) Before: $U_r = 10$.   (b) After: $U_r = 11$.

Figure 5.19 XY: Phase angle change at $Re = 100$.

Table 5.3 Phase angle change with $m^* = 1$.

Re	Y-only : U_r	XY : U_r
75	10.5	10.9
100	9.7	10.6
125	9.3	10.9
150	8.9	11.3
175	8.4	11.4

5.4.6 Vortical structure pattern

The vortical structure patterns for both XY and Y-only oscillations for the investigated Reynolds number are remarkably similar. Hence, we will present the vortical structure pattern mainly with the cases that can best represent a particular characteristic. We observe only the 2S mode and the C(2S) mode. This is similar to what has been reported in the laminar shedding regime (Singh & Mittal (2005); Prasanth & Mittal (2008)). Recall that in the 2S mode, a single vortex is shed from each side of the cylinder during the vortex shedding cycle. The C(2S) mode is a variation of the 2S mode. For which, the vortices "coalesce" in the wake region. The vortices appear as if they are organized into two rows. We shall illustrate that the hysteretic responses reported in maximum amplitude and frequency responses are associated with different vortex patterns in the flow.

We begin in the lower reduced velocity range where hysteretic responses are most often observed in the maximum amplitude results. We see the vortex patterns at around $U_r = 5.0$ for XY oscillation with $m^* = 1$ at $Re = 100$ in figure 5.20. Hysteresis in the vortex pattern can indeed be observed. More specifically, while the patterns in the decreasing direction (figures 5.20(b), 5.20(d) and 5.20(f)) remain with C(2S), the pattern in the increasing direction (figures 5.20(a), 5.20(c) and 5.20(e)) changes from 2S to C(2S). When the Reynolds number is increased, the width of hysteretic response at the low U_r values also widens slightly.

At the peak, the pattern should be always C(2S) mode. In figure 5.21, the peaks with $m^* = 1$ at $Re = 100$ for both the XY and Y-only oscillations are shown. They both exhibit the C(2S) modes. This is in agreement with what is observed by Prasanth & Mittal (2008).

When we increase the reduced velocity further, the vortex pattern changes back to 2S. This is most evident at about $U_r = 6.8$ for Y-only oscillation with $m^* = 1$ at $Re = 175$ which is shown in figure 5.22. In figures 5.22(e) and 5.22(f), the 2S vortex mode pattern can be clearly observed. At slightly lower reduced velocities, the hysteresis in the response can be seen between the increasing and the decreasing directions in figures 5.22(c) and 5.22(d). At about the same conditions, there are hysteresis in the frequency response results.

As mentioned in the previous section, there may be a phase jump at high reduced velocities. In figure 5.23, we see the vortex pattern before and after the jump with $m^* = 1$ at $Re = 175$ for Y-only oscillation. From the figures, we see that the vortex pattern remains essentially the same before and after the jump occurs. This agrees well with the observation by Prasanth & Mittal (2008).

At even higher reduced velocity, the motion may desynchronize. The Y-only oscillation at $Re \geq 150$ shows this phenomenon. In figure 5.24, the vortex patterns before and after the synchronization in the decreasing direction with $m^* = 1$ at $Re = 175$ are shown. From the number of vortices behind the cylinder, we can learn that the frequency before the

(a) $U_r = 4.6$, $\Uparrow$.

(b) $U_r = 4.6$, $\Downarrow$.

(c) $U_r = 4.8$, $\Uparrow$.

(d) $U_r = 4.8$, $\Downarrow$.

(e) $U_r = 5.2$, $\Uparrow$.

(f) $U_r = 5.2$, $\Downarrow$.
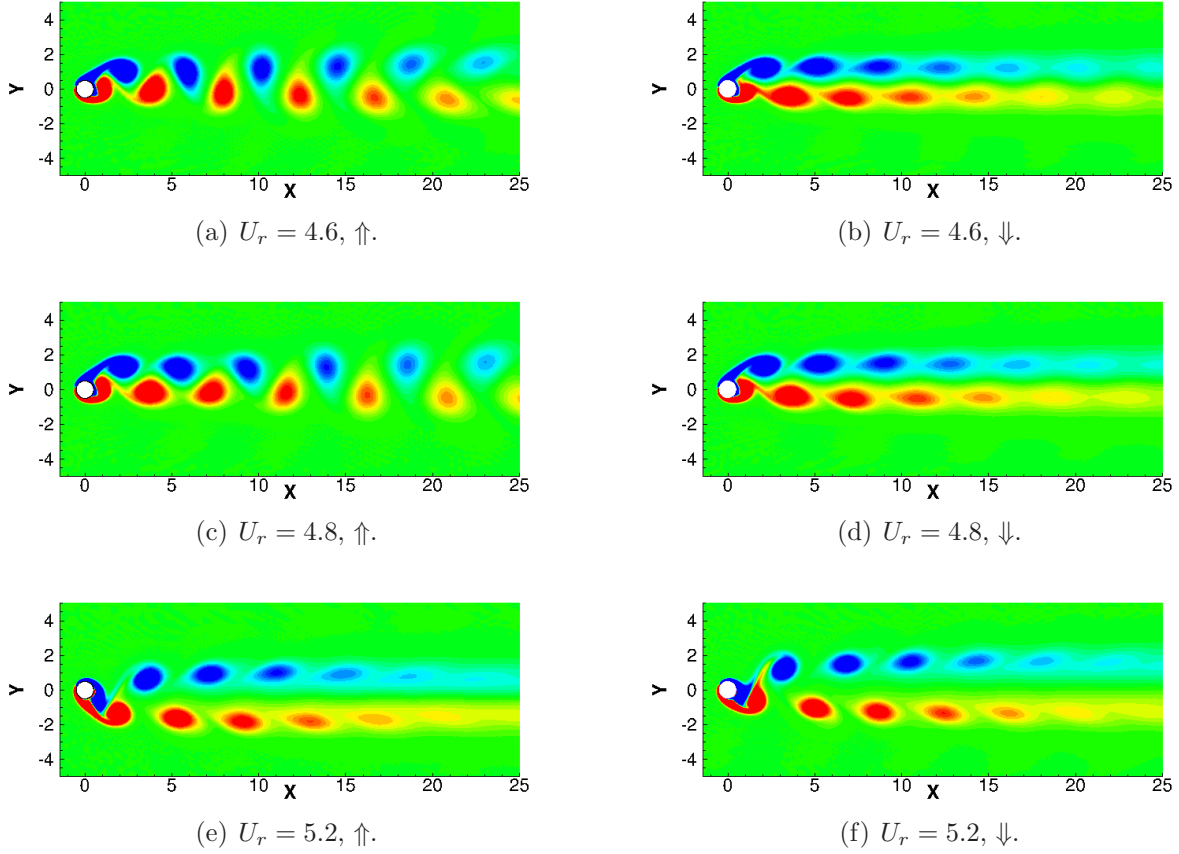
Figure 5.20 Vortex pattern at low U_r: XY: $m^* = 1$ and $Re = 100$.

(a) XY: $U_r = 5.5$, $\Uparrow$.

(b) Y: $U_r = 5$, $\Uparrow$.
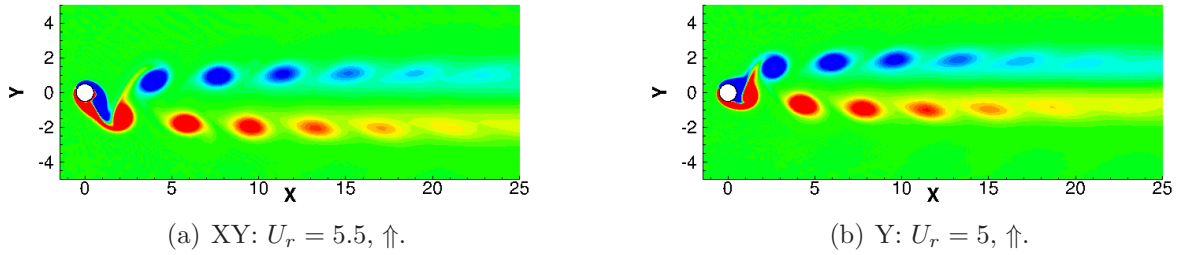
Figure 5.21 Vortex pattern at the peak : C(2S) : XY vs. Y.

synchronization at $U_r = 10$ is higher than that at $U_r = 9$.

Comparing the Y-only and the XY oscillations, the vortex patterns mainly differ in oscillation frequency. The oscillation frequency may be conveniently examined by inspecting the gap distance between the vortices. We can see in figure 5.25 that the vortex gap distance at $U_r = 8.75$ for the Y-only oscillation is slightly smaller than that of the XY oscillation. This indicates that the frequency for the Y-only oscillations is higher than that of the XY

(a) $U_r = 6.5$, $\Uparrow$.

(b) $U_r = 6.5$, $\Downarrow$.

(c) $U_r = 6.9$, $\Uparrow$.

(d) $U_r = 6.9$, $\Downarrow$.

(e) $U_r = 7.3$, $\Uparrow$.

(f) $U_r = 7.3$, $\Downarrow$.
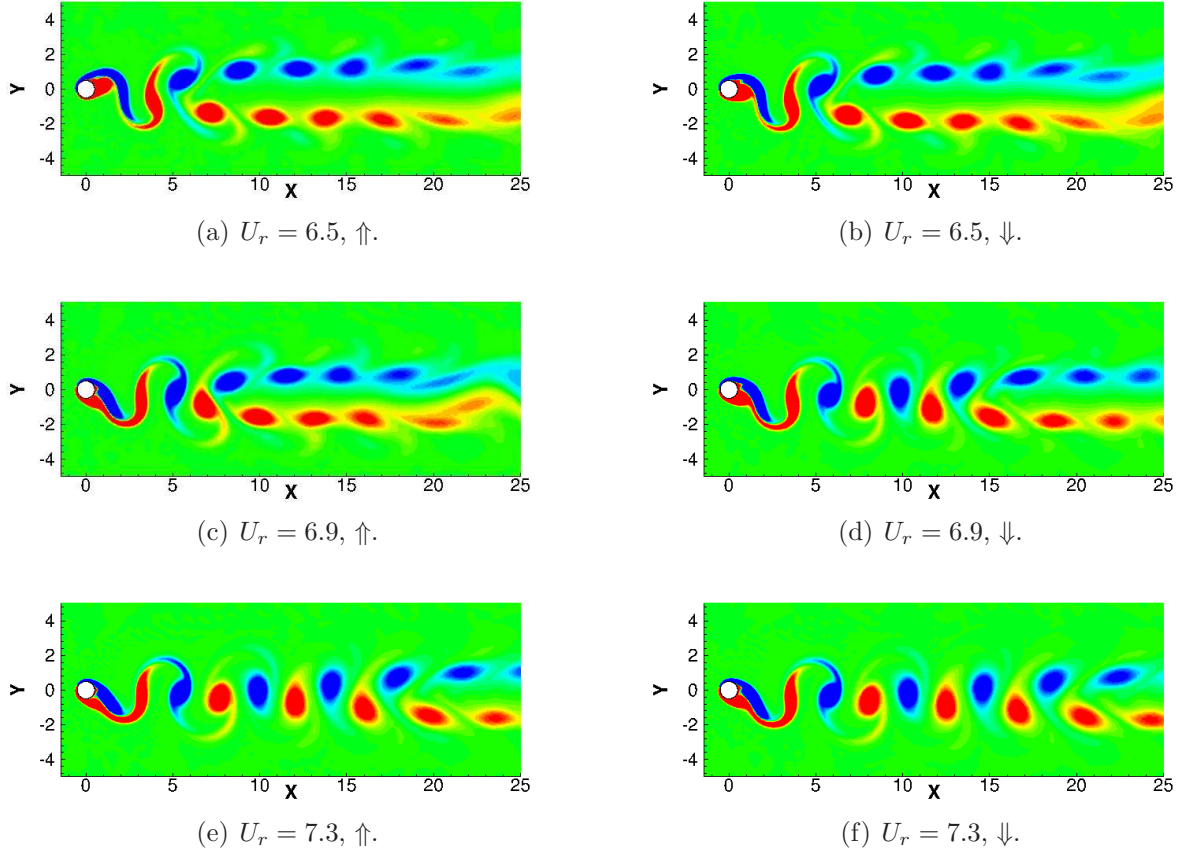
Figure 5.22 Vortex pattern mode change (C(2S) $\Rightarrow$ 2S): Y: $m^* = 1$, at $Re = 175$.

(a) $U_r = 8$, $\Downarrow$.

(b) $U_r = 9$, $\Downarrow$.
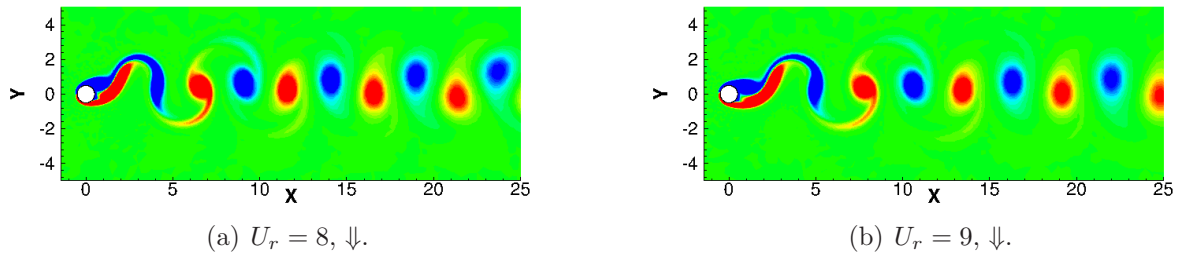
Figure 5.23 Vortex pattern at phase jump: Y: $m^* = 1$, $Re = 175$.

oscillations which is in accordance with the results in the frequency response section above.

For the Y-only oscillation with $m^* = 0$, the 2S mode begins to appear at higher values of reduced velocity just as it is the case with $m^* = 1$ in figure 5.22. However, for the XY oscillation with $m^* = 0$, we do not observe the 2S mode even at the highest limit of the investigated parameter space. The vortex patterns for both the Y-only and XY oscillations with $m^* = 0$ at $U_r = 11$ are shown in figure 5.26. While the C(2S) mode can still be

(a) $U_r = 9.9$, $\Downarrow$.

(b) $U_r = 10.9$, $\Downarrow$.
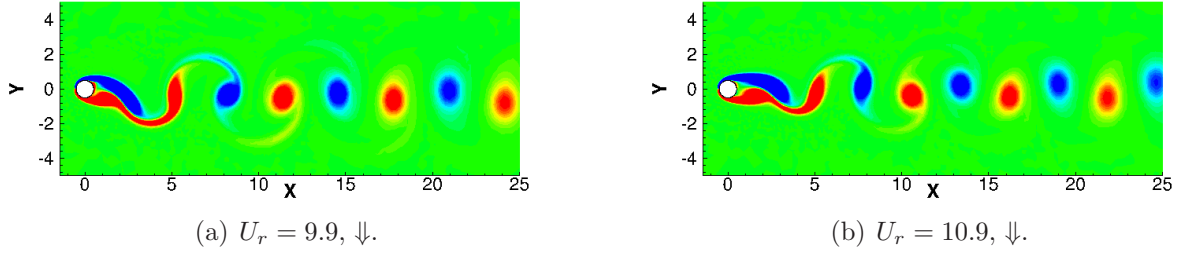
Figure 5.24 Vortex pattern at desynchronization: Y: $m^* = 1$, at $Re = 175$.

(a) XY:$U_r = 8.75$, $\Uparrow$.

(b) Y:$U_r = 8.75$, $\Uparrow$.
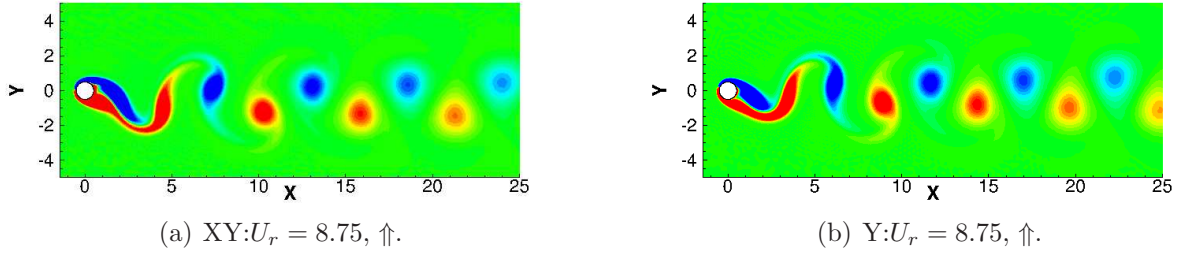
Figure 5.25 Vortex pattern: XY vs. Y, $m^* = 1$, at $Re = 100$.

identified for the XY oscillations in figure 5.26(a), the 2S mode starts to appear for the Y-only oscillations in figure 5.26(b).

(a) XY:$U_r = 11.0$, $\Downarrow$.

(b) Y:$U_r = 11.0$, $\Downarrow$.
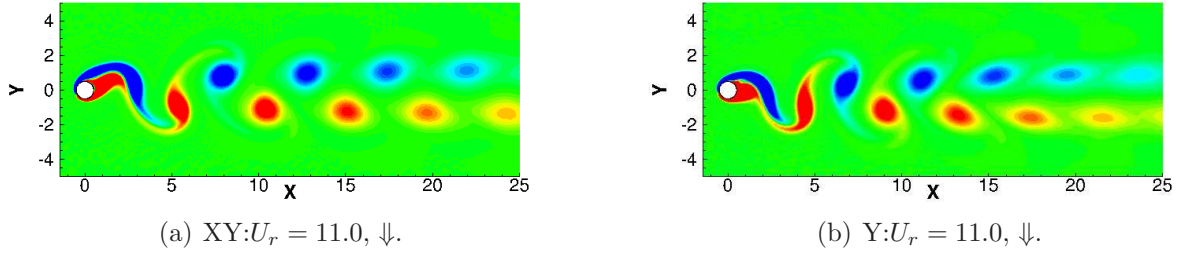
Figure 5.26 Vortex pattern: XY vs. Y, $m^* = 0$, at $Re = 100$.

5.4.7   Comparison with forced vibration

Examining the vortex-induced vibration response by varying the spring stiffness at a fixed Reynolds number allows us to have better comparisons between our free vibration results and the forced vibration experiments. In the forced vibration experiment, the cylinder is forced to oscillate at different frequencies. The cylinder and vortex synchronization limit of the oscillation response is reported. We compare the results of Y-only oscillations with the

forced vibration results at $Re = 100$ from Koopmann (1967) in figure 5.27. We have extended
the range of considered reduced velocity range to $1 < U_r < 13$.

The free vibration results are in excellent agreement with the forced vibration experimen-
tal data. The path begins at $U_r = 1$ at the center. When the reduced velocity is increased, the
responses are "locked-in". At first, the oscillation frequency is larger than the vortex-shedding
frequency and hence the response moves towards the right. The oscillation amplitude also
jumps above the synchronization limit obtained from the experiment at about $f/St_{fix} \approx 1.1$.
The response continues to travel towards the left with a decrease in oscillation frequency
ratio. As the reduced velocity increases, both the oscillation frequency f and the vortex-
shedding frequency St_{fix} increase. However, the vortex-shedding frequency St_{fix} increases
at a much faster rate than the oscillation frequency f, and hence leads to a decrease in the
ratio. When the response is desynchronized, a sudden decrease in oscillation magnitude is
observed at about $f/St_{fix} \approx 0.8$.

In the "locked-in" range, the responses with $m^* = 0$ and $m^* = 1$ in both the increasing
(up) and decreasing (down) reduced velocity directions all collapse remarkably well together.
As expected, the response with $m^* = 0$ does not desynchronize. The hysteresis in the up and
down directions are also well captured at both ends of the "locked-in" range. In particular
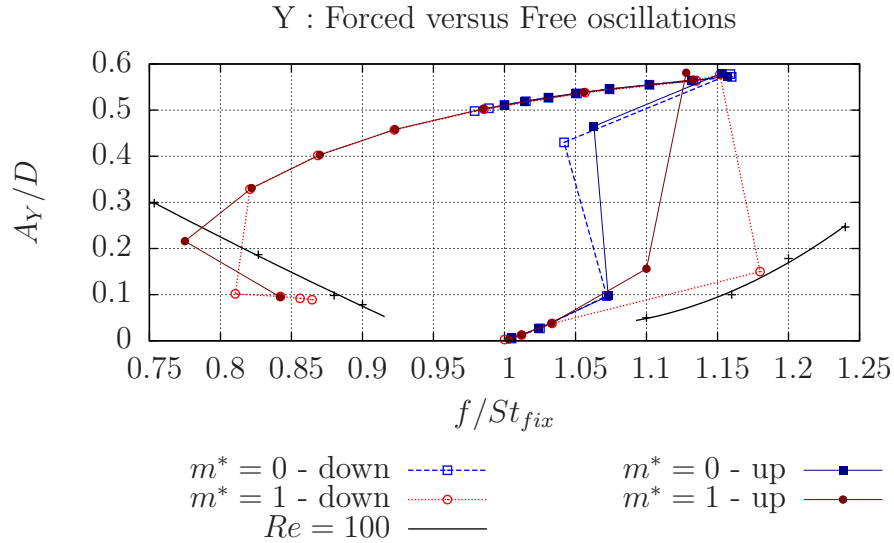for $m^* = 1$.

Figure 5.27 Comparison between free and forced vibration.

5.4.8   About critical mass ratio and branching

It is evident that the present results for Y-only and XY oscillation consist of two patterns of responses with respect to the mass ratio values. Jauvtis & Williamson (2004) estimated the critical mass ratio for a two degrees of freedom cylinder to be 0.52 at moderately high Reynolds number. For a cylinder that only vibrates transversely, Morse & Williamson (2009b) demonstrated that the critical mass ratio will decrease when the Reynolds number decreases. Govardhan & Williamson (2002) predicted the critical mass ratio for a single degree of freedom cylinder to be 0.25 at $Re = 100$ based on the numerical results of Shiels et $al.$ (2001).

We estimate the critical mass ratio of the Y-only and XY oscillations at $Re = 100$ by examining the transverse oscillation amplitudes at the reduced velocity $U_r = 100$ with various fixed mass ratios between 0.0 to 0.6 (see figure 5.28). We vary the mass ratio and observe if there is a large jump in the oscillation response which naturally marks the value of the critical mass ratio. We find that the critical mass ratio is about 0.117 for Y-only oscillation and 0.106 for XY oscillation. It is an interesting result that the critical mass ratio of XY oscillation is lower than that of the Y-only oscillation. From the results of the present study, a possible reason behind this finding may be the following: Recall that when $m^* \leq m^*_{critical}$, the cylinder oscillation and the vortex-shedding mechanism remains synchronized at the "infinite" reduced velocity (e.g. when there is no spring). From the forced vibration experiments, we learn that the cylinder oscillation and the vortex-shedding mechanism will synchronize only under specific combinations of cylinder oscillation amplitudes and frequencies. We see from the free and forced vibration comparison above that after synchronization, an increase in the reduced velocity will cause the response to shift towards the lower frequency end. And when the response crosses the synchronization limit, desynchronization occurs. From the frequency response section, we also note that for the same upstream flow condition and mass ratio, the frequency of the XY oscillation is generally lower than that of the Y-only oscillation. If the synchronization limit of the XY oscillation is similar to that of the Y-only oscillation, XY oscillation will have a "narrower buffer" before it reaches the synchronization limit. From experiments, a smaller mass ratio generally leads to a higher oscillation frequency at high reduced velocity in the lower branch (Khalak & Williamson (1999); Jauvtis & Williamson (2004)). In other words, with the upstream flow condition fixed, the XY oscillation can remain synchronized by compensating the characteristics of "lower" oscillation frequency with a "lighter" cylinder. It would demand further research about the XY oscillation synchronization limit to shed some more light on the actual mechanism.

The vortex-induced vibration response branching is traditionally determined by the location of discontinuities in the amplitude and frequency responses (Williamson & Govardhan (2004)). This identification approach so far is able to clearly describe all the different branches
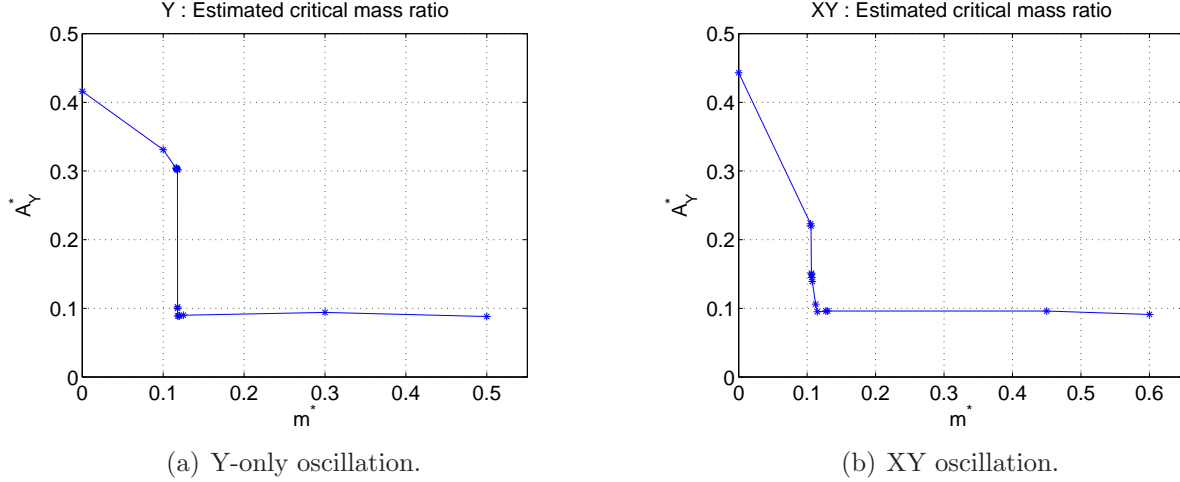
(a) Y-only oscillation.

(b) XY oscillation.

Figure 5.28 Estimated critical mass ratio.

observed in experiments. The vortex-induced vibration responses at low Reynolds number are however very smooth in general and there is no clear discontinuity in the response. Hence, branch identification at low Reynolds number is not as straightforward.

There is no universally accepted approach to identify branching at low Reynolds number. Placzek *et al.* (2009) simply stated that there is only one branch. Prasanth & Mittal (2008) suggested to use the peak maximum amplitude location to separate an initial branch in the lower reduced velocity and a lower branch in the higher reduced velocity. Both approaches seem to be incapable of fully describing the richness of the phenomenon observed in the present work.

Based on the vortex pattern observed in the previous section, perhaps it would be reasonable to consider the change in the vortex pattern as the separation boundary for branching: an "initial" branch with the 2S mode in the low U_r range, an "upper" branch with the C(2S) mode in the middle U_r range and a "lower" branch with the 2S mode in the high U_r range. At first sight, the vortex pattern change boundary seems to be applicable to the experimental results at higher Reynolds numbers as well. However, more data is needed to verify if this is indeed a good criterion to identify the separation boundary.

5.5   Conclusion

In this work, we have numerically investigated the two degrees of freedom (transverse and streamwise) responses of vortex-induced vibrations of a cylinder with zero mass ratio and zero damping in the following parameter space: Reynolds number ($75 \leq Re \leq 175$), reduced velocity ($5.0 \leq U_r \leq 11.0$). To better compare the results, we also investigate the two degrees

of freedom responses with $m^* = 1$ and the responses of transverse only oscillations. We have studied various aspects of vortex-induced vibration response: the maximum amplitude, the frequency response, the displacement trajectory, the force coefficient phase relationship, the change of total phase angle (between the lift force and the transverse displacement) and the vortical structure pattern. The presented results are generally in accordance with those from literature. The maximum amplitude response of the XY oscillation is larger than that of the transverse only oscillation. For the XY oscillation, the transverse amplitude is much larger than that of the streamwise amplitude. On the other hand, the oscillation frequency of the transverse only oscillation is greater than that of the XY oscillation. Hysteretic responses are observed and they are associated with differences in the vortical structure pattern observed for the increasing and decreasing directions. We only observe the 2S and the C(2S) modes. The present results compare well with those of the forced vibration at $Re = 100$.

At $m^* = 0$, the maximum amplitude of the XY oscillation exhibits a peak of $0.9D$, a significant 50% increase from the $0.6D$ reported previously in the laminar shedding regime. As the mass ratio is increased, the peak maximum amplitudes decrease for both the XY and Y-only oscillations. In particular, the peak amplitude of the XY oscillation decreases more rapidly than that of the Y-only oscillation. Generally, the maximum amplitude responses show an increase of amplitude when the Reynolds number is increased. For the XY oscillations, the amplitude increase is substantial. For the transverse only responses, a definitive gentle increase can also be observed. This behavior differs markedly from that observed by Williamson & Govardhan (2006) which indicates that the maximum amplitude is not influenced by the Reynolds number in the laminar shedding regime. Besides, the peak maximum amplitude location does not always appear at a fixed reduced velocity value. This is most evident from the XY oscillation response with $m^* = 0$. This is in contrast to what is observed by Etienne & Pelletier (2012) who found that the maximum amplitude always appears at the reduced velocity of 6.5 for very low Reynolds number (< 50). As a result, when we attempt to determine the peak maximum value across a range of Reynolds number, we should not assume that the peak maximum will be located at the same value of the reduced velocity.

It is evident that the results in the present study show two main patterns with respect to the mass ratio. This indicates that the investigated mass ratio values encompass the critical mass ratio. We estimate that the critical mass ratio is about 0.106 for XY oscillation and 0.117 for transverse only oscillation. If the synchronization limit of the XY oscillation is similar to that of the Y-only oscillation, then it is reasonable to observe that the critical mass ratio for the XY oscillation be smaller than that of the transverse only.

There is no discontinuity observed in the present work, except the desynchronization.

Hence, the traditional branch identification approach in the experiments, which relies on response discontinuity, cannot be applied in a straightforward manner. Based on the analysis of the vortical structure patterns, it seems that it may be a viable alternative to be used as the branch separation boundary.

REFERENCE

AGLEN, I. M. & LARSEN, C. M. (2011). Importance of added mass for the interaction between IL and CF vibrations of free spanning pipelines. *Proceedings of the ASME 2011 30th International Cconference on Ocean. Offshore and Arctic Engieering - OMAE*. ASME, New York, NY, vol. **7** of *CFD and VIV*, 545–556.

ANAGNOSTOPOULOS, P. & BEARMAN, P. (1992). Response characteristics of a vortex-excited cylinder at low Reynolds-numbers. *Journal of Fluids and Structures*, <u>6</u>, 39–50.

BLACKBURN, H. & KARNIADAKIS, G. (1993). Two- and three-dimensional simulations of vortex-induced vibration of a circular cylinder. *Proceedings of the third International Offshore and Polar Engieering Conference*. ISOPE, ISOPE, Golden, CO, 715–720.

ETIENNE, S., GARON, A. & PELLETIER, D. (2009). Perspective on the geometric conservation law and finite element methods for ALE simulations of incompressible flow. *Journal of Computational Physics*, <u>228</u>, 2313–2333.

ETIENNE, S. & PELLETIER, D. (2012). The low Reynolds number limit of vortex-induced vibrations. *Journal of Fluids and Structures*, <u>31</u>, 18–29.

FEY, U., KÖNIG, M. & ECKELMANN, H. (1998). A new Strouhal-Reynolds-number relationship for the circular cylinder in the range $47 < \mathrm{Re} < 2 \times 10^5$. *Physics of Fluids*, <u>10</u>, 1547–1549.

FLEMMING, F. & WILLIAMSON, C. H. K. (2005). Vortex-induced vibrations of a pivoted cylinder. *Journal of Fluids Mechanics*, <u>552</u>, 215–252.

GOVARDHAN, R. & WILLIAMSON, C. H. K. (2002). Resonance forever: existence of a critical mass and an infinite regime of resonance in vortex-induced vibration. *Journal of Fluids Mechanics*, <u>473</u>, 147–166.

HAIRER, E. & WANNER, G. (2002). *Solving Ordinary Differential Equations II : Stiff and Differential-Algebraic Problems*. Springer, Berlin.

JAUVTIS, N. & WILLIAMSON, C. H. K. (2004). The effect of two degrees of freedom on vortex-induced vibration at low mass and damping. *Journal of Fluids Mechanics*, <u>509</u>, 23–62.

KAJISHIMA, T. & TAKEUCHI, S. (2011). Direct Numerical Simulation of Multiphase Flows Involving Dispersed Components with Deformable Interfaces. *Heat Transfer - Asian Research*, 40, 387–403.

KHALAK, A. & WILLIAMSON, C. H. K. (1999). Motions, forces and mode transitions in vortex-induced vibrations at low mass-damping. *Journal of Fluids and Structures*, 13, 813–851.

KOOPMANN, G. H. (1967). The vortex wakes of vibrating cylinders at low Reynolds numbers. *Journal of Fluid Mechanics*, 28, 501–512.

LI, L., SHERWIN, S. J. & BEARMAN, P. W. (2002). A moving frame of reference algorithm for fluid/structure interaction of rotating and translating bodies. *International Journal for Numerical Methods in Fluids*, 38, 187–206.

LOON, R. V., ANDERSON, P. D., VAN DE VOSSE, F. N. & SHERWIN, S. J. (2007). Comparison of various fluid-structure interaction methods for deformable bodies. *Computers and Structures*, 85, 883–843.

MORSE, T. & WILLIAMSON, C. (2009a). Prediction of vortex-induced vibration response by employing controlled motion. *Journal of Fluid Mechanics*, 634, 5 – 39.

MORSE, T. L. & WILLIAMSON, C. H. K. (2009b). The effect of Reynolds number on the critical mass phenomenon in vortex-induced vibration. *Physics of Fluids*, 21.

NEWMAN, D. & KARNIADAKIS, G. (1997). A direct numerical simulation study of flow past a freely vibrating cable. *Journal of Fluid Mechanics*, 344, 95–136.

NEWMAN, D. J. (1996). *A computational study of fluid-structure interactions: Flow-induced vibrations of a flexible cable*. Ph.D., Princeton University, Ann Arbor.

PLACZEK, A., SIGRIST, J.-F. & HAMDOUNI, A. (2009). Numerical simulation of an oscillating cylinder in a cross-flow at low Reynolds number: Forced and free oscillations. *Computers & Fluids*, 38, 80–100.

PRASANTH, T. & MITTAL, S. (2008). Vortex-induced vibrations of a circular cylinder at low reynolds numbers. *Journal of Fluid Mechanics*, 594, 463 – 91.

PRASANTH, T., PREMCHANDRAN, V. & MITTAL, S. (2011). Hysteresis in vortex-induced vibrations: Critical blockage and effect of m. *Journal of Fluid Mechanics*, 671, 207 – 225.

SANCHIS, A., SæLEVIK, G. & GRUE, J. (2008). Two-degree-of-freedom vortex-induced vibrations of a spring-mounted rigid cylinder with low mass ratio. *Journal of Fluids and Structures*, 24, 907–919.

SARPKAYA, T. (2004). A critical review of the intrinsic nature of vortex-induced vibrations. *Journal of Fluids and Structures*, 19, 389–447.

SARPKAYA, T. (2010). *Wave forces on offshore structures.* Cambridge, New York, NY.

SCHLICHTING, H. & GERSTEN, K. (2000). *Boundary-layer Theory.* Springer, Berlin.

SHIELS, D., LEONARD, A. & ROSHKO, A. (2001). Flow-induced vibration of a circular cylinder at limiting structural parameters. *Journal OF Fluids and Structures*, 15, 3–21.

SHYY, W., UDAYKUMAR, H. S., RAO, M. M. & SMITH, R. W. (1996). *Computational Fluid Dynamics with Moving Boundaries.* Taylor and Francis, Washington, DC.

SINGH, S. & MITTAL, S. (2005). Vortex-induced oscillations at low Reynolds numbers: Hysteresis and vortex-shedding modes. *Journal of Fluids and Structures*, 20, 1085 – 1104.

STAPPENBELT, B. & LALJI, F. (2008). Vortex-induced Vibration Super-Upper Response Branch Boundaries. *International Journal of Offshore and Polar Engineering*, 18, 99–105.

WANDERLEY, J. B. V., SOARES, L. F., VITOLA, M., SPHAIER, S. H. & LEVI, C. (2011). Reynolds Number Effect on Vortex-Induced Vibration on a Two-Dimensional Circular Cylinder with Low Mass-Damping Parameter. *Proceedings of the ASME 2011 30th International Cconference on Ocean. Offshore and Arctic Engieering - OMAE.* ASME, New York, NY, vol. **7** of *CFD and VIV*, 69–80.

WILLIAMSON, C. H. K. (1996). Vortex Dynamics in the Cylinder Wake. *Annual Review of Fluid Mechanics*, 28, 477–539.

WILLIAMSON, C. H. K. & GOVARDHAN, R. (2004). Vortex-Induced Vibrations. *Annual Review of Fluid Mechanics*, 38, 413–55.

WILLIAMSON, C. H. K. & GOVARDHAN, R. (2006). Defining the 'modified Griffin plot' in vortex-induced vibration: revealing the effect of Reynolds number using controlled damping. *Journal of Fluid Mechanics*, 561, 147–180.

YANG, J., PREIDIKMAN, S. & BALARAS, E. (2008). A strongly coupled embedded boundary method for fluid-structure interactions of elastically mounted rigid-bodies. *Journal of Fluids and Structures*, 24, 167–182.

CHAPTER 6

ARTICLE 3: Flow-induced vibrations of in-line cylinder arrangements at low Reynolds numbers

Kintak Raymond Yu, Yves-Marie Scolan, Alexander Hay, Emmanuel Fontaine, Dominique Pelletier, Stéphane Étienne (2014). Submitted to: *Journal of Fluids and Structures.*

Abstract

The present study numerically explores the limiting two degrees of freedom (streamwise and transverse) free oscillation response of three circular cylinders, placed in an in-line configuration in a uniform flow at low Reynolds numbers, when the mass-damping factor $m^*\zeta$ is "zero". We consider three identical cylinders with a low mass ratio ($m^* = 4/\pi$) and zero damping. The spacing between the cylinders is $L/D = 4$. We vary the reduced velocity from $U_r = 2$ to $U_r = 13$ and the Reynolds number from $Re = 100$ to $Re = 200$. For comparisons, we also evaluate the free oscillation responses of an isolated cylinder and a tandem cylinder pair under the same conditions. Our results show that the dynamic behaviors of three in-line cylinders are significantly different from those of the tandem cylinder pair. While the maximum transverse oscillation amplitudes increases by about 30%, there is now a very large streamwise oscillation amplitude ($A_X/D = 1.5$), comparable to those in the transverse direction. They appear at $U_r > 9$. The frequency responses of the triple cylinder case are much richer; in particular, at higher U_r. There is a clear low frequency component which is most evident in the streamwise direction. Many of the displacement trajectories of the triple cylinder case can almost be described as "bounded random movements". The associated phase portraits and the Poincaré maps show that the nonlinearity of the free oscillations of the three in-line cylinders is considerably higher than those of the tandem cylinder pair. Even at such low Re, the free oscillations of three in-line cylinders already seem to approach a chaotic response. In particular, there is evidence that the fluid-structure system approaches to chaos via the quasi-periodic route. Due to such high level of nonlinearities, it is therefore highly risky to predict the free oscillation behaviors of multiple in-line cylinders by extrapolating those of the tandem cylinder pair.

6.1   Introduction

Wake-induced vibration (WIV) is an important fluid-structure interaction phenomenon that has recently received much of attentions (Paidoussis *et al.* (2011)). This is in part due to its practical significance and in part due to the fascinating complex fluid dynamics involved. Wake-induced vibration can occur when there are two (or more) bluff bodies (e.g. circular cylinders) subjected to a cross flow with one of them placed downstream in the wake of the other. This setting can be found, for example, in the cases of overhead electric power transmission lines subjected to the wind and clustered offshore risers subjected to ocean currents. As mentioned by Paidoussis *et al.* (2011), it has been observed that the downstream body can oscillate transversely with an excessive amplitude of $10D$ peak-to-peak. Hence, these vibrations can cause significant structural damages due to fatigue and they pose serious concerns in engineering applications.

The phenomenon of wake-induced vibration has been called differently in the literature. Ruscheweyh (1983) referred to it as "interference galloping". Bokaian & Geoola (1984) named it "wake-induced galloping". Zdravkovich (1988) called it "wake-displacement excitation". Brika & Laneville (1999) used the term "wake-galloping oscillation". More recently, Fontaine *et al.* (2006) described the phenomenon as "wake-induced oscillation" and Assi *et al.* (2013) suggested the name of "wake-induced vibration".

The flow interference characteristics between two bluff bodies are observed to behave very differently when the distance between the two bodies and the relative position with respect to the incoming flow are different. Zdravkovich & Pridden (1977) proposed a simple classification based on the arrangements of the two bodies into tandem, staggered and side-by-side configurations. If we define α to be the angle between the line joining the centers of the two bodies and the incoming flow direction, then we will have $\alpha = 0^o$ for the tandem arrangement, $0^o < \alpha < \pm 90^o$ for the staggered arrangement and finally, $\alpha = \pm 90^o$ for the side-by-side arrangement. Wake-induced vibrations are strongest for the tandem (in-line) arrangement (which, the second body is placed completely behind the first body in the streamwise direction). Naturally, this is the most common configuration considered in wake-induced vibrations investigations. Sumner (2010) provided a recent review about flow interference characteristics between two stationary cylinders in a cross flow.

The complete mechanism of wake-induced vibration is not yet fully understood. Paidoussis *et al.* (2011) presented an analysis using quasi-steady theory showing that if the upstream body is fixed, the instabilities of the downstream body is due to fluid dynamic stiffness. This result seems to be supported by a recent experiment with two circular cylinders in a tandem arrangement by Assi *et al.* (2013). In their experiment, the upstream cylinder is

fixed and the downstream cylinder is constrained to move only in the transverse direction with no damping nor spring. The downstream cylinder still experiences strong wake-induced vibrations. On the other hand, when the upstream body is also allowed to move, the flow pattern becomes more complicated such that the flow may also induce instabilities due to fluid dynamic damping as illustrated by Paidoussis *et al.* (2011).

An important parameter for wake interference is the center to center separation ratio (L/D) where L is the distance between the centers of the two bodies and D is the characteristic diameter. Zdravkovich & Pridden (1977) summarized that when the separation ratio is "sufficiently" large ($L/D > 3$ to 4), the wake of the upstream body behaves as if it is from an isolated body and only the wake of the downstream cylinder body is affected by that of the upstream body. However, when the separation ratio is small ($L/D < 3$ to 4), the wake of the upstream body is also affected by the presence of the downstream body. They referred to this region as the "proximity interference" region. This critical separation ratio of $L/D \approx 3$ to 4 is also supported by more recent experimental and numerical results (Meneghini *et al.* (2001); Mizushima & Suehiro (2005); Tasaka *et al.* (2006)). It is observed that the flow patterns experience abrupt changes at this critical value of the separation ratio. Carmo *et al.* (2010b) mentioned that the critical separation ratio is also referred to as the drag inversion separation because the drag coefficient of the downstream body changes its sign from negative when L/D is small to positive when L/D is large.

The synchronization or the "locked-in" range of two cylinders in tandem arrangement is much wider than that of an isolated cylinder. At low reduced velocities ($U_r \leq 4$), the transverse oscillation amplitude of the downstream cylinder remains small as shown by Borazjani & Sotiropoulos (2009) and Prasanth & Mittal (2009). At higher reduced velocities, the transverse oscillation amplitude of the downstream cylinder can become much larger than that of an isolated cylinder and that of the upstream cylinder. Papaioannou *et al.* (2008) demonstrated that this increase in transverse oscillation amplitude of the downstream cylinder is more significant when the separation ratio is small. Besides, the synchronization range of the downstream cylinder is wider when the separation ratio is large. For the upstream cylinder, Prasanth & Mittal (2009) showed that when the separation ratio is large, the transverse oscillation amplitude is comparable to that of an isolated cylinder. On the other hand, Borazjani & Sotiropoulos (2009) illustrated, with a tandem cylinder pair ($m^* \approx 2.5$) which can only oscillate in the transverse direction, that when the separation ratio is reduced to a small value, the transverse oscillation amplitude of the upstream cylinder can also notably exceed that of an isolated cylinder. When the separation ratio becomes very small, vortex shedding of the upstream cylinder becomes greatly disturbed. Vortices are mainly shedded from the downstream cylinder and they appear to be shedded from a single bluff body. Consequently,

Borazjani & Sotiropoulos (2009) observed that the transverse oscillation amplitude of the downstream cylinder is larger than that of the upstream cylinder in this situation.

Although there are still open questions regarding the various aspects of wake-induced vibrations, it is certain that the downstream cylinder can experience significant transverse oscillations. In light of this, it is natural to wonder: What would happen if there are more bluff bodies placed downstream to the second one?

There are only a few investigations that consider more than two bluff bodies placed in-line. Igarashi & Suzuki (1984) experimentally examined the flow characteristics of three stationary cylinders for a range of separation ratio ($1.0 \leq L/D \leq 4.0$) at a Reynolds number ranging between $Re = 1.1 \times 10^4$ and $Re = 3.9 \times 10^4$. The differences in the characteristics between the second and the third cylinders were reported. Interestingly, there are even certain different behaviors observed for the first cylinder as compared with that of the first cylinder of a fix tandem cylinder pair. Harichandan & Roy (2010) studied numerically the flow characteristics of three stationary cylinders in an in-line arrangement for two separation ratios of $L/D = 2$ and $L/D = 5$ at two Reynolds numbers $Re = 100$ and $Re = 200$. They observed that the flow characteristics are dependent on the Reynolds number even at such low values. Recently, Oviedo-Tolentino *et al.* (2013) investigated experimentally the two degrees of freedom vortex-induced vibrations responses of 10 collinear circular cylinders subject to uniform flow at low Reynolds numbers, with a moderately high mass-damping factor of $m^*\zeta = 0.13$ and a separation ratio of $L/D = 6$ between each adjacent cylinder pair. The cylinders are made of copper and zinc alloy. Thus, the mass ratio can be approximately around $m^* \approx 7$ to 9 which is rather large. They observed that the maximum oscillation amplitudes are, in general, greatly amplified, especially for cylinder 2 to 7. Their results clearly exhibit some characteristics of waked-induced vibrations. For example, the downstream cylinders show very large transverse oscillations at reduced velocities above the desynchronization of the first cylinder. Overall, we can see that the transverse oscillations for all 10 cylinders are always larger than the corresponding streamwise oscillations. In particular, the peak streamwise oscillation amplitude for all cylinders are on average only about $25 \sim 30\%$ of those in the transverse direction. The largest peak streamwise oscillation is $A_X/D \approx 0.65$ which is about 50% of the associated peak in the transverse oscillation of the same cylinder.

The investigation by Oviedo-Tolentino *et al.* (2013) clearly demonstrates that the general responses of multiple cylinders arranged in-line cannot be fully represented by the simple tandem cylinder pair. Many important aspects, e.g. low mass ratio, low mass-damping factor, the maximum amplitude, and effect of Reynolds number, etc., deserve further investigations. The present study aims to examine the free oscillation characteristics of three in-line cylinders when the mass-damping factor is at the smallest limiting case of "zero".

Leontini *et al.* (2007) demonstrated that the wake of a transversely oscillating cylinder in a uniform cross flow can effectively remain two dimensional for $Re \leq 280$ which is markedly higher than that of a fixed isolated cylinder ($Re = 185$). The oscillation of the cylinder aids to increase the correlation length of the flow vortical structures in the spanwise direction. Carmo *et al.* (2010) reported that three dimensionality can exist at $Re \approx 163$ for two fixed cylinders in a tandem arrangement. However, it seems reasonable to assume that at low Reynolds numbers, the three dimensional effects remain weak for freely oscillating cylinders in an in-line arrangement. Hence, we will employ two dimensional simulation in the present study.

We consider three identical cylinders with low mass ratios ($m^* = \rho_s/\rho_f = 4/\pi$) and zero damping. The non-dimensional center-to-center separation ratio between the two adjacent cylinders are kept constant at $L/D = 4$, which is at the boundary between the proximity and wake interference regions for a tandem cylinder pair, to provoke richer fluid dynamic interactions.

In essence, we perform a parametric study with respect to the reduced velocity U_r and the Reynolds number Re. The reduced velocity $U_r = U/f_n D$, with U being the uniform incoming flow velocity, $f_n = \sqrt{k/m_s}/(2\pi)$ the natural frequency of cylinders in air, D the diameter of the cylinder, k the spring stiffness and m_s the mass of the cylinder, is varied from $U_r = 2$ to $U_r = 13$. Note that the reduced velocity is also commonly expressed as $U_{r_{n-w}} = U/(f_{n-w}D)$ where f_{n-w} is the natural frequency of cylinders in still water. The relation between the two formulas U_r and $U_{r_{n-w}}$ is such that $U_{r_{n-w}} = \sqrt{(m^* + 1)/m^*}\, U_r$ with $m^* = \rho_s/\rho_f$ being the mass ratio. Three Reynolds numbers $Re = \{100, 150, 200\}$ are considered.

The paper is organized as follows. First, we describe the numerical method. Then, we discuss our study cases for calculation verification and validation, followed by the benchmarking results for the free oscillation of an isolated cylinder and a tandem cylinder pair. After, we present and discuss the characteristics of the free oscillations of three cylinders arranged in an in-line configuration. Next, we examine the nonlinearity of the fluid-structure system with the phase portraits and the Poincaré maps. We summarize our findings in the conclusion.

6.2 Numerical method

This section briefly describes the numerical method that is used for all computations reported here.

6.2.1 Governing equations

We model the fluid as a Newtonian incompressible fluid, for which, the flow field can be described in an Arbitrary Lagrangian Eulerian (ALE) framework with the following continuity and momentum equations (Schlichting & Gersten (2000)):

$$\boldsymbol{\nabla} \cdot \mathbf{u} = \mathbf{0}, \tag{6.1}$$

$$\rho_f \mathbf{u}_{,t} + \rho_f[(\mathbf{u} - \mathbf{v}) \cdot \boldsymbol{\nabla}]\mathbf{u} = \boldsymbol{\nabla} \cdot \boldsymbol{\sigma}. \tag{6.2}$$

where ρ_f the fluid density, $\mathbf{u}$ the fluid velocity, $\boldsymbol{\sigma}$ the total fluid stress tensor (pressure and viscous forces), and $\mathbf{v}$ the velocity of the moving reference frame. More details of its development may be found in Lacroix & Garon (1992). The associated constitutive equation is given by:

$$\boldsymbol{\sigma} = \boldsymbol{\tau} - p\mathbf{I} \quad \text{with} \quad \boldsymbol{\tau} = \mu[\boldsymbol{\nabla}\mathbf{u} + (\boldsymbol{\nabla}\mathbf{u})^{\mathrm{T}}].$$

where μ is the dynamic viscosity and p is the fluid pressure. The fluid equations are closed with the following boundary conditions,

$$\boldsymbol{\sigma} \cdot \hat{\mathbf{n}} = \bar{\mathbf{t}} \text{ on } \Gamma_N, \tag{6.3}$$

$$\mathbf{u} = \bar{\mathbf{u}} \text{ on } \Gamma_D. \tag{6.4}$$

where Γ_N denotes a boundary on which Neumann boundary conditions are applied in the form of prescribed surface forces (tractions) $\bar{\mathbf{t}}$ with $\hat{\mathbf{n}}$ the outward normal unit vector, and Γ_D corresponds to a Dirichlet boundary on which the velocity, $\bar{\mathbf{u}}$, is imposed.

The rigid cylinders are supported by constant stiffness springs and dampers in the transverse and streamwise directions. The equations of motion for the cylinder are given by the non-dimensional mass-damper-spring equations:

$$\ddot{\mathbf{x}}^* + 2\zeta \left(\frac{2\pi}{U_r}\right)\dot{\mathbf{x}}^* + \left(\frac{2\pi}{U_r}\right)^2 \mathbf{x}^* = \frac{2}{m^*\pi}[C_D, C_L]^{\mathrm{T}}. \tag{6.5}$$

where $m^* = \rho_s/\rho_f$ is the mass ratio, $\mathbf{x}^* = [x^*, y^*]^{\mathrm{T}} = \mathbf{x}/D$ the vector of non-dimensional cylinder displacements in x and y, C_D and C_L the fluid loading coefficients in each direction (drag and lift). These force coefficients are written as functions of $\mathbf{F} = [F_x, F_y]^{\mathrm{T}}$ for each direction as follows:

$$C_D = \frac{F_x}{\frac{1}{2}\rho_f U^2 A}, \quad C_L = \frac{F_y}{\frac{1}{2}\rho_f U^2 A} \tag{6.6}$$

where A is the projected area which is D for a cylinder. Time is non dimensionalized as $t^* = Ut/D$. The following constraints are applied on the surface of the cylinder:

$$\mathbf{u} = \dot{\mathbf{x}}^*, \tag{6.7}$$

$$\bar{\mathbf{t}} = \mathbf{F} \tag{6.8}$$

The coupling between the fluid and solid is achieved as follows. On the fluid side of the boundary interface, the reaction force at each node is determined by the implicit method of reaction (Dhatt (1984)). The forces onto the boundary of the solid body are set to be the opposite of the fluid reaction force. The total fluid force onto the solid are added up and used in the mass-damper-spring equation. The displacement and velocity of the rigid body can be evaluated. In the fluid domain, the displacements and velocities of the nodes on the fluid solid boundary are set to be equal to the solid rigid body displacement and velocity. These coupling relations are computed simultaneously. In other words, the fluid and solid domains are fully coupled.

To complete the formulations, we need a scheme to manage the domain deformation (i.e. to generate and control the grid motion and mesh velocities) for the Arbitrary Lagrangian Eulerian formulation. For this, there is no unique method (Donéa (2003)). We have opted to employ the pseudo-solid approach of Sackinger *et al.* (1996) because it allows for a fully coupled continuum formulation. In a nutshell, the pseudo-solid model uses the linear elastic equations to describe the time varying domain deformation. Thus, the model provides a physically-based grid motion management.

6.2.2   Solution strategy

We use a finite element method to solve the governing equations in a monolithic manner. We discretize the spatial domain with the Taylor-Hood element which is 3rd order accurate for velocity and 2nd order accurate for pressure. The degrees of freedom of the flow velocity and the fluid pressure are fully coupled to the point mass displacements of the cylinders. For time integration, we employ an adaptive backward difference formulation (BDF) scheme. We demand the velocity and the pressure to be at least 3rd order accurate temporally (Hairer (2010)). The nonlinear system of equations is linearized by the Newton-Raphson method using numerical Jacobians. The sparse system is resolved with a direct solver.

We note that this methodology is not only applicable to problems of flows with rigid body motion, but also to the general unsteady fluid-structure interaction problems. Further details of the finite element flow solver and its verification with respect to space and time accuracy can be found in Etienne *et al.* (2009).

6.3 Computational problem

The computational domains for our simulations are summarized in figure 6.1. Figure 6.1(a) shows the computational domain of the main investigation while figure 6.1(b) shows the settings for the validation case. For both cases, at the inlet, we set $u = 1$, $v = 0$. On the top and bottom boundaries, we impose a symmetry boundary condition by setting the normal velocity to zero ($v = 0$) and by prescribing zero shear force $\mu(\partial u/\partial y + \partial v/\partial x) = 0$. The outflow is assumed to be sufficiently far downstream that the flow has reverted to nearly uniform state so that we set the normal and shear forces to zero:

$$-p + 2\mu\frac{\partial u}{\partial x} = 0, \tag{6.9}$$

$$\mu\left(\frac{\partial u}{\partial y} + \frac{\partial v}{\partial x}\right) = 0. \tag{6.10}$$

On the cylinder we assume that the fluid velocity is equal to the solid velocity.

(a) Three cylinders in-line.

(b) Two cylinders in tandem.
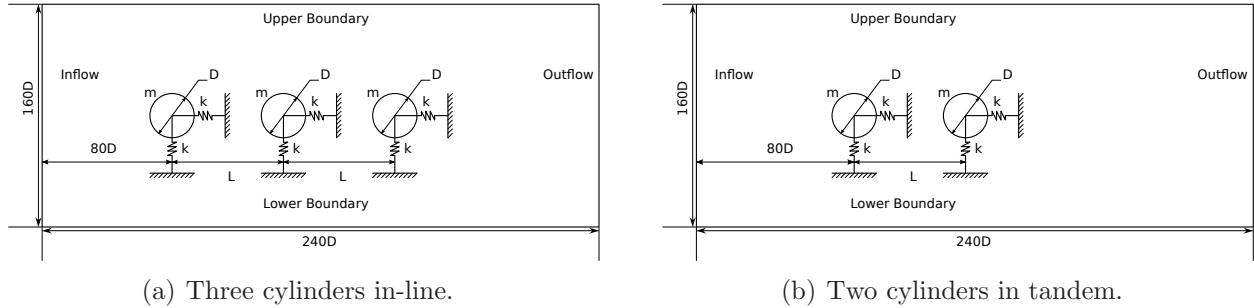
Figure 6.1 Geometry and boundaries.

6.4 Calculation verification and validation

The accuracy of a numerical simulation is highly dependent on the temporal and spatial discretizations of the computational problem. The temporal accuracy is managed by the adaptive BDF scheme. More information can be found in Hay *et al.* (2014). In this section, we verify the spatial discretization. We first perform a grid convergence study to select a mesh that provides sufficient accuracy for the problem of the free oscillations of three in-line cylinders. Then, we validate the numerical settings with two problems of two cylinders arranged in tandem which are close to the three in-line cylinders problem considered.

6.4.1 Verification

Here, we perform a grid convergence study to select a sufficiently accurate mesh for our computations. We place more elements around the cylinders and in the wake region to better capture the vortical structure and more importantly the force coefficients. Four initial meshes are generated. Their characteristics are summarized in table 6.1. The second number indicates the level of refinement. In figure 6.2, it shows the finest initial mesh M_04.

Table 6.1 Mesh characteristics : Three in-line cylinders.

Mesh	# Nodes	# Elem
M_01	26392	12838
M_02	49922	24656
M_03	109099	53789
M_04	212203	105017
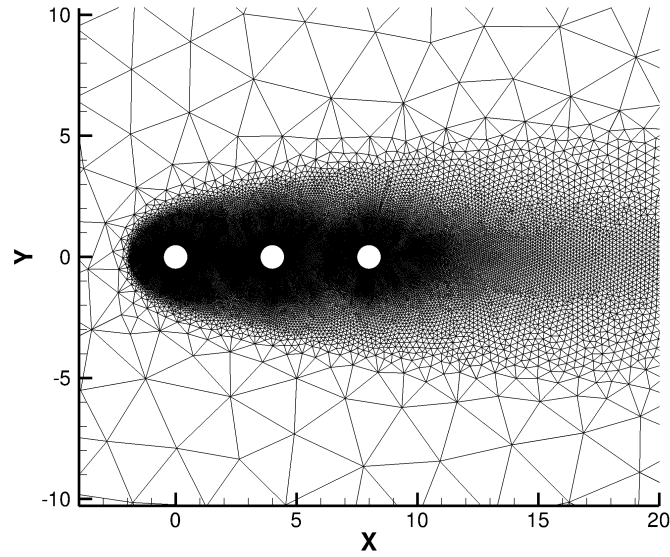
Figure 6.2 Mesh : M_04.

We first compare the meshes using the problem of three fixed in-line cylinders ($L/D = 4$) subjected to uniform incoming flow at $Re = 100$. In the analysis, we only extract the results when the simulation reaches an established oscillation state. For which, the changes in the root mean square and the standard deviation of the signals are less than 0.5%. The data

in the transient section is discarded. The results are shown in table 6.2. We can see that although $M_0 2$ only has about 50000 nodes, the obtained force coefficients differ by no more than 2.2% from those of the finest mesh $M_0 4$ which has 4 times the number of nodes of $M_0 2$. As mentioned by Sarpkaya (2010), the Strouhal frequency St is a parameter that can be easily captured. We see that the value of the Strouhal frequency converges very nicely even on the coarsest mesh $M_0 1$.

Table 6.2 Verification : Three fixed in-line cylinders at $Re = 100$, $L/D = 4$.

Mesh	St_1	Mean C_{D_1}	RMS $C_{D_1'}$	Max $C_{L_1'}$	RMS $C_{L_1'}$
$M_0 1$	0.137	1.168	0.015	0.415	0.293
$M_0 2$	0.137	1.169	0.015	0.417	0.294
$M_0 3$	0.137	1.176	0.015	0.424	0.300
$M_0 4$	0.137	1.176	0.015	0.424	0.300

Mesh	St_2	Mean C_{D_2}	RMS $C_{D_2'}$	Max $C_{L_2'}$	RMS $C_{L_2'}$
$M_0 1$	0.137	0.430	0.111	1.288	0.925
$M_0 2$	0.137	0.429	0.110	1.288	0.926
$M_0 3$	0.137	0.426	0.110	1.295	0.931
$M_0 4$	0.137	0.426	0.111	1.296	0.933

Mesh	St_3	Mean C_{D_3}	RMS $C_{D_3'}$	Max $C_{L_3'}$	RMS $C_{L_3'}$
$M_0 1$	0.137	0.270	0.035	0.825	0.585
$M_0 2$	0.137	0.267	0.035	0.818	0.580
$M_0 3$	0.137	0.263	0.035	0.809	0.574
$M_0 4$	0.137	0.263	0.035	0.811	0.577

Hence, we employ mesh $M_0 2$ to perform several preliminary investigations of the free oscillations of three in-line cylinders. Among the results, the condition at $Re = 150$ and $U_r = 8$ gives the widest wake region for the third cylinder. Therefore, we choose this condition to further examine if the mesh $M_0 2$ is sufficient for the present study.

For comparison, we develop two additional sets of meshes with slightly different considerations than the meshes M_0 above. The first set, referred to as M_1, puts more emphasis in the wake region and slightly relaxes in the area around the cylinder. The second set, referred to as M_2, further refines both regions. Their characteristics are summarized in table 6.3. In figure 6.3, the meshes $M_1 2$ and $M_2 3$ are shown.

Selected time series results are shown in figure 6.4. In the figures, the time series responses from the meshes $M_0 2$, $M_1 2$, $M_2 3$ are shown. The characteristics for the other meshes are very similar.

We first notice that there is a high degree of randomness in the responses. This is especially
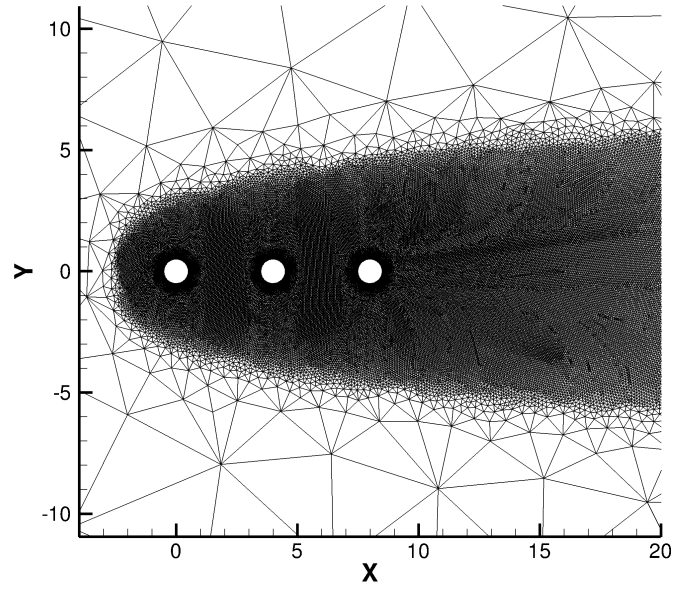
(a) Mesh : $M_1 2$.
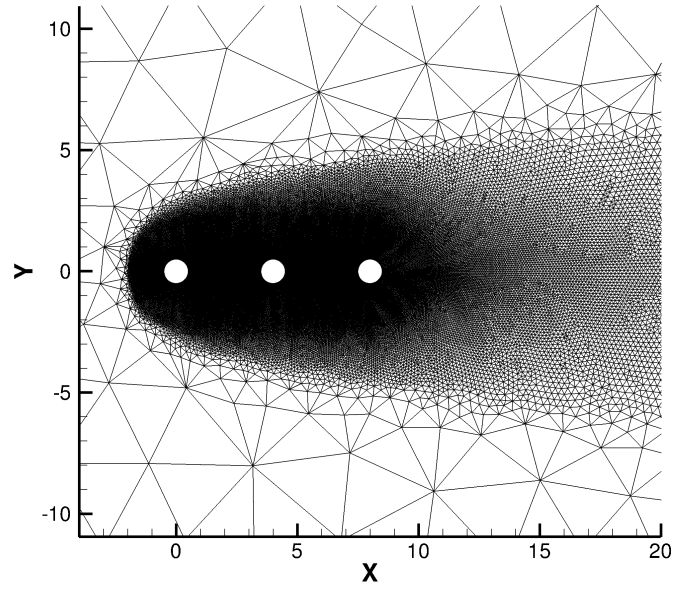
(b) Mesh : $M_2 3$.

Figure 6.3 Additional mesh.

Table 6.3 New mesh characteristics : Three in-line cylinders.

Mesh	# Nodes	# Elem
$M_1 1$	128971	64265
$M_1 2$	254970	127174
$M_2 1$	75357	37291
$M_2 2$	147172	73040
$M_2 3$	308313	153385

so for the lift coefficient of the third cylinder shown in figure 6.4(b). In particular, the lift coefficients seems to "bounce" between two different equilibrium states. Secondly, although the responses from the considered meshes are all different, they are all qualitatively similar. More specifically, the principal features of the responses (i.e. the mean values, the maximum of the average responses, the way these values increase and decrease, etc.) captured by all these different meshes do not differ significantly visually in the time series responses.

The time averaged force coefficients are summarized in table 6.4. These results further confirm that the accuracy yielded by these different meshes are quite comparable. We can see that despite its relative coarseness, $M_0 2$ can generally capture the force coefficients with at least 3 digits of accuracy as compared with the other. Given also that a smaller mesh requires less computational resources, $M_0 2$ is therefore selected for the remainder of this paper.

6.4.2 Validation

Here, we validate the numerical settings with two nearby problems reported in the literature. First, we consider the problem of two cylinders fixed in a tandem arrangement ($L/D = 4$) subjected to a uniform incoming flow at $Re = 200$ following Borazjani & Sotiropoulos (2009). The second validation problem is the problem of free oscillations of a tandem cylinder pair ($L/D = 5$) at $Re = 150$ studied by Bao *et al.* (2012). For both cases, we first prepare a mesh that can provide accurate force coefficients with errors of only about 3.0% using the procedure described in the previous section.

The results for two fixed cylinders in a tandem arrangement are shown in table 6.5. In general, the results obtained are in good agreement with those reported in the literature. However, we do not observe the abrupt change in the drag coefficient as observed by Borazjani & Sotiropoulos (2009). In particular, our results compare closely with those reported by Meneghini *et al.* (2001).

In figure 6.5, we show the maximum oscillation amplitudes of our second validation prob-

Time series of C_D of Cyl. 1

(a) C_D : Cyl 1.

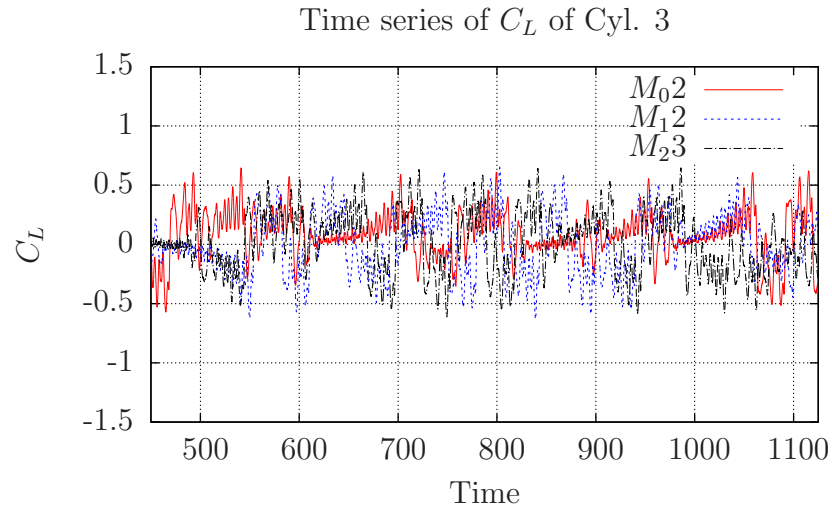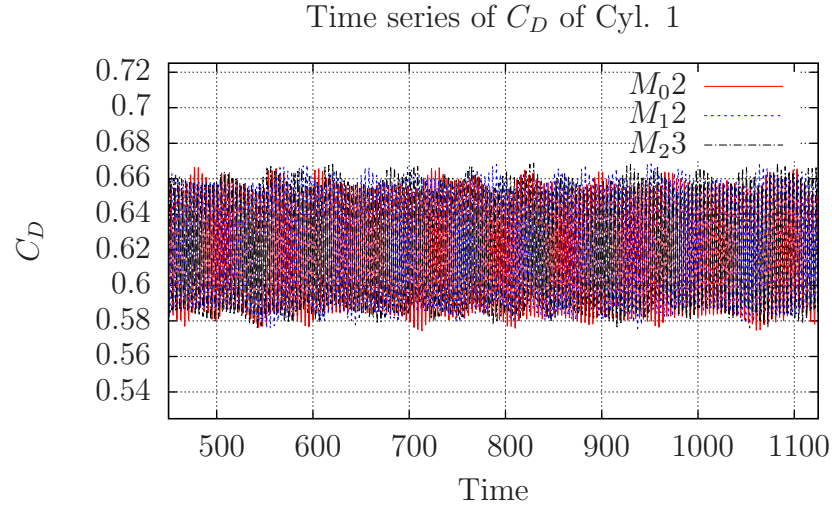Time series of C_L of Cyl. 3

(b) C_L : Cyl 3.

Figure 6.4 Verification : Time series of force coeff. : Free oscillations of three in-line cylinders.

Table 6.4 Verification : Free oscillation of three in-line cylinders at $Re = 150$, $U_r = 8$.

Mesh	Mean C_{D_1}	RMS $C_{D'_1}$	Max $C_{L'_1}$	RMS $C_{L'_1}$
$M_0 2$	1.237	0.054	0.049	0.017
$M_0 4$	1.243	0.055	0.047	0.017
$M_1 1$	1.241	0.054	0.042	0.016
$M_1 2$	1.243	0.054	0.060	0.015
$M_2 1$	1.241	0.054	0.043	0.015
$M_2 2$	1.245	0.056	0.042	0.016
$M_2 3$	1.242	0.054	0.043	0.016

Mesh	Mean C_{D_2}	RMS $C_{D'_2}$	Max $C_{L'_2}$	RMS $C_{L'_2}$
$M_0 2$	1.479	0.183	0.618	0.178
$M_0 4$	1.484	0.189	0.656	0.236
$M_1 1$	1.488	0.188	0.489	0.168
$M_1 2$	1.494	0.191	0.546	0.160
$M_2 1$	1.491	0.187	0.557	0.154
$M_2 2$	1.489	0.189	0.632	0.186
$M_2 3$	1.491	0.190	0.585	0.166

Mesh	Mean C_{D_3}	RMS $C_{D'_3}$	Max $C_{L'_3}$	RMS $C_{L'_3}$
$M_0 2$	1.056	0.286	1.285	0.433
$M_0 4$	0.970	0.281	1.215	0.475
$M_1 1$	1.046	0.276	1.287	0.475
$M_1 2$	1.012	0.283	1.295	0.503
$M_2 1$	1.010	0.274	1.335	0.531
$M_2 2$	0.986	0.287	1.222	0.466
$M_2 3$	1.006	0.284	1.282	0.522

lem, namely the free oscillations of two cylinders in a tandem arrangement ($L/D = 5$) at $Re = 150$. The results of the present study are in excellent agreement with those from Bao et $al.$ (2012).

The corresponding power spectral densities (PSD) of the force coefficients at $U_r = 4$ and $U_r = 8$ are shown in figure 6.6. They are also in good agreement with those from Bao et $al.$ (2012).

Hence, we are confident about our numerical settings to explore the free oscillation response of three in-line cylinders.
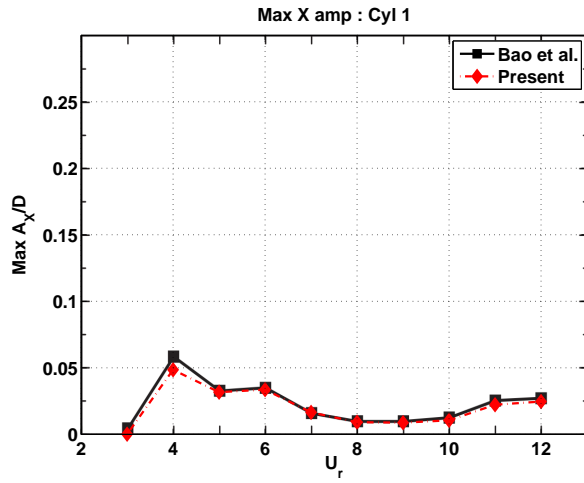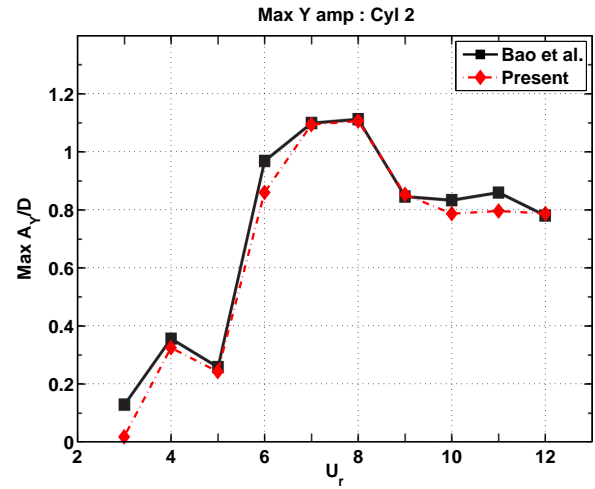
(a) Max X amplitude : Cyl 1.
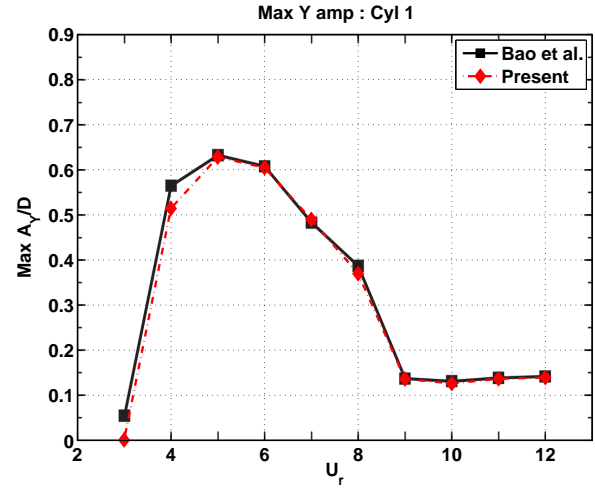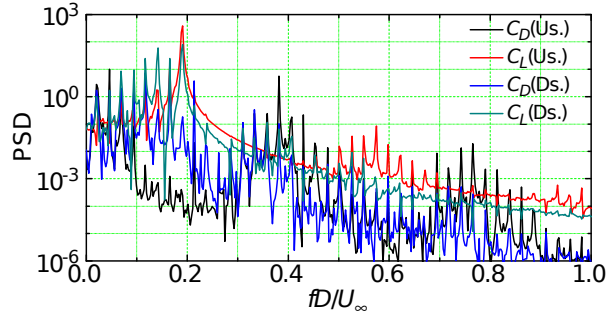
(b) Max Y amplitude : Cyl 1.
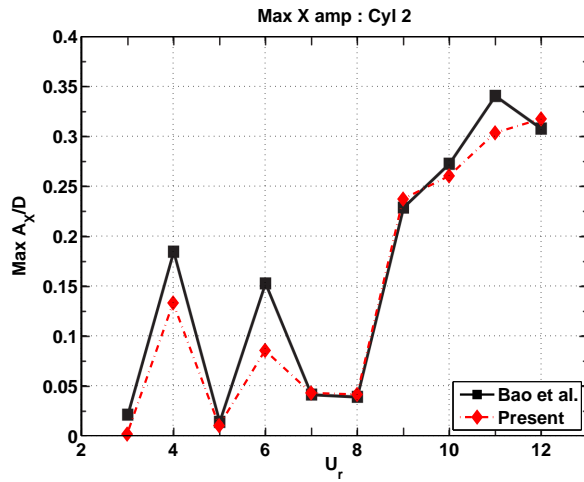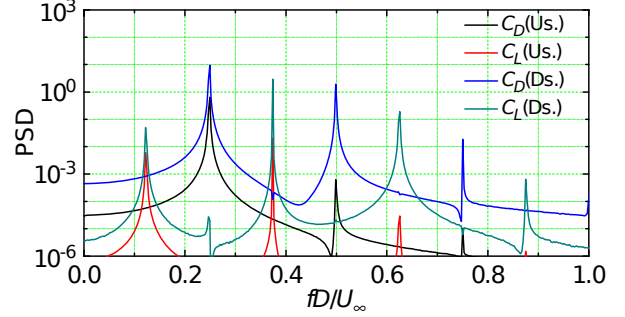
(c) Max X amplitude : Cyl 2.

(d) Max Y amplitude : Cyl 2.

Figure 6.5 Validation : Free oscillations of two cylinders in tandem at $Re = 150$, $L/D = 5$: Max amplitude.
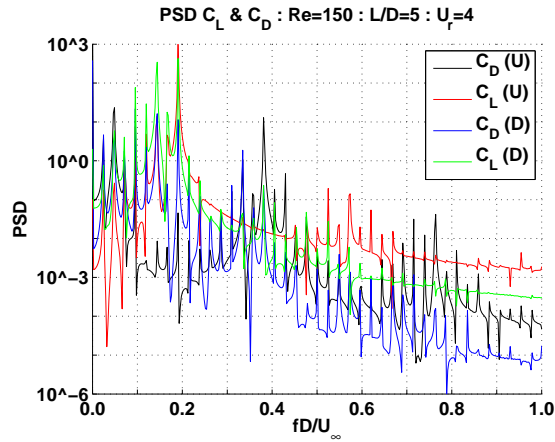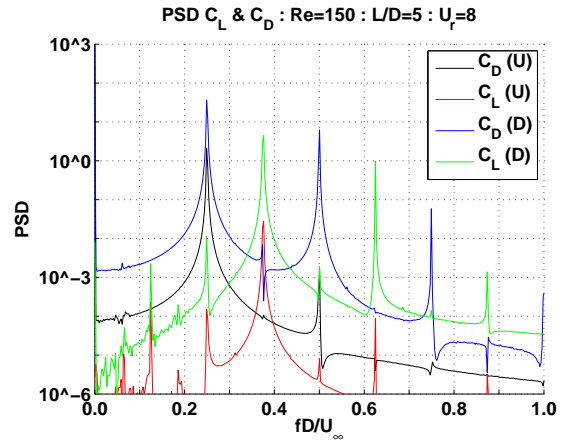
(a) PSD of forces coefficients at $U_r = 4$: Bao *et al.* 2012.

(b) PSD of forces coefficients at $U_r = 8$: Bao *et al.* 2012.

(c) PSD of forces coefficients at $U_r = 4$: Present work.

(d) PSD of forces coefficients at $U_r = 8$: Present work.

Figure 6.6 Validation : Free oscillations of two cylinders in tandem at $Re = 150$, $L/D = 5$: PSD of forces. Results from Bao *et al.* 2012 reproduced with permission from Elsevier.

Table 6.5 Validation : Two fixed cylinders in tandem at $Re = 200$, $L/D = 4$.

	Mean C_{D_1}	Max $C_{L'_1}$	St_1
Present	1.23	0.737	0.176
Borazjani & Sotiropoulos (2009)	1.29	0.745	0.185
Meneghini *et al.* (2001)	1.18	0.75	0.174
Slaouti & Stansby (1992)	1.11 ± 0.05	0.7	0.19

	Mean C_{D_2}	Max $C_{L'_2}$	St_2
Present	0.473	1.69	0.176
Borazjani & Sotiropoulos (2009)	0.6	1.9	0.185
Meneghini *et al.* (2001)	0.38	1.5	0.174
Slaouti & Stansby (1992)	0.88 ± 0.4	1.8	0.19

6.5 Results and discussion

We now present results for the free oscillations of three in-line cylinders which will be referred to as the triple cylinders configuration for brevity in the following. In particular, we examine the maximum oscillation amplitude, the force coefficients and the frequency responses in both the streamwise and the transverse directions. We also examine the displacement trajectories of the cylinders. We compare these results with those of an isolated cylinder and a tandem cylinder pair with the same structural parameters.

We first present the benchmarking results for the free oscillations of an isolated cylinder and a tandem pair of cylinder. This is followed by the main results for the free oscillations of three in-line cylinders. These results indicate that the addition of the third cylinder behind a tandem cylinder pair significantly increases the nonlinearity of the fluid-structure system. We then use the Poincaré map and phase portrait to characterize the dynamical system responses of the free oscillations of three in-line cylinders, and contrast the results with respect to the associated vortex shedding patterns.

6.5.1 Isolated cylinder

We first look at the benchmarking results of the free oscillations of an isolated cylinder.

Maximum amplitude

The maximum amplitude of the free oscillations of an isolated cylinder are shown in figure 6.7. The overall profiles of the maximum oscillation amplitude are very similar at the different Reynolds numbers considered. The synchronization ("locked-in") range is approximately

limited between $U_r = 3$ and $U_r = 10$. Inside the synchronization range, oscillations of large amplitudes are observed. Whereas, the oscillation amplitude remains small outside the synchronization range. Lastly, the maximum transverse amplitude is much larger than that of the streamwise amplitude. The peak transverse amplitude reaches $A_Y/D \approx 0.65$ which corresponds well with the values reported in the literature (Govardhan & Williamson (2006)). When the Reynolds number is increased, noticeable gradual increases in both the maximum streamwise and transverse amplitudes can be seen. At $Re = 200$, the maximum streamwise amplitude does not follow the trends of the other Reynolds numbers at $U_r = 3$ and $U_r = 9$. This turns out to be an artifact of the fact that these reduced velocities are very close to the synchronization limit. The time traces of transverse amplitude at $U_r = 3$ at the three Reynolds numbers are shown in figure 6.8. We can clearly observe the "fluctuation" of the amplitude especially at the earlier time for all three Reynolds numbers. Khalak & Williamson (1999) described the fluctuation as a quasi-periodic response which is a typical behavior at around the synchronization limit.

(a) Max X amplitude.

(b) Max Y amplitude.
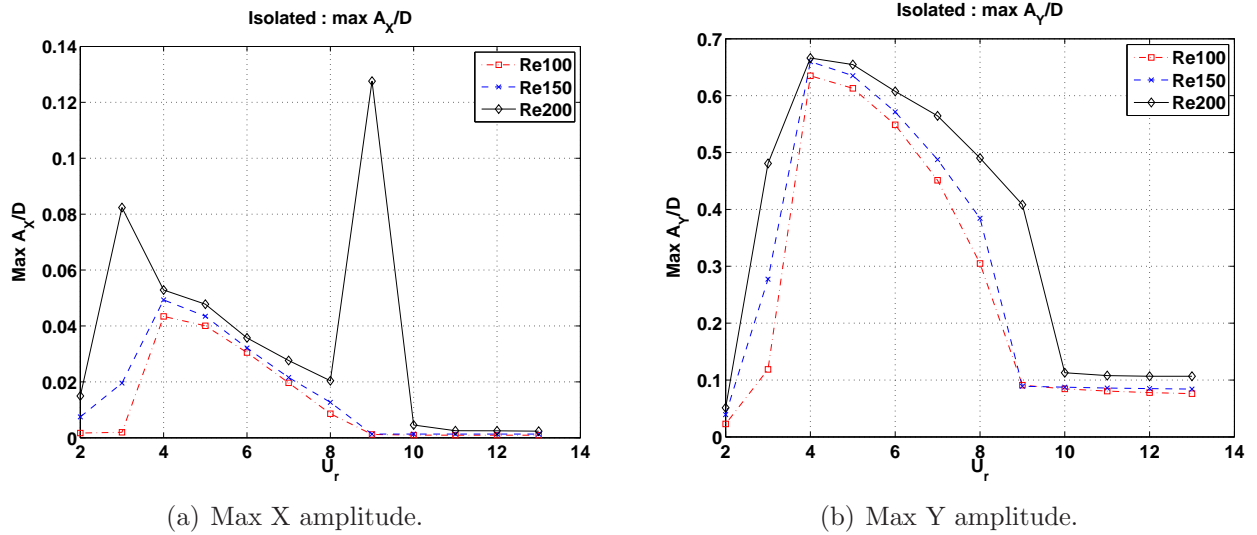
Figure 6.7 Isolated cylinder : Max amplitude.

Displacement trajectories

The displacement trajectories of a freely oscillating isolated cylinder are shown in figures 6.9 to 6.11. The dimensions are scaled to enhance the trajectory pattern. The displacement trajectories are relative to the initial position of the cylinder. Note that the scale in the streamwise direction is in fact smaller than that of the transverse direction. From the figures, we can observe two main displacement trajectory patterns. When synchronization occurs, the
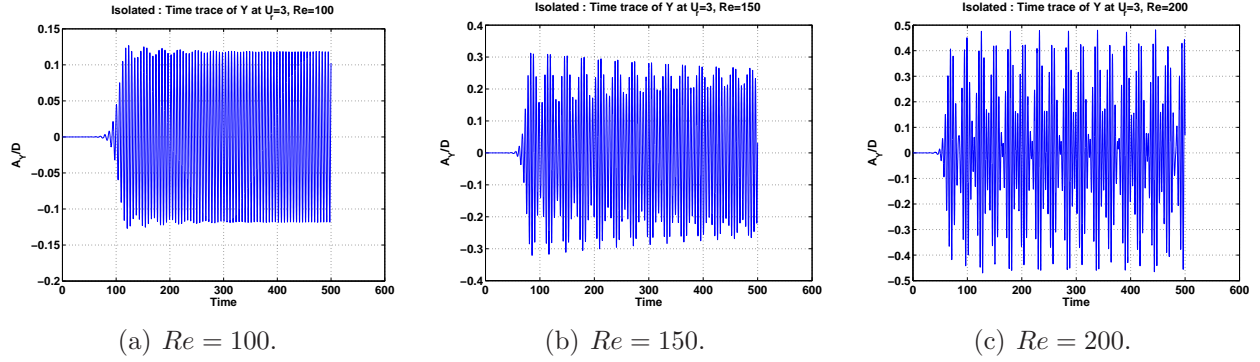
(a) $Re = 100$.   (b) $Re = 150$.   (c) $Re = 200$.

Figure 6.8 Isolated cylinder : Time trace of Y amplitude at $U_r = 3$.

trajectory traces a clear "figure-8" (e.g. in figure 6.10(e)). Outside the synchronization range, the "figure-8" trajectory becomes blurry (e.g. in figures 6.10(a) and 6.10(g)). The blurriness suggests that multiple frequencies are influencing the cylinder motions in the corresponding direction(s). These two patterns can be observed for all three Reynolds numbers investigated. These patterns regarding synchronization confirm well with those reported in the original experimental work by Jauvtis & Williamson (2004) at much higher Reynolds numbers. The results are also in good agreement with those of Bao *et al.* (2012).

Some variations of these two main patterns are observed. At low reduced velocities, the "figure-8" can be stretched and become more parabolic with convex side facing the incoming flow (e.g. in figure 6.9(b)). Finally, when the response is very close to the onset of synchronization, the trajectory can become rather sporadic. This is especially the case at $Re = 200$ (e.g. in figures 6.11(a) and 6.11(g)).

Force coefficients

The averaged forces onto a freely oscillating isolated cylinder are shown in figures 6.12 and 6.13. All the averaged force coefficients (i.e. the mean drag C_D, the RMS of the drag fluctuation C_D' and the RMS of the lift C_L) reach the maximum values at around reduced velocity $U_r = 4$ close to the onset of synchronization. When the reduced velocities continue to increase spanning the "locked-in" range, the force coefficients decrease rapidly towards smaller values. These are in good agreement with the work of Prasanth & Mittal (2008) who investigated the Vortex-induced vibrations of an isolated cylinder with no damping at low Reynolds number. From the figures, the effect of Reynolds number is not noticeable except for the RMS of the drag coefficient fluctuation which becomes larger when the Reynolds number is increased.
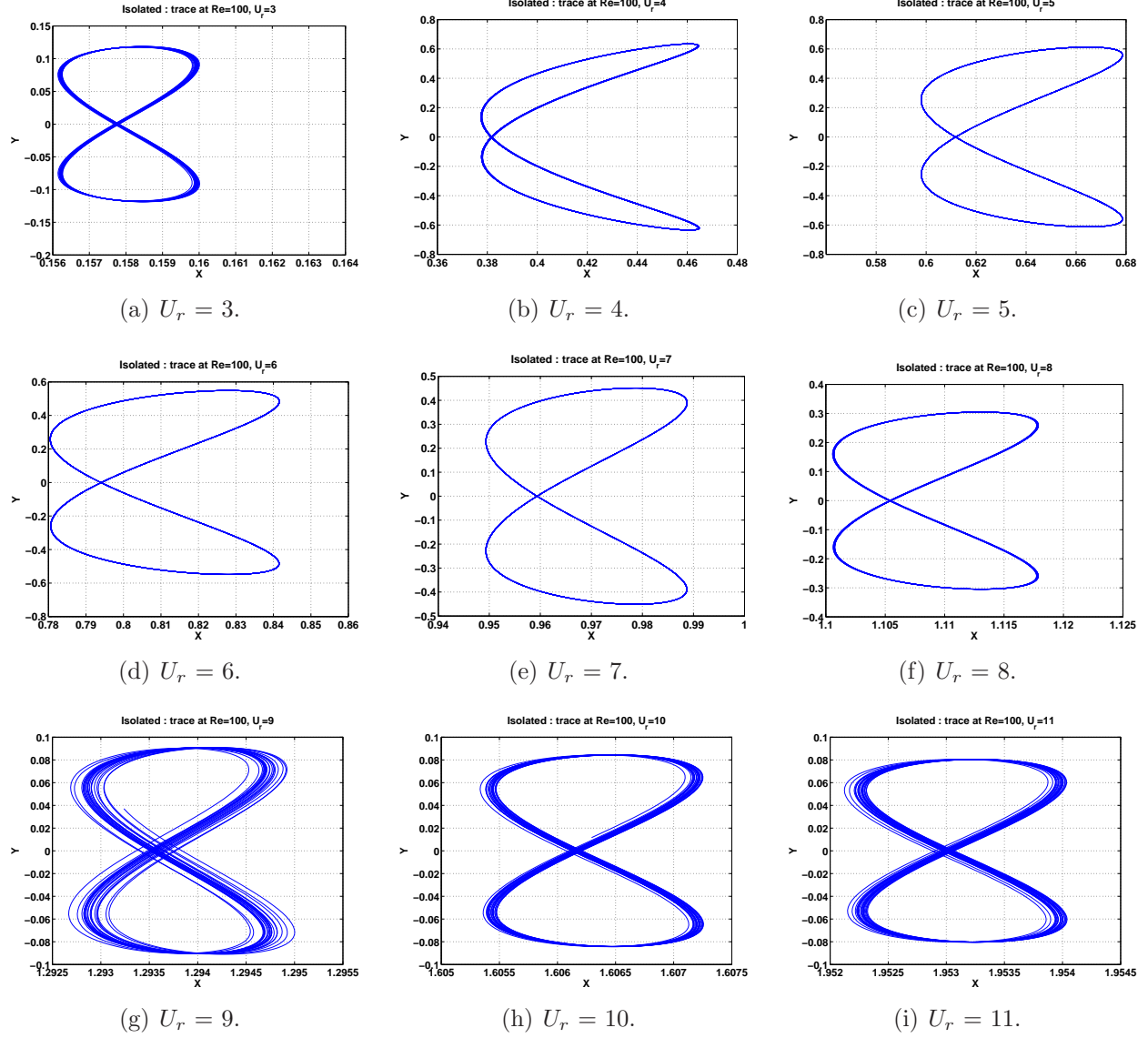
(a) $U_r = 3$.

(b) $U_r = 4$.

(c) $U_r = 5$.

(d) $U_r = 6$.

(e) $U_r = 7$.

(f) $U_r = 8$.

(g) $U_r = 9$.

(h) $U_r = 10$.

(i) $U_r = 11$.
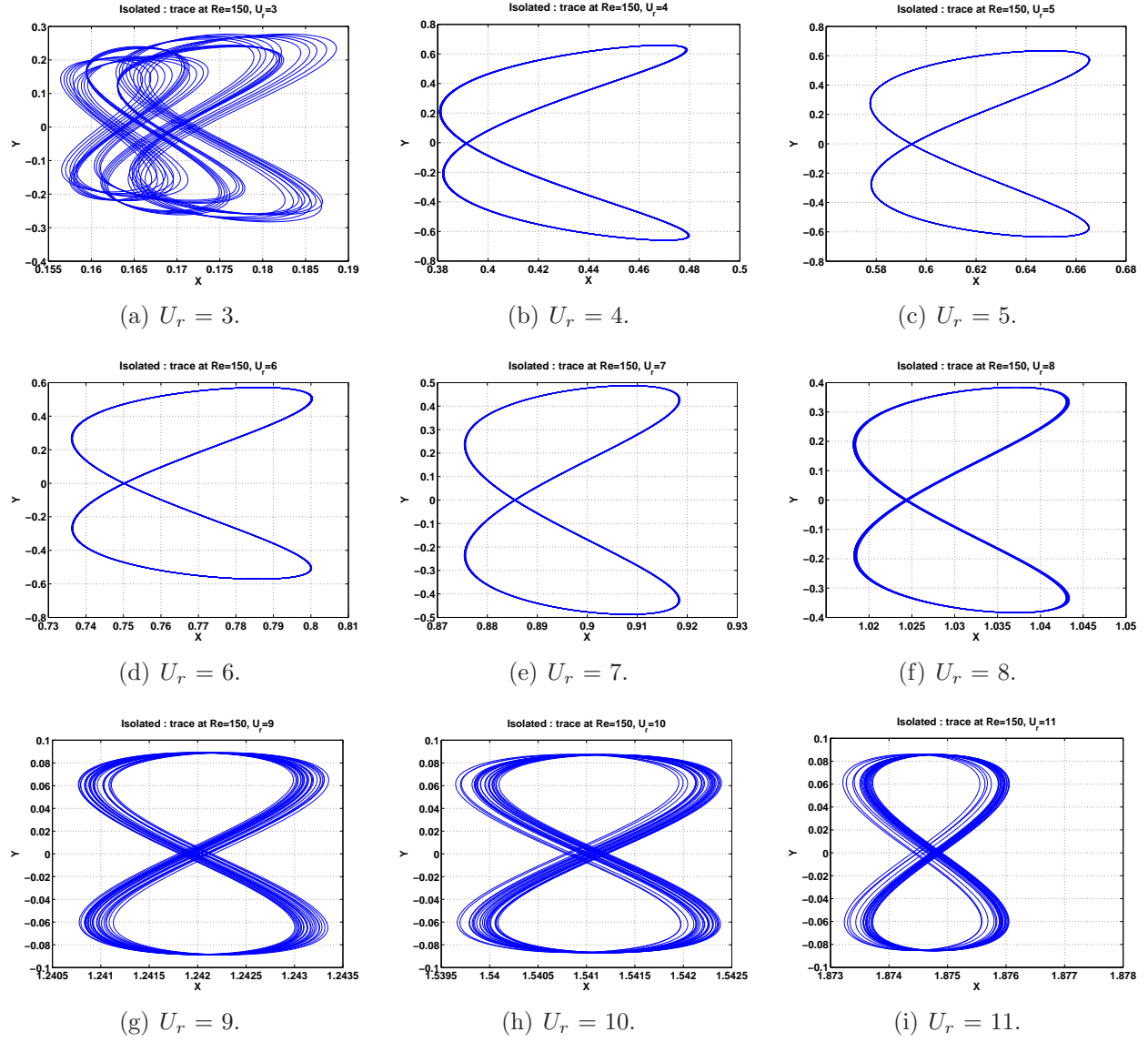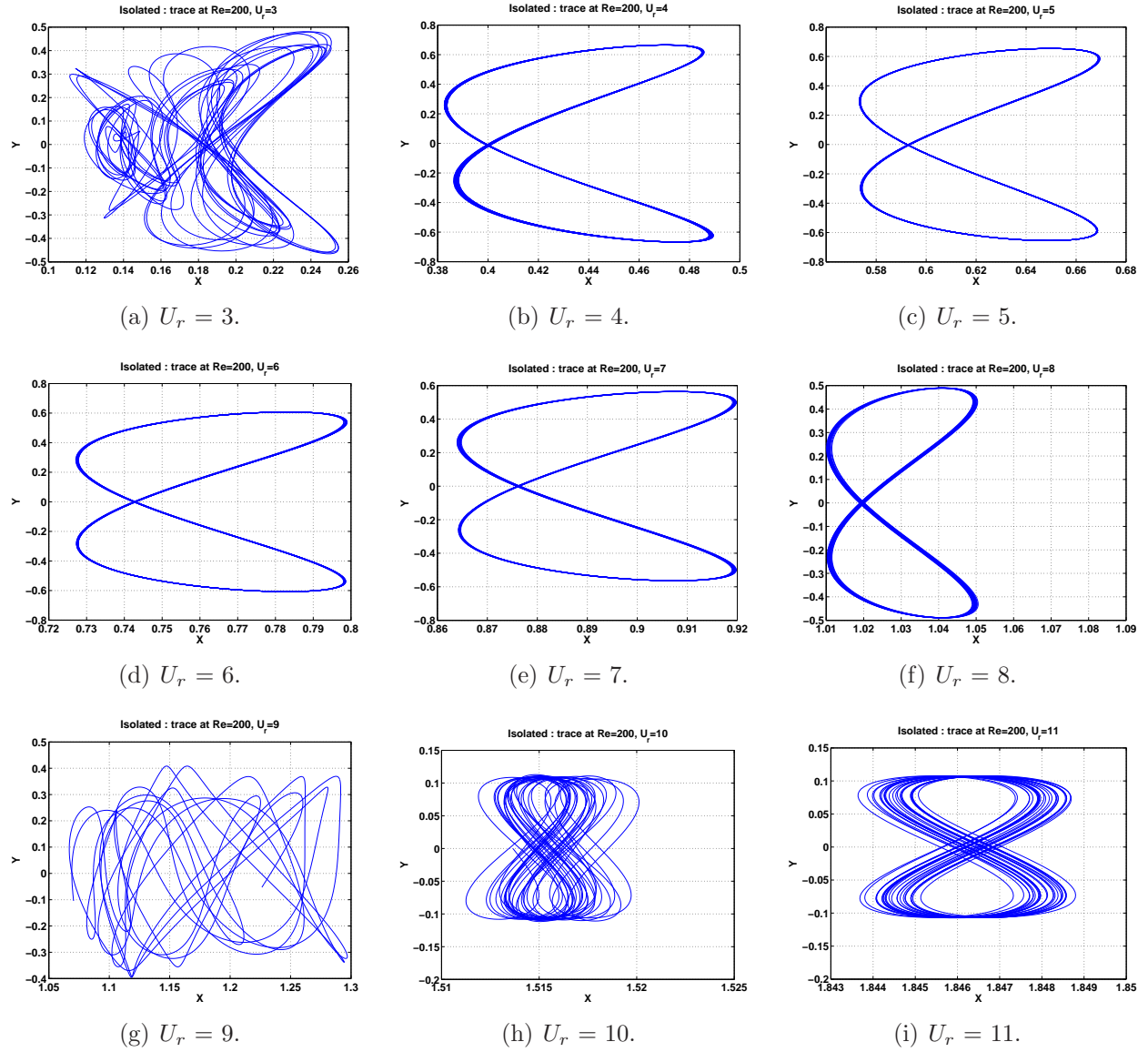
Figure 6.9 Isolated cylinder : Displacement trajectories at $Re = 100$ relative to the initial position.

(a) $U_r = 3$.

(b) $U_r = 4$.

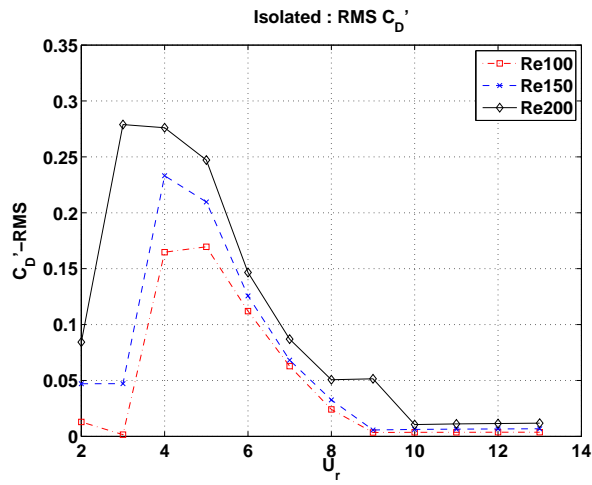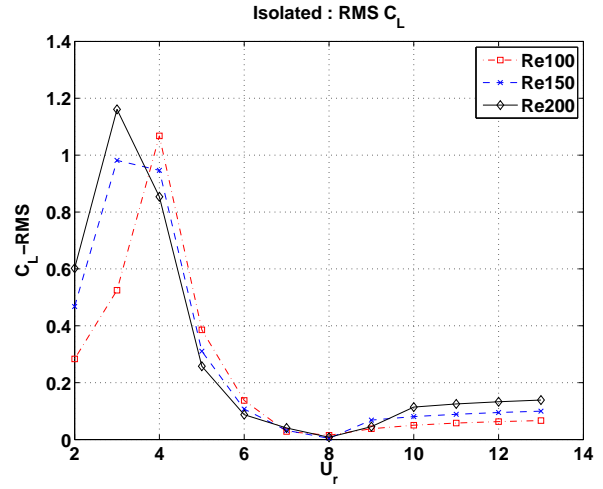(c) $U_r = 5$.

(d) $U_r = 6$.

(e) $U_r = 7$.

(f) $U_r = 8$.

(g) $U_r = 9$.

(h) $U_r = 10$.

(i) $U_r = 11$.

Figure 6.10 Isolated cylinder : Displacement trajectories at $Re = 150$ relative to the initial position.

Figure 6.11 Isolated cylinder : Displacement trajectories at $Re = 200$ relative to the initial position.
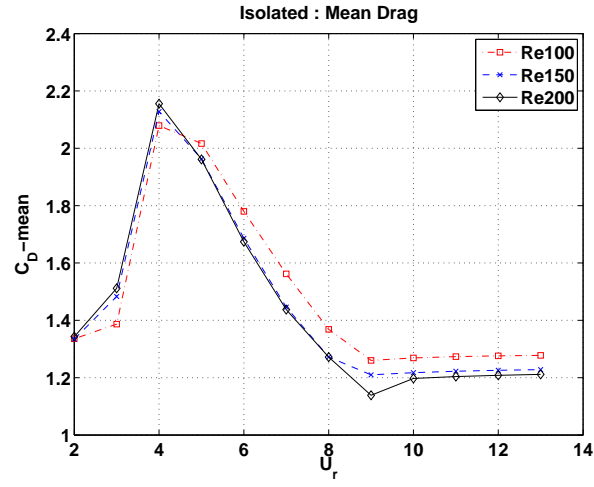
Figure 6.12 Isolated cylinder : Mean C_D .

(a) RMS C'_D.

(b) RMS C_L.

Figure 6.13 Isolated cylinder : RMS C'_D and C_L.

Frequency responses

The oscillation frequency is examined using the power spectral density (PSD) of the drag
and lift coefficients. The force coefficients provide us valuable information about the fluid dy-
namic responses. The PSD at each U_r is normalized to one by dividing by the corresponding
maximum value. The largest value is shown with the color red. Then as the value decreases,
the color shifts to orange, yellow, green, then the smallest blue in 80 levels. The normaliza-
tion per reduced velocity value is necessary since the force coefficients are not in the same
magnitude order across the considered reduced velocity range. The normalized PSD permits
us to describe the dominant frequency at each U_r with no ambiguity. On the other hand, a
drawback is that the differences in the relative frequency signal strength among the different
reduced velocities are now hidden.

The power spectral density of the fluid force fluctuation onto a freely oscillating isolated
cylinder at $Re = 150$ are shown in figure 6.14. The result of the drag force fluctuation C_D'
is shown on the left while that of the lift force C_L is shown on the right. Since the results
at $Re = 100$ and $Re = 200$ are similar, they are not shown here. These responses are in
excellent agreement to those reported by Jauvtis & Williamson (2004) for a cylinder with
low mass ratio. In the figure, there is mainly the principal frequency. Since we consider
the cylinder with zero damping, the principal frequencies identified from the power spectral
density of the force fluctuation will always be identical with those of the displacements here.
Generally, the drag force (shown on the left) oscillates at a frequency twice that of the lift
force (on the right). Note that in figure 6.14(a), we have scaled the reference structural
frequency and the Strouhal frequency with a factor of two. Inside the locked-in range, the
force coefficients resonate at frequencies close to the cylinder natural frequency. Outside this
region, the force coefficients oscillate at frequencies close to the vortex shedding frequency of
a fixed isolated cylinder. As reported by Jauvtis & Williamson (2004), we observe a third
harmonic component in the lift force (on the top of the figure 6.14(b)). For $Re = 200$ (not
shown), more harmonics appear in the spectral response of the lift force at $U_r = 3$ and $U_r = 9$
when the synchronization begins and terminates. In Jauvtis & Williamson (2004), it is also
mentioned that there are second harmonic components in the drag forces. This however is
not observed in our results here.

6.5.2   Two cylinders in tandem

Here, we present another benchmarking results of the free oscillations of two cylinders ar-
ranged in a tandem arrangement.
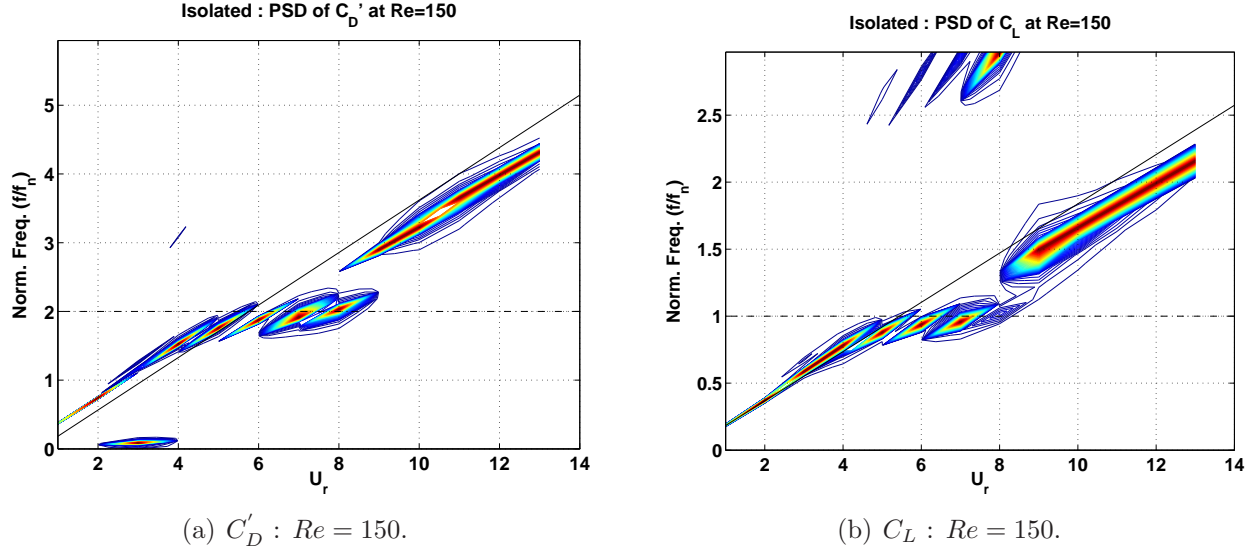
(a) C_D' : $Re = 150$.

(b) C_L : $Re = 150$.

Figure 6.14 Isolated cylinder : PSD of force coefficients.

Maximum amplitude

The maximum amplitudes of the free oscillations of a tandem cylinder pair are shown in figure 6.15. The influence onto the maximum oscillation amplitudes due to the presence of an extra cylinder is evident. The first cylinder in general behaves rather similar to an isolated cylinder in particular in the transverse direction for all three Reynolds numbers studied. The synchronization occurs approximately between $U_r = 3$ and $U_r = 9$. The peak transverse amplitude is about $A_Y/D = 0.7$. Outside the synchronization range at the higher reduced velocity, the transverse oscillation amplitude of the first cylinder is slightly larger than that of an isolated cylinder. The peak value in the streamwise direction however increases about 50% to $A_X/D \approx 0.08$ in the synchronization range. The location of the peak also shifts towards $U_r = 6$ instead of $U_r = 4$ as in the isolated cylinder case. This shift may in fact be caused by the onset of synchronization of the second cylinder. When the Reynolds number is increased, the maximum oscillation amplitudes also increase slightly.

For the second cylinder, the oscillation amplitudes in the streamwise direction are not significant except at around $U_r = 6$ which marks the onset of the lock-in region for the second cylinder. At $U_r = 6$, the streamwise oscillation amplitude can however reach values as large as $A_X/D = 0.9$ at $Re = 200$. Interestingly, the streamwise oscillation amplitude in the lock-in regime is only slightly larger than the amplitude before it synchronized. From figure 6.15(d), although the maximum transverse oscillation amplitudes begins to decrease in the higher reduced velocity range, desynchronization is not yet observed at the highest reduced velocity value ($U_r = 13$) in our parameter space. The peak value in the transverse direction is about

$A_Y/D = 1.2$ which is 70% larger than that of the first cylinder. Note however that, even before the second cylinder is synchronized at $U_r = 6$, transverse oscillation with amplitudes similar to the synchronized first cylinder ($A_Y/D \approx 0.5$) can be achieved.

These characteristics of the maximum oscillation amplitude generally confirm well with those reported by Bao *et al.* (2012). Note that they have employed a heavier cylinder pair which naturally leads to smaller oscillation amplitudes. The only difference is that their downstream cylinder experiences stronger streamwise vibrations after the upstream cylinder is desynchronized as compared with the present study. We remark that in their work, a larger separation ratio of $L/D = 5$ is considered which permits the vortices shedded from the upstream cylinder to influence the downstream cylinder differently. As the distance from the upstream cylinder becomes larger, the shielding effect from the upstream cylinder is also reduced resulting in larger impinging drag forces. Moreover, in their work, the domain employed is smaller which may introduce some blockage ratio effects. Hence, observed differences between the results from Bao *et al.* (2012) and the present study seem to be reasonable. Lastly, a larger separation ratio also leads to their observation of weaker interactions between the two cylinders.

Displacement trajectories

The displacement trajectories of a freely oscillating tandem cylinder pair are shown in figures 6.16 to 6.18. Recall that these displacement trajectories are relative to the initial positions of the cylinders. Hence, when the downstream cylinder moves to $-0.5D$, it means that it is at the position $3.5D$ behind the upstream cylinder.

In accordance with the results from the maximum oscillation amplitudes, the trajectories of the first cylinder in the tandem pair are similar to those of an isolated cylinder. When synchronized, the trajectory traces a "figure-8". Outside the synchronization range, the "figure-8" becomes blurry. However, due to the different scale employed in the streamwise direction, some "figure-8" now appear to be narrower. In particular, the stretched "figure-8" at low reduced velocities now resembles more a parabola and the blurry "figure-8" almost collapses into straight lines. The only differences are the trajectories at $U_r = 6$ when the downstream cylinder reaches the onset of synchronization. At $U_r = 6$, the trajectories for all three Reynolds numbers not only appear to be blurry, but also become asymmetric, especially for $Re = 150$ and $Re = 200$. The overall trajectory responses of the first cylinder are consistent with the observations from the maximum oscillation amplitude.
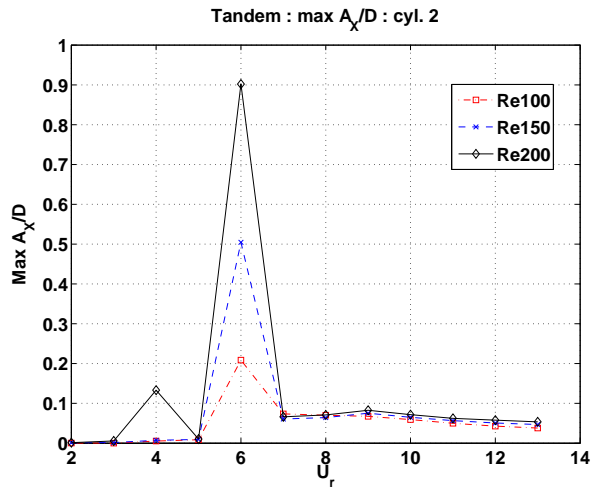
From the figures, it is evident that the downstream cylinder in the tandem cylinder pair exhibits much larger displacements than the upstream one. When synchronization occurs, the trajectory also traces a "figure-8". The "figure-8" may be skewed as in figure 6.18(e). At
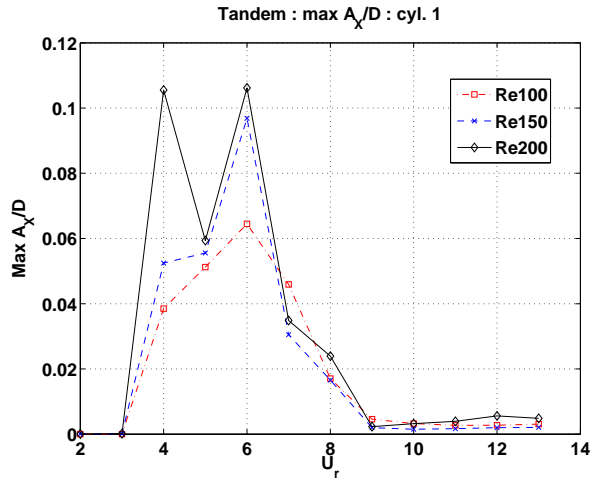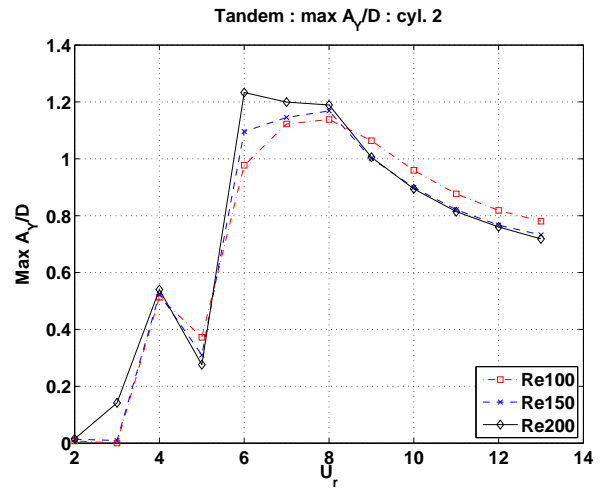
(a) Max X amplitude : Cyl 1.
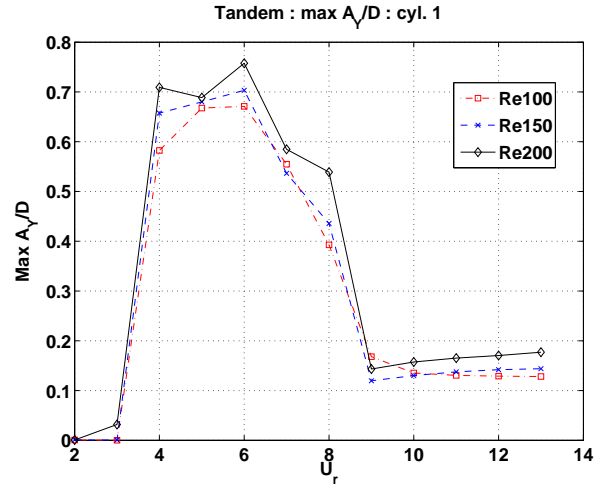
(b) Max Y amplitude : Cyl 1.

(c) Max X amplitude : Cyl 2.

(d) Max Y amplitude : Cyl 2.

Figure 6.15 Two cylinders in tandem : Max amplitude.

the onset of synchronization, the trajectory can appear to be sporadic as in figures 6.16(d) and 6.17(d).

While the trajectory of the upstream cylinder is strongly affected when the downstream cylinder begins to synchronize, the onset of synchronization of the upstream cylinder does not have an as significant effect onto the downstream one. In particular, at $U_r = 4$, only the trajectory at $Re = 200$ is affected (figure 6.18(b)). At both $Re = 100$ and $Re = 150$, the traces of the downstream cylinder do not show any particular difference at $U_r = 4$. Close to the desynchronization point of the upstream cylinder at $U_r = 9$, there are basically no observable change to the trajectories of the downstream one at all for the three Reynolds numbers studied.

These trajectories are in good agreement with those observed by Bao *et al.* (2012). The only difference is the trajectory of the downstream cylinder when the upstream cylinder is desynchronized (more precisely at around $U_r = 12$, not shown). With a closer separation ratio $L/D = 4$ in the present study, the downstream cylinder traces a "figure-8". In the work of Bao *et al.* (2012), the trajectory has a much stronger streamwise displacement as mentioned in the previous section.

Force coefficients

The averaged forces onto a freely oscillating tandem cylinder pair are shown in figures 6.19 and 6.20. As expected, the overall force coefficient characteristics of the upstream cylinder are rather similar to those of an isolated cylinder. However, the presence of the downstream cylinder generally reduces the force coefficients of the upstream cylinder at the lower reduced velocity range $U_r < 4$. It also reduces the peak mean drag of the upstream cylinder by about 10%. Moreover, it shifts the peak of the RMS of the drag coefficient slightly higher at $U_r = 5$ and aligns the peak of the RMS of the lift coefficient at $U_r = 4$. Interestingly, the trend of the RMS of the drag coefficient of the upstream cylinder does not show any particular feature at around $U_r = 6$. There is no observable differences for the average force coefficients after the upstream cylinder desynchronized at the higher reduced velocity range. Lastly, the effect of Reynolds number onto the force coefficients of the upstream cylinder is not significant.

The mean drag coefficient of the downstream cylinder peaks at the reduced velocity of $U_r = 7$ close to the onset of synchronization of the downstream cylinder. This is similar to what is observed for the upstream cylinder. At the onset of synchronization of the upstream cylinder at the reduced velocity of $U_r = 4$, there is also a smaller hump observed for the mean drag coefficient of the downstream cylinder. Unlike the upstream cylinder, the mean drag coefficient only gently reduces after the peak and remains large at the higher reduced velocity range after the upstream cylinder has desynchronized. This seems reasonable as the
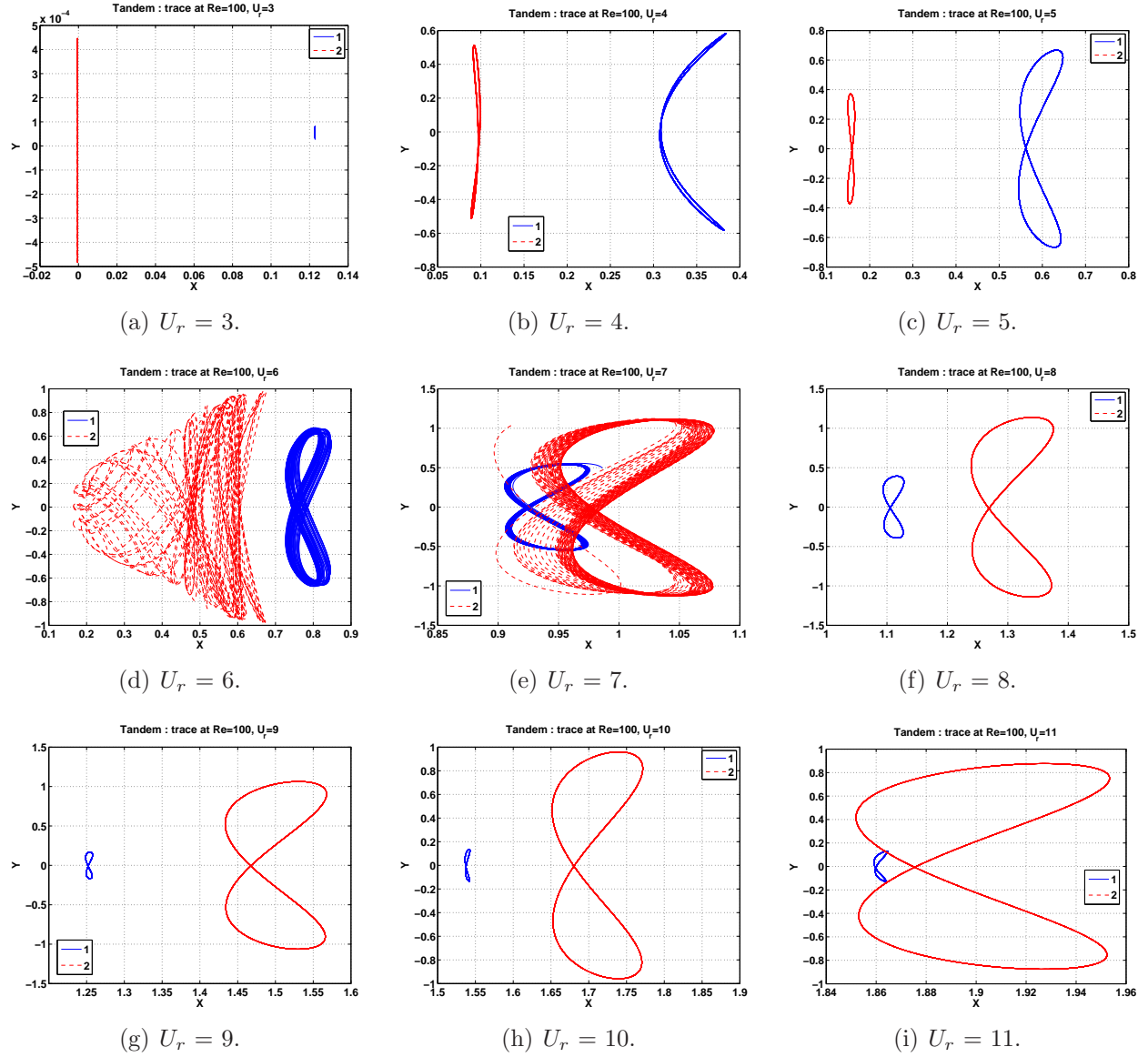
Figure 6.16 Two cylinders in tandem : Displacement trajectories at $Re = 100$ relative to the initial positions. Upstream cylinder in blue and downstream cylinder in red.
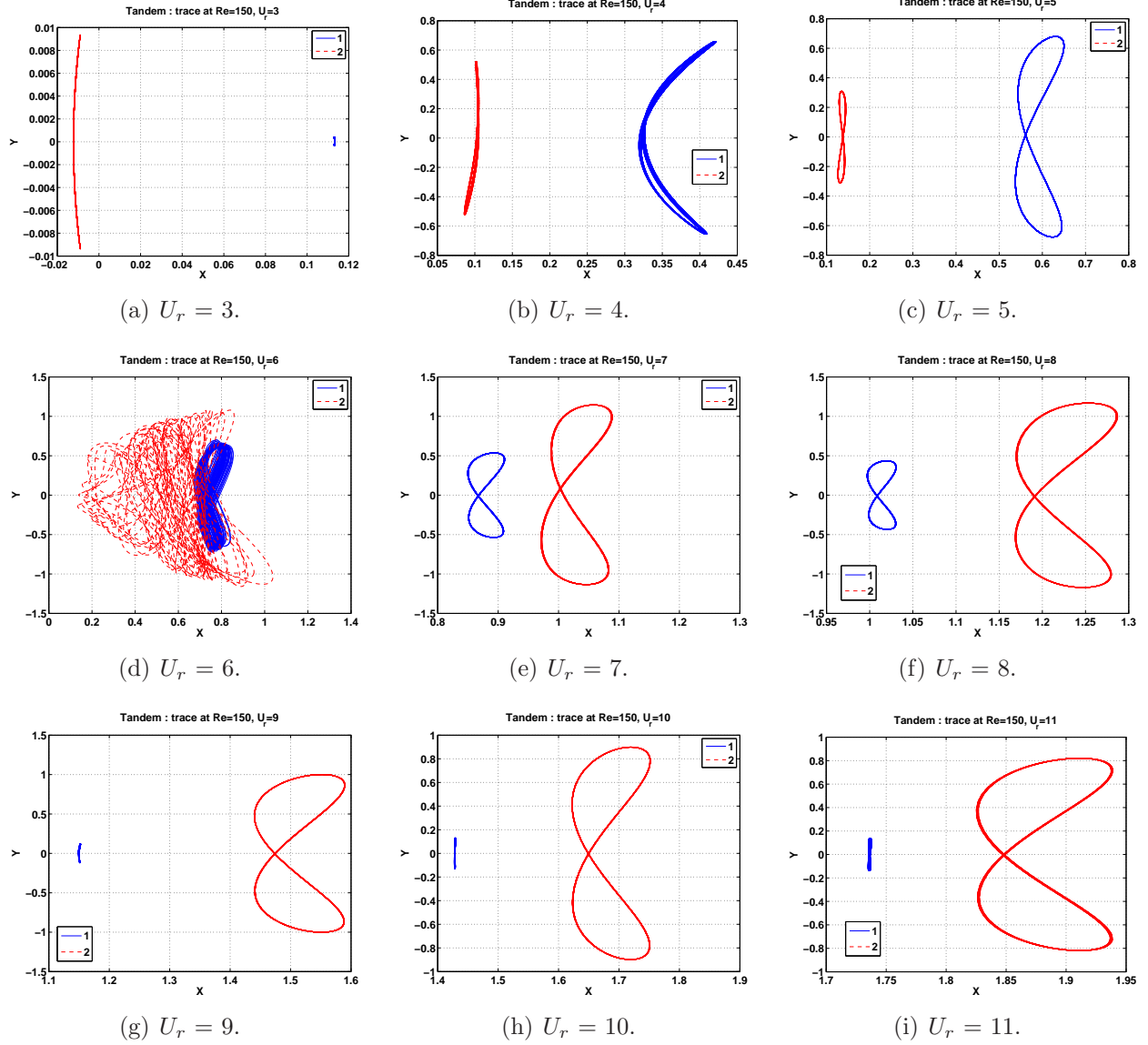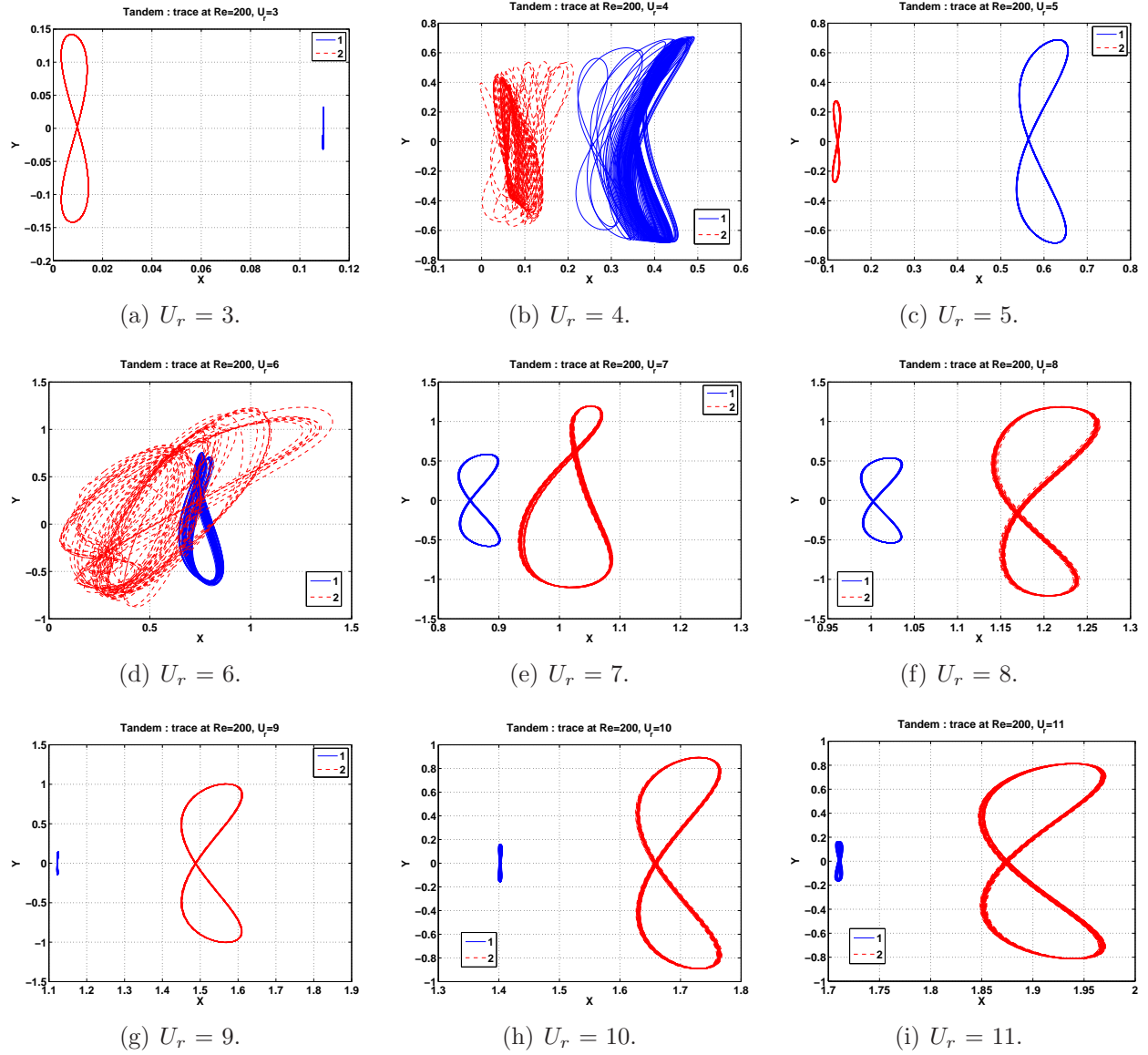
(a) $U_r = 3$.

(b) $U_r = 4$.

(c) $U_r = 5$.

(d) $U_r = 6$.

(e) $U_r = 7$.

(f) $U_r = 8$.

(g) $U_r = 9$.

(h) $U_r = 10$.

(i) $U_r = 11$.

Figure 6.17 Two cylinders in tandem : Displacement trajectories at $Re = 150$ relative to the initial positions. Upstream cylinder in blue and downstream cylinder in red.

Figure 6.18 Two cylinders in tandem : Displacement trajectories at $Re = 200$ relative to the initial positions. Upstream cylinder in blue and downstream cylinder in red.

upstream cylinder is desynchronized, the shielding provided from the upstream cylinder to the downstream cylinder reduces and hence the effective drag of the downstream cylinder increases. Similar observations can be found for the RMS of the drag and lift coefficients. Peaks occur at the locations of synchronization onset and after the upstream cylinder has desynchronized, there are large fluid dynamic forces onto the downstream cylinder. Results of all three Reynolds number studies generally follow the same trend.

The characteristics of the average force coefficients are in good agreement with those reported by Bao *et al.* (2012), especially for the upstream cylinder. Similar to the maximum oscillation amplitudes, the characteristics of the downstream cylinder again seem to be less comparable in the streamwise direction. In particular, the mean drag coefficient of their work decreases much more rapidly after the desynchronization of the upstream cylinder. At this reduced velocity range, the RMS of drag coefficient also have smaller values. This seems to go against intuitive reasoning based on the reported larger maximum streamwise amplitude at the same reduced velocity range. Possibly, the larger separation ratio of $L/D = 5$ results lead to much more complex flow patterns than those of $L/D = 4$ in the present work. Unfortunately, the time trace of neither the displacement nor the drag force is available from Bao *et al.* (2012) for further analysis.
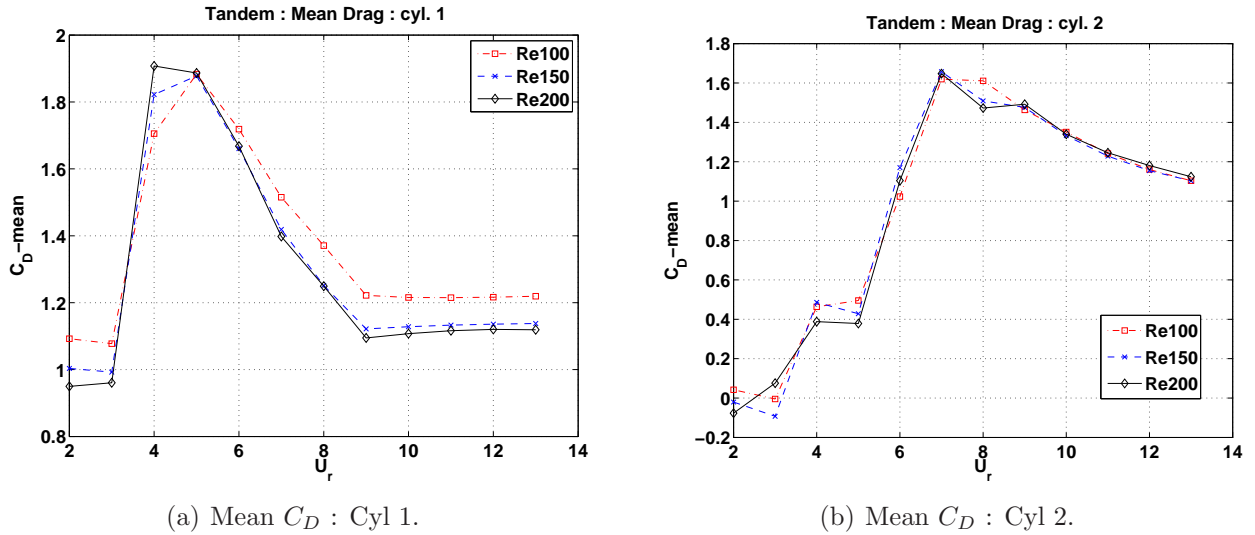

(a) Mean C_D : Cyl 1.
(b) Mean C_D : Cyl 2.

Figure 6.19 Two cylinders in tandem : Mean C_D .

Frequency responses

The power spectral density of the force fluctuations onto a freely oscillating tandem cylinder pair are shown in figures 6.21 and 6.22. The overall responses of the upstream cylinder resemble those of the isolated cylinder problem. However, the principal frequencies, especially
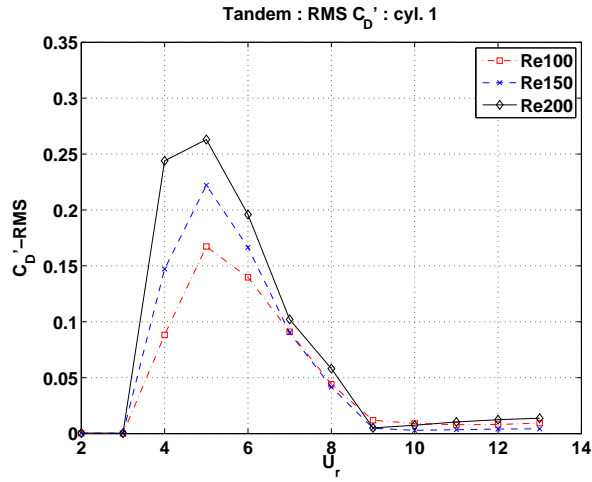
(a) RMS C_D' : Cyl 1.
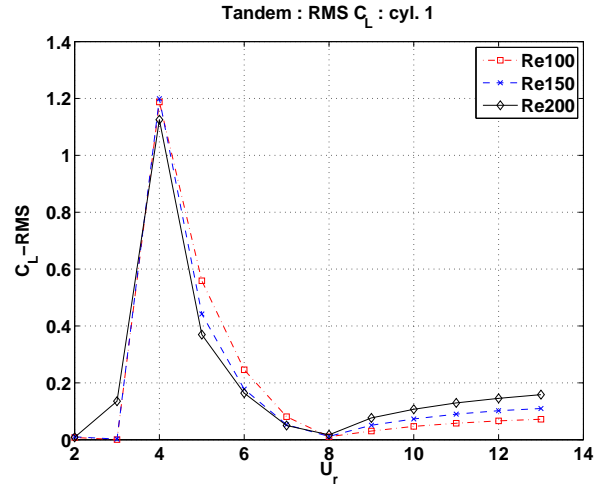
(b) RMS C_L : Cyl 1.
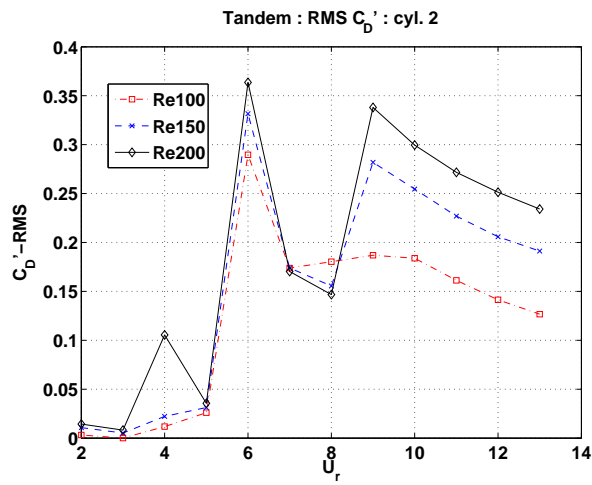
(c) RMS C_D' : Cyl 2.
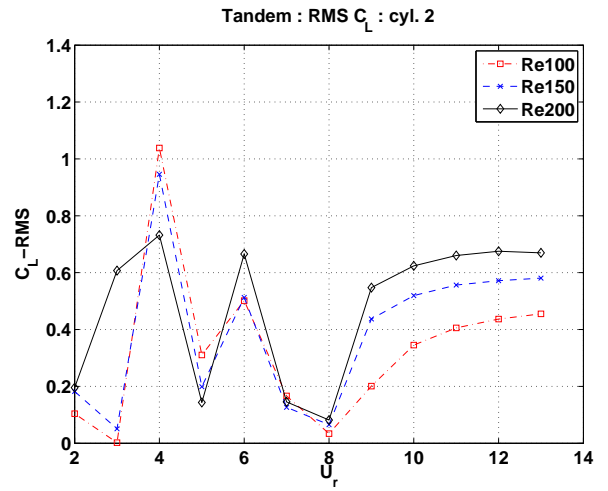
(d) RMS C_L : Cyl 2.

Figure 6.20 Two cylinders in tandem : RMS C_D' and C_L.

at the higher reduced velocity range, are noticeably lower here in the tandem case. This is true for both the drag and lift coefficients. Besides, the second harmonic component in the drag force can be observed more clearly here. When the Reynolds number is increased, the excited harmonic is also increased which is more noticeable for $Re = 200$. In figure 6.21(d), the width of the power spectral density at each U_r is clearly wider than that of the $Re = 100$ and $Re = 150$. Also, at $U_r = 6$ when the downstream cylinder begins to synchronize, there are noticeably more harmonics excited, especially in the lift force at $Re = 200$.

Next we look at the responses of the downstream cylinder. Although the maximum displacement response of the downstream cylinder is clearly different from that of the upstream, the spectral contents of the downstream cylinder are, on the other hand, very similar to those of the upstream cylinder for both the drag and lift forces. This is in accordance with the results reported by Bao *et al.* (2012) who also observed that the downstream cylinder oscillates at the same frequencies as those of the upstream cylinder. We can however see that the power spectral density of the streamwise force fluctuation are much richer than those of the transverse direction and the streamwise force fluctuation of the upstream cylinder. Comparing with the upstream cylinder, the multi-harmonic responses are now even more observable at the onset of the synchronization of the downstream cylinder at $U_r = 6$. Interestingly, while the dominant frequency of the downstream cylinder response generally follows those of the upstream cylinder and those of an isolated cylinder, the dominant frequency response of the drag coefficient at $U_r = 6$ shifts suddenly downwards to a very low value of about $f/f_n = 0.2$. The dominant frequency response of the lift force at $U_r = 6$ seems to have a minor decrease as well, although without such dramatic decrease. Lastly, the increase in Reynolds number however does not introduce any significant difference in the spectral responses for the downstream cylinder.
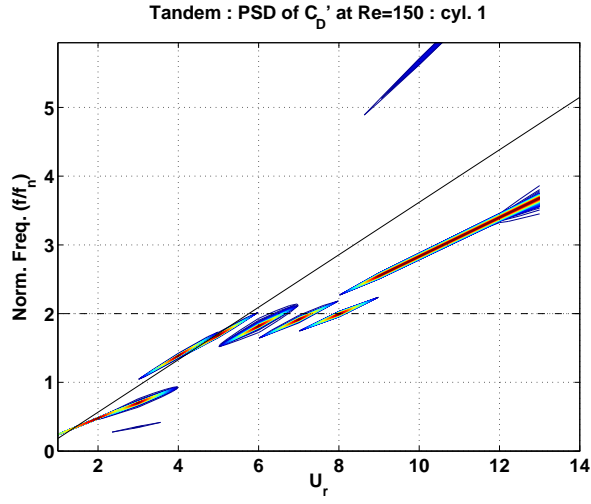
(a) $C_D^{'}$: $Re = 150$
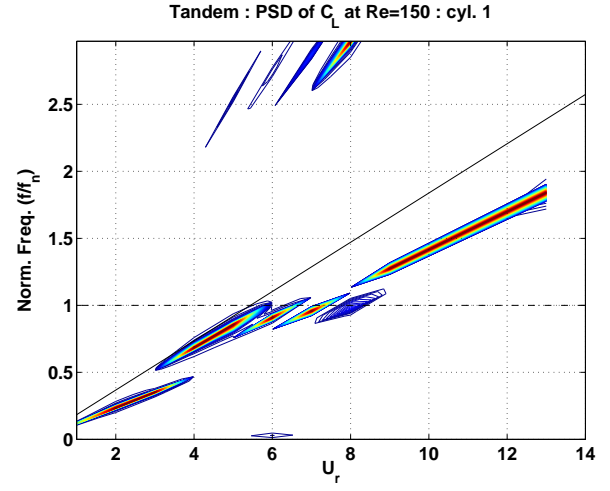
(b) C_L : $Re = 150$
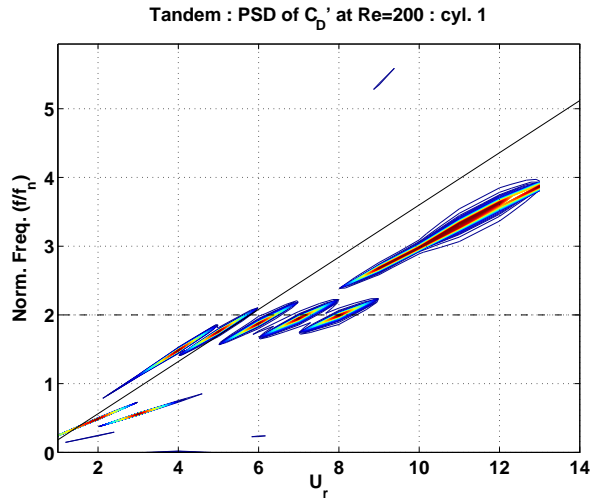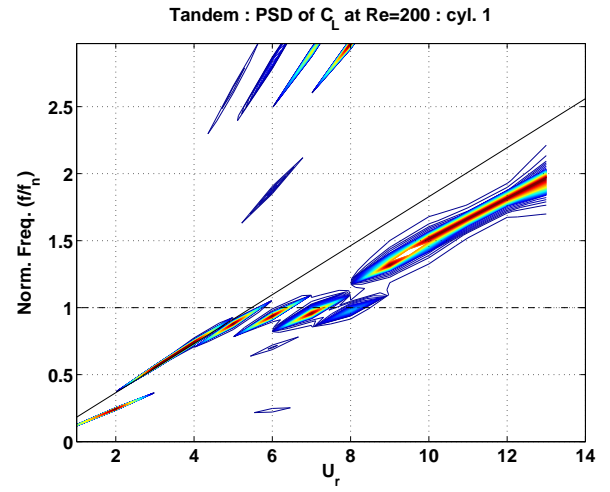
(c) $C_D^{'}$: $Re = 200$

(d) C_L : $Re = 200$

Figure 6.21 Two cylinders in tandem : PSD of $C_D^{'}$ & C_L of cyl. 1.
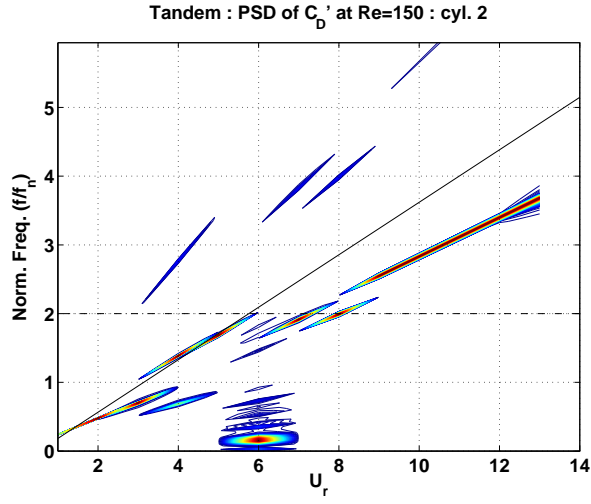
(a) $C_D^{'}$: $Re = 150$
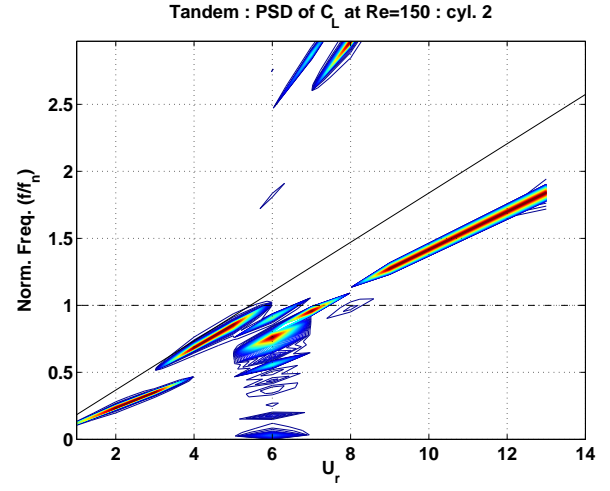
(b) C_L : $Re = 150$
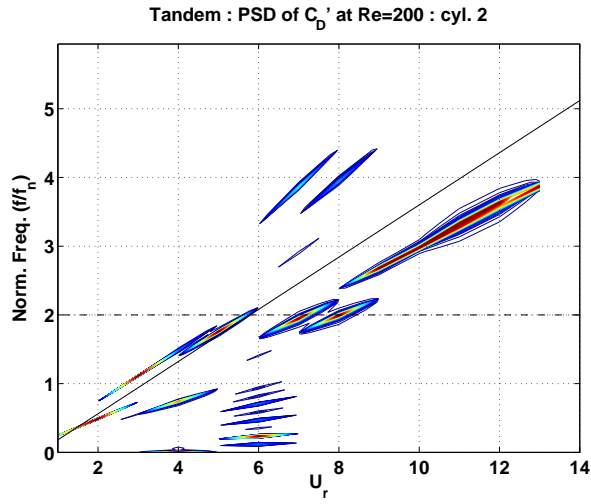
(c) $C_D^{'}$: $Re = 200$
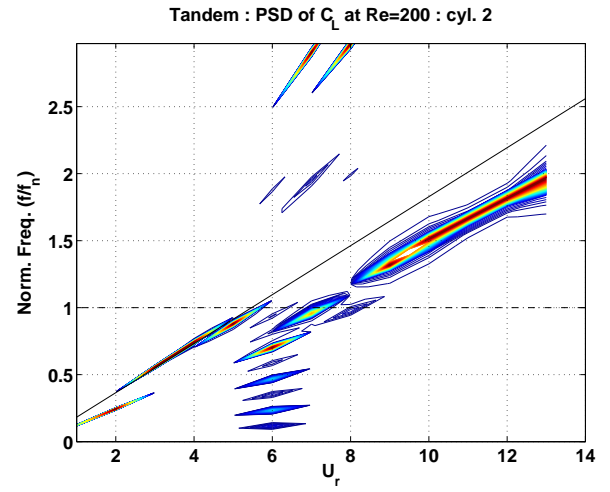
(d) C_L : $Re = 200$

Figure 6.22 Two cylinders in tandem : PSD of $C_D^{'}$ & C_L of cyl. 2.

6.5.3   Triple cylinders in-line

Here, we present the principal results for the free oscillation of three in-line cylinders.

Maximum amplitude

The maximum amplitudes of the free oscillations of three in-line cylinders are shown in figure 6.23. Overall, the maximum oscillation amplitudes have a higher level of fluctuations as compared with those of the tandem cylinder pair.

The peak transverse oscillation amplitudes of the first cylinder resemble those of the first cylinder of the tandem cylinder pair. In particular, the amplitude beyond synchronization at the higher reduced velocity range now becomes slightly larger. The peak transverse oscillation amplitude indicates that synchronization occurs between $U_r = 3$ and $U_r = 9$. In contrast, the maximum streamwise oscillation amplitudes behave rather differently. The synchronization range observed from the peak transverse oscillation amplitudes does not have any clear correspondence in the streamwise oscillation amplitudes except for $Re = 100$. The peak streamwise oscillation amplitudes for $Re = 150$ and $Re = 200$ appear to be sporadic.

Like the first cylinder, the maximum oscillation amplitudes of the second cylinder are also similar to those of the tandem cylinder pair. The maximum transverse oscillation amplitudes indicate that the synchronization starts at around $U_r = 6$ and desynchronization is not observed at $U_r = 13$. The peak values are however noticeably larger than those of the tandem cylinder pair. The maximum streamwise amplitudes also contain a large peak at around $U_r = 6$. Not only the peak values are larger, but also the profiles of the peak are wider than those of the tandem cylinder pair. Besides, only the maximum streamwise amplitude of $Re = 100$ returns to small values after the peak. For both $Re = 150$ and $Re = 200$, streamwise oscillation of rather large amplitudes ($A_X/D \approx 0.5$) are observed for the higher reduced velocity values.

The maximum oscillation amplitudes of the third cylinder show similar trends of the second cylinder. From the peak transverse oscillation amplitudes, synchronization can begin at around $U_r = 6$ to 9, and at $U_r = 13$ no desynchronization is observed. Inside the "locked-in" range, the average peak transverse amplitude reaches $A_Y/D \approx 1.5$ and the peak amplitude does not seem to decrease at the higher reduced velocity range. The maximum streamwise amplitudes of the third cylinder also contain a peak profile at around $U_r = 6$ to $U_r = 7$. The magnitudes of the peak amplitude are comparable to the second cylinder. Beyond the peak amplitude at the higher reduced velocity range, significant streamwise oscillation amplitudes are observed. At this range, the average streamwise peak amplitude reaches $A_X/D \approx 1.5$ at $Re = 150$ and $Re = 200$. The value at $Re = 100$ also reaches $A_X/D \approx 0.5$. This is in contrast

to what can be observed in the work of Oviedo-Tolentino *et al.* (2013) with $L/D = 6$ that the streamwise oscillations are at most half of those of the transverse oscillations. Certainly, this behavior in the streamwise direction greatly increases the possibility of collisions among the cylinders.

Displacement trajectories

The displacement trajectories of three freely oscillating in-line cylinders are shown in figures 6.24 to 6.26. Overall, the trajectories of the first cylinder are still similar to those of an isolated cylinder, especially for the case at $Re = 100$. When synchronized, the trajectory traces a "figure-8". Outside the synchronization range and at the onset of synchronization of the second cylinder downstream (at $U_r = 6$ to 7), the "figure-8" becomes blurry and may be asymmetric. For higher Reynolds numbers, much stronger interactions among the positions of the three in-line cylinders can be observed. The trajectories becomes blurry more often especially in the streamwise direction. The shape of the "figure-8" becomes even more asymmetric.

The trajectories of the second cylinder behave rather differently from those of the tandem cylinder pair. Only those at $Re = 100$ still trace a clear "figure-8". For both $Re = 150$ and $Re = 200$, the profiles become very blurry and skewed. They appear to be sporadic.

The trajectories of the third cylinder appear to be even more random than those of the second cylinder. The "figure-8" cannot be recognized except at the very low reduced velocity range. The large maximum oscillation amplitudes in both the streamwise and transverse directions can be clearly observed. At higher reduced velocities ($U_r > 5$), the trajectories are very distinct and behave as if they are non-periodic for all Reynolds numbers investigated. Those of $Re = 200$ at these reduced velocity range are practically random.

From the trajectories, the much stronger interactions among the three cylinders due to the presence of the third cylinder are evident. In the later section, we will show that the second and the third cylinders are subjected to forces of multiple frequencies, which directly increase the blurriness of the trajectories.

Force coefficients

The average forces onto three freely oscillating in-line cylinders are shown in figures 6.27 and 6.28. We first look at the characteristics of each cylinder individually.

As expected, the force coefficients of the first cylinder are very similar to those of the upstream cylinder of a tandem cylinder pair overall. Some differences are observed at the lower reduced velocity range ($U_r < 4$). In this range, the mean drag coefficient is slightly
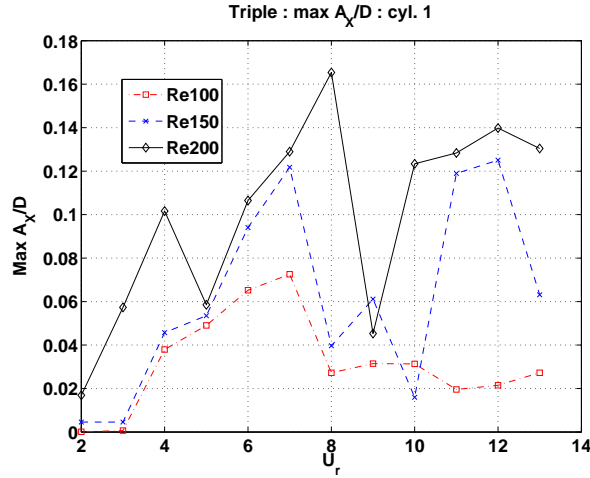
(a) Max X amplitude : Cyl 1.
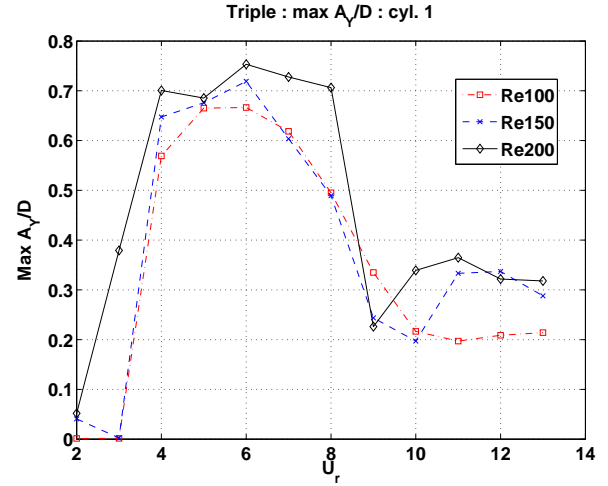
(b) Max Y amplitude : Cyl 1.
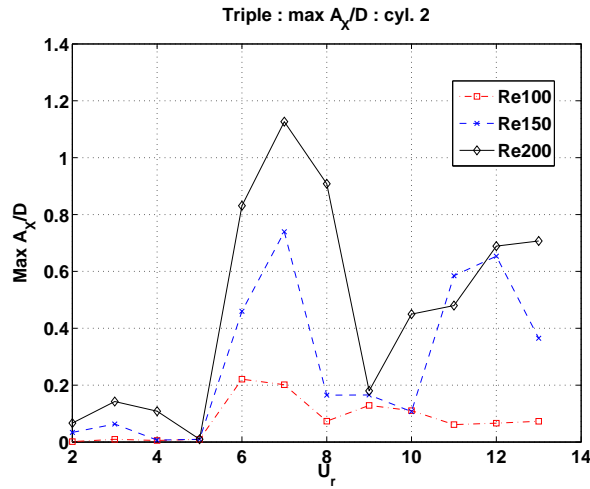
(c) Max X amplitude : Cyl 2.
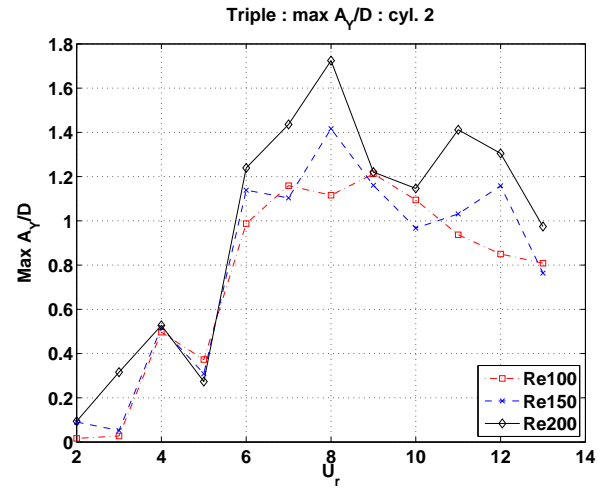
(d) Max Y amplitude : Cyl 2.
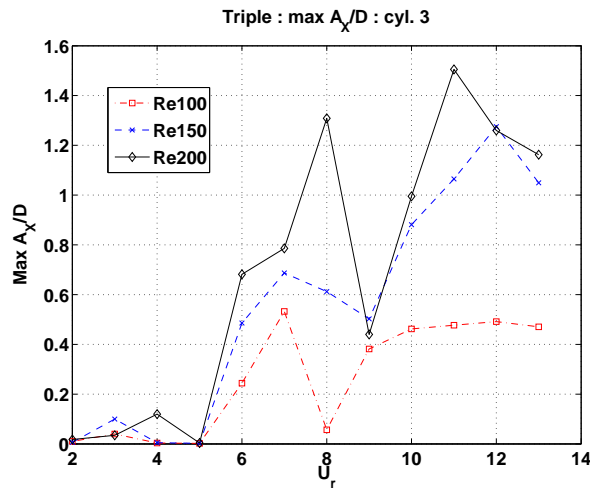
(e) Max X amplitude : Cyl 3.
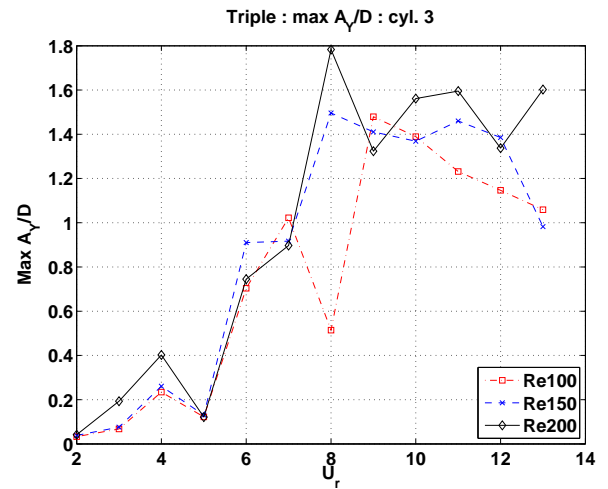
(f) Max Y amplitude : Cyl 3.

Figure 6.23 Triple cylinders in-line : Max amplitude.
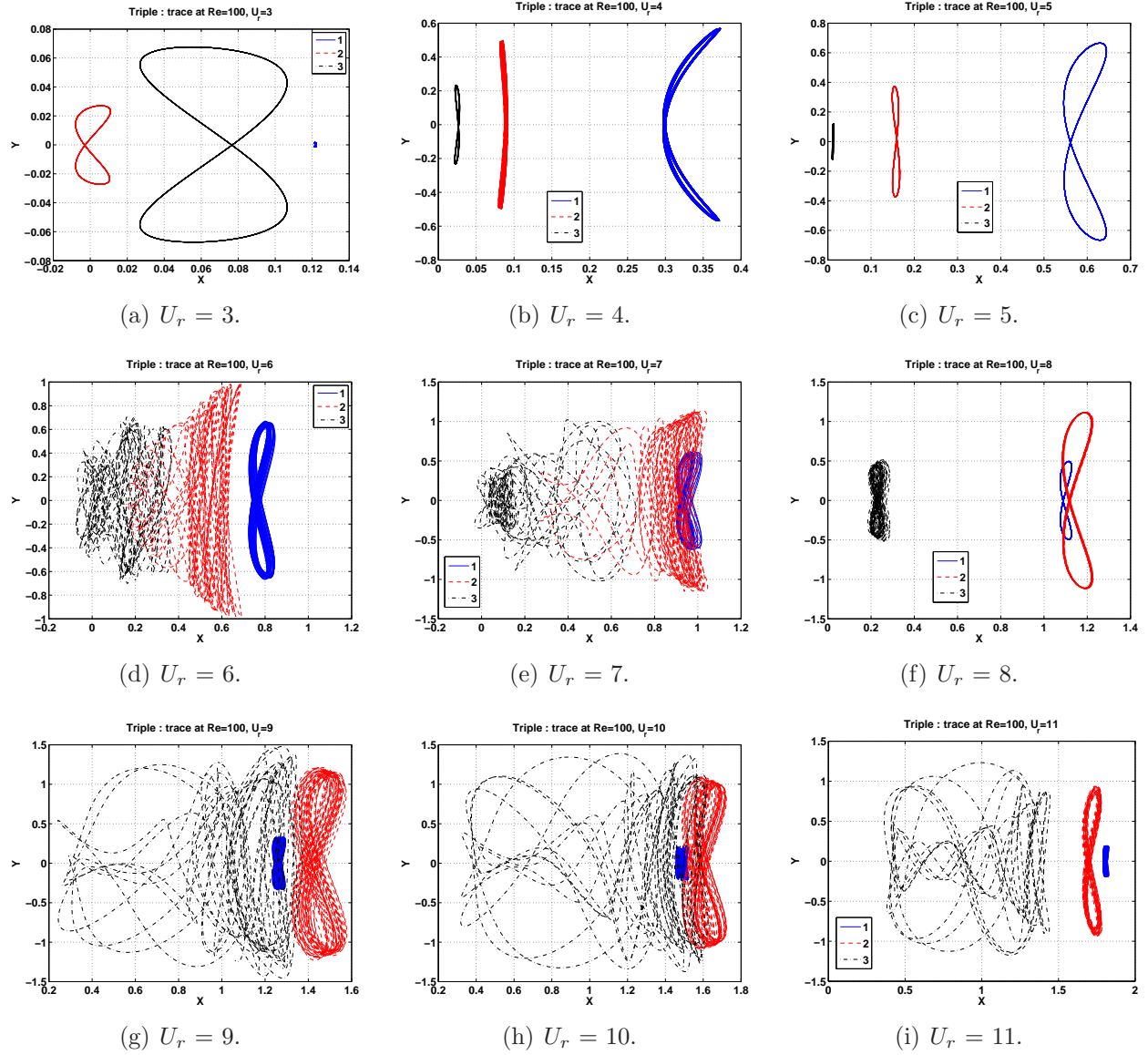
Figure 6.24 Three in-line cylinders : Displacement trajectories at $Re = 100$ relative to the initial positions. Cyl. 1 in blue, cyl 2. in red and cyl 3. in black.
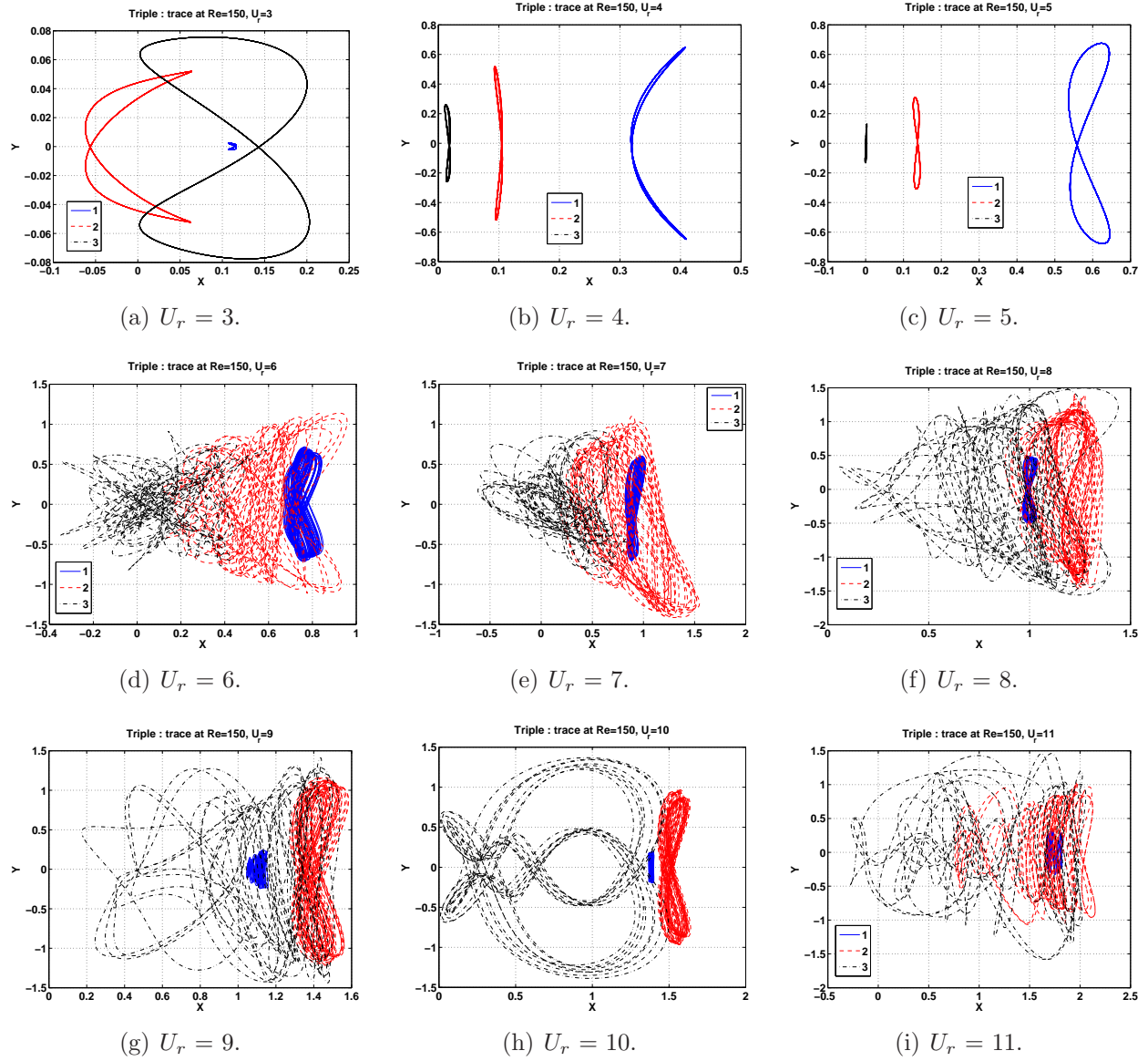
Figure 6.25 Three in-line cylinders : Displacement trajectories at $Re = 150$ relative to the initial positions. Cyl. 1 in blue, cyl 2. in red and cyl 3. in black.

Figure 6.26 Three in-line cylinders : Displacement trajectories at $Re = 200$ relative to the initial positions. Cyl. 1 in blue, cyl 2. in red and cyl 3. in black.

larger. There are also markedly higher level of force fluctuations. At higher reduced velocities, there is also higher level of drag fluctuations. The mean drag and the lift force fluctuations however do not differ significantly to those of the upstream cylinder of a tandem cylinder pair at the high reduced velocity range.
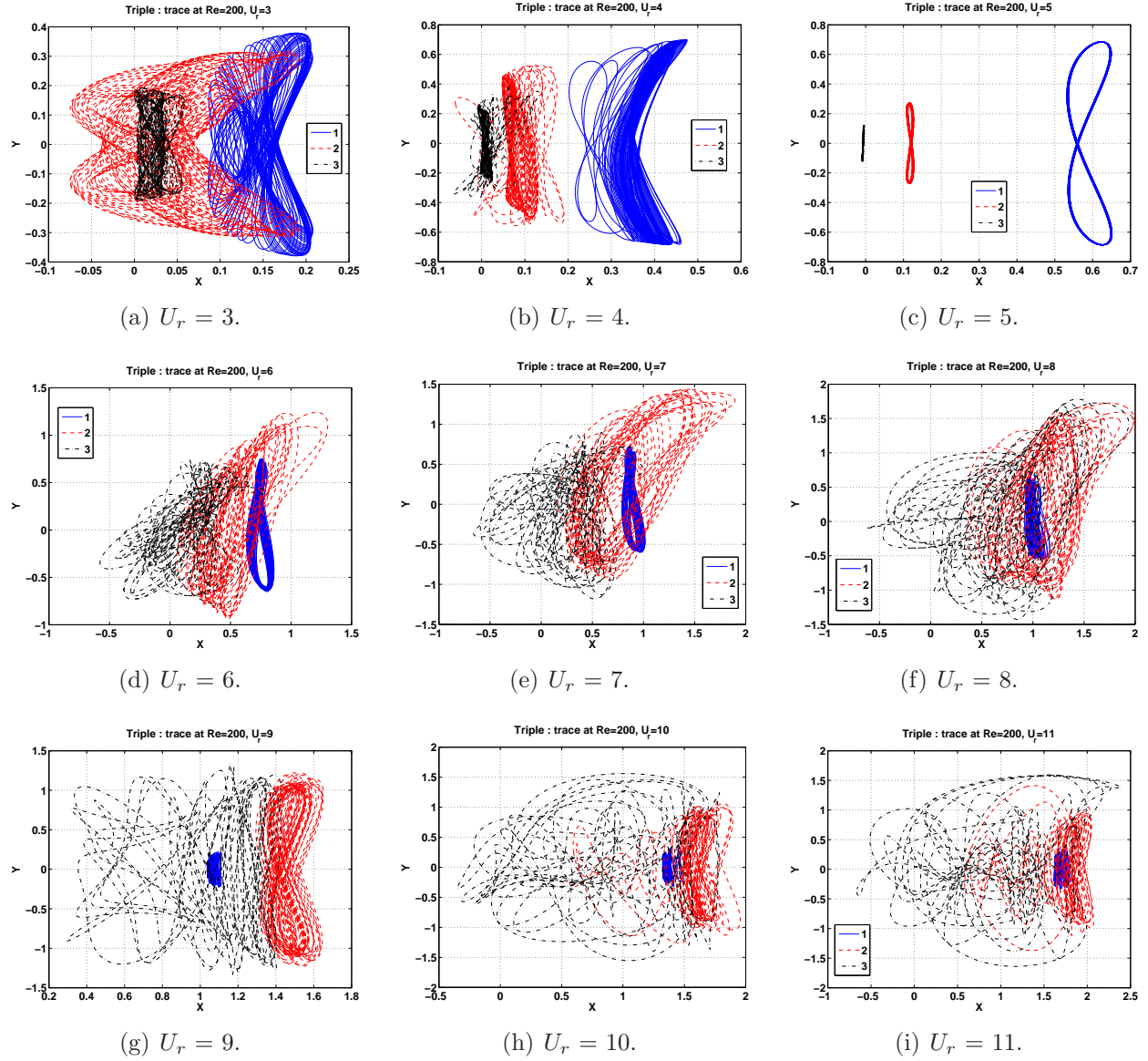
For the second cylinder, the mean drag carries rather different characteristics. The general profile becomes much rounder and wider with the peak shifted from $U_r \approx 6$ in the tandem arrangement to $U_r \approx 8$. Except for $Re = 100$, there are noticeable increases for the mean drag at low reduced velocity range ($U_r < 4$). Similar to the first cylinder, large fluctuations of the drag and lift forces can also be generally observed. This is especially noticeable at the low reduced velocity range.

The mean drag of the third cylinder resembles that of the second cylinder with the peak shifted to a higher reduced velocity. The main peak at around $U_r = 8$ ($U_r = 9$ at $Re = 100$) seems to suggest that this is the onset of synchronization of the third cylinder. At $U_r = 3$ to 4, large values of mean drag can be observed. Increasing the Reynolds number affects more significantly the mean drag at the low reduced velocities. On the other hand, the force fluctuations show much larger variations with respect to the Reynolds number. The profile appears to be more random and can only be loosely grouped into two sections separated at around $U_r = 4$ to 5. In the lower reduced velocity section, the profile generally "peaks" at around $U_r = 3$; whereas in the higher reduced velocity section, the profile is relatively "constant".

Overall speaking, the characteristics of the lift force of the three freely oscillating in-line cylinders are quite similar to those of a tandem cylinder pair. Also, the peak force coefficient magnitude of the triple cylinders case is not significantly larger than those of the tandem cylinder pair.

On the other hand, the drag force coefficients have rather different characteristics, in particular, at the low ($U_r < 4$) and the high reduced velocity ($U_r > 8$) range. Besides, the "distinct" force peaks that clearly appear in the force coefficient results of the tandem cylinder pair at the onset of the synchronization of the two cylinders respectively are completely not observable for the triple cylinders case. For which, there are much higher degrees of fluctuations. These fluctuations of the average force coefficients suggest again that the interactions of the dynamics among the three freely oscillating in-line cylinders are much stronger than those of a tandem cylinder pair. This is especially true for the second and the third cylinders.

Frequency responses

The power spectral density of the force fluctuations onto three freely oscillating in-line cylinders are shown in figures 6.29 to 6.31. We first look at the responses of the first cylinder
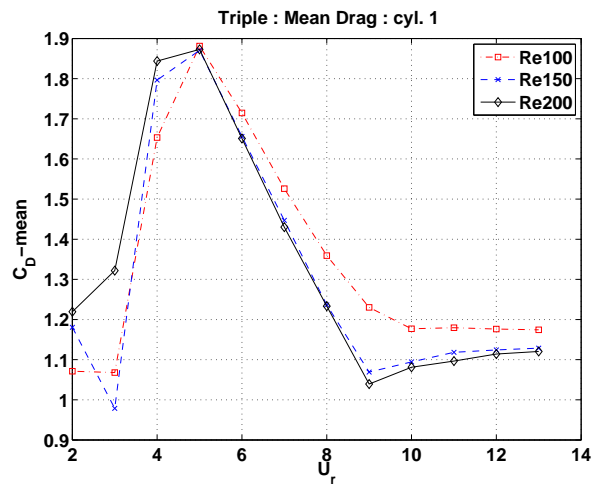
(a) Mean C_D : Cyl 1.
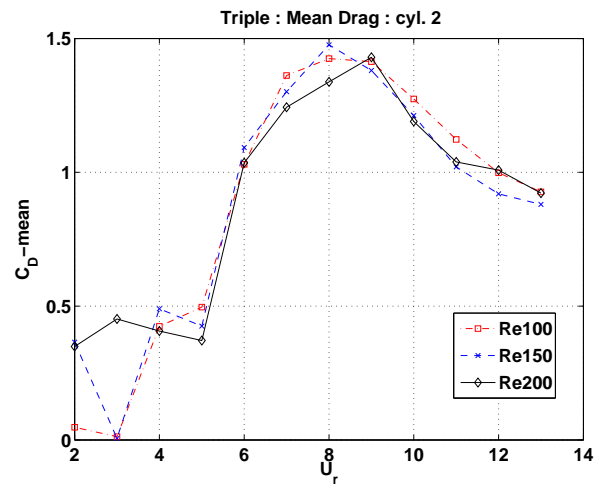
(b) Mean C_D : Cyl 2.
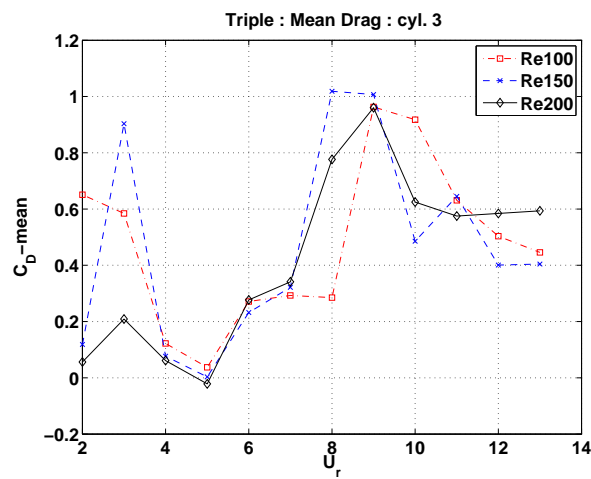
(c) Mean C_D : Cyl 3.

Figure 6.27 Three in-line cylinders : Mean C_D.
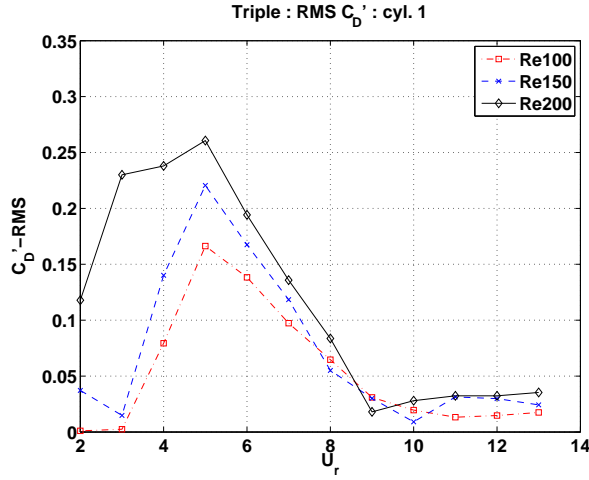
(a) RMS C_D' : Cyl 1.
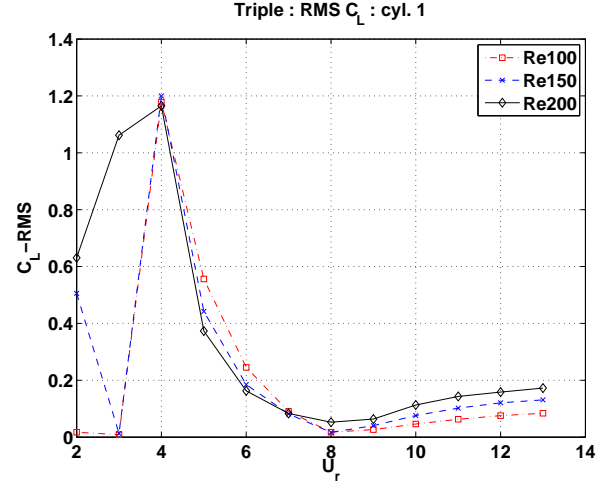
(b) RMS C_L : Cyl 1.
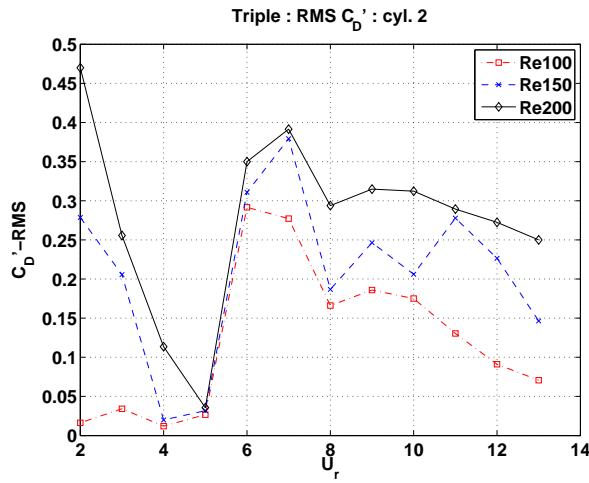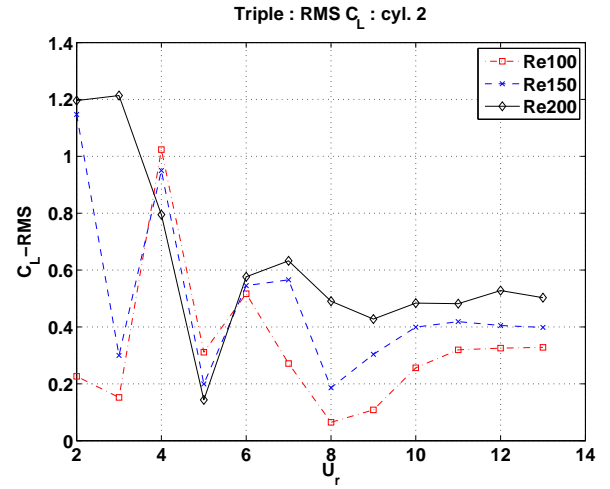
(c) RMS C_D' : Cyl 2.
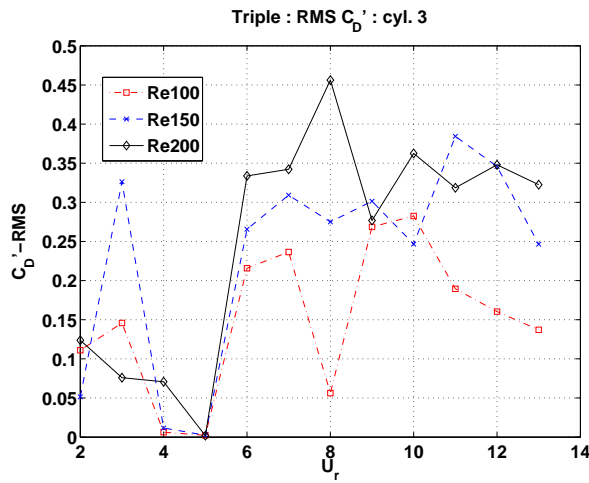
(d) RMS C_L : Cyl 2.

(e) RMS C_D' : Cyl 3.
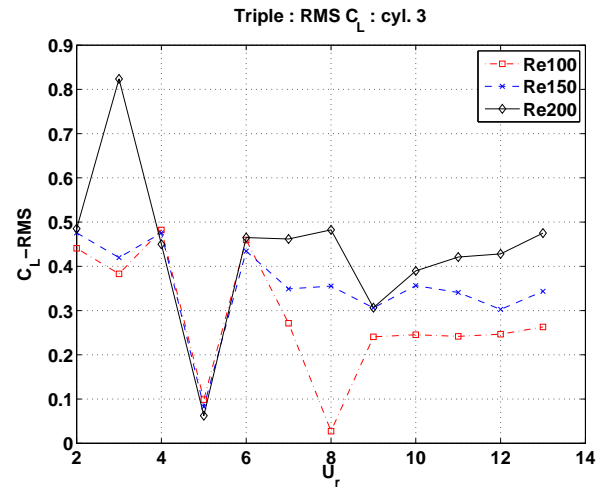
(f) RMS C_L : Cyl 3.

Figure 6.28 Three in-line cylinders : RMS C_D' and C_L.

which are shown in figure 6.29. As expected, the spectral content characteristics of the first cylinder generally resemble to those of the isolated cylinder. Similar to the tandem cylinder pair, the frequencies for both the drag and the lift forces at the higher reduced velocity section are slightly lower than those of the isolated cylinder. In contrast, the PSD of the drag force fluctuation now contains much more low frequency contents (below $f/f_n = 1$) above the reduced velocity $U_r = 6$. These low frequency contributions can be comparable to the dominant contribution (e.g. at $Re = 100$ and $U_r = 10$). Sometimes, they can even become the dominant contribution (e.g. at $Re = 150$ from $U_r = 11$ to $U_r = 12$ at about $f/f_n = 0.2$, and at $Re = 200$ from $U_r = 9$ to $U_r = 10$ at about $f/f_n = 0.25$). As the Reynolds number is increased from $Re = 100$ towards $Re = 200$, the PSD of the drag force fluctuation are notably widen at each U_r. In other words, there are more streamwise forces of different frequencies exciting at each U_r. At $Re = 150$, some low frequency contents (below $f/f_n = 0.5$) can also be observed in the PSD of the lift coefficient between $U_r = 6$ to $U_r = 9$ (figure 6.29(d)). From the same figure, we can also notice the appearance of the second harmonics of the lift coefficients, another marked difference with the response of the tandem cylinder pair. Similar to the drag coefficient spectral content, as the Reynolds number is increased, the PSD of the lift force also becomes much wider at each U_r. We can see from figure 6.29(f) that at $Re = 200$, the frequency contents of the lift coefficients are so wide at each U_r that they essentially cover the whole frequency range from $f/f_n = 0$ to $f/f_n = 3$ at the reduced velocity range from $U_r = 6$ to $U_r = 9$. In comparison with the responses of the tandem cylinder pair, it is remarkable to observe such intense frequency spectrum appear even for the first of the three in-line cylinders!

The responses of the second cylinder, which are shown in figure 6.30, are rather similar to those of the first cylinder for both the drag and lift forces similar to the tandem cylinder pair case. Likewise, the responses of the second cylinder are generally richer than those of the first one in the spectral contents across the whole reduced velocity range. The widening of the responses at each U_r can be clearly observed at the higher reduced velocity regime ($U_r > 9$). And this is especially so at around the reduced velocity of $U_r = 6$ to $U_r = 8$ when the second cylinder begins to synchronize. In contrast to the case of the tandem cylinder pair, this "widening" trend is now much more noticeable even at $Re = 100$ especially for the lift forces (figure 6.30(b))). Besides, for the second cylinder, the lower frequency content of the drag coefficient becomes noticeably "stronger". These low frequency components may become the dominant frequency contribution in a seemingly random fashion. Interestingly, when the lower frequency contents of the drag coefficient become dominant, they appear to all gather around $f/f_n = 0.1$ to $f/f_n = 0.25$ for all three studied Reynolds numbers. In figures 6.30(d) and 6.30(f), some low frequency components of the lift coefficient also become

the dominant contribution components. The dominant frequencies in these cases are close to a range from $f/f_n = 0.05$ to $f/f_n = 0.13$. Similar to the first cylinder, as the Reynolds number increases, the spectral contents of the force coefficient generally widen.

The frequency responses of the third cylinder (figure 6.31) differ from those of the second cylinder in several ways. First, the spectral responses of the force coefficients now become much richer across the range of considered reduced velocities. In particular, the PSD of the lift force coefficients are so rich that it almost covers the complete range below the boundary line from the Strouhal frequency of a fixed isolated cylinder even at $Re = 100$. Second, as the Reynolds number is increased, the widening of the spectral contents of the drag and the lift forces are much more significant. Third, in the spectral responses of the drag coefficients, the dominant frequencies are now mainly the low frequency components ($f/f_n < 1$), instead of that of the cylinder structural frequency and the Strouhal frequency of the fixed isolated cylinder. Fourth, in the spectral response of the lift coefficients, the dominant frequencies begin to "bounce" in a randomly fashion around some values close to the Strouhal frequency of a fixed cylinder, the structural frequency and the low frequency components ($f/f_n < 0.5$). Lastly, there appears more harmonics in the lift forces for $U_r > 8$.

These frequency response characteristics greatly differ from those of the tandem cylinder pair. The multiple frequencies characteristic observed is also in sharp contrast to the single oscillation frequency reported in the work by Oviedo-Tolentino et $al.$ (2013) with $L/D = 6$.

We will summarize the main features of the free oscillation of the three in-line cylinders in the following.

Summary of the free oscillations of three in-line cylinders responses

Our results show that the addition of the third cylinder behind a tandem cylinder pair introduces significantly different dynamic behaviors as compared with those of the tandem cylinder pair.

Overall, there is now a higher level of fluctuations for both the transverse and streamwise maximum oscillation amplitudes. In particular, the peak transverse oscillation amplitude is increased by about 30%. Furthermore, significant oscillations now appear in the streamwise direction at the reduced velocity above $U_r \approx 9$.

The displacement trajectories of the triple cylinders also differ greatly from those of the tandem cylinder pair. Many of the displacement trajectories of the triple cylinders can be practically described as "bounded random movements".

Regarding the force coefficients, there are again much higher degrees of fluctuations observed for the triple cylinders case.

The frequency responses of the triple cylinders case generally have a wide response range
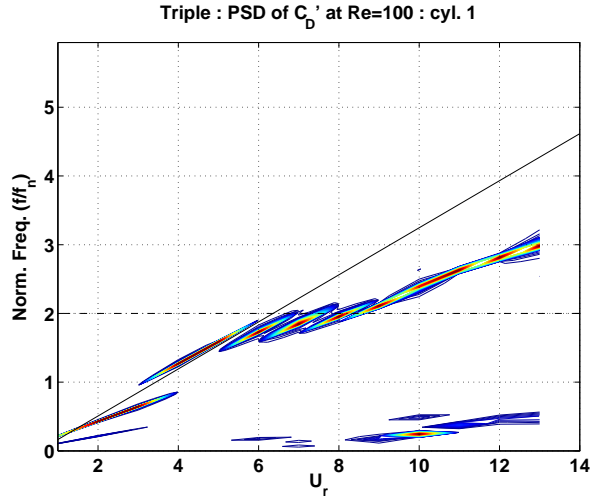
(a) C_D' : $Re = 100$
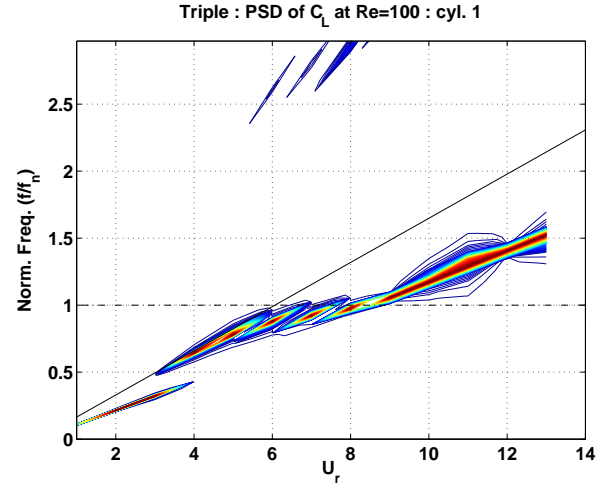
(b) C_L : $Re = 100$
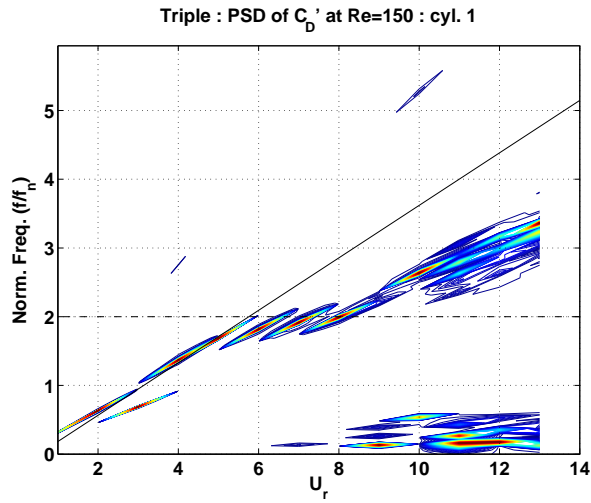
(c) C_D' : $Re = 150$
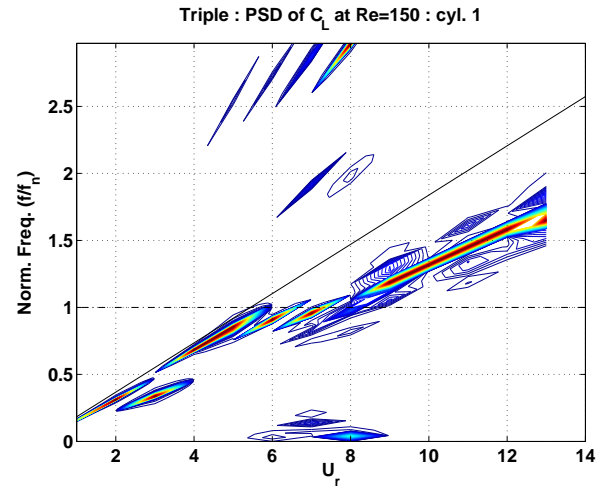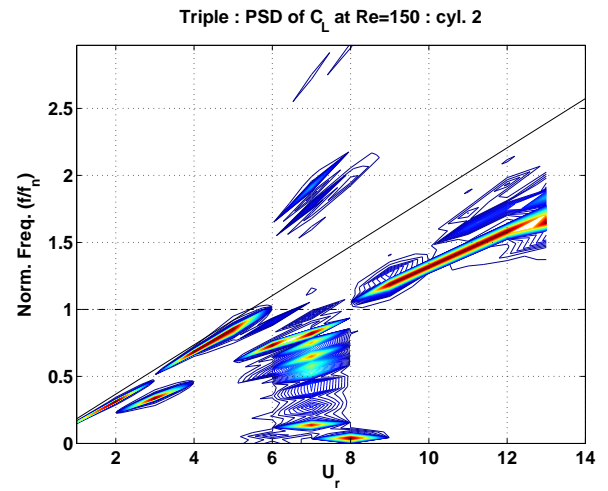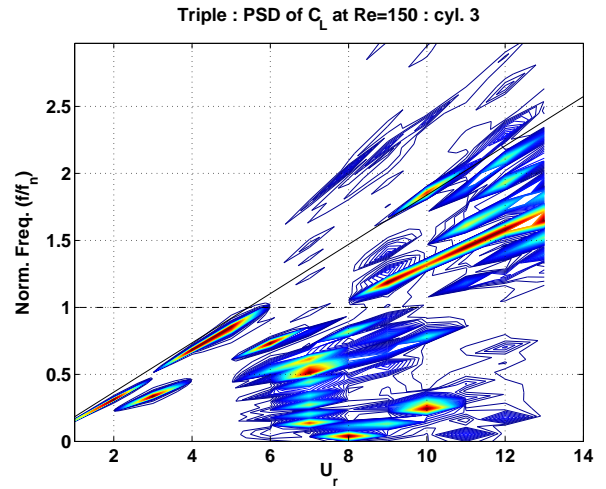
(d) C_L : $Re = 150$
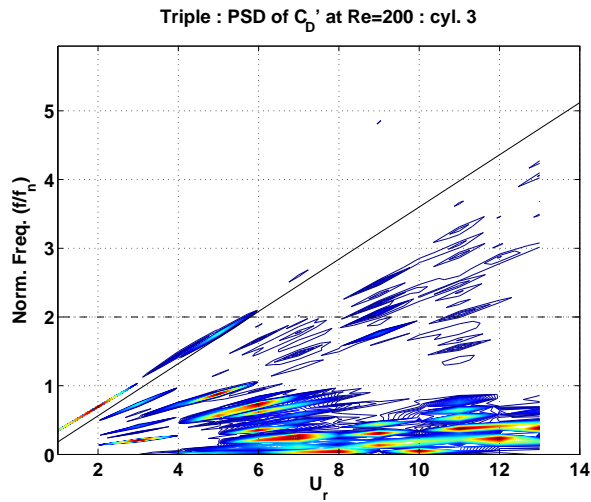
(e) C_D' : $Re = 200$

(f) C_L : $Re = 200$

Figure 6.29 Three in-line cylinders : PSD of C_D' & C_L of cyl. 1.

Figure 6.30 Three in-line cylinders : PSD of C_D' & C_L of cyl. 2.
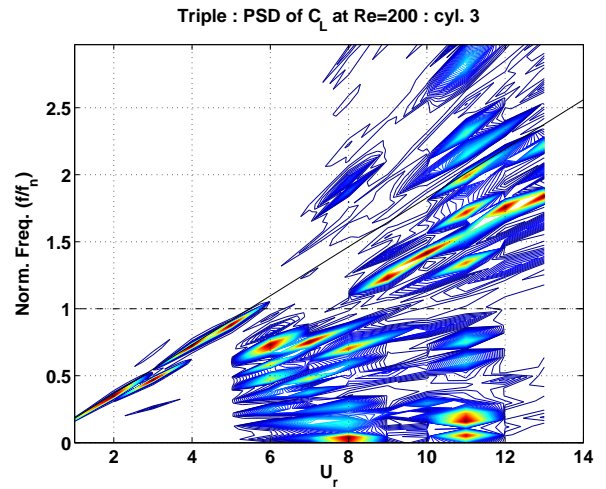
Figure 6.31 Three in-line cylinders : PSD of $C_D^{'}$ & C_L of cyl. 3.

at each reduced velocity. In other words, there are more frequencies excited for the three in-line cylinders case. In particular, the frequency responses of the third cylinder at high reduced velocities are so wide that they essentially cover the entire frequency spectrum. Another distinctive feature is that there is a clear low frequency component in the responses. This low frequency component is more observable in the streamwise direction and in some cases, it becomes the domain frequency component.

The high level of fluctuations in the maximum oscillation amplitude and the average force coefficients, especially for the second and the third cylinders, indicate that there are significant more interactions among the cylinders. The randomness in the displacement trajectories and the richness in the spectral responses seem to suggest that these stronger interactions may arise from the increase in the nonlinearity of the overall system. To examine the nature of the nonlinear dynamical behavior of three freely oscillating in-line cylinders, we look into the phase portraits and the Poincaré maps of the system in the next section.

6.5.4 Phase portrait and Poincaré map

The characteristics of nonlinear systems are often qualitatively examined by inspecting the states of the system. The phase portrait (or the phase plane) and the Poincaré map are two common tools for this purpose. The phase portrait is defined as the set of points of ($\mathbf{x}^*$, $\dot{\mathbf{x}}^*$) where $\mathbf{x}^*$ is the displacement and $\dot{\mathbf{x}}^*$ is the velocity (Moon (1992)). The Poincaré map is essentially a phase portrait filtered by certain specific guidelines which further facilitates the examination of the periodic behaviors of the system. In the following, the points on the Poincaré map are chosen for those states with the acceleration of the cylinder $\ddot{\mathbf{x}} = 0$ following Modarres-Sadeghi *et al.* (2011). In particular, we only consider those instances when the acceleration is passing from positive to negative values (Moon (1992)). Two examples of the phase portrait and the Poincaré map are given in figures 6.32 and 6.33.

The traces shown in the figures are the most typical phase portrait and Poincaré map patterns observed for the freely oscillating isolated cylinder and the tandem cylinder pair respectively. The characteristics of the freely oscillating isolated cylinder are commonly referred to as a period-1 response. On the Poincaré map, all the discrete sampling points collapse onto a single cluster.

While the phase portraits in the streamwise and the transverse directions of the freely oscillating isolated cylinder are rather similar, we can see from those of the tandem cylinder pair (figure 6.33) that this is not always the case. In particular, the characteristics shown in figure 6.33(f) are referred to as a period-2 response. There are two clusters of discrete points on the Poincaré map which indicates that there are two dominant frequency components in the system response.

(a) Phase portraits : X.

(b) Poincaré maps : X.

(c) Phase portraits : Y.
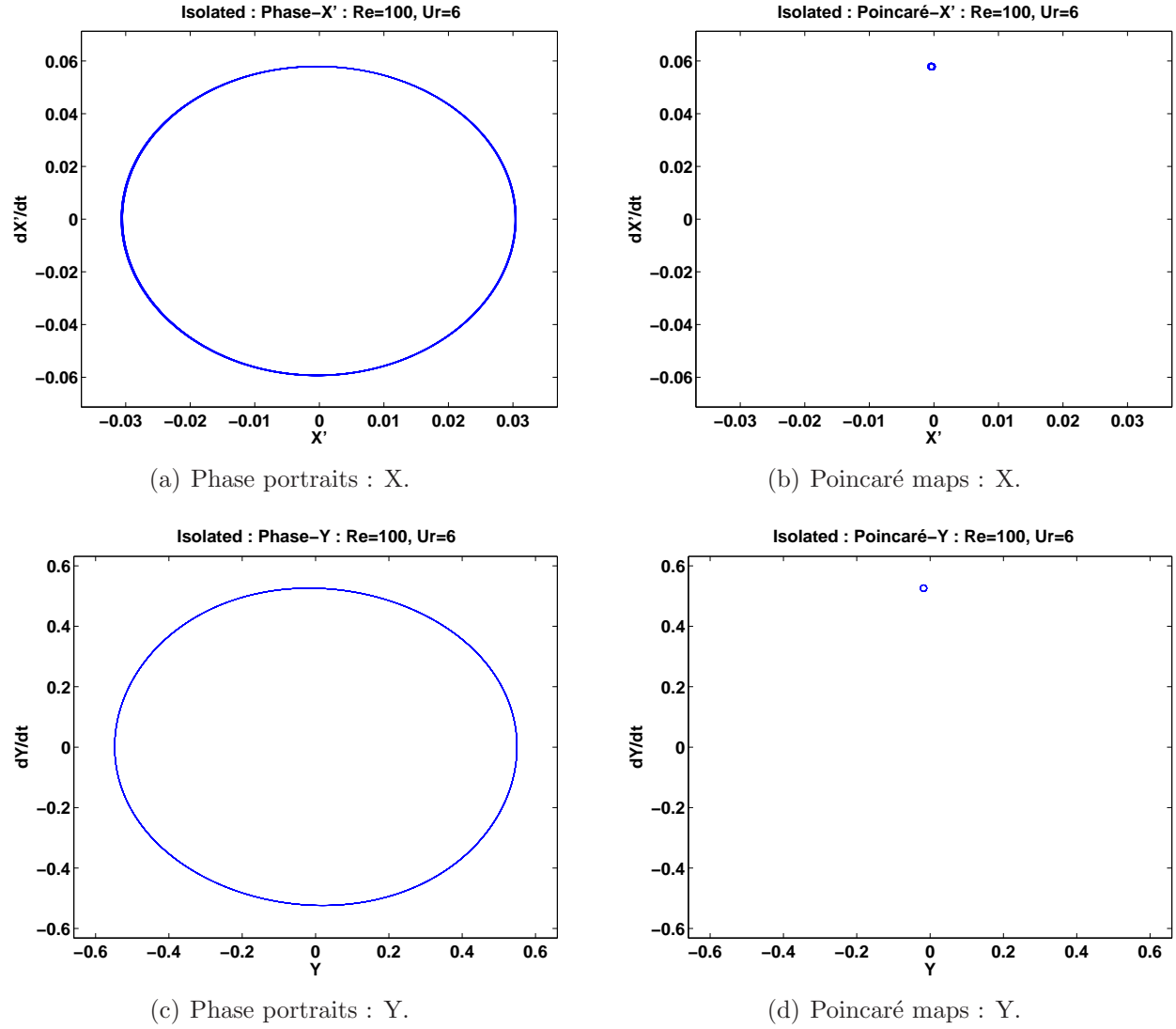
(d) Poincaré maps : Y.

Figure 6.32 Isolated cylinder : Phase portraits and Poincaré maps : At $Re = 100$, $U_r = 6$.
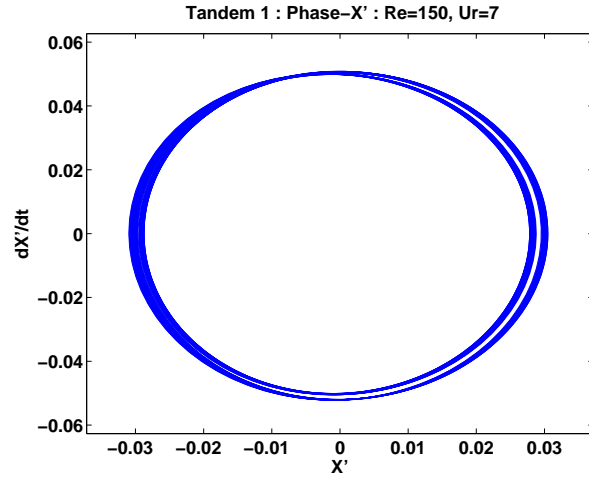
(a) Phase portraits : X : Cyl. 1.
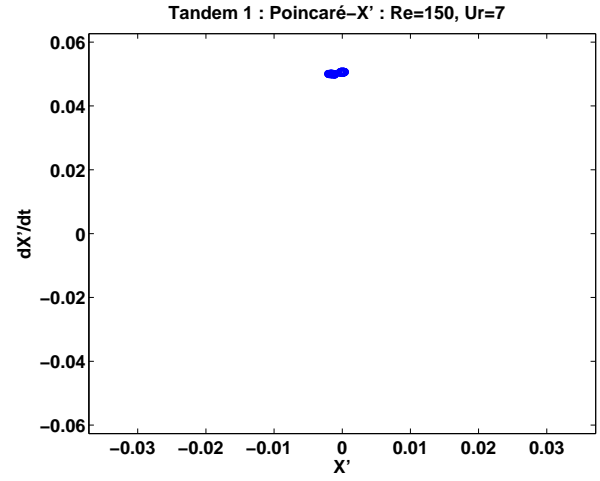
(b) Poincaré maps : X : Cyl. 1.
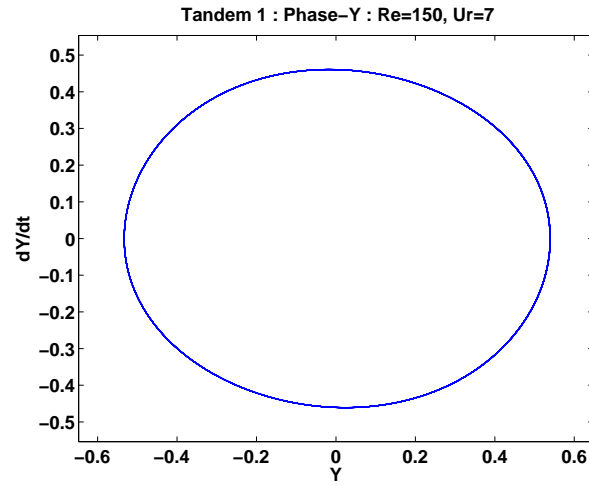
(c) Phase portraits : Y : Cyl. 1.
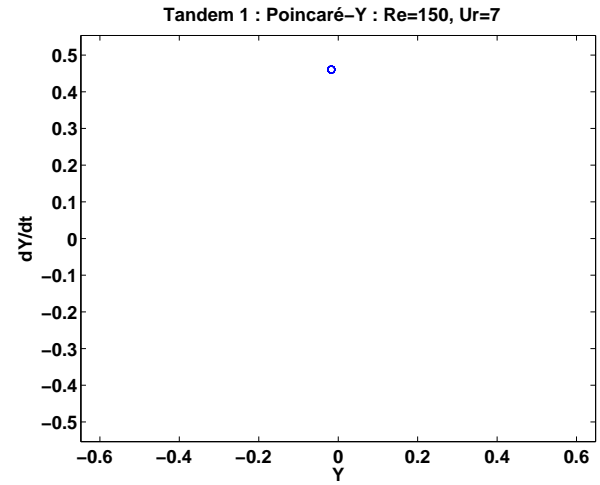
(d) Poincaré maps : Y : Cyl. 1.

Figure 6.33 Two cylinders in tandem : Phase portraits and Poincaré maps : At $Re = 150$, $U_r = 7$.
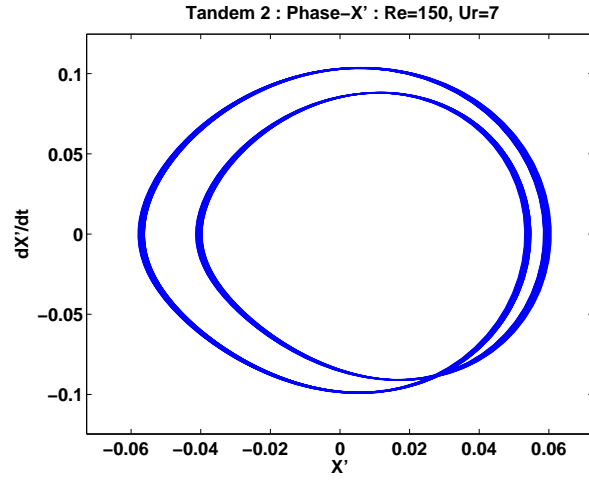
(e) Phase portraits : X : Cyl. 2.
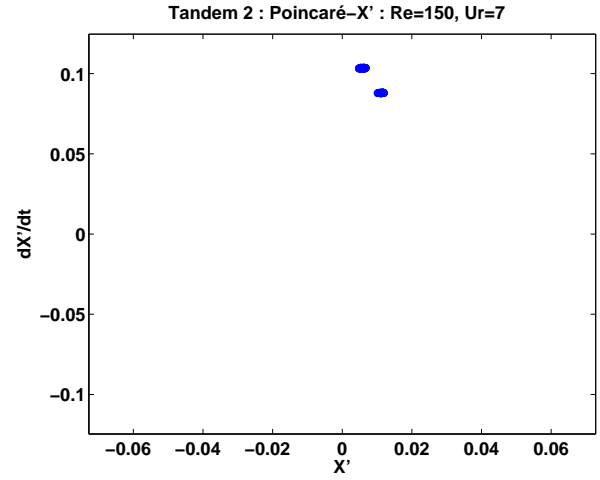
(f) Poincaré maps : X : Cyl. 2.
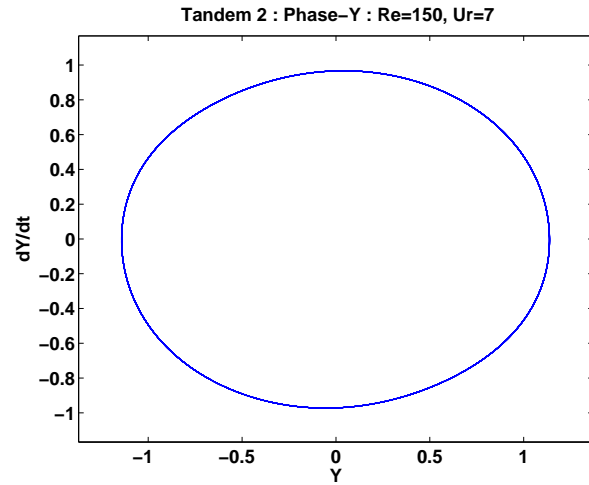
(g) Phase portraits : Y : Cyl. 2.
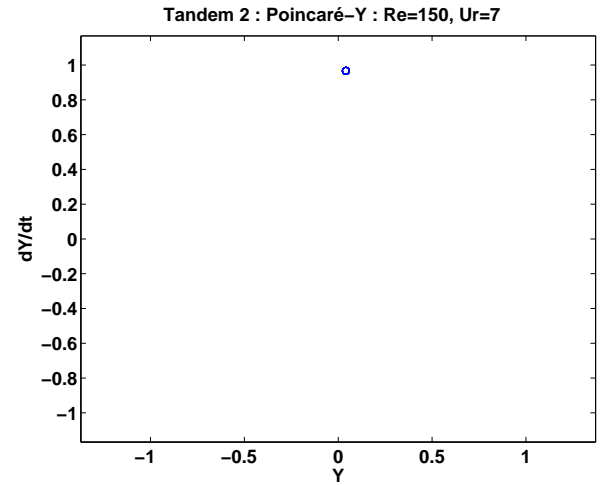
(h) Poincaré maps : Y : Cyl. 2.

Figure 6.33 Two cylinders in tandem : Phase portraits and Poincaré maps : At $Re = 150$, $U_r = 7$ (cont.).

The dynamical characteristic results of three freely oscillating in-line cylinders contains four main patterns. First, there is the period-1,2 response like those of the isolated cylinder and the tandem cylinder pair. Since the qualitative features are identical, these results are not shown here.

Secondly, there is the quasi-periodic response. For example, the response of the second cylinder at $Re = 100$ and $U_r = 6$ in the transverse direction (figure 6.34(d)). In the quasi-

(a) Phase portraits : X.

(b) Poincaré maps : X.

(c) Phase portraits : Y.

(d) Poincaré maps : Y.
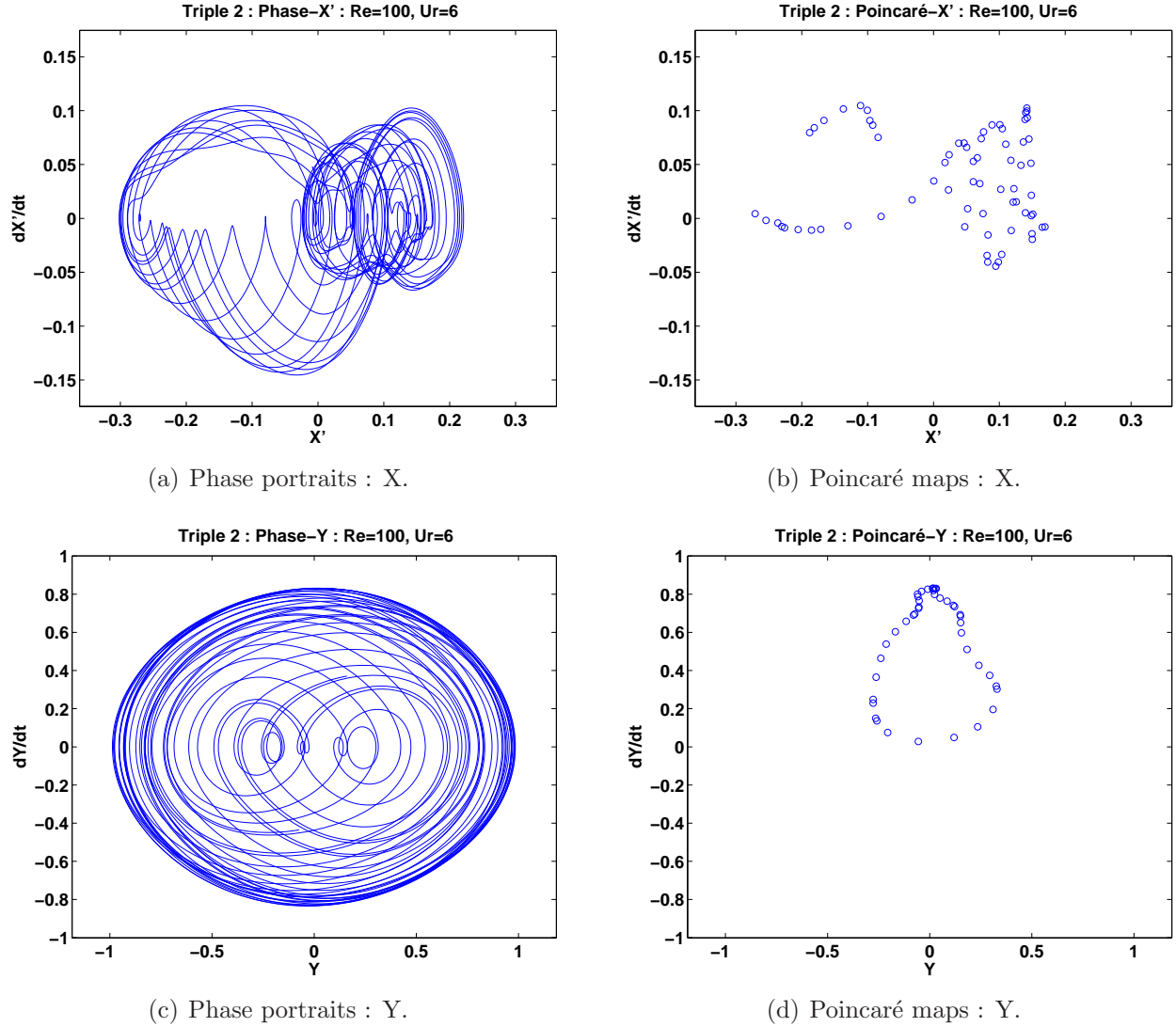
Figure 6.34 Three in-line cylinders : Quasi-periodic (Y) : Cyl. 2 : At $Re = 100$, $U_r = 6$.

periodic response, there are two (or more) incommensurate frequencies in the system response. The irrational frequency ratio causes the period to shift constantly and hence forming a loop on the Poincaré map. Here, we can see again that the streamwise and the transverse Poincaré maps are different in figure 6.34. Note that although it is less often in our results, the quasi-

periodic response can also be observed for the tandem cylinder pair. For the isolated cylinder case, a quasi-periodic like response is also observed in the streamwise direction at $Re = 150$ and $U_r = 3$.

Thirdly, there is a chaotic-like response. For example, at $Re = 200$ and $U_r = 7$, the response for the third cylinder is shown in figure 6.35. When the response is chaotic, there

(a) Phase portraits : X.

(b) Poincaré maps : X.

(c) Phase portraits : Y.
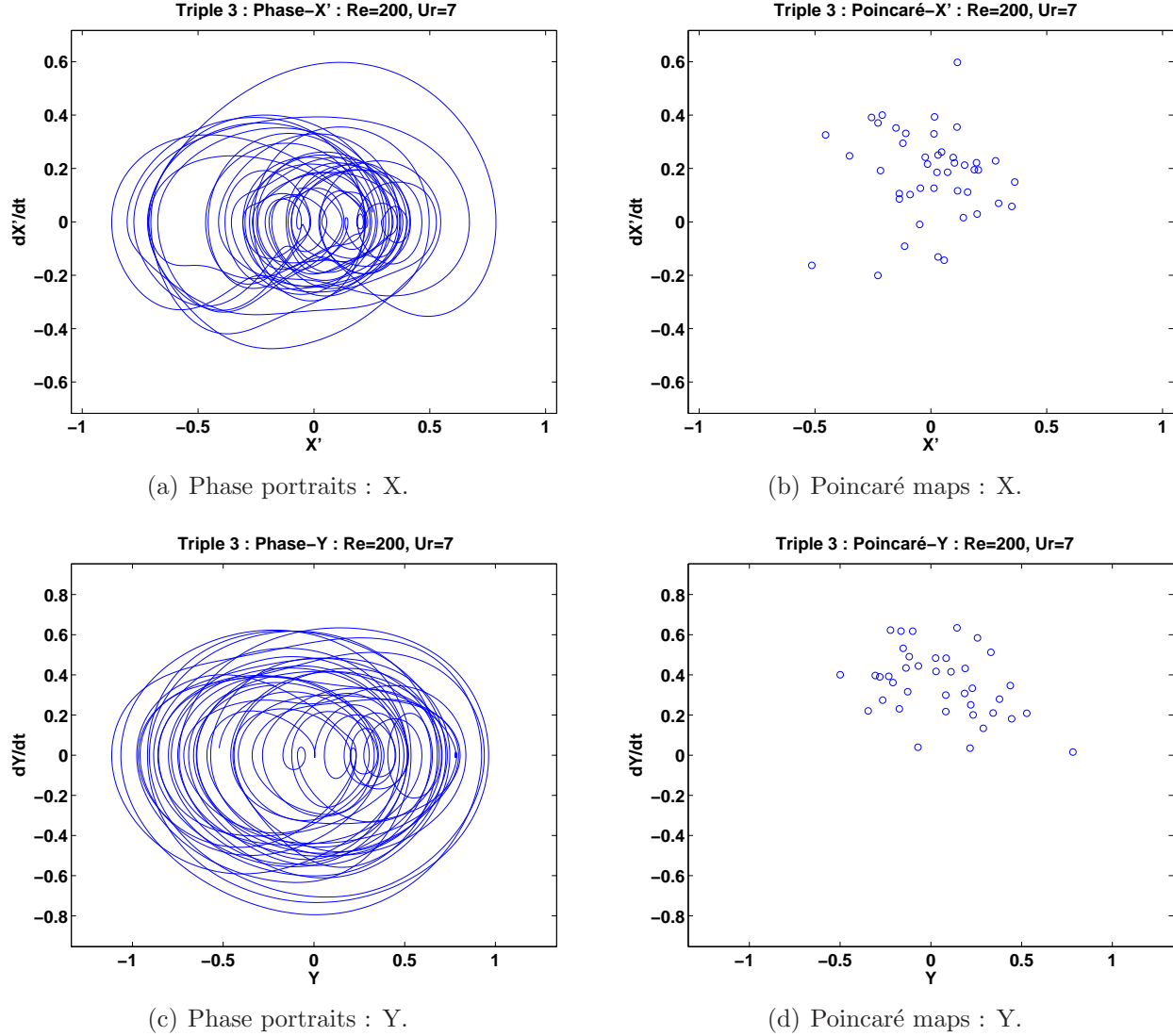
(d) Poincaré maps : Y.

Figure 6.35 Three in-line cylinders : Chaotic-like : Cyl. 3 : At $Re = 200$, $U_r = 7$.

are many frequency contributions which make the discrete sampling points of system states on the Poincaré map scatter around with no specific pattern like what is shown in figure 6.35(d). This time, both the streamwise and the transverse responses are similar. We remark that the response shown in figure 6.34 in the streamwise direction seems to contain a mixed of both the characteristics of the quasi-periodic and the chaotic motions.

Lastly, there are several higher period-n responses. Period-3, period-5 and period-6 responses can be observed. In figure 6.36, the phase portrait and the Poincaré map of the first cylinder at $Re = 150$ and $U_r = 10$ are shown. The period-5 response can be observed in figure 6.36(b) which clearly contains 5 clusters of discrete sampling points.

(a) Phase portraits : X.

(b) Poincaré maps : X.

(c) Phase portraits : Y.

(d) Poincaré maps : Y.
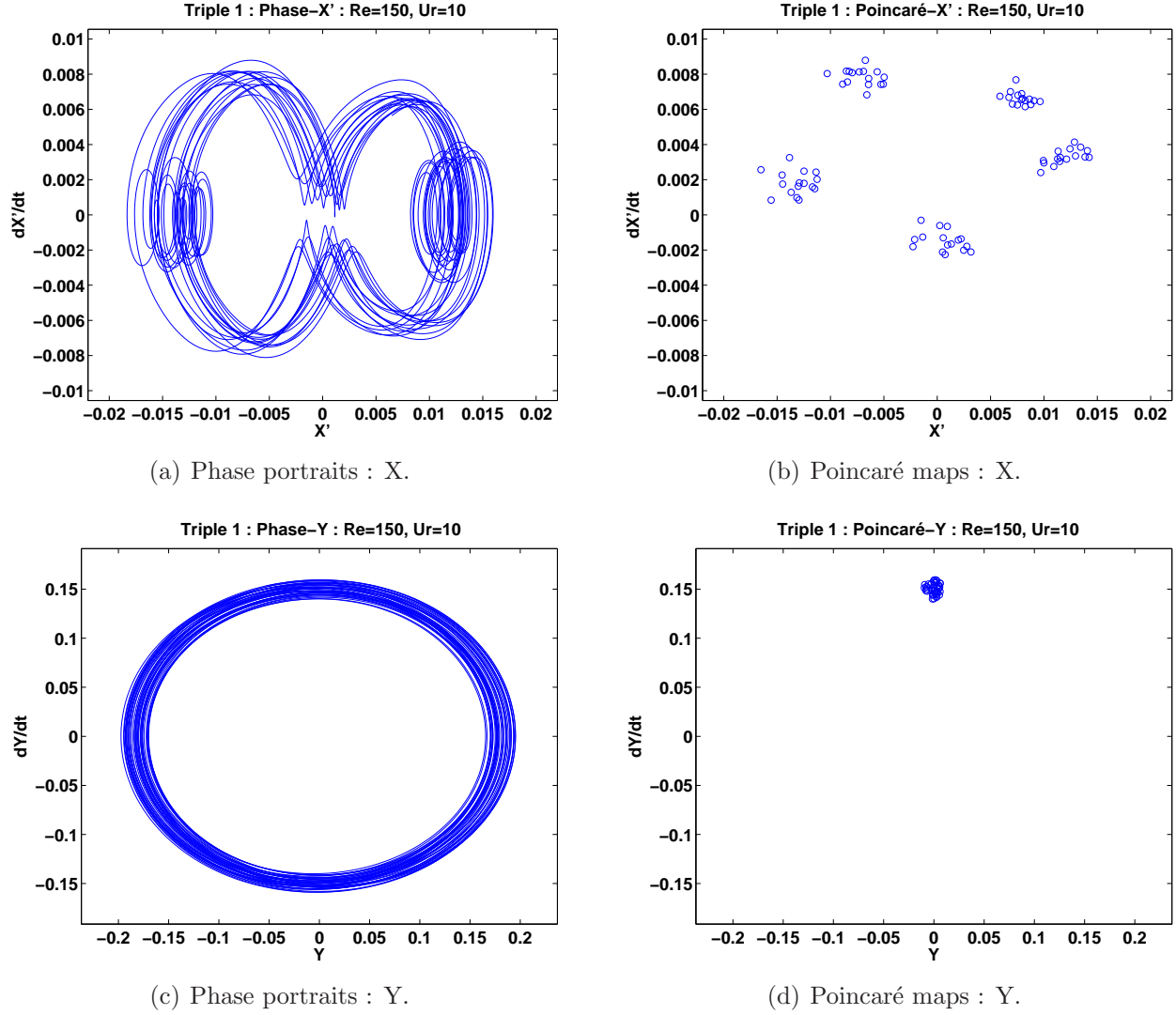
Figure 6.36 Three in-line cylinders : Period-5 (X) : Cyl. 1 : At $Re = 150$, $U_r = 10$.

In table 6.6, we summarize the characteristics of the dynamical response characteristics of three freely oscillating in-line cylinders. The corresponding results for the isolated cylinder and the tandem cylinder pair are shown in tables 6.7 and 6.8. From these tables, it is evident that the degree of nonlinearity of the triple cylinders case is significantly higher than that of the tandem cylinder pair and certainly the isolated cylinder.

Stronger nonlinearity of the three freely oscillating in-line cylinders can be observed when

the cylinders are "locked-in" as well as when the Reynolds number is increased. For the latter case, there is more energy in the flow to excite the fluid-structure system. In contrast, for the isolated cylinder and the tandem cylinders pair, the dynamical response characteristics are mainly of simple period-n types. More complex responses only appear at the reduced velocities around the onset of synchronization and desynchronization.

There seems to be a sequence for the transition of dynamical response characteristics. From a simple period-1,2 behavior, it gradually passes to the quasi-periodic motion. Sometimes higher period-n behavior may appear in between these two responses. After the quasi-periodic behavior, the motions become chaotic-like. It appears that the free oscillations of three in-line cylinders approaches to chaos via the "route of quasi-periodic behaviors" as described by Thomsen (2003).

We will now take a closer look at certain conditions which are more unique to the triple cylinders free oscillations problem. First, we will examine the results when there is an excessive streamwise oscillation for the third cylinder. From the maximum oscillation amplitude results, we see that this occurs, for example, at $Re = 150$ and $U_r = 12$. From table 6.6, at these conditions, the dynamical behaviors of the third cylinder is chaotic-like. Those of the first two cylinders are also very complex and "mostly" quasi-periodic. The responses are certainly a mix of the quasi-periodic and chaotic ones. These are in sharp contrast with those of the tandem cylinder pair at the same condition. At $Re = 150$ and $U_r = 12$, the downstream cylinder of the tandem cylinder pair exhibits excessive transverse oscillations. The dynamical characteristics for the freely oscillating tandem cylinder pair however remain more or less as simple period-n motions.

Next, we will look at the results with respect to the frequency spectrum responses. The frequency spectrum responses are generally very rich for the three freely oscillating in-line cylinders at $Re = 200$ and $U_r > 9$. We see from table 6.6 that indeed at these conditions, the dynamical behaviors of all three cylinders are mostly chaotic. Whereas for the case when there is a single dominant frequency, for example for the first cylinder at $Re = 100$ and $U_r < 9$ (figure 6.29(b)), the dynamical behaviors are generally of period-1,2 types.

Lastly, we will briefly contrast with respect to the results of the displacement trajectories of the cylinder. For the trajectories that resemble the classical "figure-8", the dynamical responses are typically of the period-1,2 types. There are some traces which seem to be systematic but not tracing the classical "figure-8". One of such conditions is at $Re = 100$ and $U_r = 6$ for the triple cylinders case (see figure 6.24(d)). In fact, the results are shown above for the second cylinder in figure 6.34. The dynamical behaviors are of those of the quasi-periodic system. Finally, there are the trajectories that are asymmetric, blurry and/or practically random. For example, for the triple cylinders case at $Re = 200$ and $U_r = 8$

(figure 6.26(f)). For such cases, there is at least in one direction the chaotic-like dynamics.

The phase portraits and the Poincaré maps complement the results in the previous sections and confirm the significant increase of nonlinearity of the free oscillations of three in-line cylinders as compared with the tandem cylinder pair. In our idealized numerical model of the fluid-structure system, the nonlinearity of the system can only arise from the fluid domain. To gain further insights into the nonlinear dynamical behaviors, we examine the vortical structure patterns in the next section.

6.5.5 Vortical structure patterns

Some vortical structure patterns of three freely oscillating in-line cylinders at $Re = 150$ are shown in figure 6.37. Overall, the vortex shedding patterns are very complex, except for those at lower reduced velocities. From table 6.6, we see that the dynamical characteristics of three freely oscillating in-line cylinders at $Re = 150$ contain all the four main patterns of dynamics. Also, the patterns are distributed in a rather even manner across the reduced velocity. Thus, the vortical structure patterns at $Re = 150$ shall be able to provide a nice contrast to the fluid-structure system dynamics results. In the following, we will denote the vortex based on the cylinder from which the vortex is formed. For example, C1-vortex refers to a vortex formed behind the first cylinder.

The vortex shedding pattern at $U_r = 2$ is shown in figure 6.37(a). From table 6.6, we can observe the P-1 and P-2 types dynamical characteristics for all three cylinders at $U_r = 2$. The pattern is relatively simple. The C1-vortices are shedded alternatively one at a time on each side. They impinge onto the front of the second cylinder and they merge with the C2-vortices. The C2-vortices are shedded with a wider base and they organize themselves into two rows: one above and one below the third cylinder. In other words, the C2-vortices do not impinge onto the front of the third cylinder, but simply passing along the side. This is perhaps the cause of the C3-vortices being rather weak. The C3-vortices, though weak, nevertheless merge with the C2-vortices on the side. Behind the three cylinders, the vortex shedding pattern look quite similar to that of the coalesced 2S pattern of a single freely oscillating isolated cylinder at low Reynolds numbers.

In figure 6.37(b), the vortex shedding pattern at $U_r = 4$ is shown. From table 6.6, we see that the dynamical characteristics are mainly of the P-1 and P-2 types for the three cylinders in general, except in the streamwise direction of the third cylinder where we can observe a quasi-periodic type characteristic. Note that the maximum streamwise displacement is actually very small for the third cylinder at $U_r = 4$. At this reduced velocity, we essentially only have the first cylinder synchronized. From figure 6.37(b), we see that the C1-vortices are shedded with a wide base due to the transverse oscillation. Both the second and the

Table 6.6 Triple : Dynamical characteristics : Period-# (P-#), quasi-periodic (QP), chaotic (C), * = most likely.

U_r	$Re = 100$						$Re = 150$						$Re = 200$					
	X_1	Y_1	X_2	Y_2	X_3	Y_3	X_1	Y_1	X_2	Y_2	X_3	Y_3	X_1	Y_1	X_2	Y_2	X_3	Y_3
2	P-2*	P-1	P-2*	P-1	P-2*	P-1	P-1*	P-1	P-1*	P-1	P-2*	P-1	P-1*	P-1	P-1*	P-1	P-1*	P-1*
3	P-2*	P-1	P-2*	P-1	P-1	P-1	P-2*	P-1	P-2	P-1	P-2	P-1	QP-2*	QP	QP	QP*	QP*	QP
4	QP*	P-1	P-2*	P-1	QP*	P-1	P-2*	P-1	P-2*	P-1	QP-2*	P-1	QP-2*	QP*	QP*	QP*	P-2*	P-1*
5	P-1*	P-1	P-2	P-1	QP-2	P-1*	P-2	P-1	P-2	P-1	QP-2*	P-1*	P-1*	P-1	QP*	P-1	C*	P-1*
6	QP*	P-1*	C*	QP	C	QP	QP*	QP*	C	QP	C	C	QP*	P-1*	C*	QP*	C	C
7	QP*	P-1*	C*	QP*	C*	QP*	QP-2*	QP*	C	QP	C	C	C*	QP*	QP*	QP	C	C
8	P-1*	P-1	P-1*	P-1	C	P-1*	C*	P-1*	QP*	QP*	C	C*	C*	QP*	P-3*	QP*	C	C
9	QP	P-1*	QP*	P-1*	QP*	QP*	C	QP*	QP*	QP*	C	C*	C	QP-2*	QP*	P-1*	C	QP*
10	QP	QP*	QP*	P-1*	QP	QP	P-5	QP*	QP*	P-2*	P-3	P-5	C*	QP*	QP*	QP*	C	C
11	QP	QP*	QP*	QP*	QP	QP	QP	QP*	QP	QP*	QP*	QP*	C*	C*	QP*	C*	C	C
12	QP	QP*	QP*	QP*	QP	QP	QP	QP*	QP*	QP-2*	C	C	QP*	QP*	QP	QP*	C	QP*
13	QP	QP*	QP	QP*	QP	QP	QP-2*	QP-2*	QP-2	QP-2*	QP-2*	QP*	QP*	P-4*	QP*	P-3*	QP-2*	P-5*

Table 6.7 Isolated cylinder : Dynamical characteristics : Period-# (P-#), quasi-periodic (QP), chaotic (C), * = most likely.

U_r	$Re = 100$		$Re = 150$		$Re = 200$	
	X	Y	X	Y	X	Y
2	P-1	P-1	P-1	P-1	P-1	P-1
3	P-1*	P-1	QP*	P-6*	QP*	QP*
4	P-1	P-1	P-1	P-1	P-2	P-1
5	P-1	P-1	P-1	P-1	P-1	P-1
6	P-1	P-1	P-1	P-1	P-1	P-1
7	P-1	P-1	P-1	P-1	P-1	P-1
8	P-1	P-1	P-1	P-1	P-2	P-1
9	P-1*	P-1	P-1*	P-1	C	QP*
10	P-1*	P-1	P-1*	P-1	P-1*	P-1*
11	P-1*	P-1	P-1*	P-1	P-1*	P-1
12	P-1*	P-1	P-1*	P-1	P-1*	P-1
13	P-1*	P-1	P-1*	P-1	P-1*	P-1

Table 6.8 Two cylinders in tandem : Dynamical characteristics : Period-# (P-#), quasi-periodic (QP), chaotic (C), * = most likely.

U_r	$Re = 100$				$Re = 150$				$Re = 200$			
	X_1	Y_1	X_2	Y_2	X_1	Y_1	X_2	Y_2	X_1	Y_1	X_2	Y_2
2	P-2*	P-1	P-2*	P-1	P-2*	P-1	P-2*	P-1	P-2*	P-1	P-2*	P-1
3	P-1*	QP*	P-2*	QP*	P-2*	P-1	P-2*	P-1	P-2*	P-1	P-2*	P-1
4	P-2	P-1	P-2*	P-1	P-2	P-1	P-2	P-1	QP*	P-1*	QP*	P-1*
5	P-2	P-1	P-2	P-1	P-2	P-1	P-2	P-1	P-2	P-1	P-2*	P-1
6	QP*	P-1*	QP*	QP	QP*	P-1*	C	QP	QP*	P-1*	QP*	P-3*
7	P-1*	P-1	QP*	P-1	P-2	P-1	P-2	P-1	P-2*	P-1	P-2	P-1
8	P-2	P-1	P-2	P-1	P-2	P-1	P-2	P-1	P-2*	P-1	P-2	P-1
9	P-2*	P-1	P-2	P-1	P-2*	P-1	P-1*	P-1	P-2*	P-1	P-1*	P-1
10	P-2*	P-1	P-2	P-1	P-2*	P-1	P-1*	P-1	C*	P-1	P-1*	P-1
11	P-2*	P-1	P-2	P-1	P-2*	P-1	P-1*	P-1	QP*	P-1	P-1*	P-1
12	P-2*	P-1	P-2	P-1	P-2*	P-1	P-1*	P-1	QP*	P-1	P-1*	P-1
13	P-2*	P-1	P-2	P-1	P-2*	P-1	P-1*	P-1	QP*	P-1	P-1*	P-1
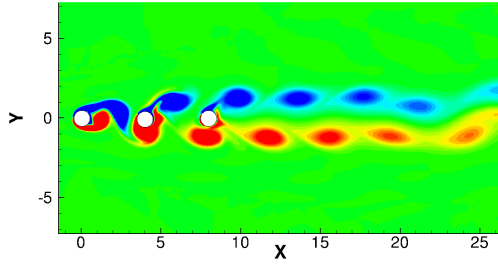
(a) $U_r = 2$.
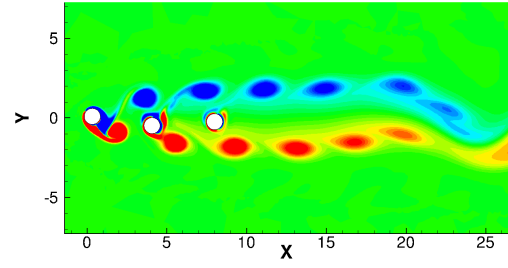
(b) $U_r = 4$.
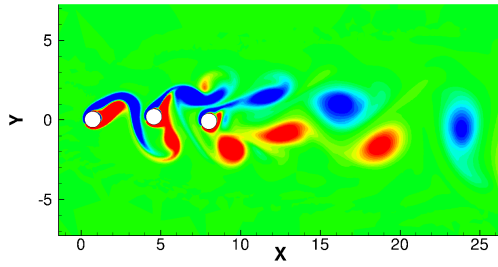
(c) $U_r = 6$.
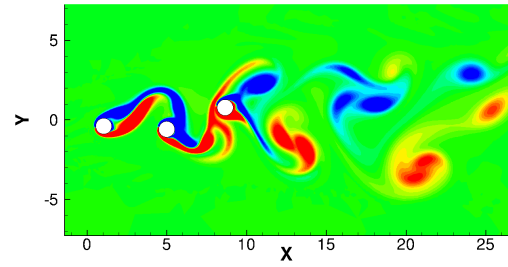
(d) $U_r = 8$.
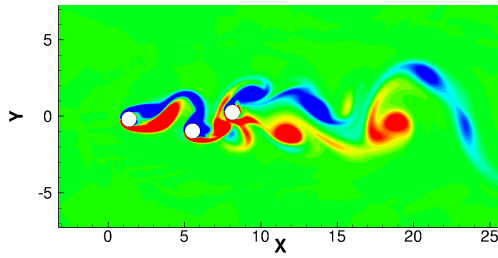
(e) $U_r = 10$.
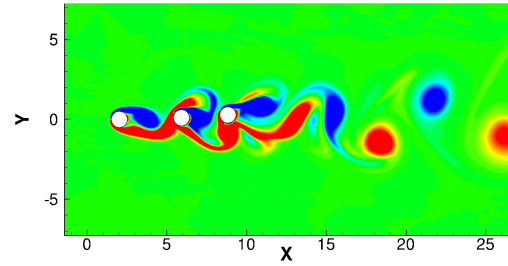
(f) $U_r = 12$.

Figure 6.37 Three in-line cylinders : Vortical structure pattern : At $Re = 150$.

third cylinders are bounded inside the two rows of C1-vortices coming from the upstream, similar to the third cylinder at $U_r = 2$. The motions of the second and the third cylinders appear to be strongly affected by the outer C1-vortex bounds. The C2-vortices are rather weak and they merge with the C1-vortices. The C3-vortices seem to be weaker than the C2-vortices and they do not extend far enough to merge with the outer C1-vortex bounds. One feature about the C3-vortices is that their orientation seems to be "rotated" by the C1-vortex bounds. If the incoming flow direction is 0° and the downstream flow direction is $\pm 180^o$, the C3-vortices appear to be shedded at around $\pm 100^o$. Possibly, the outer C1-vortices and these "rotated" C3-vortices are the driving frequencies of the quasi-periodic responses in the streamwise direction. At around $20D$ from the first cylinder, the C1-vortex bounds begin to approach to each other.

The vortex shedding pattern at $U_r = 6$ is shown in figure 6.37(c). From table 6.6, the dynamical characteristics are either the quasi-periodic or the chaotic types. The C1-vortices are noticeably stronger and longer. However, at $U_r = 6$, the second cylinder begins to synchronize and has large transverse motions. Hence, the C1-vortices can no longer completely enclose the second cylinder. Often, the oscillating second cylinder cuts off the "tail" of the C1-vortices. The shedded C1-vortices merge with the C2-vortices and either form a large round vortex or a slender long vortical structure, which may split into two medium round vortices. Greatly disturbed by these combined C1C2-vortices, the C3-vortices appear to be rather irregular. The third cylinder may either be "guided" through the complex C1C2-vortices or be directly attracted towards them. The C1C2-vortices seem to enclose the third cylinder. These complex motions agrees well with the rich and broad frequency spectrum observed for the third cylinder at this reduced velocity. Again, the C3-vortices are comparatively weaker than those from the two upstream cylinders. The C3-vortices may again merge with the C1C2-vortices. The vortical structure patterns behind the third cylinder do not show any particular organization.

The vortex shedding pattern at $U_r = 8$ is shown in figure 6.37(d). The overall wake region is very wide. From table 6.6, the dynamical characteristics are also mostly of the quasi-periodic and the chaotic types, except in the transverse direction of the first cylinder which has P-1 type dynamics. The C1-vortices are quite similar to those at $U_r = 6$. The second cylinder now seems to "follow" the tail of the C1-vortices. When the C1-vortices merge with the C2-vortices, they more often form a long slender vortical structure, instead of a larger rounder one. The motions of the third cylinder are influenced strongly by the merged C1C2-vortices. However, the third cylinder is not enclosed between the "C1C2-vortex bound" anymore. The C3-vortices are now noticeably stronger. They join the C1C2-vortices and form a trail of complex clusters of vortices, each may contain one to three vortices of different sizes

with the same rotation orientation.

In figure 6.37(e), the vortex shedding pattern at $U_r = 10$ is shown. The overall wake region now becomes narrower. From table 6.6, the dynamical characteristics are mainly of the higher period-n type. The first cylinder is desynchronized at $U_r = 10$. The C1-vortices are much more gentle and very steady. They almost directly impinge on the front of the second cylinder, and they merge with the C2-vortices. The merged C1C2-vortices seem to strongly attract the third cylinder to move upstream towards the second cylinder. As it gets closer, the presence of the third cylinder disturbs the forming of C2-vortices. The C1C2-vortices are weaken which reduces the attraction. Hence, the third cylinder flows back towards downstream and the complex cycle restarts. The C1C2-vortices do not always merge with C3-vortices.

Lastly in figure 6.37(f), the vortex shedding pattern at $U_r = 12$ is shown. From table 6.6, the dynamical characteristics are of the quasi-periodic for the first two cylinders and the chaotic type for the third cylinder. The width of the wake region is comparable to that at $U_r = 10$. The C1-vortices are steady and gentle. The second and the third cylinders switch between two movements alternatively: they either move together synchronously in the same transverse direction, or against each other in an out-of-phase manner. In figure 6.37(f), the two cylinders are moving upward together. The vortical structures are joined or splitted accordingly. The second and the third cylinders are also drawn upstream towards the corresponding cylinder by the vortices. As the gap distance is reduced, the vortices are weaken as well which "releases" the cylinders to move downstream. This seems to be related to the motion switching. The vortical structure behind the third cylinder is often the 2S. Some more random vortical structures can be observed as well in particular during motion switching.

These sample vortical structure patterns confirm that the flow characteristics around three freely oscillating cylinders are indeed very rich. When the dynamical characteristic is more complex, there are also large variations in the vortices surrounding the cylinders. These variations complicate the task of pattern recognition and classification. Clearly, each of the various types of dynamical characteristic does not express itself in the vortical structure patterns in an obvious one-to-one fashion, except perhaps those of the lower period-n types. It demands further investigations to shed some more light on this subject.

In the online version of the article, a video of the vortical structure patterns of three freely oscillating cylinders at $Re = 150$ and $U_r = 8$ is provided.

6.6   Conclusion

In the present study, we numerically explore the free oscillation responses of three circular cylinders placed in an in-line configuration subject to a uniform flow at low Reynolds numbers. The motivation is based on the recent understanding of the phenomenon of wake-induced vibrations of a tandem cylinder pair. It is well known that the downstream cylinder can experience very large transverse oscillations. It is of our interests to explore if the results of the tandem cylinder pair can be simply extrapolated to provide a good estimate for the responses of multiple in-line cylinders. A recent original experiment, with multiple collinear cylinders in uniform flow by Oviedo-Tolentino *et al.* (2013), confirms that the cylinders behind the second one can develop transverse oscillations that are even larger than those of the second cylinder. Many important aspects, e.g. low mass ratio, low mass-damping factor, the maximum amplitude, and effect of Reynolds number, etc., deserve further investigations. The present study aims to examine the free oscillation characteristics of three in-line cylinders when the mass-damping factor is at the smallest limiting case of "zero".

Our results show that the addition of the third cylinder behind a tandem cylinder pair introduces significantly different dynamic behaviors as compared with those of the tandem cylinder pair.

Overall, there are higher levels of fluctuations for both the streamwise and transverse maximum oscillation amplitudes as compared with those of the tandem cylinder pair. The profile of the maximum transverse oscillation amplitude generally resembles to the tandem case and there is an increase in the peak value of about 30%. On the other hand, the trend of the maximum streamwise oscillation amplitude shows considerable differences. In particular, significant oscillations now appear in the streamwise direction at the reduced velocity above $U_r \approx 9$. This is in contrast to what can be observed in Oviedo-Tolentino *et al.* (2013) with $L/D = 6$ that the streamwise oscillations are at most half of those of the transverse oscillations. If one would have estimated the triple cylinders response simply by putting a larger safety factor onto the responses of the tandem cylinder pair, it will result in significant errors.

The displacement trajectories of the triple cylinders differ greatly from those of the tandem cylinder pair. For all the Reynolds numbers investigated, the displacement trajectories of the freely oscillating tandem cylinder pair mostly follow the classical "figure-8" path. Many of the displacement trajectories of the triple cylinders can be practically described as "bounded random movements".

Regarding the force coefficients, the profile of the lift force coefficients of the triple cylinders case are rather similar to those of the tandem cylinder pair. On the other hand, the

drag force coefficients have more differences, in particular at the low ($U_r < 4$) and the high reduced velocity ($U_r > 8$) range. Interestingly, there is no significant increase observed for the triple cylinders case over those of the tandem cylinder pair in terms of peak force coefficient magnitude. Overall, there is again a much higher degree of fluctuations observed as compared with the tandem cylinder responses.

The main characteristic in the frequency responses of the triple cylinders case is that they have a wide response range at each reduced velocity. In other words, there are more frequencies excited for the three in-line cylinders case. In particular, the frequency responses of the third cylinder at high reduced velocities are so wide that they essentially cover the entire frequency spectrum. Another distinctive characteristic is that there is a clear low frequency component in the responses. This low frequency component is more observable in the streamwise direction and in some cases, it becomes the dominant frequency component. This is in sharp contrast to the single oscillation frequency reported in the work by Oviedo-Tolentino *et al.* (2013) with $L/D = 6$.

The phase portraits and the Poincaré maps of the three freely oscillating in-line cylinders confirm that there are significantly higher levels of nonlinearity for the free oscillations of three in-line cylinders. Even at such low Reynolds numbers, the free oscillations of three in-line cylinders already seem to approach a chaotic response. In particular, there is evidence that the fluid-structure system approaches to chaos via the quasi-periodic route.

The nonlinearity of the overall system originates from the flow. The vortical structure patterns confirm that when the dynamical characteristic is more complex, there are indeed large variations of vortices surrounding the cylinders, in particular, for the second and the third ones.

The free oscillation responses of three in-line cylinders are much more complex than those of the tandem cylinder pair. There are excessive oscillations in both the streamwise and transverse directions which can result in significant material stress and also greatly increase the probabilities of collisions causing further damages. The fluid-structure system also approaches towards chaos and it is well known that prediction of a chaotic system is essentially not possible. Control of a chaotic system also requires different strategies and methods, a further challenge. We conclude that predicting the free oscillation behavior of multiple in-line cylinders by extrapolating those behaviors of the simpler freely oscillating tandem cylinder pair is highly risky due to the effects of nonlinearities.

6.7 Acknowledgments

REFERENCE

ASSI, G., BEARMAN, P., CARMO, B., MENEGHINI, J., SHERWIN, S. & WILLDEN, R. (2013). The role of wake stiffness on the wake-induced vibration of the downstream cylinder of a tandem pair. *Journal of Fluid Mechanics*, 718, 210 – 45.

BAO, Y., HUANG, C., ZHOU, D., TU, J. & HAN, Z. (2012). Two-degree-of-freedom flow-induced vibrations on isolated and tandem cylinders with varying natural frequency ratios. *Journal of Fluids and Structures*, 35, 50–75.

BOKAIAN, A. & GEOOLA, F. (1984). Wake-induced galloping of two interfering circular cylinders. *Journal of Fluid Mechanic*, 146, 383–415.

BORAZJANI, I. & SOTIROPOULOS, F. (2009). Vortex-induced vibrations of two cylinders in tandem arrangement in the proximity - wake interference region. *Journal of Fluid Mechanics*, 621, 321 – 364.

BRIKA, D. & LANEVILLE, A. (1999). The flow interaction between a stationary cylinder and a downstream flexible cylinder. *Journal of Fluids and Structures*, 13, 579–606.

CARMO, B., MENEGHINI, J. & SHERWIN, S. (2010a). Possible states in the flow around two circular cylinders in tandem with separations in the vicinity of the drag inversion spacing. *Physics of Fluids*, 22, 054101 (7 pp.).

CARMO, B. S., MENEGHINI, J. R. & SHERWIN, S. J. (2010b). Secondary instabilities in the flow around two circular cylinders in tandem. *Journal of Fluid Mechanics*, 644, 395–431.

DHATT, G. (1984). *The finite element method displayed.* Wiley, Chichester [West Sussex] ; New York.

DONÉA, J. (2003). *Finite element methods for flow problems.* Wiley, Chichester ; Hoboken, NJ.

ETIENNE, S., GARON, A. & PELLETIER, D. (2009). Perspective on the geometric conservation law and finite element methods for ALE simulations of incompressible flow. *Journal of Computational Physics*, 228, 2313–2333.

FONTAINE, E., MOREL, J., SCOLAN, Y. & RIPPOL, T. (2006). Riser interference and VIV amplification in tandem configuration. *International Journal of Offshore and Polar Engineering*, 16, 33–40.

GOVARDHAN, R. & WILLIAMSON, C. (2006). Defining the 'modified griffin plot' in vortex-induced vibration: revealing the effect of reynolds number using controlled damping. *Journal of Fluid Mechanics*, <u>561</u>, 147 – 80.

HAIRER, E. (2010). *Stiff and differential-algebraic problems.* Springer, Berlin.

HARICHANDAN, A. B. & ROY, A. (2010). Numerical investigation of low reynolds number flow past two and three circular cylinders using unstructured grid CFR scheme. *International Journal of Heat and Fluid Flow*, <u>31</u>, 154–171.

HAY, A., ETIENNE, S. & PELLETIER, D. (2014). Time-integration for incompressible viscous flows: Stepsize and order selection based on the BDF. *32nd AIAA Applied Aerodynamics Conference*, American Institute of Aeronautics and Astronautics, AIAA Aviation.

IGARASHI, T. & SUZUKI, K. (1984). Characteristics of the flow around three circular cylinders arranged in line. *Bulletin of the Japan Society of Mechanical Engineers*, <u>27</u>, 2397 – 404.

JAUVTIS, N. & WILLIAMSON, C. H. K. (2004). The effect of two degrees of freedom on vortex-induced vibration at low mass and damping. *Journal of Fluid Mechanics*, <u>509</u>, 23–62.

KHALAK, A. & WILLIAMSON, C. H. K. (1999). Motions, forces and mode transitions in vortex-induced vibrations at low mass-damping. *Journal of Fluids and Structures*, <u>13</u>, 813–851.

LACROIX, M. & GARON, A. (1992). Numerical solution of phase change problems. an eulerian-lagrangian approach. *Numerical Heat Transfer, Part B: Fundamentals*, <u>21</u>, 57 – 78.

LEONTINI, J. S., THOMPSON, M. & HOURIGAN, K. (2007). Three-dimensional transition in the wake of a transversely oscillating cylinder. *Journal of Fluid Mechanics*, <u>577</u>, 79 – 104.

MENEGHINI, J., SALTARA, F., SIQUEIRA, C. & FERRARI, J. (2001). Numerical simulation of flow interference between two circular cylinders in tandem and side-by-side arrangements. *Journal of Fluids and Structures*, <u>15</u>, 327–350.

MIZUSHIMA, J. & SUEHIRO, N. (2005). Instability and transition of flow past two tandem circular cylinders. *Physics of Fluids*, <u>17</u>.

MODARRES-SADEGHI, Y., CHASPARIS, F., TRIANTAFYLLOU, M., TOGNARELLI, M. & BEYNET, P. (2011). Chaotic response is a generic feature of vortex-induced vibrations of flexible risers. *Journal of Sound and Vibration*, 330, 2565 – 79.

MOON, F. C. (1992). *Chaotic and fractal dynamics: an introduction for applied scientists and engineers*. Wiley, New York.

OVIEDO-TOLENTINO, F., ROMERO-MÉNDEZ, R., HERNÁNDEZ-GUERRERO, A. & PÉREZ-GUTIÉRREZ, F. (2013). Vortex-induced vibration of a collinear array of bottom fixed flexible cylinders. *Journal of Fluids and Structures*, 39, 1–14.

PAIDOUSSIS, M. P., PRICE, S. & DE LANGRE, E. (2011). *Fluid-structure interactions: cross-flow-induced instabilities*. Cambridge University Press, New York.

PAPAIOANNOU, G. V., YUE, D. K. P., TRIANTAFYLLOU, M. S. & KARNIADAKIS, G. E. (2008). On the effect of spacing on the vortex-induced vibrations of two tandem cylinders. *Journal of Fluids and Structures*, 24, 833 – 854.

PRASANTH, T. & MITTAL, S. (2008). Vortex-induced vibrations of a circular cylinder at low reynolds numbers. *Journal of Fluid Mechanics*, 594, 463 – 91.

PRASANTH, T. & MITTAL, S. (2009). Flow-induced oscillation of two circular cylinders in tandem arrangement at low re. *Journal of Fluids and Structures*, 25, 1029 – 48.

RUSCHEWEYH, H. (1983). Aeroelastic interference effects between slender structures. *Journal of Wind Engineering and Industrial Aerodynamics*, 14, 129–147.

SACKINGER, P., SCHUNK, P. & RAO, R. (1996). A newton-raphson pseudo-solid domain mapping technique for free and moving boundary problems: A finite element implementation. *Journal of Computational Physics*, 125, 83–103.

SARPKAYA, T. (2010). *Wave forces on offshore structures*. Cambridge, New York, NY.

SCHLICHTING, H. & GERSTEN, K. (2000). *Boundary-layer Theory*. Springer, Berlin.

SLAOUTI, A. & STANSBY, P. K. (1992). Flow around two circular cylinders by the random-vortex method. *Journal of Fluids and Structures*, 6, 641 – 670.

SUMNER, D. (2010). Two circular cylinders in cross-flow: A review. *Journal of Fluids and Structures*, 26, 849–99.

TASAKA, Y., KON, S., SCHOUVEILER, L. & LE GAL, P. (2006). Hysteretic mode exchange in the wake of two circular cylinders in tandem. *Physics of Fluids*, 18.

THOMSEN, J. J. (2003). *Vibrations and stability: advanced theory, analysis, and tools.* Springer, Berlin ; New York, seconde edition.

ZDRAVKOVICH, M. (1988). Review of interference-induced oscillations in flow past two circular cylinders in various arrangements. *Journal of Wind Engineering and Industrial Aerodynamics*, 28, 183–200.

ZDRAVKOVICH, M. & PRIDDEN, D. (1977). Interference between two circular cylinders, series of unexpected discontinuites. *Journal of Industrial Aerodynamics*, 2, 255–270.

CHAPTER 7

SUMMARY AND DISCUSSION

In this chapter, we will summarize and discuss the principal results of the present investigation.

7.1 Two degrees of freedom vortex-induced vibration response at low Reynolds number

After the numerical code has been verified, we first establish the limiting two degrees of freedom (transverse and streamwise) (XY oscillation) responses of vortex-induced vibrations of a cylinder with zero mass ratio and zero damping in the following parameter space: Reynolds number ($75 \leq Re \leq 175$), reduced velocity ($5.0 \leq U_r \leq 11.0$). To better compare the results, we also investigate the two degrees of freedom responses with $m^* = 1$ and the responses of transverse-only (Y-only) oscillations for both mass ratios. We have studied various aspects of vortex-induced vibration response: the maximum amplitude, the frequency response, the displacement trajectory, the force coefficient phase relationship, the change of total phase angle (between the lift force and the transverse displacement) and the vortical structure pattern. The obtained results are generally in accordance with those in the literature. The maximum amplitude response of the XY oscillation is larger than that of the Y-only oscillation. For the XY oscillation, the transverse amplitude is much larger than that of the streamwise amplitude. On the other hand, the oscillation frequency of the transverse only oscillation is greater than that of the XY oscillation. Hysteretic responses are observed and they are associated with differences in the vortical structure pattern observed for the increasing and decreasing directions. We only observe the 2S and the C(2S) modes. The present results compare well with those of the forced vibration at $Re = 100$.

At $m^* = 0$, the maximum amplitude of the XY oscillation exhibits a peak of $0.9D$, a significant 50% increase from the $0.6D$ reported previously in the laminar shedding regime. As the mass ratio is increased, the peak maximum amplitudes decrease for both the XY and Y-only oscillations. In particular, the peak amplitude of the XY oscillation decreases more rapidly than that of the Y-only oscillation. Generally, the maximum amplitude responses show an increase of amplitude when the Reynolds number is increased. For the XY oscillations, the amplitude increase is substantial. For the transverse only responses, a definitive gentle increase can also be observed. This behavior differs markedly from that

observed by Williamson & Govardhan (2006) which indicates that the maximum amplitude is not influenced by the Reynolds number in the laminar shedding regime. Besides, the peak maximum amplitude location does not always appear at a fixed reduced velocity value. This is most evident from the XY oscillation response with $m^* = 0$. This is in contrast to what is observed by Etienne & Pelletier (2012) who found that the maximum amplitude always appears at the reduced velocity of 6.5 for very low Reynolds number (< 50). As a result, when we attempt to determine the peak maximum value across a range of Reynolds number, we should not assume that the peak maximum will be located at the same value of the reduced velocity.

It is evident that the results in this study show two main patterns with respect to the mass ratio. This indicates that the investigated mass ratio values encompass the critical mass ratio. We estimate that the critical mass ratio is about 0.106 for XY oscillation and 0.117 for transverse only oscillation. If the synchronization limit of the XY oscillation is similar to that of the Y-only oscillation, then it is reasonable to observe that the critical mass ratio for the XY oscillation be smaller than that of the transverse only.

There is no discontinuity observed in this study, except at the desynchronization. Hence, the traditional branch identification approach in the experiments, which relies on response discontinuity, cannot be applied in a straightforward manner. Based on the analysis of the vortical structure patterns, it seems that it may be a viable alternative to be used as the branch separation boundary.

7.2   Comparison with results at high Reynolds number

The principal difference between the results at low Reynolds number and those at high Reynolds number is that there is no discontinuity in the response. The maximum oscillation amplitude response of the two degrees of freedom vortex-induced vibration at high Reynolds numbers have been shown in figure 2.9. The super-upper branch is not observed in the low Reynolds number results, and neither does the upper branch at least in the traditional sense. Regarding the frequency result, we can see that the low Reynolds number results seems to resemble closer to those experimental results at higher Reynolds number with a mass ratio of $m^* = 2.4$ which is shown in figure 2.7. The vortex shedding patterns differ more significantly. At high Reynolds, the 2T pattern can be seen while at low Reynolds number only the 2S and C(2S) patterns are observed. The critical mass ratio at the high Reynolds number is about $m^* = 0.52$ while those at low Reynolds number are about $m^* \approx 0.1$.

On the other hand, the trend in the difference between the XY and the Y-only oscillation at low Reynolds numbers does resemble that at high Reynolds number. The effect of the

mass ratio and the existence of the critical mass ratio are also similar. The phase plot of the displacements at high Reynolds number can also be found in the low Reynolds number results. Moreover, the results regarding the jumps in the total phase angle at low Reynolds number of a cylinder with $m^* = 1$, which occur at around $U_r \approx 11.0$, correspond relatively well to those at the high Reynolds number of a cylinder with $m^* = 2.6$, which occurs at around $U_r \approx 8.5$ (Jauvtis & Williamson (2004)). Hence, if we compare beyond the detailed differences mentioned above, we can definitely say that the low Reynolds number results do contain the basic characteristics of those responses at high Reynolds number qualitatively. From this perspective, the accurately determined simulation results at low Reynolds numbers may be considered as a "model" for the responses at high Reynolds numbers that does not required any coefficient tuning. One simply needs to bare in mind that the low Reynolds number responses are generally "smoother" and "softer" than those at high Reynolds number.

7.3   Wake-induced vibration responses of three in-line cylinders

Lastly, we numerically examine the free oscillation responses of three circular cylinders placed in an in-line configuration subject to a uniform flow at low Reynolds numbers. For the exploration of the wake-induced vibration responses of three in-line cylinders, we again carry out a parametric study with respect to the Reynolds number $Re = \{100, 150, 200\}$ and the reduced velocity $(2.0 \leq U_{r_n} \leq 13.0)$. We consider three identical cylinders of low mass ratio $(m^* = 4/\pi)$ with zero damping. The separation ratio is kept constant at $L/D = 4$ which is at the boundary between the proximity and wake interference regions for a tandem cylinder pair, to provoke richer fluid dynamic interactions. Our results show that the addition of the third cylinder after a tandem cylinder pair introduces significantly different dynamic behaviors as compared with those of the tandem cylinder pair.

   Overall, there are higher levels of fluctuations for both the streamwise and transverse maximum oscillation amplitudes as compared with those of the tandem cylinder pair. The profile of the maximum transverse oscillation amplitude generally resembles to the tandem case and there is indeed an increase in the peak value of about 30%. On the other hand, the trend of the maximum streamwise oscillation amplitude shows considerable differences. In particular, significant oscillations now appear in the streamwise direction at above the reduced velocity $(U_r \approx 9)$ which can be as large as those in the transverse direction. This is in contrast to what can be observed in Oviedo-Tolentino et $al.$ (2013) with $L/D = 6$ that the streamwise oscillations are at most half of those of the transverse oscillations. If one would have estimated the triple cylinders response simply by putting a larger safety factor onto the responses of the tandem cylinder pair, it will result in significant errors.

The displacement trajectories of the triple cylinders differ greatly from those of the tandem cylinder pair. For all the Reynolds numbers investigated, the displacement trajectories of the freely oscillating tandem cylinder pair mostly follow the classical "figure-8" path. Many of the displacement trajectories of the triple cylinders can be practically described as bounded random movements.

Regarding the force coefficients, the profile of the lift force coefficients of the triple cylinders case are rather similar to those of the tandem cylinder pair. On the other hand, the drag force coefficients have more differences, more specifically at the low ($U_r < 4$) and the high reduced velocity ($U_r > 8$) range. In terms of peak force coefficient magnitude, there is no significant increase observed for the triple cylinders case over those of the tandem cylinder pair. Overall, there are again much higher degrees of fluctuations observed as compared with the tandem cylinder responses.

The main difference in the frequency responses of the triple cylinders case generally have wider ranges at each reduced velocity as compared with those of the tandem cylinders. In other words, there are more frequencies excited for the three in-line cylinders case. In particular, the frequency responses of the third cylinder at high reduced velocities are so wide that they essentially cover the entire frequency spectrum. Another distinctive difference is that there is a clear low frequency component in the responses. This low frequency component is more observable in the streamwise direction and in some cases, it becomes the dominant frequency component. This is in sharp contrast to the single oscillation frequency reported in the work by Oviedo-Tolentino *et al.* (2013) with $L/D = 6$.

The phase portraits and the Poincaré maps of the three freely oscillating in-line cylinders confirm that there are significantly higher levels of nonlinearity for the free oscillations of three in-line cylinders. Even at such low Reynolds numbers, the free oscillations of three in-line cylinders already seem to approach a chaotic response. In particular, there is evidence that fluid-structure system approaches to chaos via the quasi-periodic route.

The nonlinearity of the overall system originates from the flow. The vortical structure patterns confirm that when the dynamical characteristic is more complex, there are indeed large variations of vortices surrounding the cylinders, in particular, for the second and the third ones.

The free oscillation responses of three in-line cylinders are much more complex than those of the tandem cylinder pair. There are excessive oscillations in both the streamwise and transverse directions which can result in significant material stress and also greatly increase the probabilities of collisions causing further damages. The fluid-structure system also approaches towards chaos and it is well known that prediction of a chaotic system is essentially not possible. Control of a chaotic system also requires different strategies and

methods, a further challenge. Based on our earlier results of the vortex-induced vibration responses at low Reynolds number, we can expect that the free oscillation responses of three in-line cylinders will be even more complex and severe as the Reynolds number increases. We can deduce that due to such high level of nonlinearities, it is therefore highly risky to predict the free oscillation behaviors of multiple in-line cylinders by extrapolating those of the tandem cylinder pair.

CHAPTER 8

CONCLUSION

In this chapter, we summarize the present investigation and outline several directions that can be pursued in the future.

8.1 Summary

This thesis aims to numerically explore the wake-induced vibration responses of three circular cylinders with low mass ratio and zero damping arranged in-line at low Reynolds numbers in order to advance the fundamental engineering knowledge regarding multiple elastically mounted bodies arranged in-line placed in a cross flow. To reach this research goal, we have identified three specific objectives.

We first verify the correctness of the numerical code using the method of manufactured solution for fluid-structure interaction problems; for which the structure can be modeled as a rigid body. The manufactured solution for this class of fluid-structure interaction problem has not yet been reported. We have developed a generic systematic synthesis procedure to construct manufactured solution which can be well applied to any fluid-structure interaction problem. The procedure involves first combining relevant one dimensional solutions together to form a base solution and then applying the base solution in a rotated coordinate to satisfy the general requirement that all terms in the governing equations to be non trivial. We demonstrate the feasibility of the synthesis procedure with two dimensional and three dimensional problems.

Then, we establish the limiting vortex-induced vibration response characteristics of an isolated cylinder with zero mass ratio, which can freely oscillate in both the streamwise and the transverse directions (XY oscillation) at low Reynolds numbers. This is needed since the responses of wake-induced vibrations are often compared with those of vortex-induced vibrations, and the results for vortex-induced vibrations of an isolated cylinder with low mass ratio at low Reynolds numbers are rather scattered. More specifically, we perform a parametric study with respect to the Reynolds number and the reduced velocity. For comparisons, we also determine the XY oscillation responses with $m^* = 1$, and the responses of transverse-only (Y-only) oscillation with both mass ratios. We observe that for a cylinder with zero mass ratio, the maximum XY oscillation amplitude is about $A_Y = 0.9D$ and for Y-only oscillation, it is about $A_Y = 0.6D$. In particular, in contrast to the results reported in

the literature, we observe that at the laminar flow regime, the vortex-induced vibration results is also affected by an increase of Reynolds number. Also, the location of the peak oscillation amplitude will not always occur at the same reduced velocity for all Reynolds number. The critical mass ratio for Y-only oscillation is about $m^*_{critical} \approx 0.117$ and $m^*_{critical} \approx 0.106$ for the XY oscillation.

A comparison between our present results with the experimental results of an isolated cylinder, with small mass ratio at moderately high Reynolds numbers, demonstrates that although the two responses are not entirely the same, the low Reynolds number responses do carry the essential of the high Reynolds number response characteristics. Therefore, simulations at low Reynolds numbers for the problems of vortex-induced vibrations, and naturally for wake-induced vibration as well, shall be able to qualitatively represent the overall characteristics of the oscillation responses at higher Reynolds numbers.

Finally, we examine the wake-induced vibration responses of three circular cylinders with low mass ratio arranged in-line at low Reynolds number. We compare the results of the three freely oscillating cylinders arranged in-line with those of a tandem cylinder pair and those of an isolated cylinder under the same conditions. The presence of the third cylinder induces distinctive response differences as compared to the case of the tandem cylinder pair. The maximum oscillation amplitude has been increased for about 30% in the transverse direction. However, significant oscillations now appear in the streamwise direction at above the reduced velocity of $U_r \approx 9$ which can be as large as those in the transverse direction. These excessive oscillations in both the streamwise and transverse directions can result in significant material stress and also greatly increase the probabilities of collisions causing further damages. Another interesting characteristic is that the frequency spectrum of the response is generally very rich and there is now a clear dominant low frequency component, in particular for the second and the third cylinders. Overall, the phase diagram and the Poincaré map show that the nonlinearity has been increased dramatically with the introduction of the third cylinder. This is confirmed with the substantial variations observed in the vortical structure pattern. Even at such low Reynolds numbers, the free oscillations of three in-line cylinders already seem to approach a chaotic response. In particular, there is evidence that fluid-structure system approaches to chaos via the quasi-periodic route. Based on our earlier results of the vortex-induced vibration responses at low Reynolds number, we can expect that the free oscillation responses of three in-line cylinders will be even more complex and severe as the Reynolds number increases. We conclude that due to such high level of nonlinearities, it is therefore highly risky to predict the free oscillation behaviors of multiple in-line cylinders by extrapolating those of the tandem cylinder pair. The effect of wake-induced vibrations must be properly addressed when multiple in-line bodies may be subjected to a cross flow.

8.2   Future work

The exploration can be extended in several different directions.

We have focused in low Reynolds number flows. Naturally, one direction will be pushing towards higher Reynolds number flow conditions. Regarding the vortex-induced vibration responses, at what Reynolds number will the "regular" upper branch start to appear? And for the wake-induced vibration responses, at what Reynolds number will we begin to observe significantly different results?

Similarly, we can consider higher values of reduced velocity for the wake-induced responses. In particular, both the second and the third cylinders do not fully desynchronized. Will they ever desynchronize at a higher reduced velocity?

We have only considered several particular values of mass ratio. As demonstrated in the two degrees of freedom vortex-induced vibration study, the mass ratio has a strong influence onto the oscillation responses characteristics. It would be worthwhile to perform a parametric study with respect to mass ratio. In particular, how would the wake-induced vibration response change when the mass ratio is at its theoretical minimum of zero?

For the wake-induced vibration response, it can also be extended to examine the responses of different separation ratios. It has been demonstrated that the wake-induced vibration response is strongly dependent on the separation ratio. It will certainly be rewarding to investigate further how the separation ratio will affect the three in-line oscillation response.

In the present investigation, we have assumed that the flow remains dominantly two dimensional. While the assumption is certainly reasonable, it may be important to confirm at what Reynolds number will we begin to have strong three dimensional vortical structure such that we must consider three dimensional simulations.

Finally, it can be expected that collision between the cylinders will occur sooner or later as the Reynolds number or the reduced velocity further increases. The Lagrangian moving boundary management scheme considered in the present investigation unfortunately will not be an ideal choice for such collision condition. Therefore, it will be essential to determine how well the Eulerian moving boundary management scheme, which can handle multiple objects collision much more naturally, can perform to examine the oscillation characteristics and in particular to determine the force coefficients onto the cylinders.

REFERENCES

AGLEN, I. M. & LARSEN, C. M. (2011). Importance of added mass for the interaction between IL and CF vibrations of free spanning pipelines. *Proceedings of the ASME 2011 30th International Cconference on Ocean. Offshore and Arctic Engieering - OMAE.* ASME, New York, NY, vol. **7** of *CFD and VIV*, 545–556.

ALAM, M., MORIYA, M., TAKAI, K. & SAKAMOTO, H. (2003). Fluctuating fluid forces acting on two circular cylinders in a tandem arrangement at a subcritical reynolds number. *Journal of Wind Engineering and Industrial Aerodynamics*, <u>91</u>, 139 – 54.

ALAM, M. M. & ZHOU, Y. (2007). Phase lag between vortex shedding from two tandem bluff bodies. *Journal of Fluids and Structures*, <u>23</u>, 339 – 347.

ANAGNOSTOPOULOS, P. & BEARMAN, P. (1992). Response characteristics of a vortex-excited cylinder at low Reynolds-numbers. *Journal of Fluids and Structures*, <u>6</u>, 39–50.

ASSI, G., BEARMAN, P., CARMO, B., MENEGHINI, J., SHERWIN, S. & WILLDEN, R. (2013). The role of wake stiffness on the wake-induced vibration of the downstream cylinder of a tandem pair. *Journal of Fluid Mechanics*, <u>718</u>, 210 – 45.

BENAROYA, H. & WEI, T. (2000). Hamilton's principle for external viscous fluid–structure interaction. *Journal of Sound and Vibration*, <u>238</u>, 113–145.

BISHOP, R. E. D. & HASSAN, A. Y. (1964). The lift and drag forces on a circular cylinder in a flowing fluid. *Proceedings of the Royal Society A: Mathematical, Physical and Engineering Sciences*, <u>277</u>, 32–50.

BLEVINS, R. D. (2000). *Flow-induced vibration.* Krieger, Malabar, Fla.

BOKAIAN, A. & GEOOLA, F. (1984). Wake-induced galloping of two interfering circular cylinders. *Journal of Fluid Mechanic*, <u>146</u>, 383–415.

BORAZJANI, I. & SOTIROPOULOS, F. (2009). Vortex-induced vibrations of two cylinders in tandem arrangement in the proximity - wake interference region. *Journal of Fluid Mechanics*, <u>621</u>, 321 – 364.

BRIKA, D. & LANEVILLE, A. (1999). The flow interaction between a stationary cylinder and a downstream flexible cylinder. *Journal of Fluids and Structures*, <u>13</u>, 579–606.

CARMO, B., MENEGHINI, J. & SHERWIN, S. (2010). Possible states in the flow around two circular cylinders in tandem with separations in the vicinity of the drag inversion spacing. *Physics of Fluids*, 22, 054101 (7 pp.).

DET NORSKE VERITAS (2009). Recommended practice DNV-RP-f203 riser interference. Rapport technique.

ECA, L., HOEKSTRA, M., HAY, A. & PELLETIER, D. (2007). On the construction of manufactured solutions for one- and two-equation eddy-viscosity models. *International Journal for Numerical Methods in Fluids*, 54, 119 – 54.

ECA, L., HOEKSTRA, M. & VAZ, G. (2012). Manufactured solutions for steady-flow reynolds-averaged navier-stokes solvers. *International Journal of Computational Fluid Dynamics*, 26, 313 – 332.

ETIENNE, S., FONTAINE, E. & SCOLAN, Y.-M. (2009). Vortex- and wake-induced vibrations of two and three cylinders arranged in-line. *Proceedings of the International Offshore and Polar Engineering Conference*. International Society of Offshore and Polar Engineers., Osaka, Japan, 1358–1364.

ETIENNE, S., GARON, A. & PELLETIER, D. (2012). Some manufactured solutions for verification of fluid-structure interaction codes. *Computers and Structures*, 106-107, 56 – 67.

ETIENNE, S. & PELLETIER, D. (2012). The low Reynolds number limit of vortex-induced vibrations. *Journal of Fluids and Structures*, 31, 18–29.

FENG, C. C. (1968). *The measurement of vortex-induced effects in flow past a stationary and oscillating circular and D-section cylinders*. MS thesis, University of British Columbia, Vancouver, BC, Canada.

FEY, U., KÖNIG, M. & ECKELMANN, H. (1998). A new strouhal-reynolds-number relationship for the circular cylinder in the range $47 < \text{Re} < 2 \times 10^5$. *Physics of Fluids*, 10, 1547–1549.

FONTAINE, E., MOREL, J., SCOLAN, Y. & RIPPOL, T. (2006). Riser interference and VIV amplification in tandem configuration. *International Journal of Offshore and Polar Engineering*, 16, 33–40.

GABBAI, R. & BENAROYA, H. (2005). An overview of modeling and experiments of vortex-induced vibration of circular cylinders. *Journal of Sound and Vibration*, 282, 575–616.

GERRARD, J. H. (1966). The mechanics of the formation region of vortices behind bluff bodies. *Journal of Fluid Mechanics*, 25, 401.

GOVARDHAN, R. & WILLIAMSON, C. H. K. (2002). Resonance forever: existence of a critical mass and an infinite regime of resonance in vortex-induced vibration. *Journal of Fluids Mechanics*, 473, 147–166.

HAGER, G. (2011). *Introduction to high performance computing for scientists and engineers*. Chapman & Hall/CRC computational science series ; 7. CRC Press, Boca Raton, FL.

HALLAM, M. G., HEAF, N. J. & WOOTTON, L. R. (1977). Dynamics of Marine Structures. Report ur8, CIRIA Underwater Engineering Group, Atkins Research and Development, London, U.K.

HARICHANDAN, A. B. & ROY, A. (2010). Numerical investigation of low reynolds number flow past two and three circular cylinders using unstructured grid CFR scheme. *International Journal of Heat and Fluid Flow*, 31, 154–171.

HARTLEN, R. & CURRIE, I. (1970). Lift-oscillator model of vortex-induced vibration. *ASCE Journal of Engineering Mechanics*, 96, 577–591.

IGARASHI, T. & SUZUKI, K. (1984). Characteristics of the flow around three circular cylinders arranged in line. *Bulletin of the Japan Society of Mechanical Engineers*, 27, 2397 – 404.

ISHIGAI, S., NISHIKAWA, E., NISHIMURA, K. & CHO, K. (1972). Experimental study on structure of gas flow in tube banks with tube axes normal to flow : part i, karman vortex flow from two tubes at various spacings. *Bulletin of JSME*, 15, 949–956.

JAUVTIS, N. & WILLIAMSON, C. H. K. (2004). The effect of two degrees of freedom on vortex-induced vibration at low mass and damping. *Journal of Fluid Mechanics*, 509, 23–62.

KHALAK, A. & WILLIAMSON, C. H. K. (1999). Motions, forces and mode transitions in vortex-induced vibrations at low mass-damping. *Journal of Fluids and Structures*, 13, 813–851.

KNUPP, P. M. & SALARI, K. (2003). *Verification of computer codes in computational science and engineering*. Discrete mathematics and its applications. Chapman & Hall/CRC, Boca Raton, Fla.

LEE, T. & BASU, S. (1997). Nonintrusive measurements of the boundary layer developing on a single and two circular cylinders. *Experiments in fluids*, 23, 187–192.

LEONTINI, J. S., THOMPSON, M. & HOURIGAN, K. (2007). Three-dimensional transition in the wake of a transversely oscillating cylinder. *Journal of Fluid Mechanics*, 577, 79 – 104.

LIN, J.-C., YANG, Y. & ROCKWELL, D. (2002). Flow past two cylinders in tandem: instantaneous and averaged flow structure. *Journal of Fluids and Structures*, 16, 1059 – 1071.

MENEGHINI, J., SALTARA, F., SIQUEIRA, C. & FERRARI, J. (2001). Numerical simulation of flow interference between two circular cylinders in tandem and side-by-side arrangements. *Journal of Fluids and Structures*, 15, 327–350.

NEWMAN, D. & KARNIADAKIS, G. (1997). A direct numerical simulation study of flow past a freely vibrating cable. *Journal of Fluid Mechanics*, 344, 95–136.

OBERKAMPF, W. L. (2010). *Verification and validation in scientific computing.* Cambridge University Press, New York.

OVIEDO-TOLENTINO, F., ROMERO-MÉNDEZ, R., HERNÁNDEZ-GUERRERO, A. & PÉREZ-GUTIÉRREZ, F. (2013). Vortex-induced vibration of a collinear array of bottom fixed flexible cylinders. *Journal of Fluids and Structures*, 39, 1–14.

PAIDOUSSIS, M. P., PRICE, S. & DE LANGRE, E. (2011). *Fluid-structure interactions: cross-flow-induced instabilities.* Cambridge University Press, New York.

PAPAIOANNOU, G. V., YUE, D. K. P., TRIANTAFYLLOU, M. S. & KARNIADAKIS, G. E. (2008). On the effect of spacing on the vortex-induced vibrations of two tandem cylinders. *Journal of Fluids and Structures*, 24, 833 – 854.

PELLETIER, D. & ROACHE, P. J. (2009). Verification and validation of computational heat transfer. *Handbook of Numerical Heat Transfer*, John Wiley & Sons, Inc. 417–442.

PLACZEK, A., SIGRIST, J.-F. & HAMDOUNI, A. (2009). Numerical simulation of an oscillating cylinder in a cross-flow at low Reynolds number: Forced and free oscillations. *Computers & Fluids*, 38, 80–100.

PRASANTH, T. & MITTAL, S. (2008). Vortex-induced vibrations of a circular cylinder at low reynolds numbers. *Journal of Fluid Mechanics*, 594, 463 – 91.

PRASANTH, T. & MITTAL, S. (2009). Flow-induced oscillation of two circular cylinders in tandem arrangement at low re. *Journal of Fluids and Structures*, <u>25</u>, 1029 – 48.

PRASANTH, T., PREMCHANDRAN, V. & MITTAL, S. (2011). Hysteresis in vortex-induced vibrations: Critical blockage and effect of m. *Journal of Fluid Mechanics*, <u>671</u>, 207 – 225.

ROACHE, P. J. (1998). *Verification and validation in computational science and engineering.* Hermosapublishers, Albuquerque, N.M.

ROSHKO, A. (1961). Experiments on the flow past a circular cylinder at very high reynolds number. *Journal of Fluid Mechanics*, <u>10</u>, 345.

ROY, C., NELSON, C., SMITH, T. & OBER, C. (2004). Verification of Euler/Navier-Stokes codes using the method of manufactured solutions. *International Journal for Numerical Methods in Fluids*, <u>44</u>, 599 – 620.

RUSCHEWEYH, H. (1983). Aeroelastic interference effects between slender structures. *Journal of Wind Engineering and Industrial Aerodynamics*, <u>14</u>, 129–147.

SANCHIS, A., SæLEVIK, G. & GRUE, J. (2008). Two-degree-of-freedom vortex-induced vibrations of a spring-mounted rigid cylinder with low mass ratio. *Journal of Fluids and Structures*, <u>24</u>, 907–919.

SARPKAYA, T. (2004). A critical review of the intrinsic nature of vortex-induced vibrations. *Journal of Fluids and Structures*, <u>19</u>, 389–447.

SARPKAYA, T. (2010). *Wave forces on offshore structures.* Cambridge, New York, NY.

SCHEWE, G. (1983). On the force fluctuations acting on a circular cylinder in crossflow from subcritical up to transcritical reynolds numbers. *Journal of Fluid Mechanics*, <u>133</u>, 265.

SHIELS, D., LEONARD, A. & ROSHKO, A. (2001). Flow-induced vibration of a circular cylinder at limiting structural parameters. *Journal OF Fluids and Structures*, <u>15</u>, 3–21.

SHYY, W., UDAYKUMAR, H. S., RAO, M. M. & SMITH, R. W. (1996). *Computational Fluid Dynamics with Moving Boundaries.* Taylor and Francis, Washington, DC.

SINGH, S. & MITTAL, S. (2005). Vortex-induced oscillations at low Reynolds numbers: Hysteresis and vortex-shedding modes. *Journal of Fluids and Structures*, <u>20</u>, 1085 – 1104.

STAPPENBELT, B. & LALJI, F. (2008). Vortex-induced Vibration Super-Upper Response Branch Boundaries. *International Journal of Offshore and Polar Engineering*, <u>18</u>, 99–105.

SUMER, B. M. (2006). *Hydrodynamics around cylindrical structures.* No. v. 26 Advanced series on Ocean Engineering. World scientific publishing, Singapore ; London, revised edition.

SUMNER, D. (2010). Two circular cylinders in cross-flow: A review. *Journal of Fluids and Structures*, <u>26</u>, 849–99.

VAN DER STEEN, A. J. (2013). Overview of recent supercomputers. Rapport technique, EuroBen Foundation, Netherlands.

WILLIAMSON, C. H. K. (1989). Oblique and parallel modes of vortex shedding in the wake of a circular cylinder at low reynolds numbers. *Journal of Fluid Mechanics*, <u>206</u>, 579.

WILLIAMSON, C. H. K. (1996). Vortex dynamics in the cylinder wake. *Annual Review of Fluid Mechanics*, <u>28</u>, 477–539.

WILLIAMSON, C. H. K. & GOVARDHAN, R. (2004). Vortex-Induced Vibrations. *Annual Review of Fluid Mechanics*, <u>38</u>, 413–55.

WILLIAMSON, C. H. K. & GOVARDHAN, R. (2006). Defining the 'modified Griffin plot' in vortex-induced vibration: revealing the effect of Reynolds number using controlled damping. *Journal of Fluid Mechanics*, <u>561</u>, 147–180.

XU, G. & ZHOU, Y. (2004). Strouhal numbers in the wake of two inline cylinders. *Experiments in fluids*, <u>37</u>, 248–256.

ZDRAVKOVICH, M. (1985). Flow induced oscillations of two interfering circular cylinders. *Journal of Sound and Vibration*, <u>101</u>, 511–521.

ZDRAVKOVICH, M. (1988). Review of interference-induced oscillations in flow past two circular cylinders in various arrangements. *Journal of Wind Engineering and Industrial Aerodynamics*, <u>28</u>, 183–200.

ZDRAVKOVICH, M. & PRIDDEN, D. (1977). Interference between two circular cylinders, series of unexpected discontinuites. *Journal of Industrial Aerodynamics*, <u>2</u>, 255–270.

ZHOU, Y. & YIU, M. (2006). Flow structure, momentum and heat transport in a two-tandem-cylinder wake. *Journal of Fluid Mechanics*, <u>548</u>, 17 – 48.